SIZE DEPENDENT FAILURE CONSTRAINED TOPOLOGY OPTIMIZATION

APPROACHES

A Thesis

Submitted to the Faculty

of

Purdue University

by

Vincenzo G. Vernacchio

In Partial Fulfillment of the

Requirements for the Degree

of

Master of Science in Mechanical Engineering

May 2019

Purdue University

West Lafayette, Indiana

THE PURDUE UNIVERSITY GRADUATE SCHOOL
STATEMENT OF THESIS APPROVAL

Dr. Thomas Siegmund, Chair

     School of Mechanical Engineering

Dr. Ganesh Subbarayan

     School of Mechanical Engineering

Dr. Pablo Zavattieri

     Lyles School of Civil Engineering

Approved by:

     Dr. Jay Gore

          Head of the School of Mechanical Engineering Graduate Program

ACKNOWLEDGMENTS

I would like to express my sincerest gratitude for the time Professor T. Siegmund has invested in both my education and this work. His efforts have guided my growth as a researcher and allowed for my success in this endeavor. I would also like to thank Professor G. Subbarayan and Professor P. Zavattieri for evaluating my work as a part of my examination committee.

TABLE OF CONTENTS

LIST OF TABLES

LIST OF FIGURES

SYMBOLS

a	Assumed flaw size
α	Christensen brittleness factor
$\tilde{\alpha}$	Normalization evolution factor
B_e	Elemental strain-displacement matrix
β	Projection shape parameter
c_f	Limit process zone length for an infinitely large specimen
$\tilde{c}$	Stress normalization factor
C	Global structural compliance
C_{ijkl}	General elastic constitutive tensor
d_e	Local size width estimate
d^{PN}	Maximum radius constraint
D_0	Length scale parameter in TO formulation
$\boldsymbol{E}_e$	Parameterized plane-stress constitutive tensor
E_0	Isotropic elastic modulus
$\boldsymbol{E}_0$	Plane-stress constitutive tensor
ε	Strain tensor
ϵ_{min}	Design variable lower bound
ϵ_{max}	Design variable upper bound
η_K	Stiffness penalization function
η_S	Stress penalization function
η_v	Volume penalization function
$\tilde{\eta}$	Projection cutoff
$\boldsymbol{f}$	Global nodal force vector
$\boldsymbol{f}_e$	Elemental nodal force vector
F	Geometric correction factor

G_f Limit energy release rate for an infinitely large specimen

Γ_D Dirilecht boundary

Γ_N Neumann boundary

H Representative physical structural height

$\boldsymbol{K}$ Global stiffness matrix

$\boldsymbol{K}_e$ Elemental stiffness matrix

K_{Ic} Critical stress intensity factor

κ Size measure density penalization

$\tilde{\kappa}$ Christensen yield surface shape factor

L Representative physical structural length

$\boldsymbol{L}_e$ Elemental assembly matrix

m Weibull modulus

μ Volume penalization coefficient

N Number of elements in FE discretization

ν Poisson's ratio

Ω Allowable structural domain

P Applied structural load

p_n Constraint cluster penalization coefficient

p_{rad} Size measure penalization coefficient

ϕ Compliance penalization coefficient

ψ Stress penalization coefficient

r_b Size measure radius estimate

r_{min} Linear filter radius

r_{max} Size measure physical search radius

$\boldsymbol{\rho}$ Projected elemental density

$\tilde{\boldsymbol{\rho}}$ Filtered elemental density

$\boldsymbol{\sigma}$ Continuum stress tensor

$\hat{\boldsymbol{\sigma}}$ Integration point stress tensor

$\tilde{\sigma}^{frac}$ Tensile fracture constraint

$\tilde{\sigma}^{Ch}$ Christensen general yield constraint

ς^f General limiting strength value

ς_C Limiting compression strength

ς_{T_0} Tensile strength parameter in TO formulation

Θ Size measure search direction

$\boldsymbol{u}$ Global nodal displacement vector

v_e Element volume

V Global structural volume

$\overline{V}$ Allowable structural volume

x_e Elemental design variable

ABBREVIATIONS

AM	Additively Manufactured
CAE	Computer Aided Engineering
DENT	Double Edge Notched Tension
FE	Finite Element
FPZ	Fracture Process Zone
KS	Kreisselmeier-Steinhauser
KKT	Karush-Kuhn-Tucker
LEFM	Linear Elastic Fracture Mechanics
MMA	Method of Moving Asymptotes
MBB	Messerschmitt-Bolkow-Bolhm beam domain
MOLE	MOnotonicity based minimum LEngth scale
RVE	Representative Volume Element
SEL	Size Effect Law
SENT	Single Edge Notch Tension
SIMP	Solid Isotropic Material with Penalization
STL	STereoLithography file format
TO	Topology Optimization
VCCT	Virtual Crack Closure Technique
XFEM	Extended Finite Element Method

ABSTRACT

Vernacchio, Vincenzo G. Masters, Purdue University, May 2019. Size Dependent Failure Constrained Topology Optimization Approaches. Major Professor: Thomas Siegmund, School of Mechanical Engineering.

New approaches in topology optimization and manufacturing techniques are generating multi-scale, physically realized mechanical components from advanced materials. Current optimization formulations do not consider the dependence of strength on feature size. By failing to account for the mechanical models of this behavior, sub-optimal structures are generated.

A currently available academic density-based topology optimization code is extended to incorporate strength constraints. A continuum theory of failure novel to the optimization field is implemented to account for both general yielding and fracture dominated failure. The fracture limit is then formulated in terms of well-established models of brittle and quasi-brittle size dependence. Additional models of size dependence based on assumed flaw sizes are considered using the theory of linear elastic fracture mechanics. To unify the optimized topology and the empirical geometric-scaling models used, a novel geometric measure of local size is proposed. This measure interprets the evolving density field using a consistent domain of support and maintains consistency with gradient-based methods of optimization. The geometric measure is evaluated using test-problems which consider a minimum compliance objective under geometric constraints.

The resulting optimized structures are presented for the geometric and size-dependent strength constrained formulations. The geometrically constrained results illustrate the flexibility and robustness of the proposed local size measure. The various models of size-dependent strength illustrate the impact and necessity of considering physical models of material within the topology optimization formulation. Results which

exhibit clear "micro-structural" features and scale transitioning architectures are presented for limited multi-scale optimization studies.

An attempt at physical validation considering a single model of quasi-brittle material failure is made. Existing approaches for generating 3D volumetric meshes from image data are leveraged to yield CAD interpretations of optimized structures. Structures are then printed using a 3D printing PolyJet process with a previously established size-dependent material. Structures are destructively evaluated under displacement controlled load testing. The resulting tests indicate that the stress states in the structure fail to induce the expected size-dependent material characteristics. Furthermore, the testing results indicate the difficulty in properly accounting for boundary conditions in the topology optimization approach.

1. INTRODUCTION

1.1 Motivation

Topology Optimization (TO) guides the utilization of engineering resources available to maximize relevant performance objectives. In contrast to sizing or shape design, TO increases the structural degrees of freedom allowing for broad exploration of the design space. This capability, coupled with the generality of common TO methods, has led to interest in utilizing these tools for topics ranging from load-bearing structures to heat-flow, optics, and fluid flow [1, 2]. Currently, the coupling of TO to Additively Manufactured (AM) technologies is an emerging field of research with a broad array of applications [3]. These technologies allow for the highly complex, multi-scale features generated through TO algorithms to be manufactured.

One challenging issue still to be overcome concerns the optimization of complex, scale-transitioning architectures. There are significant efforts underway revisiting the approach pioneered by Bendsoe and Kikuchi [4] which linked properties at the structural scale to a homogenization of assumed microstructures on a separate scale. Approaches in literature return focus to the microscale, seeking to optimize layout across scales. However, these approaches largely consider stiffness formulations. Furthermore, they disregard the effects of size on both the constitutive response and failure mechanics. It is well accepted that both mechanical phenomena are highly size dependent at certain scales [5]. Thus, it is incumbent upon researchers in the field to consider the impact of these models to drive any possible advantage out of the structures they seek to optimize.

1.2 Literature Review

1.2.1 Dependence of strength on size

It is commonly recognized that strength is a parameter dependent on the size of a given specimen. Leonardo da Vinci [5] originally recognized this behavior, stating that the strength of a wire is dependent on its overall length. In the modern era, Griffith demonstrated this supposed sized-dependence with experiments using glass fibers [6]. A formal expression of the dependence of strength on size was proposed by Weibull [7]. Through [6, 7] it was recognized that this dependence originated from critical inherent micro-flaws in each specimen dominating the fracture behavior of the investigated materials. This theory developed following these results applies to materials which exhibit brittle characteristics through fast fracture of these non-interacting micro-flaws prior to the onset of large scale crack-growth. Initial cracks must be significantly smaller than the specimen size such that any reasonable Representative Volume Element (RVE) used for stress analysis on the continuum is significantly larger than the flaw size [8]. Furthermore, upon reaching a critical stress in these materials no significant mechanism for stress redistribution may exist. Due to the fact that these micro-flaws are randomly distributed throughout the material, this theory has come to be referred to as the *Weibull statistical strength-size effect.*

In materials with flaws observed on the structural scale of the specimen, a size-dependent strength of a different form arises. This new form of scaling is dependent on the characteristic failure described using Linear Elastic Fracture Mechanics (LEFM). Early on in the development of the field, Westergaard [9] and Irwin [10] illuminated the presence of a size-dependent strength for geometrically similar specimens. This was achieved through the derivations of the crack tip stress fields local to structural flaws. The form of the scaling can be seen in the expression for the Mode I Stress Intensity Factor (SIF) of a notched tension specimen. For materials with identical Mode I SIF, the applied stress significantly far from the notch is proportional to the negative square root of the notch size. If the ratio of the member size to the notch is

held fixed, this expression dictates the strength scaling. Later, it was shown through Rice's J-integral [11,12] that this effect is driven by the increased elastic strain energy contained in larger, geometrically similar contours on the domain. LEFM scaling is largely applicable to brittle or quasi-brittle systems where fracture occurs either as a sequence of abrupt, brittle ruptures or a single catastrophic event.

The Weibull statistical strength-size effect, LEFM geometrically-similar size effect, and traditional strength formulation constitute the what are known as power-law size scaling models. The Weibull power-law scales with the material Weibull modulus, LEFM with the negative square root, and strength with zero. These three models are compared in **Figure 1.1**. Beyond the power-law scaling models, additional physical size-effect models exist. These models originate from a richer description of the fracture mechanics of a given material and illustrate the complexity of the topic of size-dependence.
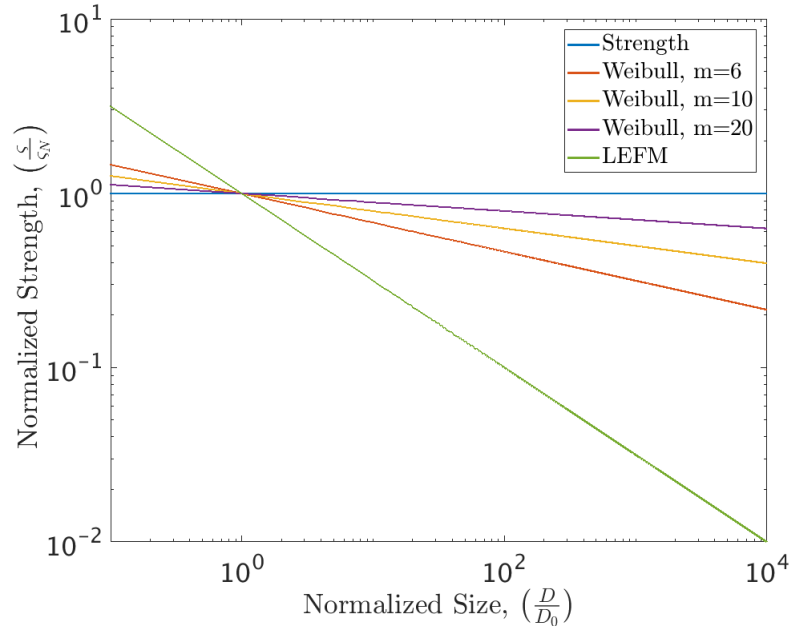
Figure 1.1. Normalized strength vs. size plot illustrating power-law size-dependent strength scaling models. Weibull moduli are varied to illustrate the varation in behavior for different classes of materials.

One of the concessions of the LEFM size scaling model is that it assumes that the structure behaves elastically throughout the material domain up to the point of rupture. This assumption neglects the presence of a Fracture Process Zone (FPZ) local to the notch. In reality, depending on the material the size of the FPZ is non-negligible and significant crack-tip non-linearity is observed. This physical phenomena is captured through the size-dependence scaling law formalized by Bažant [13]. Bažant demonstrates the energetic influence of the FPZ on the formation of new fracture surfaces. The scaling law, plotted in **Figure 1.2**, captures the transition between LEFM and a limit failure strength as the specimen size approaches the scale of the FPZ. Once these two features are on the same scale, brittle fracture ceases to occur, the FPZ dominates, and strength asymptotes to an intrinsic material limit.
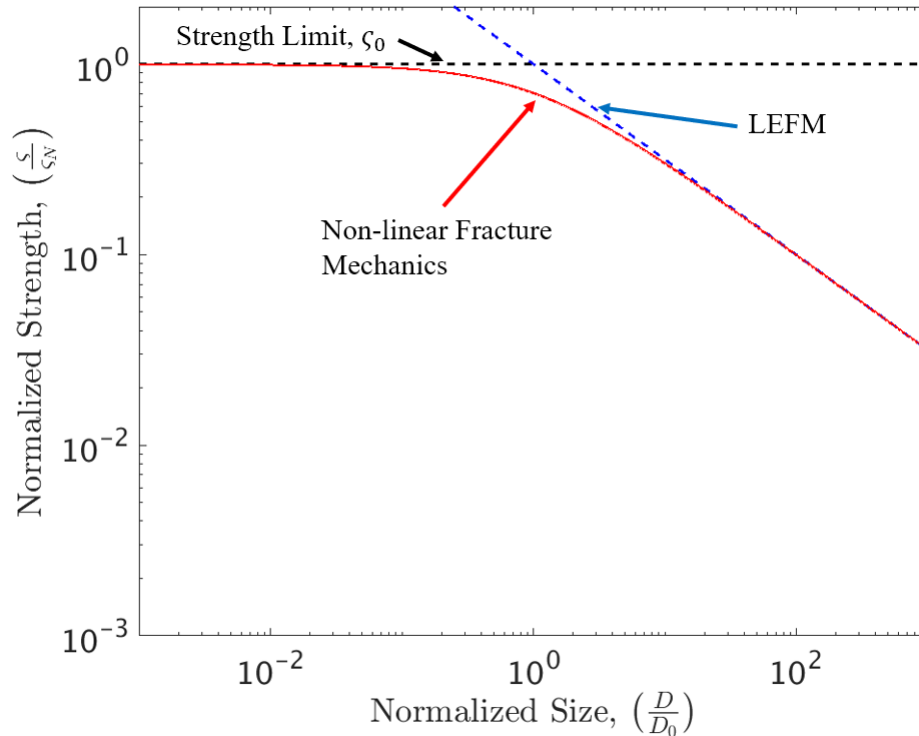
Figure 1.2. Non-linear elastic size-dependent scaling of strength.

Bažant's scaling law captures the mechanical interaction of macroscopic flaw propagation and the physical boundary of a given structural member. The law is formu-

lated in terms of ratio between the observed FPZ and the structural feature dimension in the direction of crack propagation. This ratio is inherently tied to a given flaw geometry configuration. Alternatively, the boundary interaction may also be considered by varying the structural feature size relative to an assumed flaw size. This case is analogous to engineering applications where flaws on the macro-scale are introduced by a manufacturing process and largely independent of the final component size. In classical LEFM, boundary effects enter through a geometry correction factor dependent on the flaw size ratio and structural geometry. Traditionally, the factor is obtained through empirical fitting and remains unique to a given configuration. This additional richness has been incorporated into a law similar in form to Bažant's by Duan [14]. The formulation proposed by Duan captures a transition out of the FPZ dominated region even for small specimens as the assumed flaw ratio reaches intermediate values. The strength of the structure returns to a FPZ dominated behavior as the un-cracked ligament approaches zero and the FPZ encompasses it entirely.

The field of size-dependent strength behavior is rich and still evolving. As of yet, it has not been wholly incorporated into practical engineering design. However, as more extremal structures made from novel materials are evaluated, it is clear these physical models must be considered. Therefore it is incumbent upon topology optimization approaches to provide for these situations as well.

1.2.2   Size dependence in micro-architectured design

Recent advances in manufacturing techniques for ceramic, composite, polymer, and metallic systems have sought to take advantage of material-related size effects to generate robust meta-materials [15]. These approaches have been enabled by the ever increasing precision of additive manufacturing techniques [3, 16, 17]. Examples range from ceramic printed micro-trusses investigated by Cui et al. [18], metallic systems fabricated through electroplating approaches such as those investigated by Gu and Greer [19], polymer ceramic composites produced by Meza et al. [20], to even relatively

large stereolithographic polymer structures produced by Lausic et al. [21]. All note the beneficial effects of smaller micro-truss constructions resulting from improved buckling characteristics and flaw driven tensile fracture behaviors.

However, the goals of these works largely focus on bulk material elastic and failure responses to simple loading cases. It is known that the failure characteristics of architected structures are highly dependent on loading conditions [22]. Thus, to implement these metamaterials in practical engineering components, methods for designing micro-structures under complex loading conditions must be developed. Any proposed method must be formulated to capitalize on size-effects many authors have noted as critical to the success of these materials.

1.2.3   Topology Optimization techniques

The problem of material layout subject to mechanical loading is of historical interest throughout a wide breadth of engineering disciplines. Until recently, quality layouts were obtained through manual iterative cycles of design updates and analytical verification. Starting with its emergence as a modern engineering tool, the discipline of structural optimization has formalized this previously heuristic approach through coupling mechanical analysis to optimization algorithms. Early efforts focused on determining optimal dimensions for existing parametric geometry, relying on an initial guess within the domain. As the field has matured more complex topology optimization approaches for deriving free-form shapes and general domains have been proposed and implemented. A comparison of the outcomes of parametric shape or sizing optimization compared to free-form structural design is illustrated in **Figure 1.3** The full breadth of these efforts may be appreciated through the comprehensive review article by Sigmund and Maute [23], supplemented with reviews by Deaton and Grandhi, Rozvany, and van Dijk et al. [2, 24, 25].

One such method that has gained significant popularity is the Solid Isotropic Material with Penalization (SIMP) approximation of the design domain suggested by
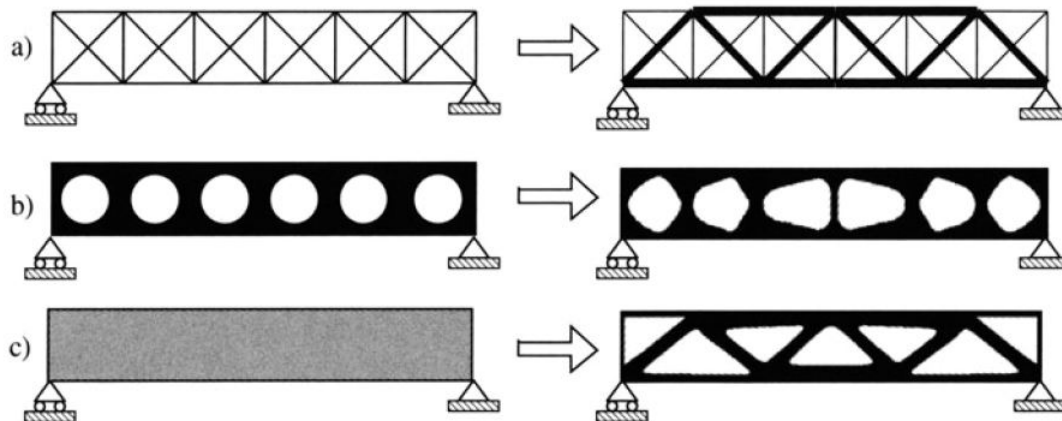
Figure 1.3. Three optimization formulations for a beam in three-point bending. (a) Sizing optimization of a ground structure, (b) shape optimization and (c) free-form or topology optimization.

Bendsoe [26] and formalized by Zhou and Rozvany [27]. The SIMP method reformulates the design domain into a discretized Finite Element (FE) problem with elementally defined intermediate densities between 0-1. Relevant structural parameters such as the elastic modulus are penalized to generate a smooth and differentiable approximation to the ideal solid-void problem. This in turn allows converged solutions to the problem to be obtained by efficient, gradient-based mathematical programming methods [23]. As the SIMP approximation is founded on the basis of algorithmic convenience and is not tethered to specific physical arguments, it can be extended to a variety of mechanical problems [1, 2]. These advantages have led to the widespread interest in SIMP within the research community [24] and nearly ubiquitous implementation of SIMP approximations within industrial level codes [2, 24, 28]

1.2.4 Static structural failure in Topology Optimization

Algorithmic Development

While once the compliance objective was overwhelmingly preferred due to its low cost and ease of implementation [1], stress-based or structural failure formulations

have been studied more extensively in recent years. Despite the additional algorithmic complexity these problems require, the need for robust and reliable structures has forced this development. The current status of the field shows significant exploration though no ideal approach has been validated. This is illustrated in the review of various approaches complied by Le et al. [29] where various algorithmic formulations optimizing the same physical problem yield markedly different results. **Figure 1.4** is taken from this review and depicts the diversity of outcomes.
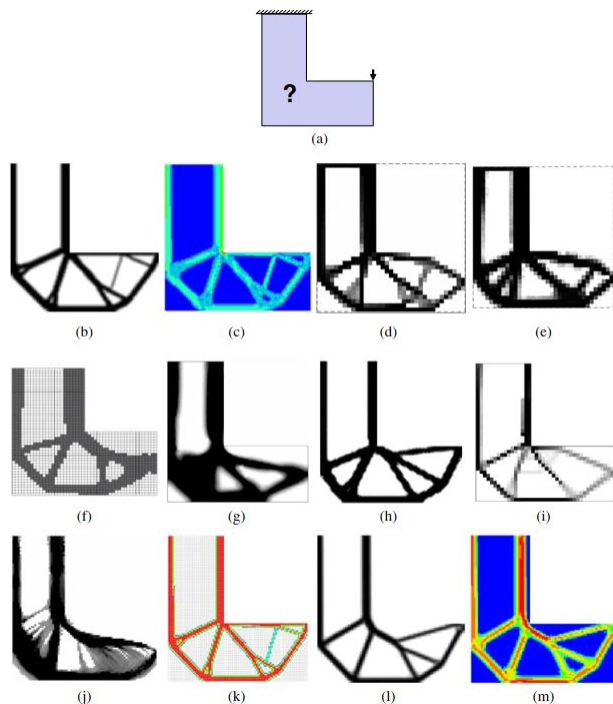
Figure 1.4.   Results obtained for various stress-based topology optimization algorithms on the L-bracket test problem domain.

When considering the challenges to implementing stress-based approaches, the primary theoretical obstacle is the stress-singularity problem. This problem has been investigated thoroughly, [30–33] originally as it pertained to truss topology optimization. The stress-singularity problem occurs when an optimal solution exists within a degenerate subspace of the feasible design space. This degenerate optimum generally occurs when parts of the structural domain ideally contain no material. As

this solution is approached, local stresses which remain defined in the SIMP methodology grow rapidly and exceed allowable stress levels. The practical result of this behavior are regions of intermediate density where voids should ideally be located. Numerous strategies have been proposed to alleviate this issue. The earliest example is described in [31] in the form of the ε-relaxation method which increases the threshold on allowable stress by relaxing the strength constraint. This relaxation enlarges the mathematically feasible domain. It is successively reduced through a continuation scheme to approach the original strictly formulated strength-constraints. Improvements in the treatment of the singularity problem have come in the form of qp-relaxation [34]. This approach has come to be employed extensively in stress-based formulations [29, 35–38]. Instead of relaxing the strength constraints, the calculated stress at intermediate densities is penalized to prevent unbounded values. This may be applied in a single optimization run, reducing the computational cost compared to the continuation approach required by ε-relaxation In addition to effectively addressing the singularity problem, qp-relaxation also drives convergence to solid-void structures.

Once the singularity problem is addressed, two additional challenges must be solved. Both relate to the complexity of the optimization problem posed and are coupled in nature. In contrast to the traditional compliance formulation, stress-based topology optimization the measures of interest are defined at each local material point. Theoretically, this implies an infinite number of stress constraints within the domain. Practically, the total number of constraints is equal to the number of finite elements in the domain [39]. It is well accepted that the quality of the FE analysis and its ability to accurately resolve stresses is directly related to the discretization of the material domain [40]. Thus, these finely meshed domains lead to prohibitively large numbers of stress constraints. One common approach in literature to reduce this cost involves the aggregation of local constraints within the domain into one or more stress measures. In the simplest case, a smooth, differentiable approximation of the global stress maximum is made through an aggregating function such as the Kreisselmeier-

Steinhauser (KS) [41, 42] or p-norm [43–46]. This approach has a limited capacity to control local stresses in the domain and may fail to reliably relieve geometric stress concentrations [46]. Numerous authors have proposed a solution in the logically apparent middle ground between global and local constraints through the use of aggregated clusters. The first variant of this strategy, termed "block aggregation", was proposed by Paris et al. [47]. It is based on regionally defined clusters using a KS approximation. Non-local clustering approaches were later proposed by Le et al. [29] and Holmberg et al. [35] who group stresses based on value as opposed to geometric location. The former [29] creates clusters of roughly equal value while the latter [35] groups according to ascending intensity. Compared to the regional method, non-local clustering leads to a constantly changing optimization problem. However, both [29] and [35] note good structural convergence behavior, though neither reports rigorous measures of optimality such as Karush-Kuhn-Tucker (KKT) measures. The ability of clustering methods to capture elevated stresses within the structural domain is highly dependent on the number of clusters used [48]. However, each cluster corresponds to a unique constraint. This serves to increase the computational cost proportionally, making clustering approaches prohibitively expensive for large problems.

To circumvent this cost increase, Kiyono et al. [36] propose a multi- p-norm approach across the entire domain in an attempt to capture both average and maximum stresses in a single clustered measure. Similarly, Wang and Qian [48] utilize a Heaviside approximation to evaluate whether the stress constraint is violated locally. Then a global constraint is formed through an integration of the Heaviside stress measure across the domain. Both approaches claim significant decreases in computational cost, with a drastic improvement for simulations in the hundreds of thousands of elements shown by [48]. Due to the limited scope of this work, the more well established approaches of Le et al. and Holmberg et al. are preferred for the present study.

Failure Models

Concerning themselves with addressing algorithmic issues in stress-based TO, most authors have utilized the quadratic von-Mises yield surface [49] to describe a relevant failure criterion. While the von-Mises criterion introduces a smooth yield surface, it only accurately describes failure in metals which exhibit pressure-invariant yielding behavior. Recently however, interest in employing failure theories for other classes of materials has grown. The general Coulomb-Mohr family of failure theories and the shear-based Tresca theory were implemented [37] with significant effort to resolve the discontinuities inherent to these yield surfaces. The Raghava and Ishai theories for pressure dependent polymers [50, 51] and the Drucker-Prager measure for cohesive materials [49] have also been employed. For anisotropic materials, Tsai-Hill criteria have been implemented [52] and validated using physical specimens printed from ABS plastic. In all cases, significant deviations from benchmark problems applying von-Mises static failure formulations are observed.

Some topology optimization approaches have considered theories of failure which are not reliant on yield or failure surfaces. Challis et al. [53] used a level-set method to maximize the structural fracture resistance through employing the Virtual Crack Closure Technique (VCCT) at potential crack growth locations in the allowable domain. Kang et al. [54] imposed a mixed formulation to minimize compliance and the energy release rate around flaws at prescribed locations in the domain. This approach is based on a rigorous formulation of the J-Integral [11] within the SIMP formulation. However, fracture characteristics are not applied throughout the domain and instead rely on an initial guess of which parts of the domain are most vulnerable to brittle failure. In a similar vein, James and Waisman [55] considered failure using Lamaitre's models for continuum damage in a non-linear FE implementation. Practically, this approach shows promise in developing structures with significantly higher toughness relative to traditional stress-based methods.

1.2.5 Recent advances in multi-scale optimization approaches

In regards to multi-scale, architected approaches in topology optimization, it must be realized that the seminal paper by Bendsoe and Kikuchi [4] considers the multi-scale problem of optimizing fully-dense structure through separation-of-scale methods. In this original approach, the micro-scale is homogenized and its behavior analyzed on the macro-scale to allow for a tractable method of analysis. Due the complexity of this implementation, issues with insuring continuity, and the lack of manufacturability of resulting structures, this initial multi-scale approach was disregarded in favor of the convenient SIMP approximation which enforces a single scale of structural feature through penalization.

In recent years, spurred on mainly by advances in precision of advanced manufacturing techniques and increased computational power [56], multi-scale approaches have been reconsidered [57]. These approaches work to move closer to ideal structures which consist solely of periodic composites with features whose minimum size is limited only by manufacturing feasibility [58]. The works of Rodrigues and his collaborators [59] sought to expand on the original formulation of Bendsoe and Kikuchi by optimizing both a single-scale microstructure and the overall macro-scale topology. While further works in this vein have improved its practical viability [60], this approach remains unable to guarantee continuity between microstructures.

Alternative approaches have arisen which attempt to resolve this issue. Lazarov and Alexandersen utilize the increased computational resources available to consider the fully discretized multi-scale model [61] with additional computational features utilized to maintain reasonable cost. Pantz and Trabelsi [62] proposed a projection method based on periodic composite mappings to interpret the SIMP based result back into a fully dense micro-structure. In this way, computational costs are kept similar to single scale problems while a reasonable level of microstructural complexity is allowed for. An interesting approach proposed by Daynes et al. [63] generates a macro-scale topology with commercial density methods to generate the iso-static lines

of the structure. Once these are in hand, a truss topology is overlaid onto the iso-static lines and a sizing optimization is performed to optimize the microstructure.

As a note, for the same reasons multi-scale approaches were not originally pursued in research, the methodology used in this thesis shall not be truly multi-scale. The effects of size within a single scale using SIMP-methodology will be used. In this way, methods of evaluating structural size will not have to consider through scale-transitions in the analysis. Thus, this discussion is included to illustrate the interest in possible multi-scale approaches and illustrate their limited consideration of failure characteristics.

1.2.6   Size-scaling in optimization

In the realm of optimization techniques, size-scaling of mechanical behavior has been minimal. This is especially true in the more limited field of topology optimization. Even the aforementioned multi-scale approaches referenced, which ostensibly provide for features across scale, consider both scales to exhibit constitutive or failure behavior independent of size.

Despite the neglect of these behaviors in multi-scale models, some work exists in literature considering higher order elasticity theories. Sigmund and Maute [64] assert that compliance sensitivity filtering using Helmholtz partial differential equations [65] is mathematically equivalent to non-local elasticity theories. However, works explicitly considering non-local elasticity models by Li and Khandelwal [66, 67] evidence markedly distinct structures with a pronounced dependence on the material model length scale. The works of Bruggi, Taliercio, and Verber have used Cosserat theories of micropolar materials for objectives of minimum compliance and maximum first eigenmode [68, 69].

While some work which accounts for the scaling of constitutive law has been undertaken, no existing topology optimization treatment considers the influence of size effects of failure. In the domain of shape optimization, limited work has been

done using Weibull statistics of failure models by Lund [70] and Rauchs [71]. These approaches rely on an accurate measure local feature size inherent to the parametric description used in shape optimization.

1.2.7 Geometric interpretation of density-based optimization structures

The interpretation of the free-form topology generated by SIMP methods into meaningful geometric shapes and parameters remains an ongoing topic of interest. The ideal measure of local geometry remains a goal of the field [72]. Historically, authors have considered this topic from two perspectives: to ensure manufacturability and to facilitate integration into existing Computer Aided Design (CAD) frameworks. While these perspectives are not necessarily exclusive, most approaches do not broadly consider both. For the purposes of this thesis, techniques which address the former are of principal interest.

The earliest motivation for a geometric measure on the domain arose from the need to impose scale independent of the FE discretization and took the form of filtering approaches. Diaz and Sigmund [73] proposed the initial sensitivity filtering approach which distributed the influence of a single design variable across a prescribed neighborhood. This technique retained the single field of design variables used by Bendsoe and Kikuchi. Later, a two-field SIMP [23] approach was proposed by Bruns and Tortorelli [74, 75] which utilized a second filtered density field to once again distribute the influence of each design variable. Both the sensitivity and density filter techniques result in similar structures. Both exhibit a characteristic gray transition region that may be addressed through continuation approaches. More recent filtering approaches, such as those built on morphological [76] and projection methods [77], provide for a third field. These approaches provide much the same result, though give a better approximation of the desired solid-void structure. All of the aforementioned filtering approaches provide a scale measure mostly to address numerical challenges through regularization [78], though their ability to ensure a minimum manufacturable

feature size has been noted [72]. However, all these techniques are prescriptive in nature and provide little to no definition of the local geometry.

As alternative to filtering approaches, constraint techniques on the domain were developed. Early constraints were formulated based on topological measures and eschewed a geometric interpretation of the structure. The approach proposed by Petersson and Sigmund limits the gradient of the elemental design variables to prohibit abrupt transitions between solid and void. Effectively, this approach results in similar behavior to the density and sensitivity filters. Poulsen [79] formulated a constraint on the monotonicity of the elemental density along prescribed search directions. These search directions were constructed on a domain of influence unique to each element. Poulsen's approach provides adequate regularization, though results in non-geometric constraints, a non-linear formulation, and a large number of constraint functions.

Attempts at geometric constraints have been made, though most constrain the amount of material within a prescribed geometric domain instead of developing geometric parameters. Guest [80] proposed a constraint on the amount of projected material on a circular domain to limit the maximum feature size. Zhang et al. [81] interpret the filtered density into a medial skeleton. The elemental densities in maximum and minimum feature size contours based of this skeleton are then restricted. Finally, Zhou et al. [82] utilize the presence of an inflection region between filtered and projected density fields to limit the presence of projected density present in this region.

Overhang constraints are a topic of recent interest with the increased viability of additive manufacturing approaches used to fabricate the highly complex structures generated by lightly constrained optimization problems. Similar to Guest's earlier works on feature size, Gaynor and Guest [83] constrain the presence of material within a conical undercut domain below dense elements. Langelaar [84] utilizes a similar approach with a more limited restriction domain based directly on the element mesh. For a wider perspective on overhang approaches not limited to SIMP based geometric constraints, Liu et al. may be consulted [3].

1.3 Thesis proposal

In this thesis, it is posited that current scale-independent failure models used in traditional topology optimization approaches inadequately characterize the broad range of materials and feature scales that they are increasingly being applied to. At best, this approach results in sub-optimal material usage considering the possible benefits of smaller structural features. At worst, it risks overestimating the strength of critical load bearing members in the domain. The objective of this work is to incorporate size-dependent models of structural strength into the SIMP-based Topology Optimization framework. These models are based on physical arguments and tied to relevant engineering materials that behavior in brittle and quasi-brittle fashions.

It is hypothesized that topology optimization methods considering size-dependent strength behavior will result in significantly different structural results. It is theorized that the optimized domain shall result in efficient architectures that transition scales. These transitions will capitalize on the scale-dependence of structural features, utilizing their enhanced strength in highly stressed regions.

In order to evaluate this hypothesis, the following research tasks will be undertaken

1. **Implement a robust strength-limited, scale-independent Topology Optimization code using a flexible phenomenological failure criterion following best practices in stress-based SIMP approaches.**

   Due to the lack of a readily available, open code for stress based topology optimization methods, the foundations of the approach utilized in this thesis must be built upon the feasible methods available in literature. The early sections of this thesis are concerned with the construction of the underlying SIMP formulation from key components found in literature. On top of this formulation, a failure criterion is used for constructing the relevant forms of stress-dependence of the optimization problem. A failure criterion novel to Topology Optimization approaches is employed for its desirable mathematical formulation and relation to physical arguments of failure.

2. **Formulate a measure of geometric size used to interpret each structural iteration with a density based Topology Optimization approach.**

   As a precursor to the imposition of a geometrically-based size-dependent strength model, a measure to interpret the local feature size of the structural domain at each optimization iteration is be proposed, formulated, and implemented. The proposed measure is compatible with efficient methods of calculating its sensitivity with respect to the design variables of the problem and remains consistent throughout the entirety of the optimization process. Prior to using the formulated measure as a foundation for size-dependent strength methods, its robustness is evaluated through imposing geometry based constraints on the common compliance-based problem.

3. **Extend the chosen failure criterion to incorporate size-dependent strength through employing physical arguments of material failure.**

   With a flexible failure-criterion and reliable measure of geometric size in hand, the two are coupled following well known models of size-dependent strength. Arguments for the means by which size-dependent strength is incorporated into the generalized yield surface used are given on the basis of physical mechanisms of failure. These arguments appeal to historical testing results on largely tensile fracture specimens. It is beyond the scope of this paper to consider the experimental approaches required to validate the proposed model for all stress states.

4. **Experimentally validate the structural performance of samples derived from the proposed method.**

   Two different formulations, size-dependent and independent strength-constrained compliance minimization, are used to generate optimal geometry. Physical specimens are printed using a PolyJet additive manufacturing process. To generate printable structures, the optimized structures are interpreted into usable 3D CAD representations. A material which has previously been shown to exhibit size dependence is used to fabricate specimens. Specimens are de-

structively tested to capture load-displacement responses of both resulting structures. The results are then compared to the predicted failure behavior underlying the optimization.

5. **Computationally validate the results of the proposed methodology through applying cohesive models of failure through the Extended Finite Element Method.**

    Using the experimental data obtained from the destructive testing, an ABAQUS /Standard model is constructed for both cases. Physical models of failure are incorporated into the FE model using the Extended Finite Element Method. Crack evolution is captured using the Cohesive Zone Method. This approach has been shown to accurately account for size-dependent strength behavior in the FEA. Using fracture properties of an assumed material, an optimized structure is considered across geometrically similar realizations.

In summary, it is expected that this work shall result in a novel expression of the topology optimization formulation that considers the physical characteristics of a broader range of structural materials. It is intended that this proposal shall act as the initial step in this direction, opening the path for continued exploration of size-dependent strength optimization techniques relevant to the ever more complex structural components enabled by emerging materials and fabrication techniques.

2. STRESS BASED CONTINUUM TOPOLOGY OPTIMIZATION

2.1 General statement of a single objective, minimization problem

The field of structural optimization, which includes topics in Topology Optimization, is the formal application of optimization methods to structural design. Following general mathematical optimization constructions, structural optimization problems are formulated to minimize a given structural objective given constraints on the mechanical parameters within the domain [85]. Thus, following this convention, statements of the various topology optimization problems in this paper shall be expressed in the form

$$
\begin{aligned}
&\underset{\boldsymbol{x}}{\text{minimize:}} && f(\boldsymbol{x}) \\
&\text{subject to:} && g_j(\boldsymbol{x}) \leq 0 && j = 1, l \\
& && h_k(\boldsymbol{x}) = 0 && k = 1, m \\
& && x_i{}^L \leq x_i \leq x_i{}^U && i = 1, n \\
&\text{where:} && \boldsymbol{x} = \{x_1, x_2, ... x_n\}
\end{aligned}
\tag{2.1}
$$

where the objective function, f, is minimized through varying a set number of design variables, x. These variables may be updated through a variety of gradient based or heuristic approaches in order to iterate the design. In the specific case of constrained optimization problems, the minimum allowable value of the objective is limited to feasible regions by equality constraints, h, inequality constraints, g, and bounds on the values the design variables themselves can assume. For structural optimization problems, the dependence of f on x is examined through the influence of x on the physical state of the the domain in response to external loading conditions.

2.2   Elastic Formulation of the Eulerian Finite Element problem

As previously mentioned, structural topology optimization approaches rely on the ability to connect the design variables to the structural response of an evolving material domain.   Given the arbitrary complexity of the converged structure, no closed form relationships between global loading and structural responses can be expressed.   Thus, the Finite Element (FE) method is relied upon to analyze the emergent structure's behavior. In the simplest embodiment of the continuum topology optimization problem an allowable structural domain, Ω in **Figure 2.1**, is considered using an Eulerian finite element mesh discretized into N regular elements. This mesh remains unchanged throughout the optimization process on the domain.
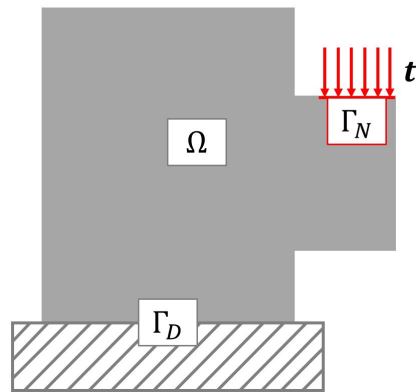
Figure 2.1. Allowable structural domain under consideration, Neumann and Dirilecht boundaries shown.

As the continuum topology optimization problem has historically been concerned with achieving structures with a maximum elastic stiffness subject to a design load, the underlying boundary value problem for the allowable structural domain is considered from an elastic formulation. It may be written as [86]

$$div(\boldsymbol{\sigma}) = 0 \quad \text{on} \quad \Omega,$$
$$\boldsymbol{u} = 0 \quad \text{on} \quad \Gamma_D,$$
$$\boldsymbol{\sigma} \cdot \boldsymbol{n} = \boldsymbol{t} \quad \text{on} \quad \Gamma_N, \qquad (2.2)$$

where $\boldsymbol{\sigma}$ is the stress tensor in the domain, $\boldsymbol{u}$ is the vector of kinematically admissible displacements, and $\boldsymbol{t}$ is the vector of applied boundary tractions. The kinematic and elastic constitutive equations are employed to relate $\boldsymbol{t}$ to $\boldsymbol{u}$ through the following relationships

$$\varepsilon_{ij} = \frac{1}{2}(u_{i,j} + u_{j,i}) \qquad (2.3)$$

$$\sigma_{ij} = \boldsymbol{C}_{ijkl}\varepsilon_{kl} \qquad (2.4)$$

where in the most general sense $\boldsymbol{C}_{ijkl}$ is the fourth order elastic constitutive tensor and ϵ_{ij} is the infinitesimal strain tensor. Through the application of the Finite Element Method, the BVP may be expressed in a more convenient form following [86]

$$\left(\sum_{e=1}^{N_e} \boldsymbol{L}_e^T \boldsymbol{K}_e \boldsymbol{L}_e\right)\boldsymbol{u} = \sum_{e=1}^{N_e} \boldsymbol{L}_e^T \boldsymbol{f}_e \qquad (2.5)$$

$$\boldsymbol{K}\boldsymbol{u} = \boldsymbol{f} \qquad (2.6)$$

where $\boldsymbol{L}_e$ are the elemental assembly matrices, $\boldsymbol{K}_e$ are the elemental stiffness matrices, and $\boldsymbol{f}_e$ are the elemental nodal forces. For this work, only 2D problems are considered to reduce computational cost and complexity. The domain is discretized using iso-parametric, bi-linear quadrilateral plane-stress elements. Thus, $\boldsymbol{K}_e$ is calculated for each element as

$$\boldsymbol{K}_e = \int \boldsymbol{B}_e^T \boldsymbol{E}_0 \boldsymbol{B}_e \quad dA = \int_{-1}^{1}\int_{-1}^{1} \boldsymbol{B}_e^T \boldsymbol{E}_0 \boldsymbol{B}_e \quad J \quad d\xi d\chi \qquad (2.7)$$

where $\boldsymbol{B}$ is the elemental strain-displacement matrix, ξ and χ are the parent coordinates of the element, and J is the transformation Jacobian. $\boldsymbol{E}_0$ is the plane-stress

constitutive tensor given in terms of the isotropic elastic modulus, E, and Poisson's ratio, ν as

$$\boldsymbol{E}_0 = \frac{E_0}{1 - \nu^2} \begin{bmatrix} 1 & \nu & 0 \\ \nu & 1 & 0 \\ 0 & 0 & \frac{1-\nu}{2} \end{bmatrix} \tag{2.8}$$

2.3 Parametrization using Solid Isotropic Material with Penalization

With a means for understanding the state responses of a evolving structural domain in hand, some relationship between the domain and the standard optimization problem needs to be posed. Conveniently, the same discretization of Ω into N elements used for the FE mesh can be utilized to represent presence of material with the continuum domain. The presence of material within the structural domain is given in terms of the design variables of the problem, x_e which are commonly thought of as local measurements of "cost" or a fictitious density [4, 23]. The optimization problem considers N total design variables mapped directly to the N elements of the finite element mesh. Bounds of $x_e \in [0, 1]$ on the design variables correspond to void and solid material regions. Finally, the design variables are linked to the mechanical response of the evolving structure through parameterizing the elemental stiffness tensor following

$$\boldsymbol{K}_e(x_e) = \int \mathbf{B}_e^T \mathbf{E}_e(x_e) \boldsymbol{B}_e \quad dA \tag{2.9}$$

where

$$\boldsymbol{E}_e(x_e) = \frac{E(x_e)}{1 - \nu^2} \begin{bmatrix} 1 & \nu & 0 \\ \nu & 1 & 0 \\ 0 & 0 & \frac{1-\nu}{2} \end{bmatrix} \tag{2.10}$$

When considering the form of the parameterization $E(x_e)$ it is accepted that a discrete formulation of the design variables results in an optimization problem which

lacks solutions for the continuum domain [78]. Following the arguments given by Sigmund and Petersson [78], each design variable must be relaxed through continuous variation of its allowable value. This was achieved in the initial work on continuum TO design by Bendsøe and Kikuchi [4] through optimization of a multi-scale problem with a homogenized micro-structure. However this early approach readily allowed for regions with intermediate elemental density values to arise within the domain. Without additional treatment, converged structures following this homogenization approach arise with significant regions of intermediate density. These domains are known to be theoretically optimal for compliance based problems in particular [58]. To achieve results similar to the intended 0-1 structures, it is necessary to penalize these intermediate values of density. The Solid Isotropic Material with Penalization methodology proposed by Bendøe [26] and expanded upon by Zhou and Rozvany [27] efficiently achieves this. Following this methodology, the dependence of the modulus on the design variables is given by

$$E(x_e) = x_e{}^{\phi} E_0 \tag{2.11}$$

where ϕ is the penalization coefficient of the design variable. It is generally accepted that $\phi = 3$ provides adequate penalization without inducing unstable convergence behavior [1, 29]. In effect, SIMP works by reducing the volume efficiency of intermediate density elements. These elements exhibit a marked drop in stiffness compared to their cost. This efficiency is only recovered for the two limiting cases of 0 and 1, thus the optimal structure is driven towards a fully solid or void topology.

2.4   Regularization and filtering

Density based topology optimization schemes are prone to fundamentally flawed computational results if insufficient effort is put into the implementation of the FE problem. These flaws originate from two separate issues, mesh dependence and checkerboarding. Mesh dependence of the TO solution on the domain results from the

coupling between the FE mesh used for solving the structural problem and the parameterization of the presence of material within the domain. As expressed by Sigmund in [78], mesh refinement in TO problems is intended to provide a better discretized geometric representation of a structure. Additionally, a finer mesh allows for a better numerical approximation of the underlying continuum problem solution following arguments founded in fundamental FE theory [40]. However, as each element corresponds to a density value in the design vector, discretization in the TO problem also increases the degrees of freedom of the optimization problem. Thus, compared to a coarsely meshed domain, finer and finer structures may arise from the same allowable domain. Checkerboarding arises due errors in the finite element approximation when bi-linear quadrilateral elements are used. It is known that the approximation leads to artificially high stiffness values for a given patch when compared to alternative composite constructions of solid and void material [73].

Both phenomena are illustrated using the MATLAB implementation provided by Andreassen et al. [87] with regularization features removed in **Figure 2.2**. Here, the allowable structural domains remain fixed but the size of the FE problem is increased. The size of individual elements is correspondingly decreased and finer converged structural features may be obtained. If the intention is to maintain physical scale across finer FE discretizations to verify convergence, it is clear that some regularization across element scales must be enforced.

Issues in mesh dependence and checkerboarding are commonly alleviated through the use of single flexible technique: filtering of the design variables on the domain. Historically, filtering methods seeking to ensure efficient and robust reformulation of the design variables into some physically meaningful features have been studied extensively [76, 88]. Filtering of the variables implicitly enforces a domain dependent minimum length scale. Throughout this thesis, density filtering will be achieved through convolution of the design domain with a linear filter [74, 89]. In this manner, the elemental filtered densities, $\tilde{\boldsymbol{\rho}}$, on the domain are evaluated as
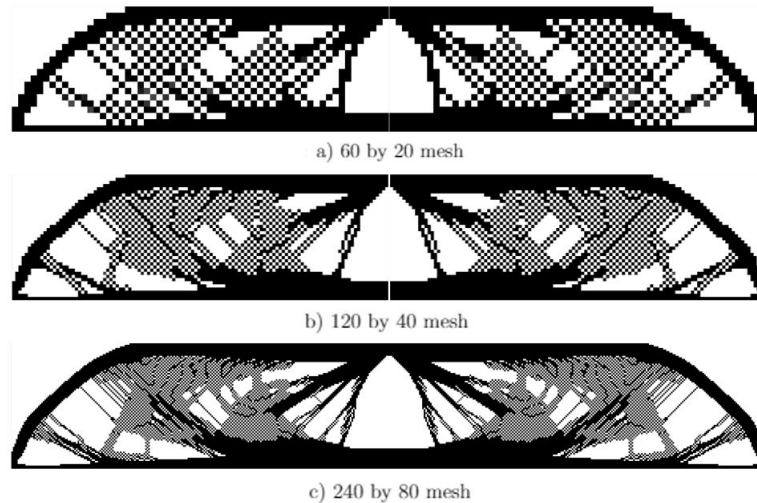
Figure 2.2. Mesh dependence of the 240 mm x 40 mm MBB compliance minimization problem. Results generated from basic Andreassen et al. MATLAB implementation with regularization features removed.

$$\tilde{\rho}(\boldsymbol{x}) = \frac{1}{\sum_{i \in N_e} H_{ei}} \sum_{i \in N_e} H_{ei} x_i \tag{2.12}$$

where

$$H_{ei} = \max[0, r_{min} - \Delta(e, i)] \tag{2.13}$$

and $\Delta(e, i)$ is the center-to-center distance between elements in the filter radius. The filtered densities can be considered the physical results of the structural optimization. They replace the design variables in the penalization of the elastic modulus resulting in

$$E[\tilde{\rho}(\mathbf{x})] = [\tilde{\rho}(\mathbf{x})]^{\phi} E_0 \tag{2.14}$$

Following this method, solid region boundaries in the domain are smoothed into a halo of intermediate densities. These intermediate densities, penalized following the SIMP method, are progressively removed from the domain preventing the occurrence of checkerboarding. To alleviate mesh dependence, the size of the filter is scaled relative to the FE discretization on the domain. This ensures that features smaller

than the filter radius are discouraged and consistent physical scale is imposed. In the implementation proposed in this thesis, the filter size is expressed in terms of the number of elements not the physical size of the domain and must be scaled relative to the discretization. However, for reporting results in this paper the filter radius will always be given in terms of physical units.

To maintain consistency in the filtering approach, boundaries to the allowable domain must be treated carefully [76]. These boundaries must be interpreted physically such that the imposed scale is not artificially truncated. Prior to filtering the densities, the boundaries of the domain must be expanded proportional to the radius of the filter. Support regions are treated as solid on this expanded domain; regions with prescribed tractions, zero or otherwise, are treated as void. For boundaries with enforced symmetry, the density measures are mirrored across the symmetry line or plane. After the filtering convolution, the boundaries may be truncated down to the allowable structural domain for calculation of the FE problem.

The principle drawback of employing the density filter as shown takes the form of a characteristic blurred gray region with a width proportional to the radius of support specified for the convolution exterior to each solidified structural member. This gray region, coupled with the aforementioned accuracy issues resulting from using a fixed FE mesh for stress evaluations, lead to issues in transferring the mathematical optimality of the domain to physical structures. For approaches to circumvent these issues, refer to the discussion by Kiyono et al. [36]. Despite these limitations, the density filter still retains popularity for stress constrained problems due to its relative simplicity [29, 35, 37, 88, 90].

2.5   Three field implementation and projection approach

A popular extension to the filtered density approach used to remove gray regions is the "three-field" projection methodology [23]. Originally proposed by Guest [77] for a nodal variable based method, three-field approaches implement a thresholding approach within the framework of gradient based optimization. The goal of this threshold is to enforce discrete solid-void structural domains. It results in a third parameterization of the structural domain, the projected density field, which replaces the filtered density field in the penalization of all mechanical quantities. Unlike the filtered density field, the support of the projected density field is limited to the local element. Because of this, calculation of the projected field is efficient. In this thesis, the approximation by Wang et al. [91] of the intermediate projection filter proposed by Xu et al. [92] is used. This formulation gives the projected density as

$$\rho_e(\tilde{\rho}_e) = \frac{tanh(\beta\tilde{\eta}) + tanh[\beta(\tilde{\rho}_e - \tilde{\eta})]}{tanh(\beta\tilde{\eta}) + tanh[\beta(1 - \tilde{\eta})])} \tag{2.15}$$

The intermediate density filter allows for the threshold level to be set between solid and void limits by adjusting $\tilde{\eta}$. In comparison to other projection approaches, the intermediate density filter preserves the volume of the third field relative to the filtered field for $0 < \tilde{\eta} < 1$. However, these values also cause the implicit mesh regularization achieved using density filtering to be violated [91]. For $\tilde{\eta} = 0$ the original Heaviside-filter is returned while $\tilde{\eta} = 1$ returns the modified-Heaviside filter [93]. The trade-offs encountered for different values of $\tilde{\eta}$ in the size-dependent formulation are discussed in the results section of this thesis.

2.6 Compliance-minimization problem formulation

Having discussed the underlying FE formulation and parameterization of the structural domain, the original compliance problem put forth by Bendsøe and Kikuchi [4] can be stated. The goal of this formulation is to maximize the structural stiffness of the solid domain, a common objective in automotive and aerospace applications [94]. The elastic strain energy is expressed within the FE framework as the minimization objective function. The structural problem is implicitly required to satisfy the discretized statement of equilibrium. Additionally, it is constrained by a limitation on the consumption of material normalized against the overall admissible volume. Stated formally, the optimization problem is given as

$$
\begin{aligned}
(\mathbb{P}_1) \quad \underset{\boldsymbol{x}}{\text{minimize:}} \quad & C(\boldsymbol{x}) = \boldsymbol{u}^T \boldsymbol{K} \boldsymbol{u} \\
\text{subject to:} \quad & \boldsymbol{K}(\boldsymbol{x})\boldsymbol{u}(\boldsymbol{x}) = \boldsymbol{f} \\
& V(\boldsymbol{x}) = \sum_{e=1}^{N} v_e \rho_e(\boldsymbol{x}) \leq \overline{V} \\
& \epsilon^{min} \leq \rho_e(\boldsymbol{x}) \leq \epsilon^{max} \qquad \forall e \in \Omega \\
\text{where:} \quad & \boldsymbol{x} = \{x_1, x_2, ... x_N\}
\end{aligned}
\tag{2.16}
$$

where $\overline{V}$ is the limiting volume fraction and v_e is geometric volume of each element in the domain divided by the overall domain volume. In the implementation used in this thesis, the projected density field is restricted by ε^{min} and ε^{max}, with limits set to 1×10^{-3} and 1 respectively. These two limits correspond to void and solid elements [87].

2.7   Stress problem formulation

2.7.1   Relaxation of elemental stress

In order to access feasible topologies within the admissible structural domain, a relaxation method must be employed to avoid the singularity problem explored by Rozvany [33] and Cheng and Guo [30–32]. In this thesis, the qp-penalization proposed by Bruggi and Venini [34] is applied. This method is advantageous due to its consistency with the SIMP formulation and its continuation-free robustness.

At its core, the qp-penalization approach works by weighting each structural quantity of interest on an elemental basis. For a three field SIMP approach, this takes the form of a power law relationship as shown

$$
\begin{aligned}
\eta_v[\rho_e(\boldsymbol{x})] &= [\rho_e(\boldsymbol{x})]^\mu \\
\eta_K[\rho_e(\boldsymbol{x})] &= [\rho_e(\boldsymbol{x})]^\phi \\
\eta_S[\rho_e(\boldsymbol{x})] &= [\rho_e(\boldsymbol{x})]^\psi
\end{aligned}
\tag{2.17}
$$

The formulation is identical for a two-field SIMP formulation with $\tilde{\rho}$ replacing ρ. Each weight is applied to the elemental volume, elasticity matrix, and stress tensor respectively. The interaction between the penalization of the constitutive and stress tensors the In combination, these three weights can be used to strongly penalize intermediate densities as well. In order to achieve these features, the three weighting powers must be chosen such that (1) all three weighting function are monotonically increasing, (2) yield values of 0 and 1 at filtered density values of 0 and 1, (3) $\eta_K(\rho) < \eta_v(\rho) < 1$ across $0 < \rho < 1$, and (4) $\eta_K(\rho) < \eta_S(\rho) < 1$ across $0 < \rho < 1$. These requirements ensure that the domain can generate structurally relevant voids without converging to the degenerate all-void solution. In this paper, values of $m = 1$, $q = .5$, and $p = 3$ are employed following successful implementation of this scheme as demonstrated by Le et al. [29] and Holmberg et al. [35]. This penalization is illustrated for the bounded projected density domain in **Figure 2.3**.
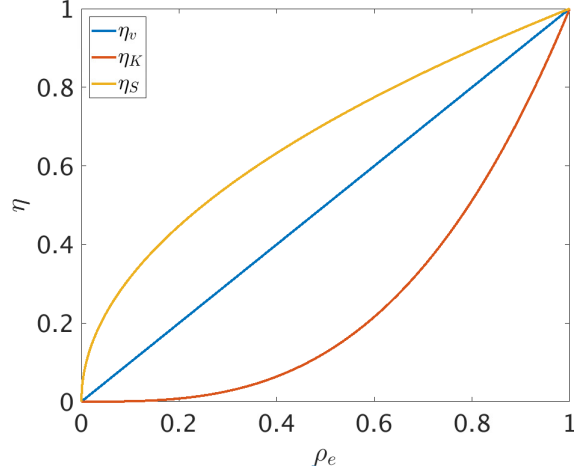
Figure 2.3. Plot of the penalization functions relative to projected density.

Using this penalization, the infinitesimal stress tensor, $\hat{\boldsymbol{\sigma}}_a$, given using the FE formulation as

$$\hat{\boldsymbol{\sigma}}_a = \boldsymbol{E}_0 \boldsymbol{B}_a \boldsymbol{u}_e \tag{2.18}$$

is penalized to yield the tensor, $\boldsymbol{\sigma}_a$

$$\boldsymbol{\sigma}_a = \rho_e^{\psi} \hat{\boldsymbol{\sigma}}_a \tag{2.19}$$

This formulation provides for stresses calculated at the integration points, a, independent from elemental locations e. For all stress analysis in this thesis, elemental stress is calculated at the single hyper-convergent Gauss point of the bi-linear iso-parametric element [40]. This maps a and e as one to one for all elements.

2.7.2 Strength constraint aggregation

With the issue of the vanishing element stress singularity addressed, attention may be paid to insuring the effective enforcement of a relevant strength criterion. The interpretation of strength constraints applied to the allowable structural domain follows from elastic structural design. Failure is defined as the point at which any

infinitesimal volume within the domain ceases to behave according to the model of linear elasticity. Formally this may be expressed as

$$|\boldsymbol{\sigma}^\gamma(\mathbf{x})| \leq |\varsigma^f| \quad \forall \mathbf{x} \in \Omega \tag{2.20}$$

This point is characterized by a given stress measure, σ^γ, and limited by a prescribed failure strength value, ς^f. The origins and physical mechanisms of the particular stress measures and failure strengths utilized within this thesis will be expanded upon in later sections. The importance of this definition within the framework of constrained topology optimization is that the traditional definition of structural failure corresponds to local constraint on the domain. This is in distinct contrast to the traditional global volume and compliance formulations.

This characteristic implies that strength constraints should be treated independently for each element in the structural domain. Early approaches to the stress problem employed N independent constraints corresponding to the N elements of the FE mesh [39]. Practically, this method is never employed in modern approaches. Instead, it is realized that the onset of failure in a structure occurs if any element in the structural domain exceeds ς^f. It follows that $\boldsymbol{\sigma}^\gamma(\mathbf{x})$ is effectively limited with a single, aggregated constraint that captures the maximum value of stress on the domain. To allow the use of gradient based optimization schemes, maximum stress is approximated using a continuous function. Commonly either a p-norm or Kreisselmeier-Steinhouser [41] function is applied. In this thesis, p-norm aggregations are used. Local stress constraints are aggregated into a single global constraint

$$\sigma^{PN}(|\boldsymbol{\sigma}^\gamma|) \leq |\varsigma^f| \tag{2.21}$$

where

$$\sigma^{PN}(|\boldsymbol{\sigma}^\gamma|) = \left[\frac{1}{N}\sum_{a \in \Omega}(|\sigma^\gamma|)^{p_n}\right]^{1/p_n} \tag{2.22}$$

To remove the absolute value operator and alleviate issues with constraints of different orders of magnitude, the p-norm equation is normalized to yield the form

$$\tilde{\sigma}^{PN} = \left[\frac{1}{N} \sum_{a \in \Omega} \left(\frac{\sigma^\gamma}{\varsigma^f} \right)^{p_n} \right]^{1/p_n}$$

(2.23)

In Eq. 2.22, p_n is the approximating power. As $p_n \to \infty$, the p-norm closely approximates the maximum, however large values of p_n lead to numerical instability. In practice, this trade-off prevents the large values of p_n necessary for an effective global stress constraint. Instead, clustered constraints are preferred for stress approaches [29, 35, 46]. The stress level aggregation method proposed by Holmberg et al. [35] is used in this thesis. Due to the possible dependence of ς^f on the design variables of the optimization, the local penalized stress measures are normalized by the local strength then sorted by ascending value. Clusters are formed following the scheme given below

$$\underbrace{\frac{\sigma_1^\gamma}{\varsigma_1^f} \leq \frac{\sigma_2^\gamma}{\varsigma_2^f} \leq \dots \leq \frac{\sigma_{\frac{i}{n_c}}^\gamma}{\varsigma_{\frac{i}{n_c}}^f}}_{\text{cluster } 1} \leq \dots \leq \underbrace{\frac{\sigma_{\frac{(n_c-1)i}{n_c}}^\gamma}{\varsigma_{\frac{(n_c-1)i}{n_c}}^f} \leq \frac{\sigma_{n_e}^\gamma}{\varsigma_{n_e}^f}}_{\text{cluster } n_c}$$

(2.24)

which results in n_c distinct stress clustered p-norm values of the form

$$\tilde{\sigma}_i^{PN} = \left[\frac{1}{N_i} \sum_{a \in \Omega_i} \left(\frac{\sigma_i^\gamma}{\varsigma^f} \right)^{p_n} \right]^{1/p_n}$$

(2.25)

For all problems considered, n_c is selected to keep N_i on $\mathcal{O}(10^3)$. To account for any deviation of the aggregated stress measure from the maximum on the cluster domain, the adaptive normalization approach proposed by Le et al. [29] is used. This method calculates an adjustment to the p-norm approximation using the preceding iteration's stress calculations. The factor is calculated by

$$\tilde{c}_i^I = \tilde{\alpha}^I \frac{(\sigma_i^\gamma/\varsigma^f)_{max}^{I-1}}{(\sigma_i^{PN})^{I-1}} + (1 - \tilde{\alpha}^I)\tilde{c}_i^{I-1}$$

(2.26)

and is applied at every iteration to the calculated aggregated cluster. α^I is a factor used to restrict oscillation of the normalization. For problems in this thesis $\alpha^I = 1$.

2.7.3 Strength-constrained problem formulations

There are two interesting formulations of the strength-constrained problem posed in literature and both will be considered here. The first concerns the minimization of the structural volume subjected to static failure constraints ensuring structural feasibility. In this thesis, this problem follows the form given below

$$
\begin{aligned}
(\mathbb{P}_3) \quad \underset{\boldsymbol{x}}{\text{minimize:}} \quad & V(\boldsymbol{x}) = \sum_{e=1}^{N} v_e \rho_e(\boldsymbol{x}) \\
\text{subject to:} \quad & \boldsymbol{K}(\boldsymbol{x})\boldsymbol{u}(\boldsymbol{x}) = \boldsymbol{f} \\
& \tilde{c}_i^I \tilde{\sigma}_i^{PN}(\boldsymbol{x}, \sigma^f) \leq 1 \qquad i = 1, N_i \\
& \epsilon^{min} \leq \rho_e(\boldsymbol{x}) \leq \epsilon^{max} \quad \forall e \in \Omega \\
\text{where:} \quad & \boldsymbol{x} = \{x_1, x_2, ...x_N\}
\end{aligned}
\tag{2.27}
$$

Alternatively, the original compliance formulation can be extended with additional stress constraints. This effectively reduces the occurrence of stress concentrations in the maximum stiffness structures obtained with the standard compliance formulation. This optimization problem takes the form

$$
\begin{aligned}
(\mathbb{P}_2) \quad \underset{\boldsymbol{x}}{\text{minimize:}} \quad & C(\boldsymbol{x}) = \boldsymbol{u}^T \boldsymbol{K} \boldsymbol{u} \\
\text{subject to:} \quad & \boldsymbol{K}(\boldsymbol{x})\boldsymbol{u}(\boldsymbol{x}) = \boldsymbol{f} \\
& V(\boldsymbol{x}) = \sum_{e=1}^{N} v_e \rho_e(\boldsymbol{x}) \leq \overline{V} \\
& \tilde{c}_i^I \tilde{\sigma}_i^{PN}(\boldsymbol{x}, \sigma^f) \leq 1 \qquad i = 1, N_i \\
& \epsilon^{min} \leq \rho_e(\boldsymbol{x}) \leq \epsilon^{max} \qquad \forall e \in \Omega \\
\text{where:} \quad & \boldsymbol{x} = \{x_1, x_2, ...x_N\}
\end{aligned}
\tag{2.28}
$$

Additionally, the compliance objective can be used to improve convergence for stress-constrained problems that would otherwise have closely grouped local minima.

2.8 Sensitivity analysis for compliance- and stress-based problems

To leverage available efficient gradient based algorithms for solving large-scale optimization problems, the first order sensitivities of all relevant functions must be calculated. These sensitivities are calculated with respect to the design variables of the problem, $\boldsymbol{x}$ and must consider the effects of the filtered and projected density fields. The sensitivity of the volume constraint is given through the chain rule as

$$\frac{\partial V}{\partial x_b} = \frac{\partial V}{\partial \rho_e} \frac{\partial \rho_e}{\partial \tilde{\rho}_e} \frac{\partial \tilde{\rho}_e}{\partial x_b} \tag{2.29}$$

The first two terms of Eq. 2.29 are analytic derivatives of the volume measure and projected density respectively and are ommitted for brevity. The third gives the sensitivity of the filtered density field with the design variables on the domain. Practically, this support field is convolved with the other terms of the derivative, an approach common to any equation where this partial arises. This convolution is calculated using the convenient form presented by Andreassen et al. [87] given below

$$\frac{\partial \Psi_w}{\partial x_b} = \sum_{f \in N_b} \frac{\partial \Psi_w}{\partial \tilde{\rho}_f} \frac{\partial \tilde{\rho}_f}{\partial x_b} = \sum_{f \in N_b} \frac{1}{\sum_{i \in N_e} H_{fi}} H_{bf} \frac{\partial \Psi_w}{\partial \tilde{\rho}_i} \tag{2.30}$$

While the sensitivity of the volume constraint is relatively simple, both the compliance and stress measures depend on the displacement vector. This vector is in turn implicitly dependent on the design variable vector. In light of this dependence, an adjoint sensitivity approach is followed to calculate the derivative. This approach is preferred for problems with many design variables but a limited number of constraints [1]. Following this approach, the compliance objective is restated with an additional term corresponding to the zero function

$$C = \boldsymbol{f}^T \boldsymbol{u} - \tilde{\boldsymbol{\lambda}}^T (\boldsymbol{K}\boldsymbol{u} - \boldsymbol{f}) \tag{2.31}$$

Differentiating and rearranging yields

$$\frac{\partial C}{\partial \rho_e} = (\boldsymbol{f}^T - \tilde{\boldsymbol{\lambda}}^T \boldsymbol{K}) \frac{\partial \boldsymbol{u}}{\partial \rho_e} - \tilde{\boldsymbol{\lambda}}^T \frac{\partial \boldsymbol{K}}{\partial \rho_e} \boldsymbol{u} \tag{2.32}$$

where

$$\boldsymbol{f}^T - \tilde{\boldsymbol{\lambda}}^T \boldsymbol{K} = 0 \tag{2.33}$$

is the adjoint equation for the problem. Obviously, Eq. 2.33 is satisfied if $\tilde{\boldsymbol{\lambda}} = \boldsymbol{u}$. Thus the compliance objective is considered self-adjoint and its derivative given by

$$\frac{\partial C}{\partial \rho_e} = -\phi \rho_e^{\phi-1} E_0 \boldsymbol{u}^T \boldsymbol{K}_e \boldsymbol{u} \tag{2.34}$$

which is then multiplied by the projection sensitivity and treated via Eq. 2.30 to give the sensitivity with respect to the design variable vector.

Sensitivity of the stress constraint follows a similar analysis, though with added complexity as this measure is shown to not be self-adjoint. The sensitivity is given below for a general aggregated stress-measure in terms of the penalized stresses, $\boldsymbol{\sigma}_a$. The full derivation given in Holmberg et al. [35] is omitted for brevity.

$$\frac{\partial \sigma_i^{PN}}{\partial x_b} = \sum_{a \in \Omega_i} \frac{\partial \sigma_i^{PN}}{\partial \sigma_a^\gamma} \left(\frac{\partial \sigma_a^\gamma}{\partial \boldsymbol{\sigma}_a} \right)^T \psi \rho_e^{\psi-1} \frac{\partial \rho_e}{\partial \tilde{\rho}_e} \frac{\partial \tilde{\rho}_e}{\partial x_b} \hat{\boldsymbol{\sigma}}_a - \rho_e^\psi \tilde{\boldsymbol{\lambda}}_i^T \left[\sum_{r=1}^{n_e} \frac{\partial \boldsymbol{K}}{\partial \rho_r} \frac{\partial \rho_r}{\partial \tilde{\rho}_r} \frac{\partial \tilde{\rho}_r}{\partial x_b} \boldsymbol{u} \right] \tag{2.35}$$

where the stress-cluster adjoint vector is given as the solution to the equation

$$\boldsymbol{K} \tilde{\boldsymbol{\lambda}}_i = \sum_{a \in \Omega_i} \frac{\partial \sigma_i^{PN}}{\partial \sigma_a^\gamma} \boldsymbol{B}_a^T \boldsymbol{E}_0^T \frac{\partial \sigma_a^\gamma}{\partial \boldsymbol{\sigma}_a} \tag{2.36}$$

2.9   The Method of Moving Asymptotes

In search of an algorithm to solve the non-linear optimization problems posed above, a significant portion of academic research has gravitated towards using the Method of Moving Asymptotes (MMA) algorithm proposed by Svanberg [95] and made publicly available in code as a complement to [96]. The MMA method is particularly well suited to the problems considered in this paper, where an exceptionally large design space is constrained by a handful of limiting functions. It works by

reformulating the non-linear optimization problem into a series of convex linear approximations to direct a series of sequential minimization steps on the design vector. As an input, only the values of the various optimization functions and their first order sensitivities must be calculated, making it relatively inexpensive compared to alternative algorithms.

The MATLAB implementation of the algorithm is used to direct convergence for the problems posed in this paper. The algorithm easily allows for variation of the optimization formulation and does not require passing of functions or an excessive number of parameters. Additionally, unlike some other black-box algorithms the user is given suitable control over updating the approximation move limits. This allows the convergence behavior of the algorithm to be adjusted as dictated by the behavior of the problem. For all numerical examples in the following sections, unless otherwise specified, the MMA move limit parameters used are as given in **Table 2.1**.

Table 2.1. MMA Update Parameters

Parameter	Use	Value
move	Inner problem move limit	0.10
asyinit	Initial outer problem move limit	0.05
asyincr	Outer problem increase move limit	1.05
asydecr	Outer problem decrease move limit	0.70

2.10 Karush-Kuhn-Tucker conditions and stopping criteria

Through the use of the MMA algorithm to approximate the non-convex stress-based topology optimization problem, the optimality of the approximation can be estimated using the KKT conditions. In essence, these conditions provide a first-derivative test for verifying the necessary and sufficient conditions of the original

problem [96]. For the general MMA formulation, the inner-problem is given in the form

$$
\begin{aligned}
\underset{\boldsymbol{x}}{\text{minimize:}} \quad & h_0(\boldsymbol{x}) \\
\text{subject to:} \quad & h_i(\boldsymbol{x}) \leq 0, \quad i = 1, ..., m
\end{aligned}
$$

(2.37)

and the KKT conditions may be expressed in terms of the vector of Lagrange multipliers λ_i as

$$
\begin{aligned}
\frac{\partial h_0}{\partial x_j}(\hat{\boldsymbol{x}}) + \sum_{i=1}^{m} \lambda_i \frac{\partial h_i}{\partial x_j}(\hat{\boldsymbol{x}}) &= 0, \quad j = 1, ..., n \\
h_i(\hat{\boldsymbol{x}}) &\leq 0, \quad i = 1, ..., m \\
\lambda_i &\geq 0, \quad i = 1, ..., m \\
\lambda_i h_i(\hat{\boldsymbol{x}}) &= 0, \quad i = 1, ..., m
\end{aligned}
$$

(2.38)

These conditions are the stationary, primal feasibility, dual feasibility, and complementarity conditions respectively. Due to the numerical nature of the optimization problem, it is not feasible to require that the strict inequalities are met. Instead, the stopping criterion is given as a tolerance value on the Euclidean norm of the four combined conditions. For all problems in this paper, a tolerance value of 1×10^{-3} is prescribed.

In addition to the KKT stopping criterion provided, a second criterion is provides for the event in which optimality conditions remain unsatisfied but practical convergence is observed. Here practical convergence is defined as the result of a study where the objective function is invariant with successive optimization search steps. This may occur if the MMA algorithm leads to a degenerate region in the feasible design space. To conserve computational resources, the criterion given below is used to terminate the optimization search

$$
\Delta_c \leq \Delta_{tol}
$$

(2.39)

where

$$\Delta_c = \max\left[\left|1 - \frac{f_{i-1}(\boldsymbol{x})}{f_i(\boldsymbol{x})}\right|, \left|1 - \frac{f_{i-2}(\boldsymbol{x})}{f_{i-1}(\boldsymbol{x})}\right|\right]$$

and $f_i(\boldsymbol{x})$ is the value of the objective function at optimization iteration i. Effectively, this exit condition allows for termination of the MMA algorithm after three successive iterations which show no change in objective. The change tolerance, Δ_c, used for all examples in this paper is 1×10^{-5} unless otherwise specified.

Finally, for any optimization run which fails to converge under the aforementioned criteria, an iteration timeout is prescribed to prevent an infinite search. Unless otherwise specified, this timeout is set to 1500 iterations for all problems considered in this thesis.

2.11   MATLAB Implementation

Taken together, the preceding sections constitute the theoretical and analytic underpinnings of SIMP-based TO for stress formulations. In this thesis, these components are incorporated into the academic framework provided for MATLAB by Andreassen et al [87]. The flowchart of functions utilized in the basic stress algorithm is illustrated in **Figure 2.4**. This code is further expanded upon in **Section 3.6** for size dependent strength behaviors and is presented in its entirety as a supplement to this thesis.
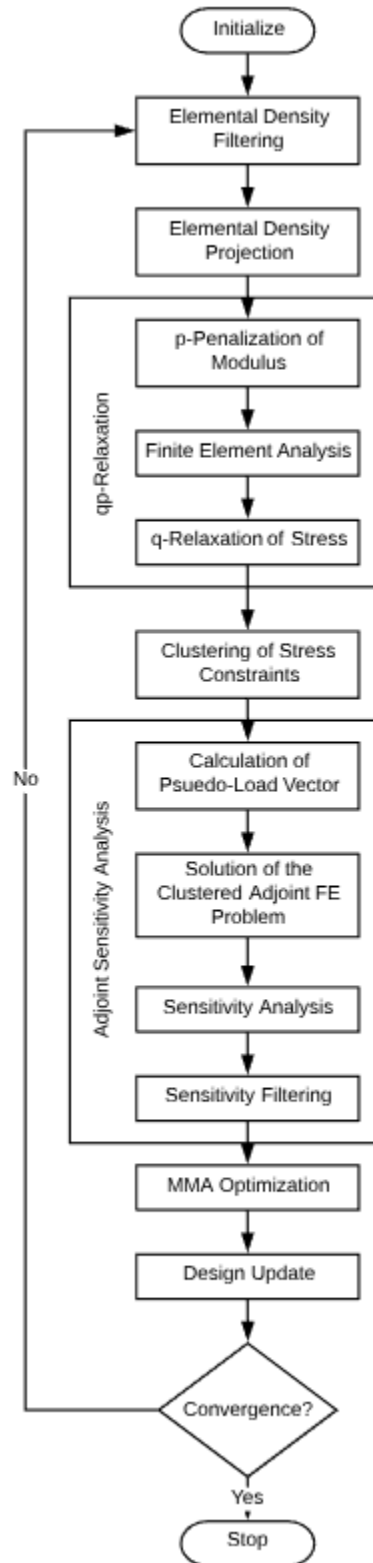
Figure 2.4.   Flowchart illustrating major functions of basic stress constrained TO algorithm.

3. SIZE-DEPENDENT STRENGTH TOPOLOGY OPTIMIZATION

3.1 Physical models of size dependence

As previously discussed, the field of size dependent strength characteristics is rich with complexity and remains an ongoing field of inquiry. It is not the intention of this thesis to add to the mechanistic arguments of the discipline nor to interrogate novel material models. Instead, several established strength scaling laws are presented and their physical ties to real material behavior briefly addressed. This section establishes the analytic forms these scaling laws take within the proposed TO framework.

3.1.1 Weibull scaling

The scaling model proposed by Weibull is considered first. Traditionally, Weibull's model considered to be analogous to the failure of a system dominated by the strength of its "weakest link". Weibull failure statistics are commonly used to describe the failure behavior of materials or material systems that exhibit brittle tensile failure. These systems rupture suddenly when the applied load initiates the mode-I cracking of favorably oriented inclusions within the material. As these micro-structural features cannot be practically controlled for in manufacturing processes, the observed phenomenological strength is described statistically [5]. The Weibull probably of failure function is given as

$$P_f(\sigma_{Wb}) = 1 - exp\left\{ \int_V \bar{c}[\boldsymbol{\sigma}(\boldsymbol{x})]dV(\boldsymbol{x}) \right\} \tag{3.1}$$

where

$$\bar{c}[\boldsymbol{\sigma}(\boldsymbol{x})] \approx \frac{\sum_i P_1(\sigma_i)}{V_0} \tag{3.2}$$

P_1 is the cumulative probability of failure of in each of the three principal loading directions. V_0 is a representative uniaxial tensile test specimen volume used for calibrating the model. For this thesis, P_1 is described using the 2-parameter Weibull model as

$$P_1(\sigma) = \left(\frac{\sigma}{\varsigma_0}\right)^m \tag{3.3}$$

where ς_0 is used to scale the model and m is the Weibull modulus. Intuitively, since the entirety of the Weibull model is formulated with respect to a reference tensile test with representative feature size, a strength scaling relation follows. For the general local stress state, the size-scaling of the average material strength is given as

$$\overline{\varsigma}_{Wb} \propto L_{Wb}^{-\frac{n_d}{m}} \tag{3.4}$$

where L_{Wb} in this case is a characteristic feature size and $n_d = 1, 2, 3$ for the level of loading similarity. Finally, applying the strength and feature size from the known reference specimen, the scale-dependent strength is calculated as

$$\varsigma_{Wb} = \varsigma_0 \left(\frac{V_{Wb}}{V_0}\right)^{-1/m} \tag{3.5}$$

Thus the strength scaling is given by the power $-\frac{1}{m}$. Materials with a lower modulus exhibit a wide spread of structural strength. Conversely, materials with a high modulus approach a power-law with exponent of zero. This indicates size-independent strength characteristics. Weibull modulus values on the order of 10-20 are common in high quality engineering ceramics.

For the plane stress TO formulation used in this thesis, Eq. 3.5 must be written in terms of the approximated local feature size. As thickness of the structure remains fixed throughout the optimization, it is absorbed into σ_0 into the reference specimen strength. Then the Weibull scaling model is discretized throughout the domain. Each element assumes a power-law dependence on some estimate of local feature size on the FE domain, d_e. This width is estimated local to the element of interest within

the discretization. A means for calculating d_e is proposed later in this chapter. This approach results in the expression

$$\varsigma_{TWb} = \varsigma_{T_0} \left(\frac{d_e}{D_0} \right)^{-1/m} \tag{3.6}$$

where D_0 is the width of the reference tensile specimen. Using this equation, the Weibull scaling is not considered in terms of the elemental volume relative to the specimen volume. Instead, it is scaled to the non-local structural feature volume. Compared to the more common form of the discretized Weibull model, the proposed scaling captures the effect of increasing the structural width of a given member under a constant stress field across this width. This formulation fails to accurately capture the beneficial effects of stress localization for bending dominated members. For structures with strain gradients across the member width, the proposed Weibull formulation acts as a conservative constraint on stress. It effectively over-predicts the statistical likelihood of failure through assuming a deflated value of strength.

From this formulation and physical intuition, it is clear that larger specimens exhibit a higher likelihood of a encountering a critical micro-flaw. This implies that for materials governed by statistical effects, smaller features exhibit higher nominal strength. This implies that static-failure based TO models disregarding size scaling will exhibit markedly different results if they are realized on different physical scales. Physical structures with large structural features produced through TO approaches with size-independent strength will overestimate their load carrying capacity unless the constraining stress is taken from test results on a similar scale. The opposite effect will be realized on physically small structures. In this case, load carrying capacity may be underestimated. Considering both results, it is concluded that size-independent schemes result in sub-optimal structures at best and physically in-feasible results at worst.

As a note, the Weibull strength-scaling effect is only applicable to material tensile strength, following physical arguments on micro-crack opening. Arguments advocating for statistical strength-effects in compression failure are not considered.

3.1.2   Linear Elastic Fracture Mechanics Scaling

While the Weibull model of size-dependent describes failure due to propagation of material micro-cracks, a separate scaling law governs the failure behavior of cracks or flaws on the structural feature scale. This behavior is captured by considering the LEFM of geometrically-similar flawed specimens. Starting with Irwin's [10] equation for the nominal structural strength relative to the fracture toughness of a specimen, it may be seen that geometric feature size is critical to LEFM behavior. Irwin's equation is given as

$$\varsigma_N = \frac{K_{Ic}}{\sqrt{2\pi a}F\left(\frac{a}{W}\right)} \tag{3.7}$$

where ς_N is the nominal member strength, K_{Ic} is the critical fracture toughness of the material, F is a geometric correction factor, W is the specimen width of interest, and a is the crack length. **Figure 3.1** provides context for the various parameters of Irwin's fracture toughness formulation for a tension member with a single sharp flaw. This specimen is commonly referred to by its geometry as a Single Edge Notched Tension (SENT) configuration. For $a \geq 0.2$ [14], this equation holds for describing the nominal strength of the structural feature. If geometrically similar specimens are considered, $\frac{a}{W}$, and by extension F, remain constant. However, a varies independently of ς_N. This implies the following relationship

$$\varsigma_N \propto a^{-\frac{1}{2}}$$

and by extension

$$\varsigma_N \propto W^{-\frac{1}{2}} \tag{3.8}$$
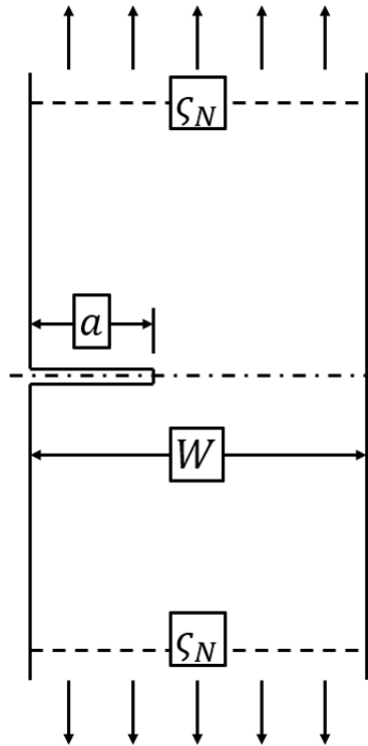
Figure 3.1. SENT specimen geometry reference.

Following this equation, the nominal strength for geometrically similar specimens scales with a power-law form such that larger specimens are weaker than their smaller counterparts. LEFM results in a size-scaling law identical to the Weibull formulation, though with an increased scaling coefficient. With this knowledge in hand, a TO form of the LEFM scaling can be written similar to Eq. 3.6 as

$$\varsigma_{T_{LEFM}} = \varsigma_{T_0} \left(\frac{d_e}{D_0} \right)^{-1/2} \tag{3.9}$$

where in this case ς_{T_0} corresponds to a reference strength and D_0 corresponds to a reference length both determined from fracture experiments. In this case, the TO interpretation of the representative feature length is more intuitive and corresponds directly to the specimen width in the context of LEFM. Compared to the Weibull model of scaling, the lessons in applying LEFM to TO are similar, but more pro-

nounced. Scaling effects are heightened, raising the risk of the two less than ideal outcomes discussed above occurring over smaller ranges of structural feature size.

3.1.3   Bažant Type II Size Effect Law and the Fracture Process Zone

While the LEFM strength scaling model is well behaved and applies broadly to most brittle materials, size-scaling in materials which follow non-LEFM is significantly more diverse [14]. Despite this fact, significant inroads have been made in describing the size-dependent strength of a class of materials that exhibit quasi-brittle failure characteristics. Materials behave in a quasi-brittle fashion if they exhibit stable crack growth through progressive failure of structural elements. Examples of quasi-brittle materials include reinforced concrete, composite laminates, some polymer systems [5], and most metallic systems on micro- or nano-scales [97]. Quasi-brittle behavior is fundamentally driven by the interaction between the material's FPZ and the geometric boundaries of the structure in question.

For this thesis, the size scaling considered takes the form of Bažant's first deterministic tensile Size Effect Law (SEL). Arguments including a compressive size effect [98] are neglected due to the complexity of buckling behaviors and to remain consistent with the Weibull based model for comparison. The field of quasi-brittle size scaling is rich and many alternative models of scaling exist [97]. However, the SEL is well-regarded, founded on fundamental FM quantities, and serves to illustrate the important physical implications for the purposes of incorporating these models in TO based design. The original, Type II SEL was derived in [13] through energy release analysis and may be expressed as

$$\varsigma_{N_{SEL}} = \frac{Bf_t'}{\sqrt{1 + D/D_0}} \tag{3.10}$$

where Bf_t' and D_0 are empirical constants fit to the results of representative fracture specimen tests and D is the relevant structural element cross-section. Bf_t' is analogous to a limiting strength far from sharp crack obtained from fracture experiments. It

was later shown that Eq.3.10 can be expressed in terms of fundamental fracture quantities [99] as

$$\varsigma_{N_{SEL,II}} = \sqrt{\frac{E'G_f}{g(\frac{a}{W})D + g'(\frac{a}{W})c_f}} \tag{3.11}$$

where G_f is the critical energy release rate of the material, E' is the Young's modulus modified for either plane stress or plane strain, c_f is a characteristic material length proportional to the FPZ size, and $g(\frac{a}{W})$ is equivalent to $F(\frac{a}{W})$. Eq. 3.11 is generally referred to as the Type II SEL. Thus, unlike the LEFM-scaling model, the SEL depends not only on the geometric feature scale but its relationship to a material dependent intrinsic length scale. This length scale dictates the location of a transition region from LEFM to FPZ dominated rupture behavior in the un-cracked structural ligament. This transition is illustrated in the asymptotic plot shown in **Figure 3.2**.
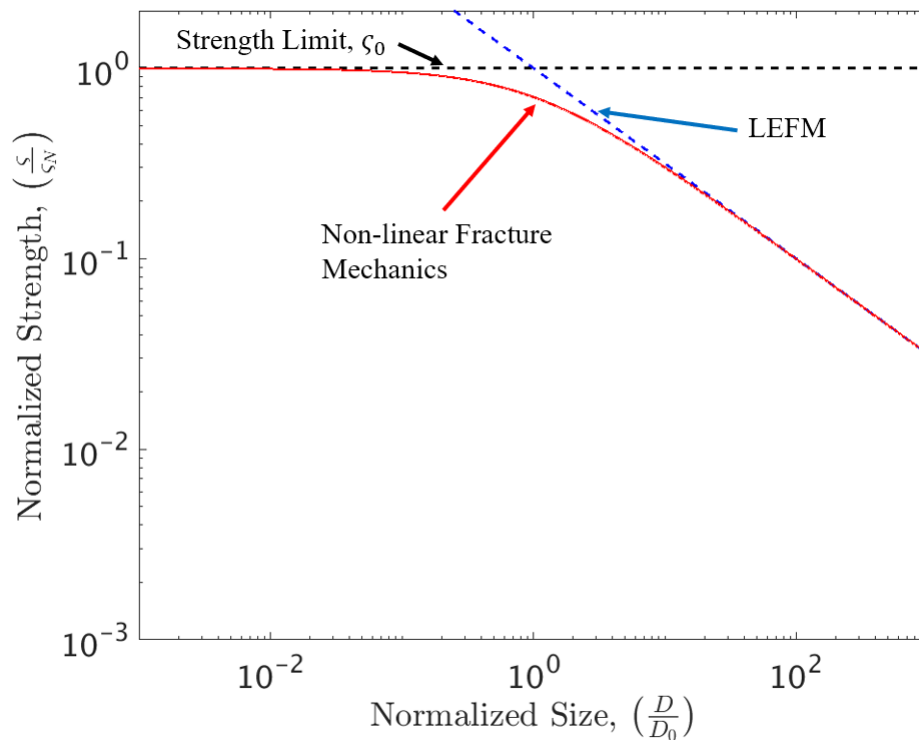
Figure 3.2. Bažant SEL relative to strength and LEFM scaling asymptotes.

In the context of the size dependent TO formulation, Bažant's Type II SEL law corresponds to structural features on the domain which exhibit sub-critical crack growth up to a critical limiting stress $\sigma_{T_{SEL}}$. The specific mechanism for this sub-critical crack growth is not unique and may controlled by reinforcement, time-dependent deformation, or chemical processes [98]. Regardless of the underlying driving force, through applying the Type II SEL the failure mode of abrupt tensile fracture upon reaching a critical crack ratio is constrained. In terms of the relevant TO parameters, the Type II SEL is formulated as

$$\varsigma_{T_{SEL}} = \varsigma_{T_0} \left(1 + \frac{d_e}{D_0} \right)^{-1/2} \tag{3.12}$$

where ς_{T_0} is the asymptotic limiting strength for a reference specimen for a given critical crack ratio. For the SEL d_e is compared to an empirically fit D_0 of a given material obtained through fracture experiments. This form is similar to the LEFM scaling-law, though the dependence on the material length-scale introduces a strength-saturation effect in design.

For structures with features many orders of magnitude larger than the material length scale, LEFM-scaling dominates and the member effective strength scales with the power of $-\frac{1}{2}$. However unlike the power-law models discussed above the Type II SEL-effect asymptotes to a limit. For structures with features many orders of magnitude smaller than the material length scale, members experience FPZ dominated rupture and strength scaling is largely negligible. This result is common to lab-scale concrete structures. Evidence also exists that shows the SEL transition region occurs for features sizes relevant to design for some polymers [100] and additively manufactured materials [101].

In this thesis, the later Universal Size Effect Law (USEL) formalized by Hoover and Bažant [102] is not considered due to the large number of fitting parameters and the need to calculated strain gradients for general stress states. However, the methods proposed within do not preclude use of the USEL for relevant materials and design domains.

3.1.4 Geometric scaling and fixed defect size

Returning to Irwin's fracture toughness relationship given in Eq. 3.7, when the requirement on the geometric similarity of specimens is relaxed and crack size is held constant, a distinct scaling behavior is observed. The implication of these two concepts is illustrated in **Figure 3.3**. If the FPZ of the material is negligible [14], size-scaling theoretically arises only from $F\left(\frac{a}{W}\right)$ and adheres to the models of LEFM. In real specimens, the geometric boundary effect observed within LEFM is not independent of the strain-softening driven Bažant SEL [97, 103]. However, the combination of these two behaviors is still under investigation and will not be considered at length in this paper.
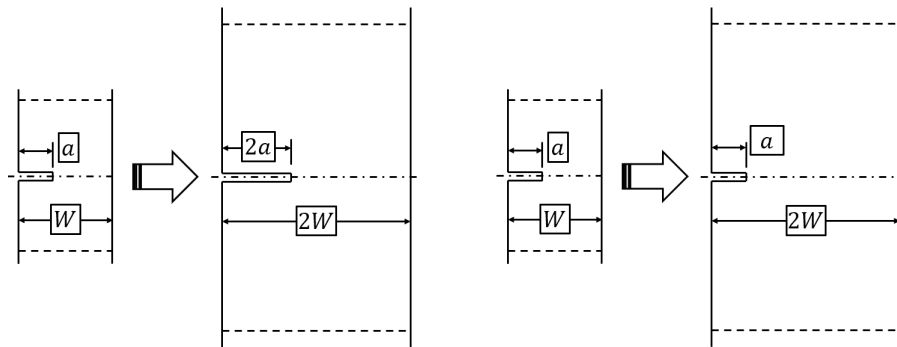
Figure 3.3. Contrasting geometrically similar flaw size scaling and fixed flaw size for two geometrically similar scaled specimens.

To illustrate the form of the geometric boundary scaling model, Irwin's fracture toughness relationship is rearranged here to yield the mode I critical fracture toughness, K_{Ic}

$$K_{Ic} = \varsigma_N \sqrt{2\pi a} F\left(\frac{a}{W}\right) \tag{3.13}$$

which is an intrinsic material property. Therefore, for two model geometries with identical crack sizes but geometrically similar boundaries, the following must hold

$$K_{Ic} = \varsigma_1 \sqrt{2\pi a} F_1\left(\frac{a}{W_1}\right) = \varsigma_2 \sqrt{2\pi a} F_2\left(\frac{a}{W_2}\right) \tag{3.14}$$

Rearranging to give the ratio of strengths yields

$$\frac{\varsigma_2}{\varsigma_1} = \frac{F_1\left(\frac{a}{W_2}\right)}{F_2\left(\frac{a}{W_1}\right)} \tag{3.15}$$

Finally, if it is assumed that ς_1 corresponds to the case where the assumed flaw is vanishingly small compared to the structural size, or $\frac{a}{W_2} \to 0$, Eq. 3.15 becomes

$$\varsigma_{Bnd} = \frac{\zeta \varsigma_T}{F\left(\frac{a}{W}\right)} \tag{3.16}$$

where ζ is an empirical constant that is shown to be equal to 1.122 for all forms of $F\left(\frac{a}{W}\right)$.

To apply models of geometric boundary scaling to topology optimization, the form of $F\left(\frac{a}{W}\right)$ must be provided and the meaning of a and W must be defined. In practice, no general closed form expression for $F\left(\frac{a}{W}\right)$ may be derived. Its behavior is highly dependent on the unique geometry considered in each member. Approximations for $F\left(\frac{a}{W}\right)$ have been derived over time using LEFM, testing, and FE methods. The resulting empirically fit models are tabulated in various references. In this thesis, fits are chosen from Tada, Paris, and Irwin's handbook on the subject [104].

Considering the meaning of a and W within density based TO, it is clear that there is no obvious analogue for a while W is given by the diameter measure, d_e. Thus the implementation of a needs to be considered in further detail. In real engineering applications of ideal structures, a is interpreted to be surface flaws that occur as a result of materials processing. The size of these flaws is captured through materials inspection processes. In the event that no flaws are observed, an assumed flaw equal to the sensitivity limit of the inspection process is taken to be present through the entire structure. To incorporate this form of LEFM analysis into the proposed size-dependent formulation, a similar assumption is made. At the start of the analysis, a measure a_0 is assumed to exist throughout the admissible structural

domain. Obviously, when a material element tends to a void solution, this assumed flaw has no physical meaning. Physical intuition is again violated if the assumed flaw is larger than the boundaries of a single element. Regardless, this assumed flaw size remains a useful abstraction for structuring the size-dependent model. It is essentially a statement that any dense material element is certain to have a favorably aligned flaw passing through it. In summary, within the TO framework of this paper, the geometric scaling is given by the function

$$F_{TO}\left(\frac{a_0}{d_e}\right) = F\left(\frac{a}{W}\right) \tag{3.17}$$

To interrogate this form of size-scaling behavior, two fracture cases are considered. Both concern model geometry with sharp surface flaws or notches. The first fracture model, commonly referred to as a Single Edge Notch Tension (SENT) load case, contains a single sharp notch located at the mid-plane of the structural feature. This model geometry is illustrated by **Figure 3.4**. For this fracture model, $F_{TO}\left(\frac{a_0}{d_e}\right)$ is given as a least squares fit of the form [105]

$$F_{TO}\left(\frac{a_0}{d_e}\right) = 1.122 - 0.231\left(\frac{a_0}{d_e}\right) + 10.550\left(\frac{a_0}{d_e}\right)^2 - 21.710\left(\frac{a_0}{d_e}\right)^3 + 30.382\left(\frac{a_0}{d_e}\right)^4 \tag{3.18}$$

Compared to more accurate fits, such as Tada et al. [104], Eq. 3.18 overestimates $F_{TO}\left(\frac{a_0}{d_e}\right)$ for values of $\frac{a_0}{d_e}$ approaching 1. Practically, converged structures will be driven away from this case, so Eq. 3.18 is preferred for its simple mathematical form.

The second fracture case considered is that of a Double Edge Notch Tension (DENT) load case. In this model, two co-linear sharp notches are located at the structural feature mid-plane as shown in **Figure 3.5**. The chosen fit for this model is given by Tada et al. [104] as

$$F_{TO}\left(\frac{2a_0}{d_e}\right) = \frac{1.122 - 0.561\left(\frac{2a_0}{d_e}\right) - 0.205\left(\frac{2a_0}{d_e}\right)^2 + 0.471\left(\frac{2a_0}{d_e}\right)^3 - 0.190\left(\frac{2a_0}{d_e}\right)^4}{\sqrt{1 - \frac{2a_0}{d_e}}}$$

$$\tag{3.19}$$

where the factor of 2 is used to align d_e with the assumptions of the specimen geometry. To illustrate the effect of the assumed initial flaw size a_0, **Figure 3.6** gives plots
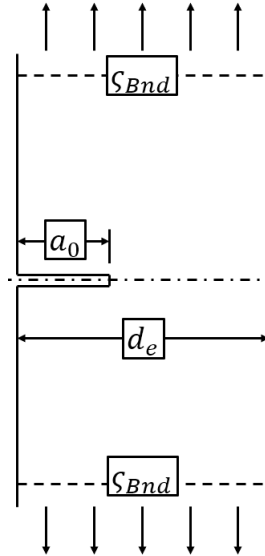
Figure 3.4. SENT load bearing member assumed configuration.

of the strength scaling laws for both the SENT and DENT geometries. In both cases, for members with width less than the assumed flaw size no load can be supported. This is consistent with physical intuition. For the DENT model, this is the overriding effect of the scaling and the model is similar to a damage-tolerant approach. However, for the SENT model significant strength reduction is predicted even for $\frac{a_0}{d_e} > 5$. This indicates that even small flaws should exhibit a significant effect on overall structural strength for intermediate member sizes.

The geometric boundary scaling runs in opposition the models discussed previously and instead suggests larger structural members are necessary to mitigate the effects of intrinsic flaws. Practically, this effect causes issues within the strength-constrained TO framework. As elements approach the fully void condition, their strength approaches zero. Under a normalized local-strength constraint this results in a significant contribution to the p-norm approximation of the maximum strength violation. In turn, these void regions heavily influence the stress-result in a non-realistic manner.
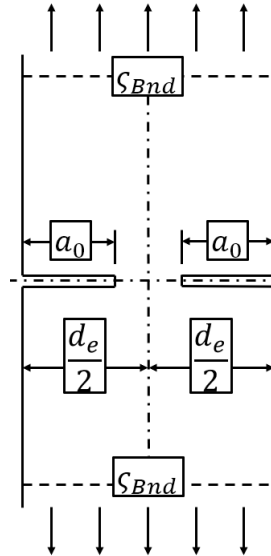
Figure 3.5. DENT load bearing member assumed configuration.

To remove the influence of these regions, a simple elemental deactivation strategy is implemented for these problems. Upon reaching a density threshold, structural elements are removed from the strength clustering approach detailed in Eq. 2.24. This amends the cluster approach so that only reasonably dense features are strength constrained. For all problems in this thesis, a cutoff density of 0.3 is applied. Though this approach lacks sophistication, it allows for reasonable structural convergence and mitigates void region strength issue.

As a note, both the chosen geometric fits and Irwin's fracture toughness assume that $L > W$ and for real world applications, $L > 3W$ for good agreement with the analysis. This guidance is not enforced within the topology optimization framework used herein. Therefore, for short members or elements located near structural nodes the empirical fracture model is likely to be improperly applied. These regions may be bending dominated or exhibit multiaxial stress states which drive more complex fracture behaviors. Furthermore, for certain materials these features will interact with the strain-softening FPZ and drastically change the fracture behavior of the structure.
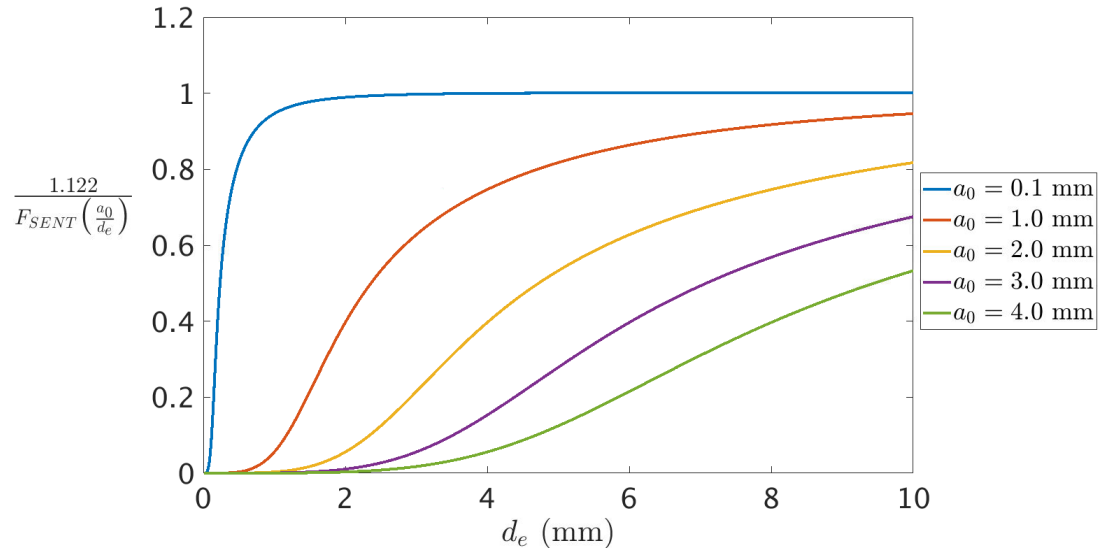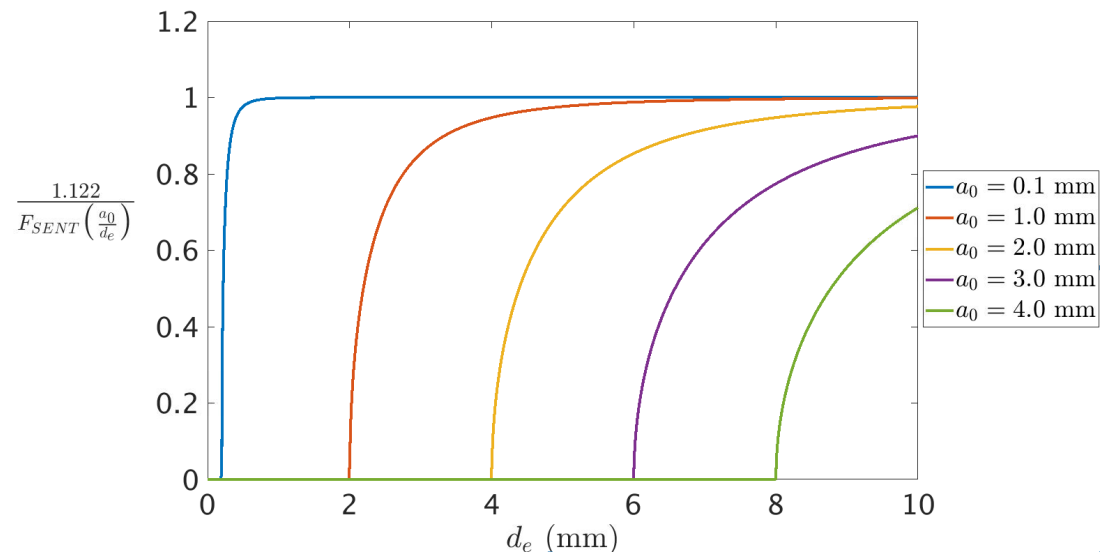
Figure 3.6. (a) SENT-based strength scaling for various assumed flaw sizes, a_0; (b) DENT-based strength scaling for various assumed flaw sizes, a_0.

For cases like this, it is likely more appropriate to apply a J-integral LEFM method [54] for relevant cracking locations identified through prior optimization executions.

3.1.5 Summary

The **Table 3.1** is provided below summarizing the scaling laws considered herein and their corresponding physical failure behaviors. This list of scaling models is not intended to be exhaustive. By considering a few well known scaling models, the wide breadth of material behaviors which must be considered complex TO problems is illustrated.

Table 3.1. Summary of size-dependent failure models

Model	Strength-scaling form, $\varsigma_T(d_e)$	Applicability
Weibull	$\varsigma_{T_{Wb}} = \varsigma_{T_0}\left(\frac{d_e}{D_0}\right)^{-1/m}$ **(3.6)**	Ceramics, brittle systems; micro-cracking dominated.
LEFM	$\varsigma_{T_{LEFM}} = \varsigma_{T_0}\left(\frac{d_e}{D_0}\right)^{-1/2}$ **(3.9)**	Geometrically similar structures with macroscopic flaws.
SEL	$\varsigma_{T_{SEL}} = \varsigma_{T_0}\left(1 + \frac{d_e}{D_0}\right)^{-1/2}$ **(3.12)**	Geometrically similar structures with macroscopic flaws; features which interact with FPZ length scale.
Fixed Flaw	$\varsigma_{T_{flaw}} = 1.122\varsigma_{T_0}\left[F\left(\frac{a_0}{d_e}\right)\right]^{-1}$ **(3.16)**	Fixed macroscopic flaw-size from processing.

3.2 Size-dependent multiaxial failure criterion

Though numerous phenomenological failure criterion have been considered for stress-based topology optimization problems, little consideration has been paid to the physical mechanisms underlying each assumed yield surface. In this thesis, properly accounting for the mechanisms behind various size effect behaviors is of great importance. As such, an adequate failure criterion will address these behaviors and incorporate the size dependence formulations.

For all physical models of size-dependent strength models considered in this thesis, the size-dependence of the material is arises from an observed fast-fracture mode of failure. For the models of brittle and quasi-brittle failure founded on fundamental fracture mechanics concepts this occurs due to Mode I cracking of macro-scale flaws or notches; for Weibull-statistical size dependence this behavior arises from Mode I cracking of favorable micro-scale features. Taking inspiration for the common treatment of Weibull statistical failure in design problems [98], each size-dependent strength forms is considered using a maximum principal stress or Rankine failure criterion. Since converged TO structures with low admissible volumes result in uni-axial loading dominated structures approaching the Michell optimal truss, tri-axial loading effects on these models are neglected.

With a tensile failure criterion established, the remainder of the plane stress failure surface must be defined. Despite the brittle tensile failure modes of the materials considered, compression failure in these systems often occurs at much higher loads and in a somewhat ductile manner. Thus it is clear that an asymmetric criterion is necessary. From a mechanics perspective, it is not unreasonable to assume a failure surface in the form of a Brittle Coloumb Mohr model. However, criteria of this type are only C^0 continuous preventing accurate sensitivity analysis of the failure surface. While this has been addressed in topology optimization by Jeong et al. [37] through smooth approximation of the failure surface, the smoothing factor adds significant mathematical complexity to the implementation with limited benefit. Alternative

models in the form of the Raghava [106] and Drucker-Prager [107] pressure dependent yield formulations for polymers and geological materials respectively provide the C^1 continuity required to calculate first order derivatives. The Drucker-Prager model is limited by the openness of the failure surface under tri-axial and particular plane-stress loading [108]. The elliptical shape of the Raghava yield surface is more robust under conditions of general stress loading.

With the discussion of the failure criteria given above in mind, a formulation combining a principal stress limit and a pressure dependent general failure surface is implemented. This approach was initially proposed by Christensen in [109] and discussed further in [110–112]. The first component of the combined criteria describes general yielding/failure behavior through an elliptic yield surface of the form

$$\alpha\left(\frac{\sigma_{ij}}{\tilde{\kappa}}\right) + \frac{3}{2}\left(1 + \alpha\right)\left(\frac{s_{ij}}{\tilde{\kappa}}\right)\left(\frac{s_{ij}}{\tilde{\kappa}}\right) \leq 1 \tag{3.20}$$

where s_{ij} is the deviatoric stress tensor

$$s_{ij} = \sigma_{ij} - \frac{1}{3}\delta_{ij}\sigma_{kk} \tag{3.21}$$

The two parameters α and $\tilde{\kappa}$ are the shape and scaling parameters of the yield surface. They are given by the experimentally measured uni-axial tension, ς_T, and compression, ς_C, generalized yield strengths as

$$\tilde{\kappa} = |\varsigma_C| \tag{3.22}$$

$$\alpha = \frac{|\varsigma_C|}{\varsigma_{T_0}} - 1 \tag{3.23}$$

The proposed yield surface is generally valid for $\alpha \geq 0$. To capture the distinct mode of brittle tensile fracture, the elliptic yield/failure surface is supplemented by the maximum normal stress criterion of Rankine and Lamé expressed as

$$\sigma^I \leq \varsigma_{T_0}; \qquad \frac{\varsigma_{T_0}}{\varsigma_C} \leq \frac{1}{2} \tag{3.24}$$

At $\frac{\varsigma_{T_0}}{\varsigma_C} = \frac{1}{2}$, the fracture cutoff is tangential to the quadratic yield surface. Brittle versus ductile failure is captured in this framework by the additional parameter

$$
\begin{aligned}
\sigma_H &< \tfrac{2-\alpha}{1+\alpha}, \quad \text{(Ductile)} \\
\sigma_H &> \tfrac{2-\alpha}{1+\alpha}, \quad \text{(Brittle)}
\end{aligned}
\tag{3.25}
$$

The effect of these features together form the various plane-stress failure surfaces illustrated in **Figure 3.7** taken from [111].
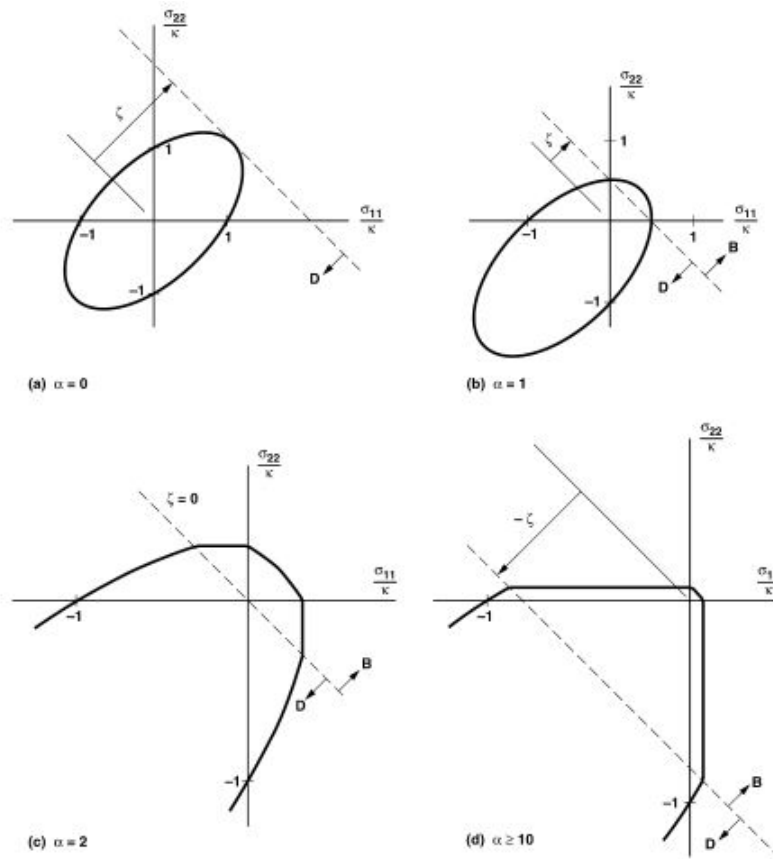
Figure 3.7. The Christensen failure surface for different values of α. (a) $\alpha = 0$, von Mises elliptic yield surface; (b) $\alpha = 1$, asymmetric elliptic failure surface; (c) $\alpha = 2$, elliptic surface with tensile cutoff for moderately brittle materials; (d) $\alpha = 10$, elliptic surface with tensile cutoff for highly brittle materials.

This combined criterion expresses a closed, C_0 continuous yield surface in the plane stress case. As the final converged solutions of most structural topology opti-

mization problems are dominated by axially dominated truss members oriented along principal stress lines within the domain, the illustrated yield surfaces are highly relevant. Failure to incorporate these cutoffs may lead to multiple members which exceed stresses required to incur physical fracture.

Christensen's generalized failure surface is formulated to be size independent [108]. It does not purport to answer the open mechanics question of size-dependent failure under a general stress state. Furthermore, Christensen's quadratic yield surface formulation implies that their exists some fundamental material brittleness measure that can be captured by the difference in uni-axial tension and compression strengths. This leaves two paths available for incorporating size-dependence into the Christensen yield surface: either assume that both tension and compression strengths scale equally with local member size or that the quadratic yield surface should be considered analogous to the strength asymptote present in quasi-brittle materials.

In the case of Weibull failure of highly brittle systems, it is known that the first case does not occur as the micro-cracks which dominate tensile failure in the material do not meaningfully effect the compression behavior of the system. Similar arguments can be made for brittle systems with large crack dominated failure. From these arguments, only the tensile strength of the yield surface should be affected by the structural feature dimension. Using the framework of the Christensen failure criterion the size-dependence of tensile strength is held within the definition of the fracture cutoff while the quadratic yield surface is formulated as a size-independent limiting condition. This approach is taken as the definition of the size-dependent multi-axial failure surface remains an open question in the field of mechanics. No conclusive studies were found that dealt with the topic of brittle size-dependent failures in materials subjected to general stress states.

Following these assumptions, in 2-D plane stress the Christensen elliptic failure surface is expressed as

$$\sigma_{Ch,s} = \left(\frac{1}{\varsigma_{T_0}} - \frac{1}{\varsigma_C}\right) \ \left[\sigma_{11}(\boldsymbol{x}) + \sigma_{22}(\boldsymbol{x})\right] +$$
$$\frac{1}{\varsigma_{T_0}\varsigma_C}\left\{\frac{1}{2}\left[\left(\sigma_{11}(\boldsymbol{x}) - \sigma_{22}(\boldsymbol{x})\right)^2 + \sigma_{22}(\boldsymbol{x})^2 + \sigma_{11}(\boldsymbol{x})^2\right] + 3\sigma_{12}(\boldsymbol{x})^2\right\}$$
$$(3.26)$$

Unlike the Mises measure, the Christensen elliptic failure surface is formulated to be normalized in terms of the relevant strength values. This feature is convenient for incorporating the stress measure in the optimization problem and obviates the need to scale the contributions of the constraints to the MMA search scheme.

For the Rankine fracture criterion, the two plane-stress principal stresses are calculated as

$$\sigma^I = \frac{\sigma_{11} + \sigma_{22}}{2} + \sqrt{\left(\frac{\sigma_{11} + \sigma_{22}}{2}\right)^2 + \sigma_{12}^2} \qquad (3.27)$$

$$\sigma^{II} = \frac{\sigma_{11} + \sigma_{22}}{2} - \sqrt{\left(\frac{\sigma_{11} + \sigma_{22}}{2}\right)^2 + \sigma_{12}^2} \qquad (3.28)$$

Using this approach,

$$\sigma^I > \sigma^{II}, \quad \forall e \in \Omega \qquad (3.29)$$

Within the proposed TO framework, the fracture criterion is imposed on the maximum principal stress, σ^I, and through Eq. 3.29 the constraint is implicitly applied to the minimum principal stress as well. Within the size-dependent framework, Eq. 3.24 becomes

$$\sigma^I \leq \varsigma_T(d_e); \qquad \frac{\varsigma_T(d_e)}{\varsigma_C} \leq \frac{1}{2} \qquad (3.30)$$

where the size scaling is given by the corresponding equation given in **Table 3.1**. Taken together, the two criteria are illustrated in three dimensional, size-dependent stress space $(\sigma^I, \sigma^{II}, d_e)$ in **Figure 3.8**. Various size-dependent strength parameters and models are used to illustrate the behavior of the tensile fracture cutoffs in this space.
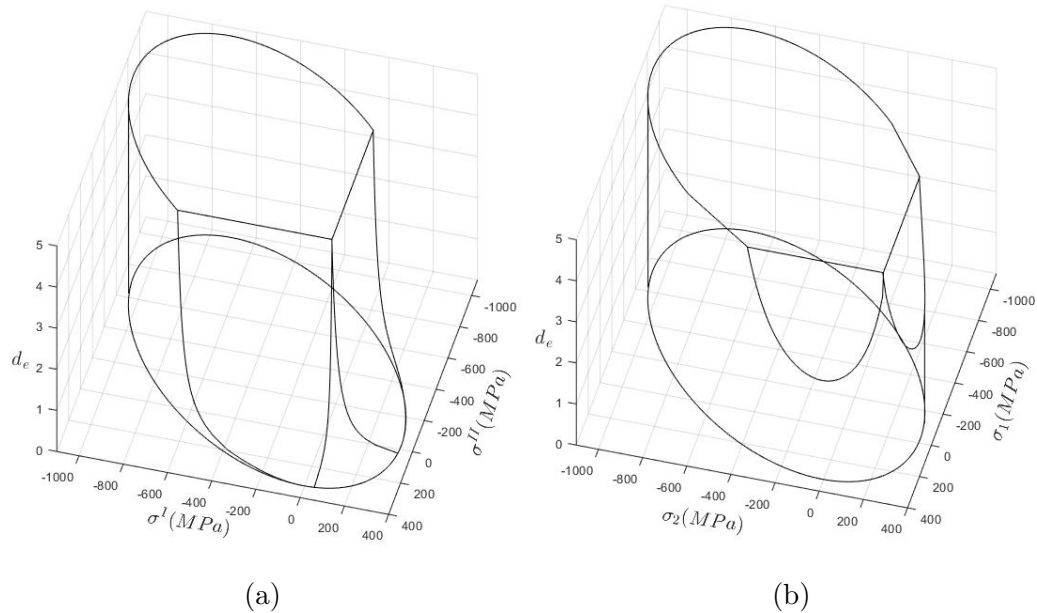
Figure 3.8. Illustration of plane-stress yield surface dependence on local size. Fracture cutoff driven by LEFM scaling law. (a) $D_0 = 0.1$; (b) $D_0 = 2$.

3.3   Definition and evaluation of local size

Within the size-dependent Christensen formulation given in the preceding section, strength is expressed in terms of a local parametric feature size. This size is analogous in 2D to the geometric width of a particular structural member as it varies along its larger length dimension. In 3D it corresponds to the smallest Cartesian measurement of a structural feature. In both cases, this local size measure is equivalent to the diameter D_e of the largest inscribed circular or spherical domain that includes the element of interest. Within density-based topology optimization methods, the interpretation of geometric features remains an open challenge.

Out of all the methods of geometric control explored in literature, none seek to expressly interpret the domain parametrically. Instead, these methods are formulated as restriction methods. In Guest's work using projection methods [80], geometric features are controlled by restricting a measure of material within a circumscribed domain local to each element. Guest's measure fails to capture unique structures on

the region until it is saturated. The "looking glass" approach used cannot differentiate between a node or strut topology if each contain equal amounts of material on the restriction domain. Zhang et al. [81] interpret the structural domain through skeleton extraction using non-differentiable approaches [72]. They then evaluate the presence of material on minimum and maximum scale restriction domains, constraining the sum on each domain to a prescribed threshold. Zhou et al. [82] utilize an inflection region interpreted between the filtered density domain and an additional projected density domain [76]. The constraint formulation on this interpreted restriction domain is similar in form to the one used by Zhang et al, though it is more sensitive to the choice of model parameters [113]. Additionally, Zhou et al. impose this restriction domain as a modification to the ongoing optimization algorithm in order to allow better convergence to the global optimum solution. This approach is not viable for size-dependent strength models due to the abrupt change in strength of any converged structural members that would result from such a modification. At best, it could be expected that convergence to a local minimum may occur far from the global optimal solution.

Thus, it has been made clear that approaches available in literature for the geometric control of the structural domain fail to meet the needs of a size-dependent strength framework. With insight from the limitations of these approaches, a viable parametric measure of the structural domain must incorporate the following features

1. Differentiability in terms of the optimization design variables.
2. Definition on each design iteration.
3. Consistent support on the domain at each design iteration.
4. Ability to differentiate unique structural topologies on the domain of interest and capture the geometry of structural nodes.

3.3.1 Proposed measure and algorithm

With these requirements in mind, construction of the desired size measure, d_e which approximates the actual member size D_e is now considered. Conceptually, the neighborhood or "looking glass" methods developed by Guest et al. [80, 83, 113] serve as a primary inspiration. These methods identify a local neighborhood of support unique to each element within the structural FE discretization. The amount of dense structure allowed on this neighborhood is then restricted. As a size-dependent strength TO implementation requires a size measure as opposed to a size restriction, these methods do not address the needs of this thesis.

In order to give the intermediate state of a partially filled neighborhood meaning, the total amount of material on the domain can be scaled to the maximum material allowed on a prescribed domain. Applying this method to the circular neighborhood method proposed in [80], a measure of the intermediate inscribed circle or sphere may be made. However, applying the "looking glass" method in this manner overestimates the local thickness of both nodes and lamellar structural features.

An alternative to Guest's "looking glass" support domain is given by the "giraffe neck" domain of support used by Poulsen in his MOnotonicity based minimum LEngth scale (MOLE) approach [79]. Poulsen's method maintains a regularized feature scale as an alternative approach to the filtering methods prominent in literature. A constraint measure is formulated to restrict the gradient of the design variable along prescribed linear search directions on the structural domain. Along these directions, the design variable may only vary monotonically, thus preventing checkerboarding.

The "giraffe neck" domain of support is useful for calculating a measure of local size along a prescribed direction. Beginning with this concept, for an element of interest b, local size is evaluated in terms of physical density along a physical vector j, of length r_{max} inclined at an angle Θ from horizontal. This physical vector is imposed on the TO FE discretization using a Bresenham line-drawing algorithm [114]. The mapping remains invariant throughout the optimization process and relies on the

Eulerian definition of the TO mesh. Following this approach, the estimate of the local size along j is given as

$$(r_b)_j = \frac{r_{max}}{\Lambda} \sum_{m=1}^{\Omega_j(r_{max},\Theta)} \prod_{n=1}^{\Omega_m} \rho_n(\boldsymbol{x})^\kappa \tag{3.31}$$

where

$$\Lambda = \sum_{m=1}^{\Omega_j(r_{max},\Theta)} \epsilon_{max}$$

The ratio of r_{max} to Λ relates the physical search domain to the projected density field. ϵ_{max} is the upper bound on the elemental density and is always equal to 1. κ is a penalization parameter which draws inspiration from similar factors in the qp stress-relaxation methodology. It is used as a means to interpret intermediate densities when calculating the size measure. As $\kappa \to \infty$, intermediate densities are interpreted as void elements. Conversely, as $\kappa \to 0$ intermediate densities contribute to the size measure as though they were fully solid. In practical application the thickness of the void element domain between dense structural features may be tailored through varying κ. A parametric study on this behavior is given in **Section 4.4.1**.

The local size measure is given in terms of the product of all preceding densities along the prescribed direction in order to properly account for the influence of a void element along the search direction. Effectively, a single void element reduces the contributions of any successive elemental densities along the search direction to zero. This approach provides a robust means of capturing the size of perforated structures accurately. However, the use of a product of the densities significantly increases the complexity of the sensitivity calculation. It also drastically increases the number of calculations required to evaluate the elemental sensitivities which now scales with

$$N_e \left[\sum_{m=1}^{\Omega_j(r_{max},\Theta)} m \right]$$

as opposed to N_e alone.

While Eq. 3.31 gives an estimate of structural size, it is only given along a single linear search direction. To determine the smallest inscribed circle (2D) or sphere (3D), multiple $(r_j)_b$ must be aggregated. This is accomplished in practice using an approximation of the minimum function for these multiple search directions. A similar approach is used to estimate the morphological filters proposed by Sigmund [76]. Here, a p-norm formulation is used to maximize the inverse of the directional radius calculation. The final expression for the smallest inscribed circle in 2D is given as

$$r_b = \min[(r_b)_j] \approx \left[\frac{1}{N_j} \sum_{j=1}^{N_j} \left[\frac{1}{(r_b)_j} \right]^{p_{rad}} \right]^{-\frac{1}{p_{rad}}} \tag{3.32}$$

where N_j is the number of search directions and p_{rad} is the p-norm penalization factor. In Eq. 3.31, Θ_j becomes the search direction angle from horizontal parameterized by N_j. Throughout all examples in this paper, $p_{rad} = 25$ to provide a close approximation of the minimum radius. The proposed formulation with user-defined N_j is used to allow for accurate estimation of the local geometry. If $N_j = 4$, this corresponds to the 90° neighborhood searched in [76] while $N_j = 8$ is the 45° neighborhood of Poulsen's MOLE method. If r_{max} encompasses only the first layer of surrounding elements, $N_j = 8$ is sufficient to reasonably estimate the local size. As $r_{max} \to \infty$, N_j must approach ∞ to capture the geometry of the local neighborhood. Conceivably, if the greyscale skeleton can be inferred using image derivatives, [115] only two directions need to be searched to determine the transverse thickness. Practically, utilizing image derivatives within a gradient based TO approach introduces intractable issues with the sensitivity analysis of the measure. Feasible values of N_j are explored in the results section of this thesis.

To this point, the formulated size measure provides a reasonable greyscale approximation of the discrete Euclidean distance transform. This approximation is not useful for the intended stress formulation however as it approximates the distance to the closest structural boundary as opposed to the feature size for elements far from the structure's medial skeleton. For this thesis, the empirical local size depen-
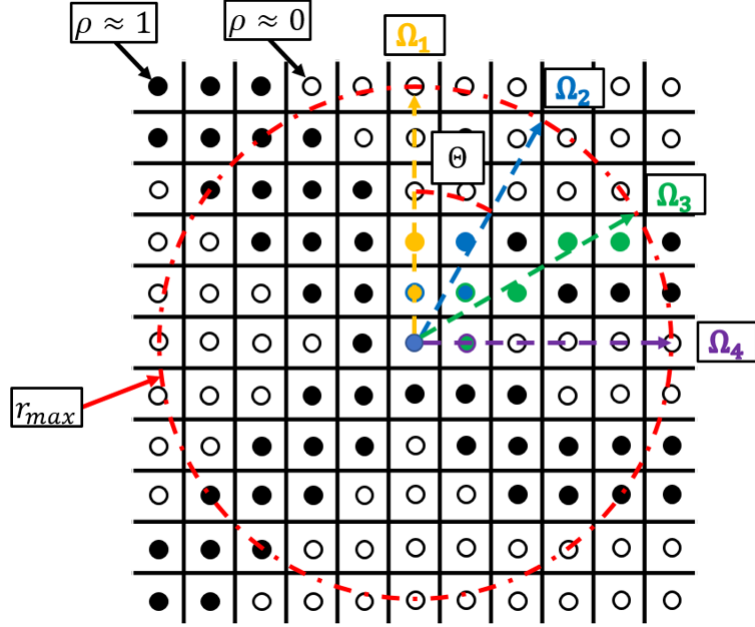
Figure 3.9. Calculation of the directional radius estimate on the allowable domain. Physical radius of support, r_{max} illustrated. Four estimate domains, Ω_j on the FE mesh are illustrated.

dent strength models are formulated in terms of the estimate of the local structural width, d_b. This can be obtained by reformulating the proposed measure to capture the inscribed circle without restricting its center to the element of interest.

Mathematically, this is achieved by calculating the minimum two-sided length measure for the element. An estimate of this measure is calculated along a given direction using the previously obtained values of $(r_b)_j$ and yields

$$(d_b)_n = (r_b)_n + (r_b)_{n+N_j/2} \tag{3.33}$$

Compared to the radius-based formulation, the two-sided "diameter" measure provides a constant estimate of the local width across the structural thickness. The same sum-of-products formulation given by Eq. 3.31 underlies the diameter measure in order to capture the effects of voids within the domain. While the diameter formulation is not strictly necessary for all optimization examples discussed in this paper, for consistency it is utilized for all results shown.

As a note, the proposed size measure is given in a general form independent of the chosen physical density value. Thus, it can be applied to any form of density based TO framework ranging from the original homogenization approach through density and robust methods. For these later methods, challenges with the interaction between the non-linearity of the measure and projection scheme arise.

3.3.2 Consistent size-measure and filtering approach

Following the aside in **Section 2.4**, both the filter and size-measure must consistently interpret the admissible domain boundaries. In the simplest case, this requires padding of the domain with void elements to properly capture the void boundaries of the domain. For the filtering approach, this padding is imperative as it prevents the artificial volume-efficiency of design variables near the on the boundary. However, the chosen size measure estimate is capable of resolving abrupt boundaries and zero padding does not affect its results. More critical are the support and symmetry boundaries. In these cases, the arguments for dense element padding are identical for both the filtering and size measure. If dense elements are not added for the size measure, members which intersect with solid boundaries are interpreted instead as freestanding and artificial corners arise in the size estimate.

For calculating both the filtered radius as well as the diameter measure, the allowable domain is extended with a border of elements proportional to r_{min} and r_{max} respectively, as shown in **Figure 3.10**. Symmetric and support regions are populated with solid elements while regions with prescribed tractions, non-zero or otherwise, are populated with void elements. Both convolutions are calculated separately. After each, the domain is truncated to return the original admissible domain for the FE analysis. The same boundary extension approach is applied for sensitivity calculations of all functions.

(a)

(b)
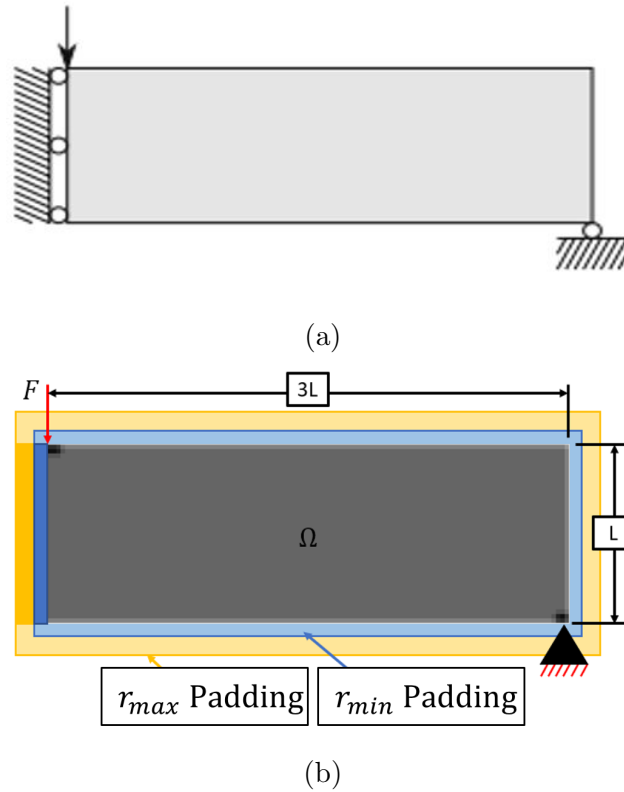
Figure 3.10. (a) Topology Optimization problem domain. (b) Two extensions of domain boundaries with void and solid elements. The blue region illustrates the extended domain for the density filter convolution; the yellow for the diameter measure calculation.

3.4   Geometry constrained problems

3.4.1   Maximum diameter constraint formulation

From the works discussed in the introduction, it is clear that the motivation for the estimate of geometric measures in TO originates from manufacturing concerns. Both maximum and minimum feature sizes are restricted in practice by the limitations of manufacturing methods ranging from additive manufacturing, high-speed machining, casting, and a variety of others. Therefore, this thesis utilizes the proposed size measure to constrain the maximum feature size in the context of the basic compliance minimization framework. By doing so, the behavior of the size-measure can be

explored without interacting with the algorithmic and mathematical complications required to enforce the size-dependent strength constraint.

The maximum diameter constraint used in this thesis draws heavily from the aggregation methods common in stress-based TO. A "size-level" approach similar to the Holmberg et al. stress level method [35] is used. This aggregation follows the ascending value sorting scheme given below

$$\underbrace{d_1 \leq d_2 \leq ... \leq d_{\frac{n_i}{n_c}}}_{\text{cluster 1}} \leq ... \leq \underbrace{d_{\frac{(n_c-1)n_i}{n_c}} \leq d_{n_e}}_{\text{cluster } n_c} \tag{3.34}$$

where n_c is the total number of clusters. As the maximum diameter constraint is applied as a constant across the domain, only the local diameters are sorted. A more general approach would include local maximum diameter constraints. Each cluster is aggregated using a p-norm approximation of the maximum given as

$$d_i^{PN}(\boldsymbol{x}) = \left[\frac{1}{N_i} \sum_{b \in \Omega_i} \left[\frac{d_b(\boldsymbol{x})}{d_{max}}\right]^{p_g}\right]^{1/p_g} \tag{3.35}$$

where N_i is the number of elements in cluster n_i and p_g is the p-norm penalization coefficient for the aggregation. With the clustered maximum diameter measure in hand, the formal maximum thickness constrained, volume constrained, compliance minimization problem can be stated. This problem takes the form

$$
\begin{aligned}
(\mathbb{P}_4) \quad \underset{\boldsymbol{x}}{\text{minimize:}} \quad & C(\boldsymbol{x}) = \boldsymbol{u}^T \boldsymbol{K} \boldsymbol{u} \\
\text{subject to:} \quad & \boldsymbol{K}(\boldsymbol{x})\boldsymbol{u}(\boldsymbol{x}) = \boldsymbol{f} \\
& V(\boldsymbol{x}) = \sum_{e=1}^{N} v_e \rho_e(\boldsymbol{x}) \leq \overline{V} \\
& d_i^{PN} \leq 1 \qquad\qquad i = 1, i \\
& \epsilon^{min} \leq \boldsymbol{x} \leq \epsilon^{max} \qquad \forall e \in \Omega \\
\text{where:} \quad & \boldsymbol{x} = \{x_1, x_2, ... x_N\}
\end{aligned}
\tag{3.36}
$$

In choosing the number of clusters i, arguments considering the approximation of the maximum given in **Section 2.7.2** are followed for the diameter constrained problem as well.

3.4.2 Maximum diameter constrained sensitivity analysis

This section extends on the discussion provided in **Section 2.8** to consider the sensitivity of the maximum diameter constraint. Compared to the stress or compliance equations, the maximum diameter constraint is not related to the elastic response of the structure. Thus, the sensitivity of the size measure is independent of the FE problem. In light of this, this sensitivity is calculated analytically over the relatively limited domain of support relevant for each respective elemental measure.

To begin, Eq. 3.35 is differentiated with respect to the design variable vector

$$\frac{\partial d_i^{PN}(\boldsymbol{x})}{\partial x_b} = \left[\frac{1}{N_i}\sum_{w \in n_i}\left[\frac{d_w(\boldsymbol{x})}{d_{max}}\right]^{p_g}\right]^{\frac{1}{p_g}-1}\frac{1}{N_i d_{max}}\left[\frac{d_w(\boldsymbol{x})}{d_{max}}\right]^{p_g-1}\frac{\partial d_w}{\partial x_b} \tag{3.37}$$

Through the chain rule, the partial $\frac{\partial d_b}{\partial x_b}$ emerges. This partial may be further interrogated following an additional application of the chain rule and results in

$$\frac{\partial d_w}{\partial x_b} = \frac{\partial d_w}{\partial d_n}\frac{\partial d_n}{\partial \rho_e}\frac{\partial \rho_e}{\partial \tilde{\rho}_e}\frac{\partial \tilde{\rho}_e}{\partial x_b} \tag{3.38}$$

In this form, each component of the sensitivity may be treated separately. The first term is the dependence of the minimum approximation of the local diameter on each diameter measure calculated on n-rays. It is given in a similar form to Eq. 3.38 as

$$\frac{\partial d_w}{\partial d_n} = \left[\frac{1}{N_n}\sum_{n=1}^{N_n}\left(\frac{1}{d_n}\right)^{p_{rad}}\right]^{-\frac{1}{p_{rad}}-1}\frac{1}{N_n}\left(\frac{1}{d_n}\right)^{p_{rad}+1} \tag{3.39}$$

The second term relates each diameter measure back to the projected density field. As the diameter measure is expressed as a combination of two radii measures separated by 180°, this derivative is expressed ases

$$\frac{\partial d_n}{\partial \rho_e} = \frac{\partial r_n}{\partial \rho_e} + \frac{\partial r_{n+N_j/2}}{\partial \rho_e} \tag{3.40}$$

where the two partials of the radii measure are given by

$$\frac{\partial r_j}{\partial \rho_e} = \frac{\kappa r_{max} \rho_e(\boldsymbol{x})^{\kappa-1}}{\Lambda} \left[\prod_{l=e-1}^{\Omega_j} \rho_l^{\kappa} \left(1 + \sum_{m=e+1}^{\Omega_j} \prod_{n=1}^{\Omega_m} \rho_n(\boldsymbol{x})^{\kappa} \right) \right] \tag{3.41}$$

The third component is the analytic derivative of the projected density field with respect to the filtered field and is omitted for brevity. Finally, the last component in Eq. 3.38 is given by the convolution of the partial up to the last term with the derivative of the elemental density filter through the formulation given in Eq. 2.30

Practically, the computational implementation of Eq.3.41 is somewhat complex. The sensitivity of the local diameter is highly non-linear and requires information across the domain of support to calculate its value at a single element. Because of this, it is infeasible to store all of the required support regions in memory. Instead, Eq. 3.41 is calculated each iteration for each active element in the optimization. Due to the dependence of the sensitivity on the calculated local diameter measure, this domain of support must be searched twice. The radii is calculated first, then the sensitivity on the second search. The computational cost of this approach is detailed further in the results section.

3.5   Size-dependent strength constrained problems

3.5.1   Size-dependent strength formulation

With both an appropriate size-dependent stress criterion and measure of local size, the problems originally considered in **Section 2.7.3** are extended to incorporate size-effects. For strength constrained problems, the size-dependent of the formulation enters through the limiting strength of Christensen's tensile fracture criterion. With this in mind, the minimum volume, size-dependent strength constrained problem is given as

$$(\mathbb{P}_6) \quad \underset{\boldsymbol{x}}{\text{minimize:}} \quad V(\boldsymbol{x}) = \sum_{e=1}^{N} v_e \rho_e(\boldsymbol{x})$$

$$\text{subject to:} \quad \boldsymbol{K}(\boldsymbol{x})\boldsymbol{u}(\boldsymbol{x}) = \boldsymbol{f}$$

$$\tilde{c}_i^{I,frac} \tilde{\sigma}_i^{frac}[\boldsymbol{x}, \boldsymbol{\sigma}_i^I, \boldsymbol{\varsigma}_i^T(\boldsymbol{d}_e)] \le 1 \quad i = 1, N_i$$

$$\tilde{c}_l^{I,Ch} \tilde{\sigma}_l^{Ch}(\boldsymbol{x}, \boldsymbol{\sigma}_l^{Ch}) \le 1 \qquad\qquad l = 1, N_l \qquad (3.42)$$

$$\epsilon^{min} \le \boldsymbol{x} \le \epsilon^{max} \qquad\qquad \forall e \in \Omega$$

$$\text{where:} \quad \boldsymbol{x} = \{x_1, x_2, ...x_N\}$$

where $\tilde{\sigma}_i^{frac}$ and $\tilde{\sigma}_l^{Ch}$ represent the Christensen fracture and quadratic failure surfaces, respectively. Their values are given by

$$\tilde{\sigma}_i^{frac} = \left[\frac{1}{N_i}\sum_{a \in \Omega_i}\left[\frac{\sigma_{I_a}}{\varsigma_a^T(D_e)}\right]^{p_m}\right]^{1/p_m} \qquad (3.43)$$

$$\tilde{\sigma}_l^{Ch} = \left[\frac{1}{N_l}\sum_{a \in \Omega_l}\left(\sigma_a^{Ch}\right)^{p_n}\right]^{1/p_n} \qquad (3.44)$$

In both Eq. 3.45 and Eq. 3.43 ς^T, is given by the various models of **Table 3.1**. Additionally, for all problems in this thesis $N_i = N_l$ and $p_m = p_n$ for simplicity. The two stress measures provided in the Christensen approach are sorted and clustered independently by their normalized stress values, σ_a/ς_a^T, following the approach given by Eq. 2.24.

The minimum compliance, volume and size-dependent strength constrained problem considered is similar in form and is given as shown below

$$(\mathbb{P}_5) \quad \underset{\boldsymbol{x}}{\text{minimize:}} \quad C(\boldsymbol{x}) = \boldsymbol{u}^T \boldsymbol{K} \boldsymbol{u}$$

$$\text{subject to:} \quad \boldsymbol{K}(\boldsymbol{x})\boldsymbol{u}(\boldsymbol{x}) = \boldsymbol{f}$$

$$V(\boldsymbol{x}) = \sum_{e=1}^{N} v_e \rho_e(\boldsymbol{x}) \leq \overline{V}$$

$$\tilde{c}_i^{I,frac} \tilde{\sigma}_i^{frac}[\boldsymbol{x}, \boldsymbol{\sigma}_i^I, \boldsymbol{\varsigma}_i^T(\boldsymbol{d}_e)] \leq 1 \quad i = 1, N_i \qquad (3.45)$$

$$\tilde{c}_l^{I,Ch} \tilde{\sigma}_l^{Ch}(\boldsymbol{x}, \boldsymbol{\sigma}_l^{Ch}) \leq 1 \qquad\qquad l = 1, N_l$$

$$\epsilon^{min} \leq \boldsymbol{x} \leq \epsilon^{max} \qquad\qquad \forall e \in \Omega$$

$$\text{where:} \quad \boldsymbol{x} = \{x_1, x_2, ...x_N\}$$

3.5.2   Size-dependent strength sensitivity analysis

This section extends on the discussion provided in **Section 2.8** to consider the additional sensitivity of the size dependent strength. As the quadratic yield surface of the Christensen criterion is formulated to be size-independent, the local size measure sensitivity must only be considered for the fracture limit approximated by Eq. 3.43. To begin with the derivation of the sensitivity of this measure, the chain rule of the p-norm with respect to the design variables is carried out to the first level

$$\frac{\partial \tilde{\sigma}_i^{frac}}{\partial x_b} = \sum_{a \in \Omega_i} \frac{\partial \tilde{\sigma}_i^{frac}}{\partial \sigma_a^I} \frac{\partial \sigma_a^I}{\partial x_b} + \sum_{a \in \Omega_i} \frac{\partial \tilde{\sigma}_i^{frac}}{\partial \varsigma_a^T} \frac{\partial \varsigma_a^T}{\partial x_b} \qquad (3.46)$$

The first component of Eq. 3.46 gives the stress measure dependency on the design variable and is solved through the adjoint approach. This results in a component identical in form to Eq. 2.35. The second component contains the strength dependency of the p-norm approximation. Upon further examination, this component yields

$$\sum_{a \in \Omega_i} \frac{\partial \tilde{\sigma}_i^{frac}}{\partial \varsigma_a^T} \frac{\partial \varsigma_a^T}{\partial x_b} = \sum_{a \in \Omega_i} \frac{\partial \tilde{\sigma}_i^{frac}}{\partial \varsigma_a^T} \frac{\partial \varsigma_a^T}{\partial d_w} \frac{\partial d_w}{\partial x_b} \qquad (3.47)$$

The final component of Eq. 3.47 corresponds to Eq. 3.38 and follows an identical sensitivity analysis. The middle term is dependent on the form of the size-scaling law used for the constraining function. This is obtained by taking the analytic derivative

of the equations given in **Table 3.1**. As with the maximum radius constraint, the contribution of the size measure to the sensitivity of the strength-constraint is simple to evaluate. In both cases the size measure remains independent of the solution to the structural FE problem.

3.6 Code implementation

Expanding on the basic flowchart presented in **Figure 2.4**, the TO algorithm is extended to incorporate the additional features given in the prior sections of this chapter. This algorithm is implemented on the MATLAB 2018a release on Windows and Linux operating systems. The flow of the extended algorithm for maximum radius constrained problems is depicted in **Figure 3.11** and for stress-based problems in **Figure 3.12**.
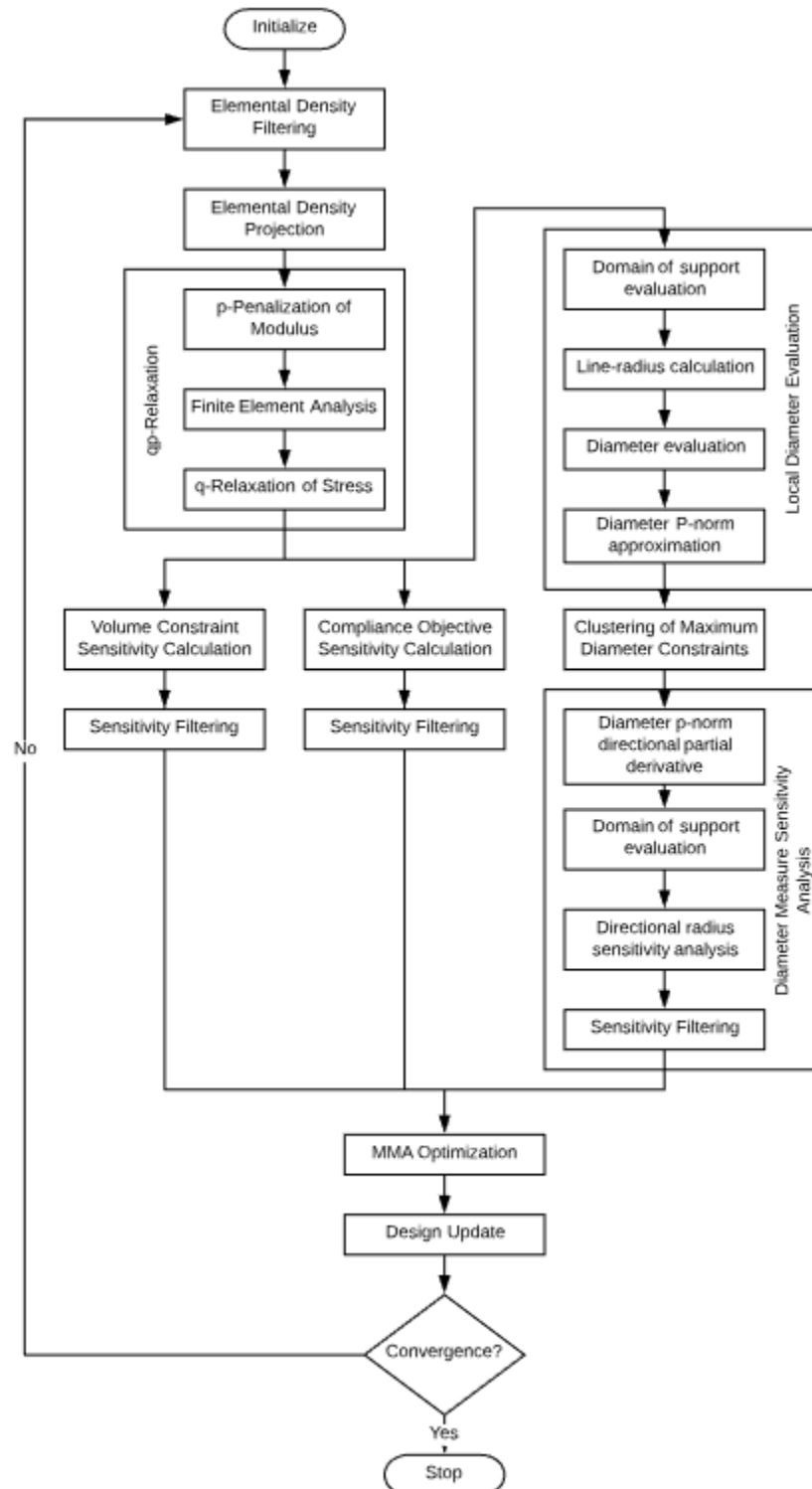
Figure 3.11.   Flowchart illustrating major functions of maximum diameter constrained TO.
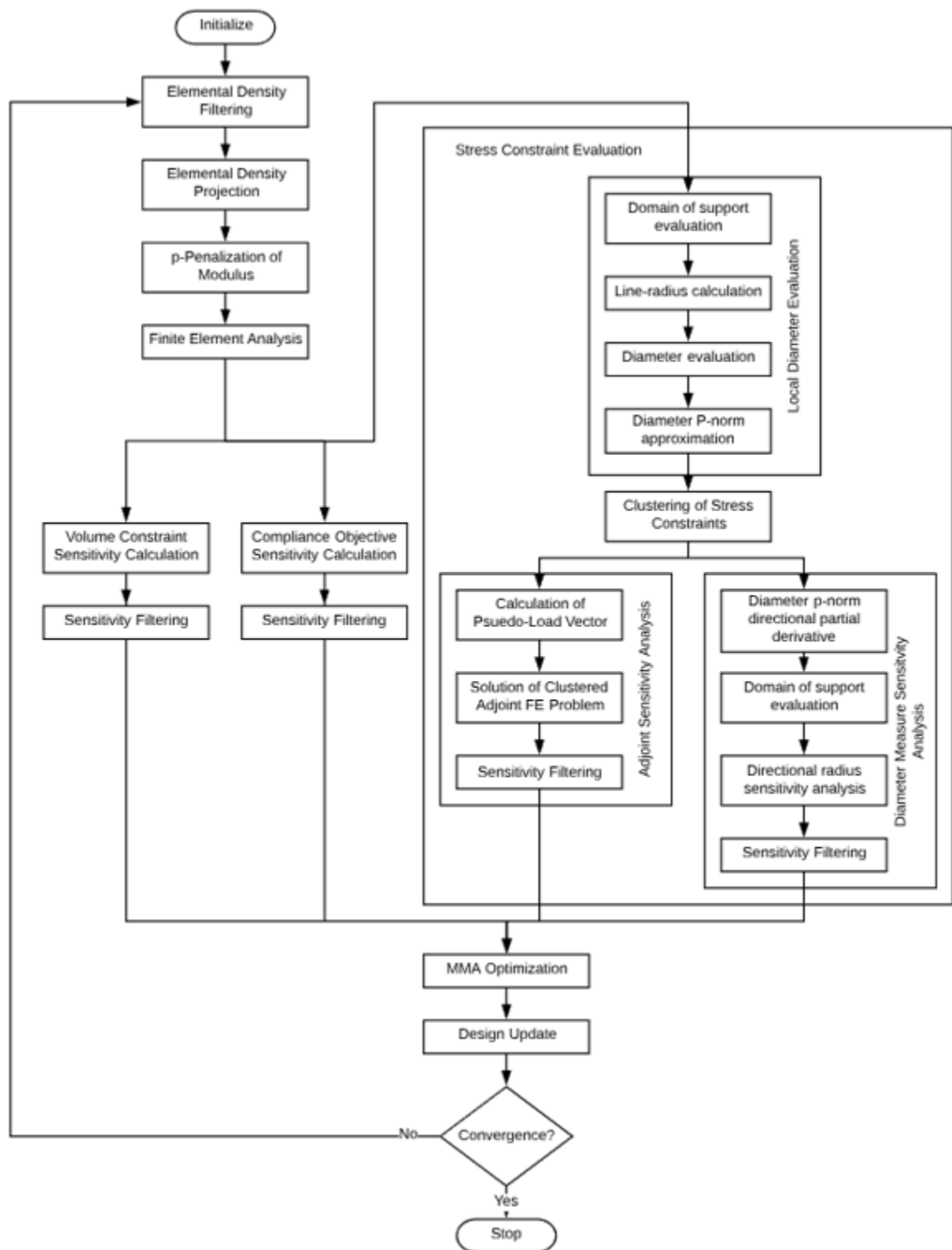
Figure 3.12. Flowchart illustrating major functions of stress constrained TO.

3.7   Optimized results to realized geometry

With the results obtained from the MATLAB implementation described previously, the geometric information is contained within the discretized FE structural mesh. This format does not allow for manipulation of the resulting optimal structures with Computer Aided Engineering (CAE) software. The results must be interpreted and translated. Within TO, numerous authors have worked to develop these translation methods [116,117]. Most interpret density isolines using triangulation methods in order to generate Stereolithography files (.STL). This file format is widely interpreted by additive manufacturing systems [117]. However, this file format only contains information about the surface mesh of the geometry. For most general FE software, knowledge about the internal mesh geometry must be developed.

To achieve this internal mesh geometry, this thesis implements the iso2mesh MATLAB utility built by Fang and Boas [118] using the CGAL meshing algorithm toolbox [119]. Using this approach, 3D representations of the plane-stress optimized geometry are developed. First, the 2D grayscale structural image is re-sampled to the physical scale of the problem with voxels of 1mm x 1mm dimension using MATLAB's imresize standard bicubic interpolation. The 2D image is then stacked to the desired physical depth into a 3D projection. This projection is fed into the iso2mesh 'volume2mesh' function with a prescribed isosurface density value and a minimum mesh face area. The density value is set based on the converged structural. Values are selected to preserve major structural features while not excessively thickening the overall domain. The volume2mesh function utilizes the 'cgalsurf' utility to first generate a triangular surface mesh then fill in a tetrahedral volumetric mesh.

At this stage, the resulting mesh is highly irregular and contains much of the angular geometry inherent in the regular quadrilateral FE mesh used for the TO algorithm. The surface mesh is smoothed using the iso2mesh 'smoothsurf' utility. This function is used to apply 20 iterations of the lowpass mesh smoothing method implemented by Taubin [120] with a characteristic node smoothing factor of 0.5. The

process of smoothing the mesh surface only alters the position of surface nodes of the mesh. This leads to highly distorted elements along the boundaries of the structure. To restore the quality of the volumetric mesh, the 'surface2mesh' utility is used to generate a new internal mesh from the smoothed surface.

This entire process results in a unified set of surface and volumetric meshes. Both describe the same geometric features and express the optimized structure in a physically realizable format. The volumetric mesh is interpreted into the ABAQUS .inp file framework using the iso2mesh function 'mesh2abaqus'. The surface mesh is used to generate a printable .STL file using the 'savebinstl'. The progression of the intermediate meshing steps is illustrated in **Figure 3.13**. The full mesh generation code is included as a supplement to this thesis.

(a)

(b)
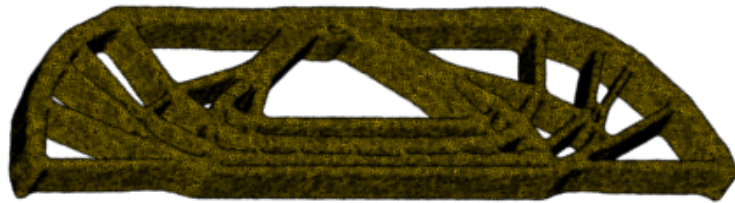
(c)

(d)

Figure 3.13.   Example 3D tetrahedral mesh progression. (a) Scaled and stacked converged domain. (b) *cgalsurf* isosurface tetrahedral mesh, $\tilde{\rho} = 0.4$ cutoff. (c) Smoothed surface mesh. (d) Final output mesh.

3.8 Validation using commercial FEA

In transitioning to a fully realized 3D geometry, the ABAQUS/Standard FE software is utilized to validate the assumptions underlying the TO linear, elastic plane stress FE solution. First, the results of the mesh generation process detailed in the prior section are imported into the solver using the ABAQUS linear tetrahedral continuum elements, C3D4. Tetrahedral elements are preferred to accommodate the highly complex geometries of the resulting TO outputs.

With a valid 3D mesh in hand, the size-dependent and independent results can be interrogated by successive validation steps. Initially, an applied load model is analyzed using the same value as during the optimization. An infinitesimal strain theory of deformation is assumed. This analysis validates the applicability of the plane stress approximation to the thick, 3D geometry. Following this, a finite-strain displacement load condition is evaluated to assess the possible impact of geometric non-linearity on the response of the structure.

Finally, a formal failure model is applied to the domain in the form of the Cohesive Zone Model (CZM) originally developed by Barenblatt [121] and Dugdale [122] within the framework of the Extended Finite Element Method (XFEM) [123]. The ability of the CZM approach to capture size-dependent strength characteristics have been well established in the works of Bažant [98,124]. Using the ABAQUS/Standard formulation, a linear CZ traction separation relation is defined. The initiation criteria is driven by a maximum principal stress, or MAXPS model. For simplicity, mixed mode cracking is treated using a power-law approach with a value of unity. The size of the softening tail of the CZM is driven by the total cohesive strength in the bond, equivalent to the limit energy release rate, G_F of the material. Minimal cohesive stabilization is applied to improve the numerical convergence of the underlying Newton solution approach.

3.9 Verification of results using additively manufactured structures

Test specimens were prepared for printing using the Stratsys Objet Studio software package. Cleaned and smoothed 3D .STL files generated following the approach in **Section 3.7** were imported onto the build plate in Objet Studio and configured for printing. All specimens were fabricated using a Polyjet process on a Connex 350 printer [125] in an uncontrolled room environment. Samples were fabricated using the VeroWhite Plus resin [126] utilized previously by Bell and Siegmund [101]. All specimens were fabricated using the Digital Material setting of the printer with layer thickness of 30 µm and build speed of 12 mm/h. Resolution in the X-Y print plane was 600 dpi, with the X-direction being oriented along the path of the print-head. All specimens were printed using the "glossy" print setting to reduce support material usage. All specimens were oriented with the region of highest first principal stress aligned to the printer Y-direction. This was chosen to take advantage of reduced ductility of the material observed in this direction by Bass et al. [127]

To determine the properties used for optimization of structures fabricated using Verowhite Plus, limited tensile coupon testing was undertaken. Specimens consisted of traditional dog-bone shaped coupons with nominal gauge dimension of 1.25 mm $\times$ 1.25 mm by 8 mm long. Testing was performed using a Bose ELF 3200 Electroforce axial-torsion test system [128] with 225 N load capacity and 225 N load cell configuration. A simple manual screw clamp was used to affix coupons in place as shown in **Figure 3.14**. All specimens were displaced at a strain rate of 0.00625 mm/mm/sec to a total strain of 0.5 or failure, whichever occurred first.

Figure 3.14. Tensile coupon test configuration.

Figure 3.15. EnvisionTec UVCA 2000 Post-curing system.

A UV post-cure study was undertaken to develop a fully cured exterior on the specimens and further embrittle the VeroWhite polymer. Brittleness has been shown to increase with age for this material system [127] with UV exposure providing the greatest contribution to this effect. Brittle material behavior is generally associated with a reduced K_{Ic} and heightened notch sensitivity. Furthermore, it is likely that a material boundary layer will develop under post curing as the UV radiation will fail to penetrate to the core of the fabricated specimen. Both effects will work to predispose the specimens to quasi-brittle or brittle failure relative to the as-printed material.

An EnvisionTec UVCA 2000 curing chamber [129] shown in **Figure 3.15** was utilized. This chamber provides UV-A frequency light with three 18 W bulbs to a rotating and mirrored sample platen. Tensile specimens were prepared, carefully cleaned by hand, then rinsed with pressurized water prior to the post-cure treatment. Cure periods of 30 minutes, 1, 2, 3, and 4 hours were considered.

Specimens were fabricated along the X-direction of the printer. Two specimens from each group were tested immediately post-cure and two were tested 48 hours post-cure. The resulting stress-strain plots for both groups are plotted in **Figures 3.16** and **3.17**, respectively.
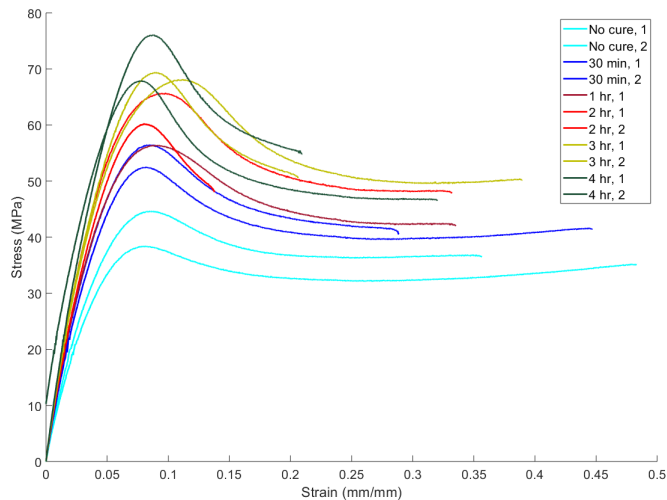
Figure 3.16. Tensile test for UV cure study of VeroWhite, tested immediately post-cure.
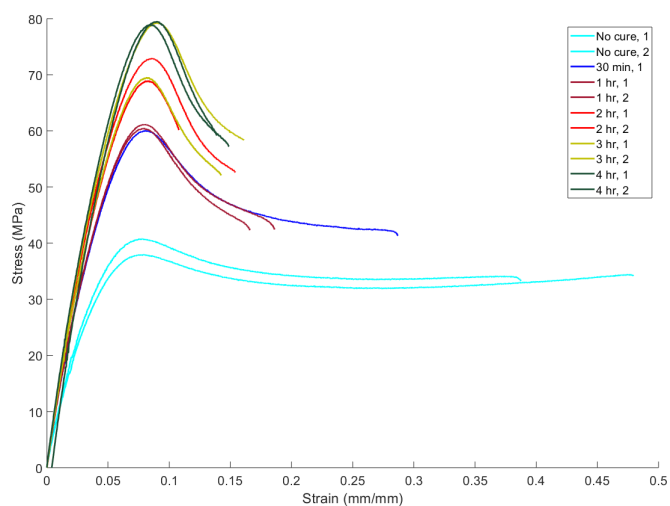
Figure 3.17. Tensile test for UV cure study of VeroWhite, tested 48 hours post-cure.

From these plots, the trends for modulus of elasticity, peak tensile strength, and elongation at break were calculated and plotted in **Figure 3.18**. Due to the relatively shallow, non-linear elastic region the modulus is calculated through a single secant approximation up to the peak tensile strength.
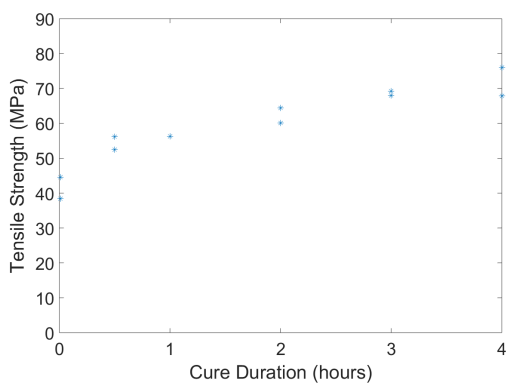
(a) Tensile strength, no rest
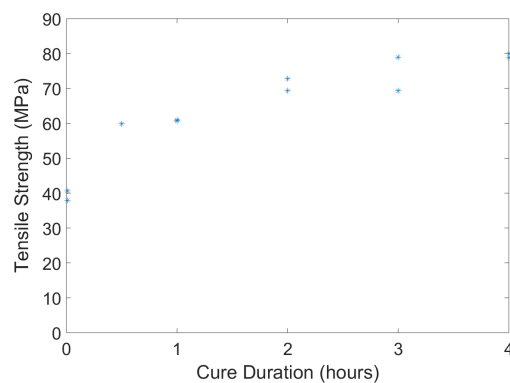
(b) Tensile strength, 48 hour rest
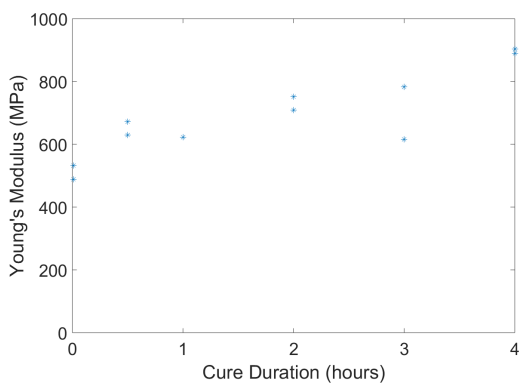
(c) Young's Modulus, no rest
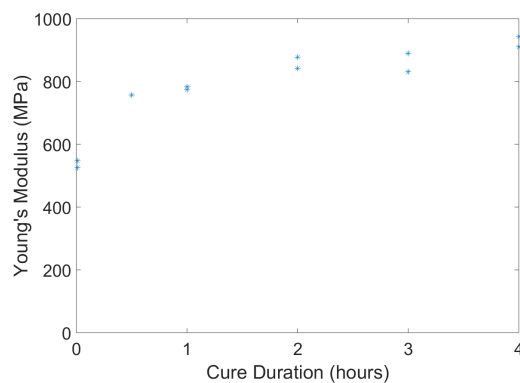
(d) Young's Modulus, 48 hour rest
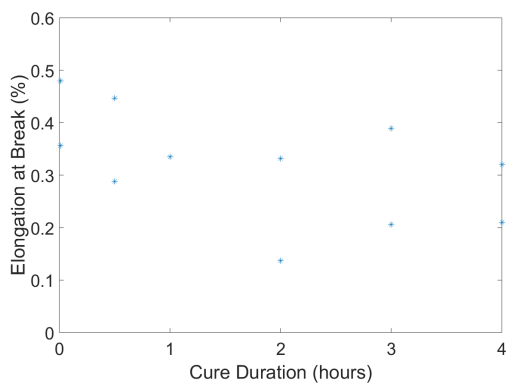
(e) Elongation at Break, no rest
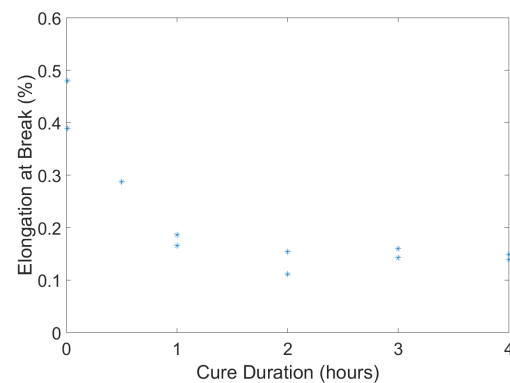
(f) Elongation at Break, 48 hour rest

Figure 3.18.   Material property trends of UV cured VeroWhite.

Considering these results, all fabricated TO structures are treated with a 4 hour UV cure dosage and allowed to rest a minimum of 48 hours prior to testing. Values of $E_0 = 1$ GPa and $\varsigma_{T_0} = 65$ MPa are applied to the TO framework to account for the expected material properties. The slightly inflated modulus is selected to account for measurement of strain occurring at the grips instead of at the gauge section. An intermediate value of strength from the range of cure treatments is chosen in deference to the Verowhite specification sheet which claims an identical value [126]. To maintain consistency with Christensen's yield surface, ς_C is chosen to equal 130 MPa. It has been shown by Weiss et al. [130] that Verowhite Plus exhibits tension-compression strength asymmetry for uni-axial testing configurations; thus the choice of limiting ς_C is physically reasonable. A Poisson's ratio $\nu = 0.4$, typical of pressure dependent plastics, is assumed.

Considering the size-dependent failure characteristics of the material, Bell and Siegmund [101] demonstrate a SEL-like failure behavior for uncured, un-aged VeroWhite Single Edge Notch Bending (SENB) specimens. These specimens also exhibited a weakening behavior for small sizes due to a postulated increased importance of print layer imperfections for the smallest specimens. Bell and Siegmund report values of limit fracture toughness, K_F, and limit FPZ length, c_f, of 59.8 MPa $\sqrt{\text{mm}}$ and 0.65 mm respectively. Without replicating their experiments, both values are taken to be representative for the cured material. The limit FPZ length is assumed to correspond to D_0 in the TO formulation of the SEL. Layer effects are neglected and a monotonically decreasing strength trend is assumed.

The soft modulus and significant non-linearity of the elastic response of VeroWhite plus illustrates the shortcomings of the underlying FE implementation of the proposed TO formulation. Nevertheless, given the ability of the Polyjet process to realize complex TO generated geometries and the availability of this particular polymer, verification testing was attempted using this compound.

Testing of the fabricated beam structures was conducted on an Instron 3345 Universal Testing system [131] with 5kN load and sensing capacity. This system generates

force using an electro-mechanical displacement drive system. All load tests utilized a standard 3-point bend flexural setup with 10 mm diameter loading nose and support fixtures. Tests were displacement controlled and run at a maximum fiber strain rate of 0.01 mm/mm/sec in accordance with the ASTM D790 specification for flexural testing of plastics [132].

To confirm each print conforms to the established material parameters, a set of five tensile dog-bone coupons with nominal gauge dimension of 1.25 mm $\times$ 1.25 mm by 8 mm long were printed for both the X and Y print directions. The tensile strength, elastic modulus in tension, and ductile/brittle mode of failure for each batch of prepared MBB specimens were then calculated and verified. Verification coupons were displaced at a rate of 0.00625 mm/mm/sec to a total strain of 0.3 or failure, whichever occurred first.

4. RESULTS AND DISCUSSION

4.1 Summary of structural design formulations considered

Before considering the emergent structural behavior of the various optimization design problems posed in the preceding sections, each formulation is finalized and summarized below in **Table 4.1**. This table establishes the reference shorthand for all results presented within this section and clarifies any remaining generalities in the formulations given prior.

4.2 Test problem loads and domains

Following the guidance given in [23], common test problems shall be utilized to assess the validity and behavior of the proposed formulation. These benchmarks are described in greater detail in the following subsections and contextualized in terms of the structurally optimal behavior they seek to illustrate. With regards to the computational implementation of these test problems, all results presented for these problems were obtained using two identical Linux compute servers with Intel Xeon E5-2630 v3 CPU's (16 cores @ 2.4 GHz) and 128 GB of memory. Both servers run on Redhat Release 6.10. The release of MATLAB used for all computations is 2017a.

Table 4.1. Summary of optimization problem formulations

Prob.	Description	Formulation
$\mathbb{P}_1$ **(2.16)**	Volume constrained compliance minimization	$$\min_{\boldsymbol{x}} \quad C(\boldsymbol{x}) = \boldsymbol{u}^T \boldsymbol{K} \boldsymbol{u}$$ $$\text{s.t.} \quad \boldsymbol{K}(\boldsymbol{x})\boldsymbol{u}(\boldsymbol{x}) = \boldsymbol{f}$$ $$V(\boldsymbol{x}) = \sum_{e=1}^{N} v_e \rho_e(\boldsymbol{x}) \leq \overline{V}$$
$\mathbb{P}_2$ **(2.28)**	Volume and strength constrained compliance minimization	$$\min_{\boldsymbol{x}} \quad C(\boldsymbol{x}) = \boldsymbol{u}^T \boldsymbol{K} \boldsymbol{u}$$ $$\text{s.t.} \quad \boldsymbol{K}(\boldsymbol{x})\boldsymbol{u}(\boldsymbol{x}) = \boldsymbol{f}$$ $$V(\boldsymbol{x}) = \sum_{e=1}^{N} v_e \rho_e(\boldsymbol{x}) \leq \overline{V}$$ $$\tilde{c}_i^{I,frac} \tilde{\sigma}_i^{frac}(\boldsymbol{x}, \boldsymbol{\sigma}_i^I) \leq 1 \quad i = 1, N_i$$ $$\tilde{c}_l^{I,Ch} \tilde{\sigma}_l^{Ch}(\boldsymbol{x}, \boldsymbol{\sigma}_l^{Ch}) \leq 1 \quad l = 1, N_l$$
$\mathbb{P}_3$ **(2.27)**	Strength constrained volume minimization	$$\min_{\boldsymbol{x}} \quad V(\boldsymbol{x}) = \sum_{e=1}^{N} v_e \rho_e(\boldsymbol{x})$$ $$\text{s.t.} \quad \boldsymbol{K}(\boldsymbol{x})\boldsymbol{u}(\boldsymbol{x}) = \boldsymbol{f}$$ $$\tilde{c}_i^{I,frac} \tilde{\sigma}_i^{frac}(\boldsymbol{x}, \boldsymbol{\sigma}_i^I) \leq 1 \quad i = 1, N_i$$ $$\tilde{c}_l^{I,Ch} \tilde{\sigma}_l^{Ch}(\boldsymbol{x}, \boldsymbol{\sigma}_l^{Ch}) \leq 1 \quad l = 1, N_l$$
$\mathbb{P}_4$ **(3.36)**	Volume and maximum radius constrained compliance minimization	$$\min_{\boldsymbol{x}} \quad C(\boldsymbol{x}) = \boldsymbol{u}^T \boldsymbol{K} \boldsymbol{u}$$ $$\text{s.t.} \quad \boldsymbol{K}(\boldsymbol{x})\boldsymbol{u}(\boldsymbol{x}) = \boldsymbol{f}$$ $$V(\boldsymbol{x}) = \sum_{e=1}^{N} v_e \rho_e(\boldsymbol{x}) \leq \overline{V}$$ $$d_i^{PN} \leq 1 \quad i = 1, i$$

Prob.	Description	Formulation
$\mathbb{P}_5$ **(3.45)**	Volume and size-dependent strength constrained compliance minimization	$\displaystyle\min_{\boldsymbol{x}} \quad C(\boldsymbol{x}) = \boldsymbol{u}^T \boldsymbol{K} \boldsymbol{u}$ $\text{s.t.} \quad \boldsymbol{K}(\boldsymbol{x})\boldsymbol{u}(\boldsymbol{x}) = \boldsymbol{f}$ $\displaystyle V(\boldsymbol{x}) = \sum_{e=1}^{N} v_e \rho_e(\boldsymbol{x}) \leq \overline{V}$ $\tilde{c}_i^{I,frac} \tilde{\sigma}_i^{frac}[\boldsymbol{x}, \boldsymbol{\sigma}_i^I, \boldsymbol{\varsigma}_i^T(\boldsymbol{d}_e)] \leq 1 \quad i = 1, N_i$ $\tilde{c}_l^{I,Ch} \tilde{\sigma}_l^{Ch}(\boldsymbol{x}, \boldsymbol{\sigma}_l^{Ch}) \leq 1 \qquad\quad l = 1, N_l$
$\mathbb{P}_6$ **(3.42)**	Size-dependent strength constrained volume minimization	$\displaystyle\min_{\boldsymbol{x}} \quad V(\boldsymbol{x}) = \sum_{e=1}^{N} v_e \rho_e(\boldsymbol{x})$ $\text{s.t.} \quad \boldsymbol{K}(\boldsymbol{x})\boldsymbol{u}(\boldsymbol{x}) = \boldsymbol{f}$ $\tilde{c}_i^{I,frac} \tilde{\sigma}_i^{frac}[\boldsymbol{x}, \boldsymbol{\sigma}_i^I, \boldsymbol{\varsigma}_i^T(\boldsymbol{d}_e)] \leq 1 \quad i = 1, N_i$ $\tilde{c}_l^{I,Ch} \tilde{\sigma}_l^{Ch}(\boldsymbol{x}, \boldsymbol{\sigma}_l^{Ch}) \leq 1 \qquad\quad l = 1, N_l$

4.2.1 Messerschmitt-Bolkow-Bolhm three point loading beam

In order to verify the basic SIMP-based compliance formulation, the ubiquitous Messerschmitt-Bolkow-Bolhm (MBB) [23, 133] three point loading support beam is considered. The loading domain and boundary conditions are depicted in **Figure 4.1** where horizontal symmetry is imposed on the left edge of the allowable domain. The physical height, H, and length, L, of the allowable domain are commonly varied throughout literature, though typically a ratio of 1:3 is maintained. The thickness of the domain is commonly taken as unity in the desired unit system; in this thesis thickness is prescribed to ensure consistency with physically realized structures.

For all formulations considered, a region of dimension $0.05H$ mm $\times$ $0.025L$ mm is fixed to be solid around both the loading and kinematic boundary condition locations. This modelling feature is applied to mitigate the development of stress concentrations

local to the loading or fixed constraint. Additionally, the applied load is distributed across the top line of solid elements such that the nodal load is applied to only assumed solid elements. The roller displacement constraint on the bottom right hand side of the domain is inset horizontally a distance equal to r_{min} to prevent forcing a cantilevered member local to the support.
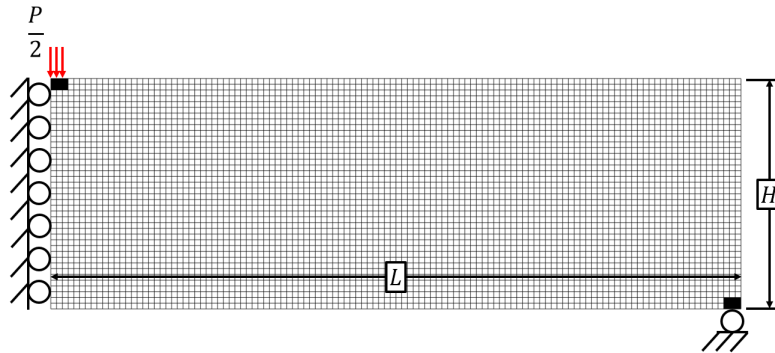
Figure 4.1. MBB test problem domain, load, and boundary conditions.

The MBB benchmark has been studied extensively in the algorithmic development of TO methods. A summary of the results obtained from various treatments was compiled by Lee [134] and illustrates the usefulness of this common domain for comparing approaches. Furthermore, the theoretically close-to-optimal [135] Michell structural topology is well known for this problem domain. The derivation of the Michell topology [136] illustrates the distribution of material along principle stress lines within the domain that also arises within continuum, linear-elastic TO based solutions. As such, the MBB Michell topology is generally used as a qualitative reference [135].

4.2.2 Short-beam

Similar to the MBB test problem, various cantilevered beam domains have been considered with compliance based TO methods. In this thesis, the short cantilever domain optimized with length-scale control by Zhang et al [81] is utilized. This choice was made in order to provide a direct comparison between the radius restric-

tion schemes utilized herein and by Zhang et al. The short beam domain is shown in **Figure 4.2**. A built in support condition is assumed on the left-hand side of a 160 mm × 80 mm allowable domain. For this domain, only compliance based formulations are considered. This results in an algorithmic insensitivity to loading stress concentrations. As such, the desired load may be applied as a point load. For all problems shown, this load is equal to 1000 N.
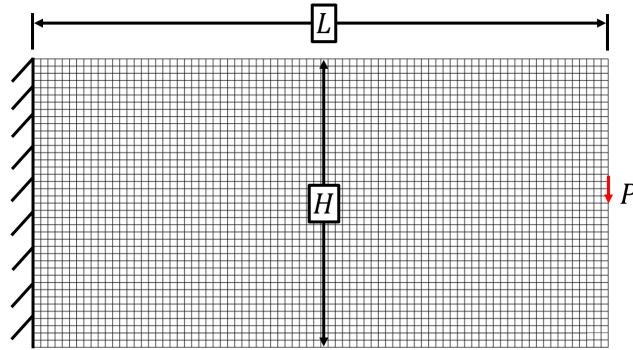
Figure 4.2. Short beam test problem domain, load, and boundary conditions. $L = 160\,\text{mm}$; $H = 80\,\text{mm}$; $P = 1000\,\text{N}$.

4.2.3 L-bracket

Initially proposed by Duysinx and Bendsøe in [39], the L-Bracket problem domain illustrated in **Figure 4.3** has been established as the standard test problem for stress-based TO approaches. Unlike the MBB and short-beam domains, the L-bracket domain introduces implicit complexity into the converged solution through the re-entrant corner of the allowable domain. This forces a stress concentration in the initial FE-solution of the uniformly dense structure. Compliance-based formulations result in converged structures that retain this stress concentration. At a minimum, it is expected that a viable stress-based TO method is capable of removing this concentration in a resulting optimal solution.

Within the TO FE implementation, the entire square structural domain of 200 mm × 200 mm is meshed. The structure in the upper right hand square domain of 60

mm $\times$ 60 mm is restricted to design density equal to ϵ_{min} to approximate the behavior of a large void region. The top of the vertical member of the L-bracket is constrained using a built in support condition. A region of $0.06L$ mm $\times 0.02L$ mm local to the tip of the horizontal member is assumed to be fully dense. A downward vertical load of 1000 N is applied across all of the fully dense nodes on the right edge of the region. The allowable domain for dense material is meshed with 6,400 elements.
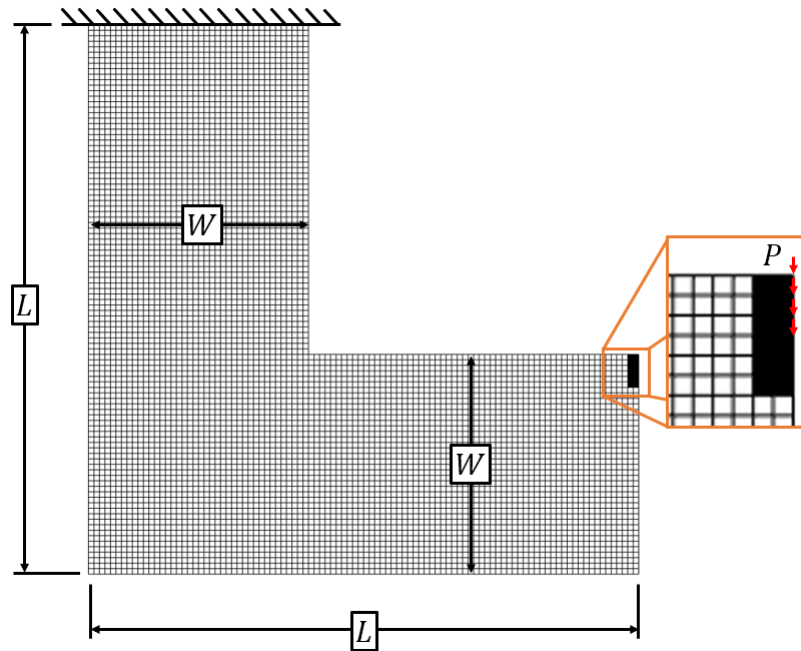
Figure 4.3. L-Bracket test problem domain, load, and boundary conditions. $L = 200$ mm; $W = 80$ mm; $P = 1000$ N

4.3 Converged solutions for standard problems

The TO implementation utilized in this thesis is constructed from a variety of approaches throughout literature and incorporates a diverse array of features. It is imperative to present the baseline results obtained for the benchmarks problem domains discussed in the prior section. For each problem, the $\mathbb{P}_1$, $\mathbb{P}_2$, and $\mathbb{P}_3$ converged solutions are presented. Both the $\mathbb{P}_2$ and $\mathbb{P}_3$ formulations are evaluated over a range

of α to illustrate the influence of the failure surface asymmetry on the converged results.

The first set of reference results are given for the MBB problem domain. For this problem, an allowable structural domain of $300 \times 100 \times 1$ mm is discretized using 120 $\times$ 40 plane stress elements. A load of 1000 N is applied to the symmetric half-domain. A fictitious material with an Elastic Modulus of 70 GPa and a Poissons ratio of 0.33 is assumed. A value of $\varsigma_{T0} = 350$ is held constant while three different α values of 2, 1, and 0 are investigated. A filter radius of $r_{min} = 2.0$ elements is imposed. All volume constrained problems are limited to $\overline{V} = 0.4$ and each problem is initialized with an initial design variable vector of $\boldsymbol{x} = 0.5$ throughout the domain. The resulting converged structures are illustrated in **Figure 4.4**. For all three problem formulations, good practical and formal convergence behavior is observed. Most problems result in fully solid-void structures as allowed within the limitations of the linear density filter approach. However, the $\mathbb{P}_3$ formulations with $\alpha = 2$ result in structures with gray converged compression members. This occurs due to the ability of these regions to satisfy strength constraints even under penalization as illustrated by the plots of the σ_{Ch} shown in **Figure 4.5**. With the strong combined penalization observed in the mixed formulation, these regions fail to arise.

(a) $\mathbb{P}_1$

(b) $\mathbb{P}_2$, $\alpha = 2$ (c) $\mathbb{P}_2$, $\alpha = 1$ (d) $\mathbb{P}_2$, $\alpha = 0$

(e) $\mathbb{P}_3$, $\alpha = 2$ (f) $\mathbb{P}_3$, $\alpha = 1$ (g) $\mathbb{P}_3$, $\alpha = 0$
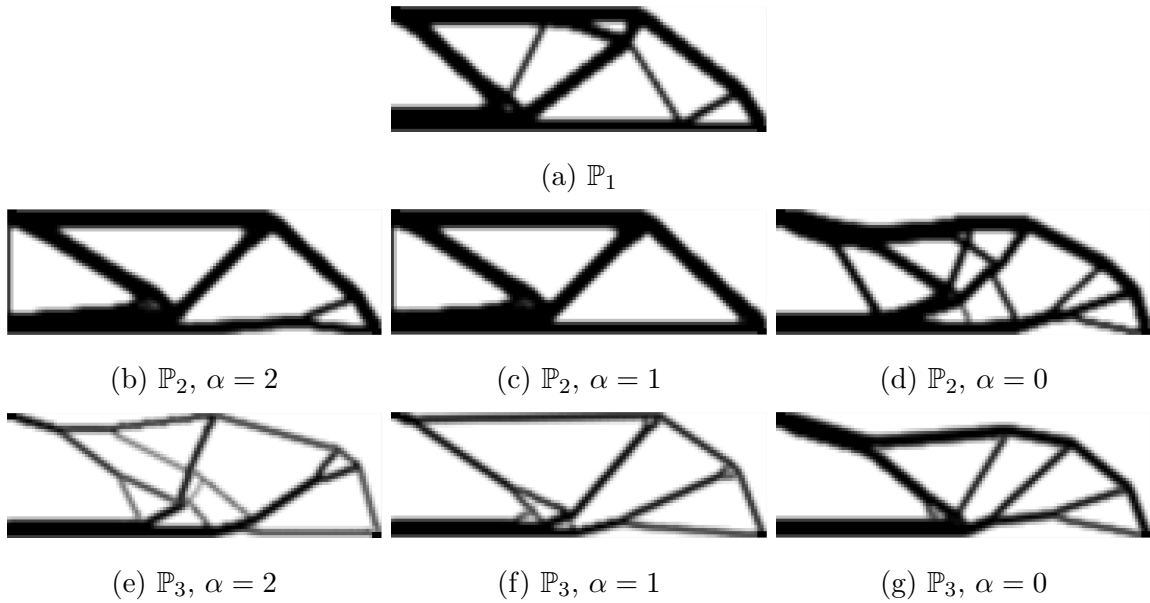
Figure 4.4.   Comparison of converged structures for the $\mathbb{P}_1$, $\mathbb{P}_2$, and $\mathbb{P}_3$ problem formulations on the MBB test domain. Effect α considered for the stress-based forms.

(a) $\mathbb{P}_1$, $\alpha = 0$

(b) $\mathbb{P}_2$, $\alpha = 2$ (c) $\mathbb{P}_2$, $\alpha = 1$ (d) $\mathbb{P}_2$, $\alpha = 0$

(e) $\mathbb{P}_3$, $\alpha = 2$ (f) $\mathbb{P}_3$, $\alpha = 1$ (g) $\mathbb{P}_3$, $\alpha = 0$
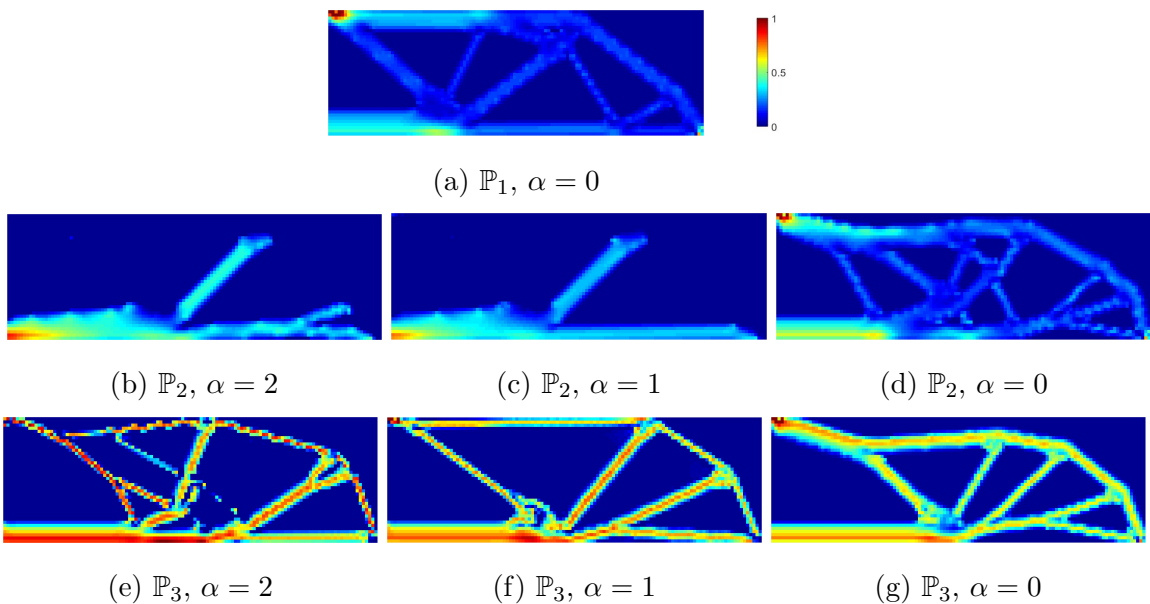
Figure 4.5.   Christensen strength measure on the converged structures for the $\mathbb{P}_1$, $\mathbb{P}_2$, and $\mathbb{P}_3$ problem formulations on the MBB test domain. Effect α considered for the stress-based forms.

In addition to the σ_{Ch} plot that captures general failure conditions, a comparison of normalized first principal stresses is given in **Figure 4.6**. Both of these stress mea-

sure plots illustrate that for the given domain, the loading conditions are not sufficient to shift the converged result towards a strength-driven solution with the exception of the Mises equivalent constraint shown in (d). For the solely stress constrained problems, the Christensen plots illustrates that all members exist under highly stressed conditions. The effect of the tensile fracture cutoff can be observed through comparing result (b) in both stress plots. This comparison shows that the tensile members which connect the main tensile member to the compression truss members are closer to failure under the fracture criterion and serve as the limiting constraint within the optimization algorithm.

(a) $\mathbb{P}_1$, $\alpha = 0$

(b) $\mathbb{P}_2$, $\alpha = 2$ (c) $\mathbb{P}_2$, $\alpha = 1$ (d) $\mathbb{P}_2$, $\alpha = 0$

(e) $\mathbb{P}_3$, $\alpha = 2$ (f) $\mathbb{P}_3$, $\alpha = 1$ (g) $\mathbb{P}_3$, $\alpha = 0$
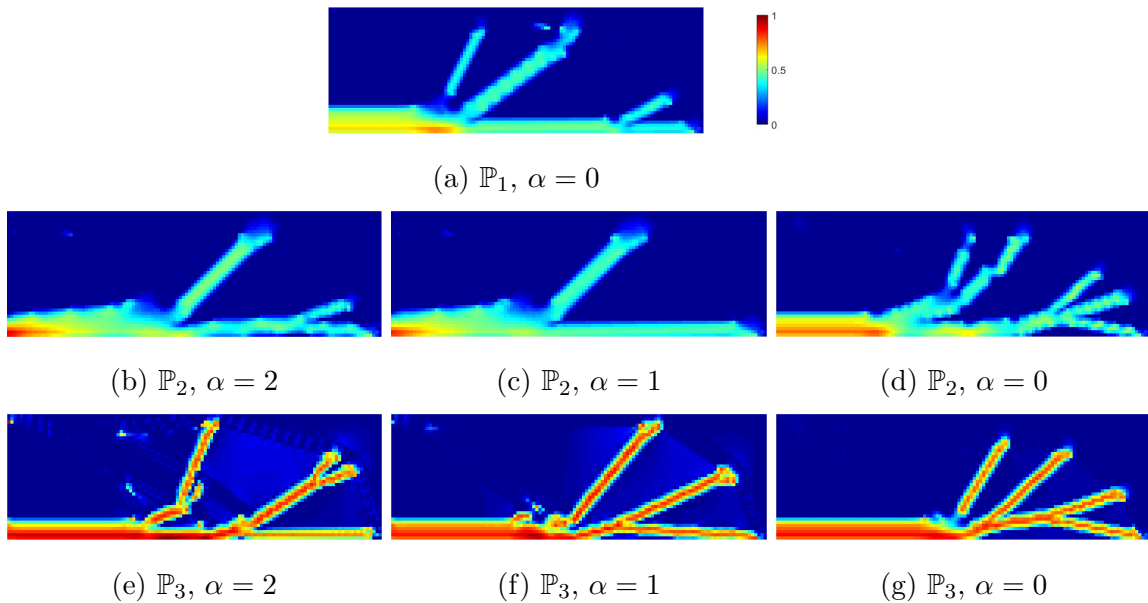
Figure 4.6. Maximum principal stress normalized with local material strength on the converged structures on the $\mathbb{P}_1$, $\mathbb{P}_2$, and $\mathbb{P}_3$ problem formulations on the MBB test domain. Effect α considered for the stress-based forms.

The resulting converged structures are presented for the L-bracket problem domain in **Figure 4.7**. All mechanical properties for this problem are identical to the MBB-case. The filter radius for the results shown is $r_{min} = 2$ elements. For the $\mathbb{P}_2$ problem, the stress concentration at the re-entrant corner is somewhat mitigated for higher values of α but largely unchanged for the Mises equivalent problem. The compliance objective prevents the migration of material from the compression region of the domain. In contrast, for the $\mathbb{P}_3$ formulation the compression members in the domain progressively thin with increasing α, as expected. Interestingly, this behavior does not greatly effect the converged volume fraction, with values of 0.314, 0.309, and 0.308 for problems (e), (f), and (g). Instead, the compliance values of these structures are heavily influenced resulting in values of 6706.95, 6390.96, and 5758.10 N-mm, respectively. This is allowed to occur as a compliance objective or constraint is not included as a part of the $\mathbb{P}_3$ formulation.

(a) $\mathbb{P}_1$ (b) $\mathbb{P}_2$, $\alpha = 2$ (c) $\mathbb{P}_2$, $\alpha = 1$ (d) $\mathbb{P}_2$, $\alpha = 0$

(e) $\mathbb{P}_3$, $\alpha = 2$ (f) $\mathbb{P}_3$, $\alpha = 1$ (g) $\mathbb{P}_3$, $\alpha = 0$
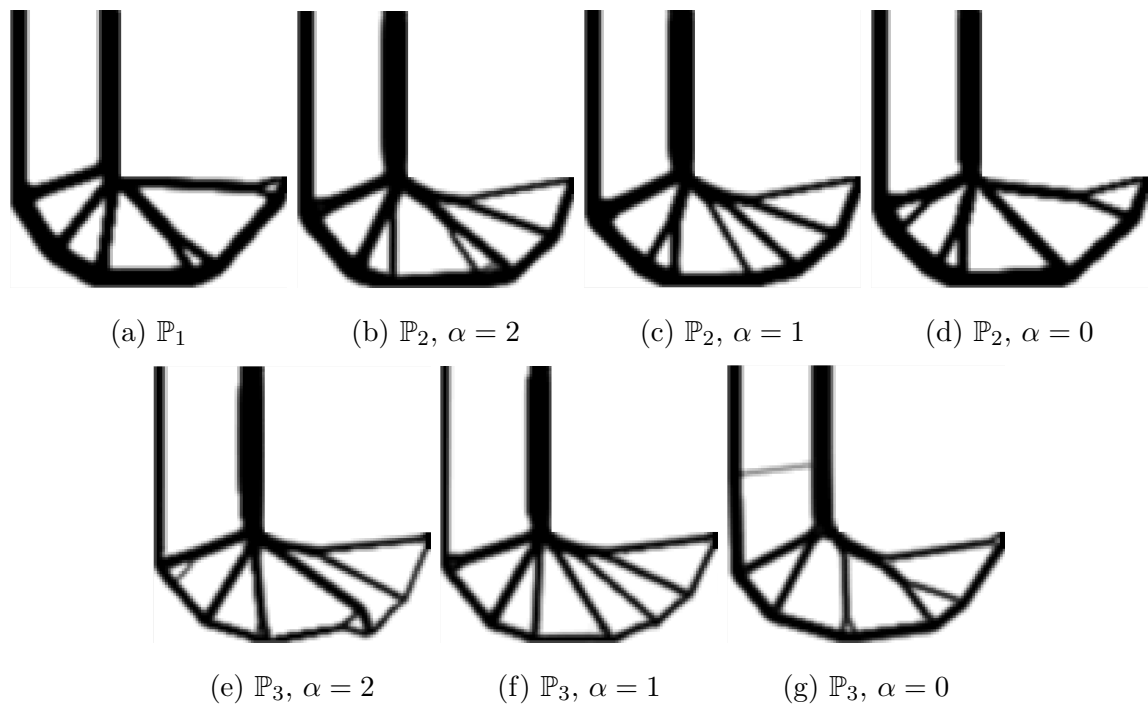
Figure 4.7. Comparison of converged structures for the $\mathbb{P}_1$, $\mathbb{P}_2$, and $\mathbb{P}_3$ problem formulations on the L-Bracket test problem. Effect of stress constraints and asymmetry of the material yield surface considered.

Finally, results for the $\mathbb{P}_1$ formulation of the short beam domain are illustrated for different volume fractions in a manner similar to Zhang et al [81]. As a note, the converged structures illustrated in **Figure 4.8** exhibit a second cross truss in the nose of the short beam, unlike those in Zhang et al. This likely arises from the difference in convergence observed between the sensitivity filtering applied by Zhang et al. and the density filtering used herein. Additionally, Zhang et al. utilize a filtering radius with $r_{min} = 1.2$ elements while a radius of $r_{min} = 3$ elements is used herein as an implicit restriction on the minimum feature size.

(a) $\overline{V} = 0.3$ (b) $\overline{V} = 0.4$ (c) $\overline{V} = 0.5$
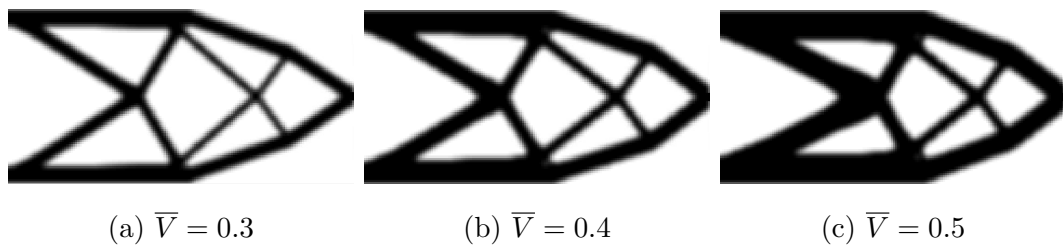
Figure 4.8. Comparison of various volume fractions for volume constrained compliance minimization, $\mathbb{P}_1$, of the Short-beam test problem meshed with 12800 elements; filtered density formulation used. $r_{min} = 3$ elements.

4.4   Maximum radius constrained problems

4.4.1   Effect of size measure definition

With converged solutions to the chosen TO test problems established for the three well-known structural formulations, focus is now shifted to the three novel optimization forms. The optimization behavior of the maximum radius constrained problem, $\mathbb{P}_4$ with a two-field SIMP formulation is considered first. By doing so, the various parameters of the local size measure given by Eq. 3.35 may be interrogated without further complications introduced by adjoint sensitivity calculation inherent to stress-based problems.

Beginning with the MBB problem domain, the effect of these parameters is explored through observations of the resulting structures achieved through parametric

studies. The two most interesting parameters for the proposed size measure in terms of performance and cost are the density penalization, κ and the number of search directions, N_j.

Regarding κ, the local diameter is independent of the penalization for both fully solid and fully void domains. However, changing κ affects the interpretation of the initialized domain. This in turn changes the initial descent direction chosen by the MMA algorithm. Numerically, by choosing a value of $\kappa > 1$ gray regions are interpreted as void for the size measure calculation. Conversely, $\kappa < 1$ interprets gray regions as solid. Due to the product formulation of the size measure, κ also controls the rate of decay of the size measure. This rate of decay interacts with the chosen density value of interest; for problems where the filtered density is analogous to the physical structure κ interacts significantly with filter radius.

While the optimal value of κ must be determined from converged test problem results, the ideal choice of N_j is prohibitive from a practical perspective yet intuitive from a theoretical one. N_j yields Θ through the relation

$$\Theta = \frac{N_j}{2\pi}$$

As previously discussed, for an arbitrary geometry, as $\Theta \to 0$, $2\pi/\Theta \to \infty$ and it would be expected that $d_b \to D_b$. Thus, the choice of N_j is governed solely by the expense of sampling additional search directions. Otherwise, it is expected that the converged structures will themselves converge to a particular solution with decreasing Θ.

With these considerations in mind, the converged structures for the $\mathbb{P}_4$ MBB domain test problem are interrogated for values of $\kappa = \frac{1}{3}, 1, 3$ and $\Theta = \frac{\pi}{2}, \frac{\pi}{4}, \frac{\pi}{8}$. These treatments are applied to MBB compliance minimization problem considered previously with a limiting $\overline{V} = 0.4$ and a constraint on the maximum member diameter of $d_{max} = 6$ elements. The resulting structures are illustrated in **Figure 4.9** and key performance parameters are summarized in **Table 4.2**.

(a) $\kappa = \frac{1}{3}, \Theta = \frac{\pi}{2}$ (b) $\kappa = \frac{1}{3}, \Theta = \frac{\pi}{4}$ (c) $\kappa = \frac{1}{3}, \Theta = \frac{\pi}{8}$

(d) $\kappa = 1, \Theta = \frac{\pi}{2}$ (e) $\kappa = 1, \Theta = \frac{\pi}{4}$ (f) $\kappa = 1, \Theta = \frac{\pi}{8}$

(g) $\kappa = 3, \Theta = \frac{\pi}{2}$ (h) $\kappa = 3, \Theta = \frac{\pi}{4}$ (i) $\kappa = 3, \Theta = \frac{\pi}{8}$
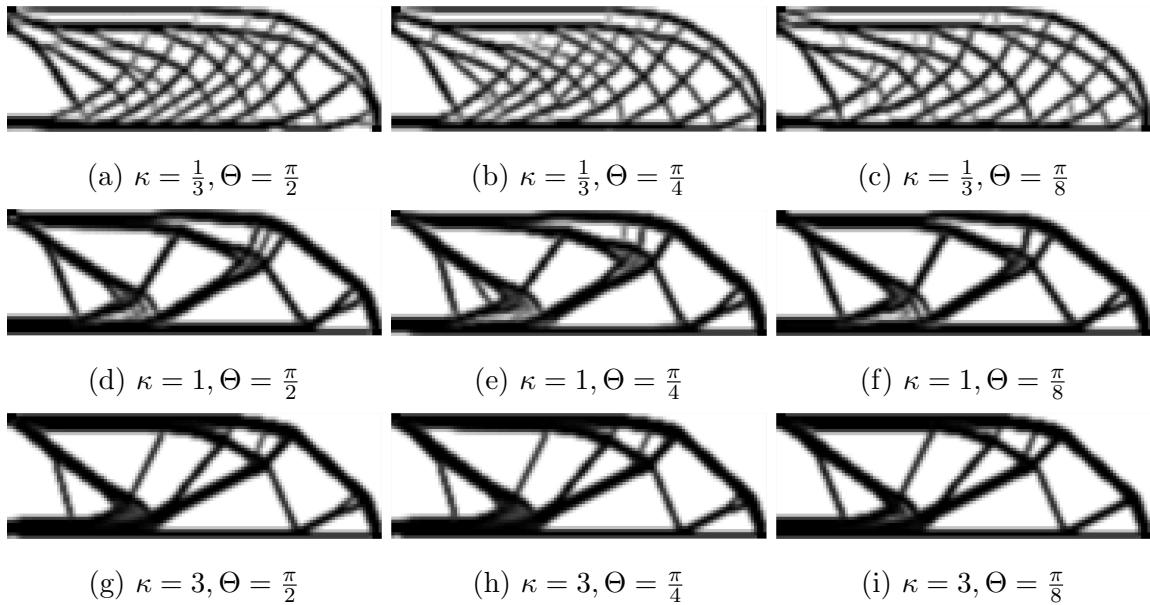
Figure 4.9. Comparison of the maximum radius constrained compliance minimization formulation, $\mathbb{P}_4$, on the MBB domain; filtered density formulation used. $r_{min} = 5$ mm and $d_{max} = 15$ mm; variation of κ and Θ are considered.

From these results, it is immediately clear that values of $\kappa > 1$ result in an undesirable interpretation of local geometry. Nodal domains of the structure with thick geometry are not removed using this penalization. Instead, the core of these nodes exhibits a small reduction of filtered density. Due to the large penalization factor, these regions are interpreted as near void for the size measure and are thus permitted under the maximum radius constraint. Setting $\kappa = 1$ yields domains that begin to alleviate the thick nodal regions, however the resulting structures replace these domains with poorly converged gray regions. Reducing κ to a value of less than 1 results in a significantly different converged topology. A highly cross-linked truss is observed with thinned horizontal members. These thinned members allow for multiple smaller nodes to transfer load to redundant shear-bearing members. Under this formulation, the upper compression load path is separated into two wholly distinct members entirely. Gray regions outside of the transition region inherent to the filtering strategy are largely eliminated and may be further reduced through selecting tighter convergence criteria. However, this penalization strategy results in a significant increase in

structural compliance. This is likely due to the significant increase in gray transition region necessitated by the increase in the number of structural members though it also may be driven by the split compression load path.

Table 4.2. Comparison of $\mathbb{P}$ formulation converged results for study of κ and Θ size measure parameters.

Case	Iterations	KKT Norm	Time (s)	Time per iter. (s)	Compliance (N mm)
(a)	447	5.290	1389.8	3.11	6711.7
(b)	297	15.10	976.98	3.28	6816.6
(c)	512	6.171	1907.4	3.72	6803.4
(d)	500	2.880	1544.5	3.09	4311.0
(e)	202	41.81	655.17	3.24	4519.1
(f)	473	2.206	1606.2	3.40	4295.2
(g)	121	36.07	392.36	3.24	4004.3
(h)	143	17.27	469.41	3.28	4015.3
(i)	312	2.042	1031.4	3.30	3916.3

Turning attention to the choice of Θ, it is clear that its effect on the converged structures is qualitatively minimuml. No marked transitions in topology are observed for any of the three penalization strategies. Quantitatively, referring to **Table 4.2**, the effect of Θ on the compliance appears minimuml while any effect on the convergence parameters appears inconclusive. However, the added computational cost per iteration incurred by decreasing Θ is negligible for all three penalization levels.

With these results in mind, it can be concluded that ideally the smallest practical value of Θ should be selected for a given problem domain while values of $\kappa > 1$ are discouraged. Initially, it appears that values of $\Theta = \frac{\pi}{8}$ and $\kappa = 1$ should be used for novel problem domains and optimization formulations. The performance of the optimization should then be evaluated and these parameters adjusted to correctly address difficulties with emergent gray regions or violations of geometric feature controls.

With this behavior in mind, $\mathbb{P}_4$ is also evaluated on the L-Bracket problem domain using the same two-field SIMP formulation. For this problem, the maximum radius constraint is applied with values of $\kappa = 1, \frac{1}{3}$ and $\Theta = \frac{\pi}{8}$ following the results of the MBB problem study. Here however d_{max} is varied between 8 and 20 mm while r_{min} is fixed to be 4 mm. The results of this formulation are illustrated in **Figure 4.10**.

(a) $d_{max} = 8$ mm, $\kappa = 1$

(b) $d_{max} = 12$ mm, $\kappa = 1$

(c) $d_{max} = 16$ mm, $\kappa = 1$

(d) $d_{max} = 20$ mm, $\kappa = 1$

(e) $d_{max} = 8$ mm, $\kappa = \frac{1}{3}$

(f) $d_{max} = 12$ mm, $\kappa = \frac{1}{3}$

(g) $d_{max} = 16$ mm, $\kappa = \frac{1}{3}$

(h) $d_{max} = 20$ mm, $\kappa = \frac{1}{3}$
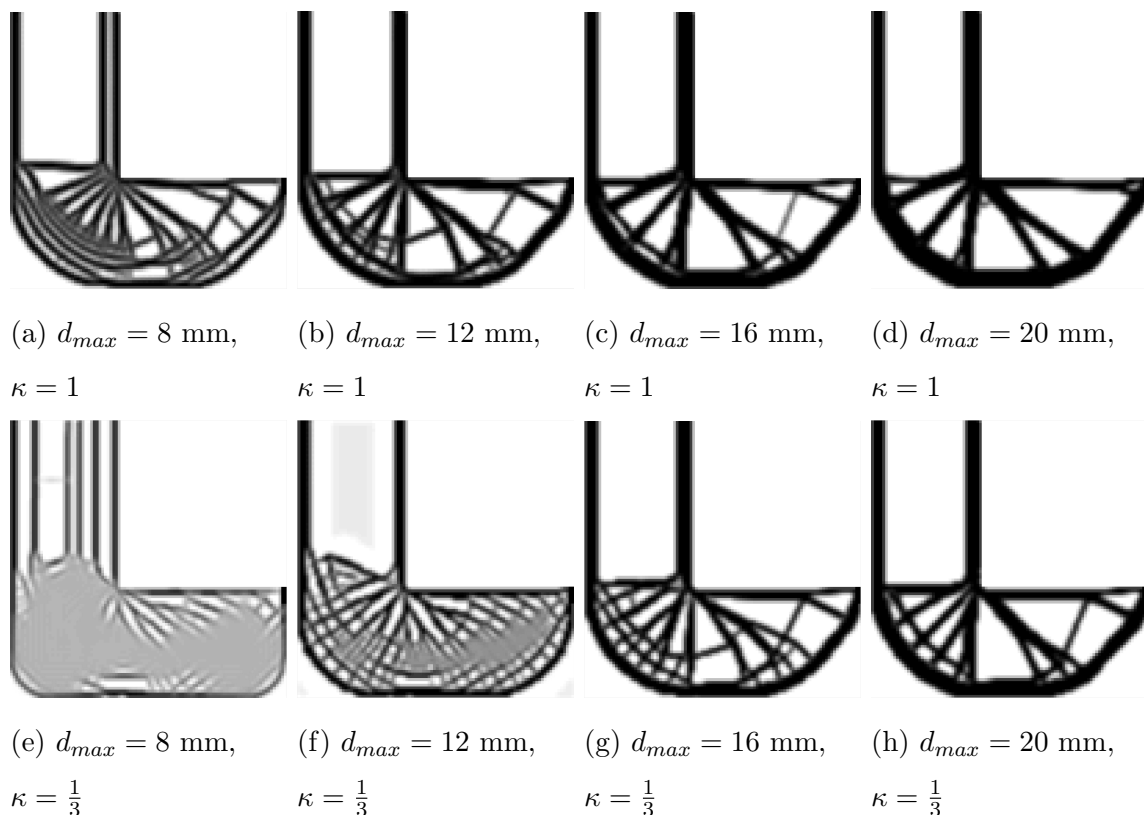
Figure 4.10. Comparison of maximum radius constrained compliance structures, $\mathbb{P}_5$, for the L-Bracket domain for various limiting d_{max} and penalization κ; filtered density formulation used. $r_{min} = 4$ mm.

For results with $\kappa = 1$, reasonable convergence is observed though distinct dark gray regions emerge near the natural node point located at the re-entrant corner. For problem (a) where $d_{min} = d_{max}$, this effect is somewhat mitigated. Interestingly, despite the equivalence of the filter and constraint diameters a largely solid-void converged structure emerges. Decreasing κ to $\frac{1}{3}$ yields poor convergence for the $d_{max} = 8$ mm and $d_{max} = 12$ mm constrained problems. This is expected for the

$d_{max} = 8$ mm problem as the gray transition regions are interpreted as close to solid for the local size measure. However, the poor convergence and light gray region in the vertical member of the $d_{max} = 12$ mm is unexpected and lacks an intuitive cause.

Under close inspection converged structures (b) and (g) as well as (c) and (h) result in highly similar topologies. This reinforces the idea that the penalization κ indeed acts as a interpretation parameter of the density field as the constraint values differ by exactly the value of the filter radius. However, the slight manner in which these pairs differ is instructive. For the $\kappa = \frac{1}{3}$ structures, the re-entrant node is more clearly separated into distinct structural members. Additionally, additional void separation is present between fully dense structural members for the $\kappa = \frac{1}{3}$ cases. This follows from the need to force void regions close to the ε_{min} bound in order to prevent local lamellar structures from contributing to the local size measure.

4.4.2 Effect of density projection

From the preceding results, it is clear that the maximum diameter constraint formulation suffers for a difficulty interpreting gray regions. This challenge remains a common issue with density-based TO approaches which may addressed with the projection approach discussed in **Section 2.5**

In employing the Wang form of the projection scheme, a highly conservative optimization strategy is applied. In essence, two optimization problems are solved. The first consists of the $\mathbb{P}_4$ two-field SIMP formulation utilized previously with a relaxed KKT-residual and objective-change convergence criteria of 5×10^{-3} and $\Delta_c = 5 \times 10^{-5}$, respectively. Following convergence under this criteria, a second optimization which applies the projection field through a continuation approach begins. This allows good convergence to a solid-void topology before imposing the highly non-linear projection. This choice was made in order to limit excessive interaction between the non-linearity of the local size measure and the projection field.

Under this second optimization problem, the projected density, ρ, replaces the filtered density, $\tilde{\rho}$, as the relevant structural density. It is calculated using Eq. 2.15. Under the continuation scheme, β is initialized to 1 and grows following

$$\beta = \beta + 1.1^{\omega} \tag{4.1}$$

where ω is an incremental variable that increases by 1 every 20 design iterations.

In order to compare results with the method proposed by Zhang et al, $d_{max} = 7$ mm is prescribed. In addition to the maximum restriction, Zhang et al. also apply a minimum member size constraint. No such explicit constraint is applied within the algorithm employed in this thesis. Instead, for the two-field problem an implicit minimum scale is imposed by the selected filter radius. This value is selected to be 3 mm in accordance with the problem setup given by Zhang et al. For the three-field approach, minimum feature size is also implictly controlled by the filter radius. This approach has been previously cited as being able to control geometric parameters for the case where $\eta = 0$ [77]. From the definition of the projection, it is apparent that different values of η impose different implicit limiting radii. This effect arises based on the location of the Heaviside approximation within the transition region imposed by the filtering approach. The practical implications of this approach are illustrated by the converged structures presented in this section.

With the continuation scheme established, the resulting structures for the Short-beam $\mathbb{P}_4$ test problems are illustrated in **Figures 4.11** and **4.12**. In comparing the two-field SIMP results with $\kappa = 1$ and $\kappa = \frac{1}{3}$, the same trends observed in **Section 4.4.1** emerge. Two-field structures with $\kappa = 1$ exhibit significant regions of intermediate density near node locations in the domain while structures with $\kappa = \frac{1}{3}$ yield unsolvable amorphous gray regions. The latter effect arises due to the lack of separation between the definition of the filter radius and the maximum feature diameter. Increasing the difference between the two should result in better convergence.

In comparing the three-field results with $\eta = 0.5$, the results are initially promising for low volume fractions. **Figure 4.11 (d)** illustrates good solid-void convergence and

(a) $\tilde{\rho}, \overline{V} = 0.3$ (b) $\tilde{\rho}, \overline{V} = 0.4$ (c) $\tilde{\rho}, \overline{V} = 0.5$

(d) $\rho, \overline{V} = 0.3, \eta = 0.5$ (e) $\rho, \overline{V} = 0.4, \eta = 0.5$ (f) $\rho, \overline{V} = 0.5, \eta = 0.5$

(g) $\rho, \overline{V} = 0.3, \eta = 0$ (h) $\rho, \overline{V} = 0.4, \eta = 0$ (i) $\rho, \overline{V} = 0.5, \eta = 0$
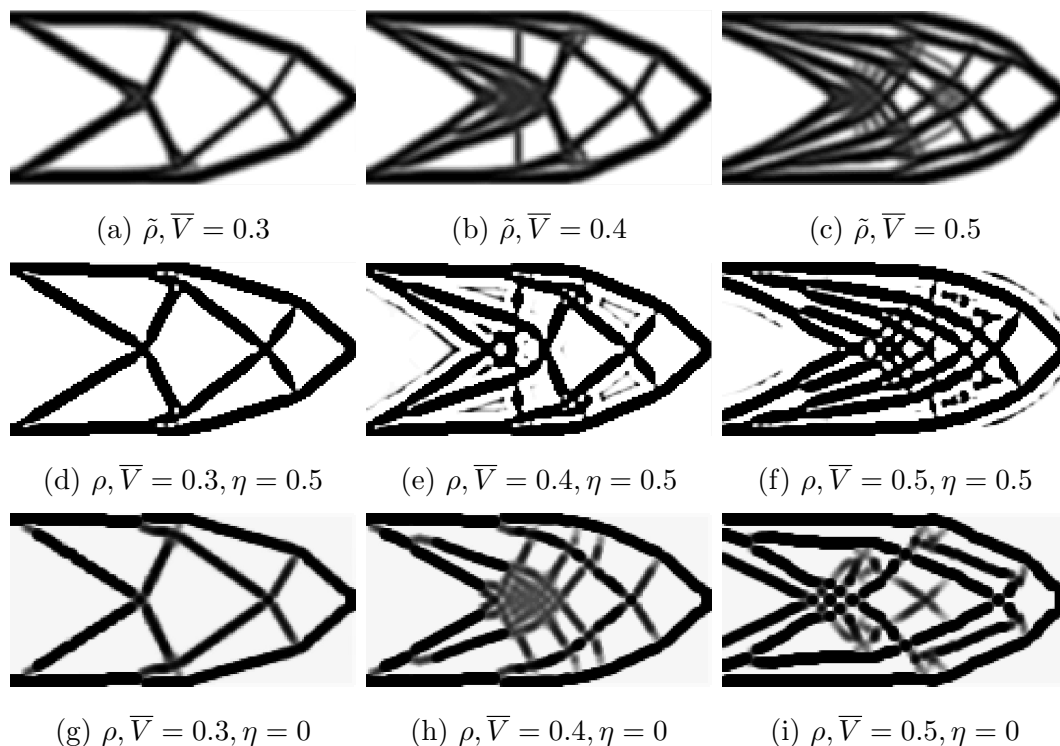
Figure 4.11. Volume and maximum radius constrained compliance minimization, $\mathbb{P}_4$, results for the Short Beam problem. Filtered density, $\eta = 0.5$ projection, $\eta = 0.0$ projection compared. $r_{min} = 3$ mm. $d_{max} = 7$ mm. $\kappa = 1$.

proper restriction of nodal thicknesses. However, increasing either $\overline{V}$ or κ reduces the efficacy of this approach. For higher volume fractions and $\kappa = 1$, the radius constraint forces structural hinges to arise. Secondary disconnected domains arise as a result to supplement the numerical stiffness of the beam. These features are obviously non-physical and undesirable. However, it is likely this effect could be mitigated through the imposition of an explicit minimum feature size constraint. Interestingly, for $\kappa = \frac{1}{3}$ and $\eta = 0.5$ vertical symmetry of the structural domain is broken. This indicates that these parameters are highly numerically sensitive and the formulation may benefit from tightened move-limits.

Reducing the projection cutoff to $\eta = 0$ results in structures which do not develop solid/void hinges and have a reduced occurrence non-physical secondary structures. However, due to the lack of volume-preservation [76, 77] of this projection, converged

(a) $\tilde{\rho}, \overline{V} = 0.3$ (b) $\tilde{\rho}, \overline{V} = 0.4$ (c) $\tilde{\rho}, \overline{V} = 0.5$

(d) $\rho, \overline{V} = 0.3, \eta = 0.5$ (e) $\rho, \overline{V} = 0.4, \eta = 0.5$ (f) $\rho, \overline{V} = 0.5, \eta = 0.5$

(g) $\rho, \overline{V} = 0.3, \eta = 0$ (h) $\rho, \overline{V} = 0.4, \eta = 0$ (i) $\rho, \overline{V} = 0.5, \eta = 0$
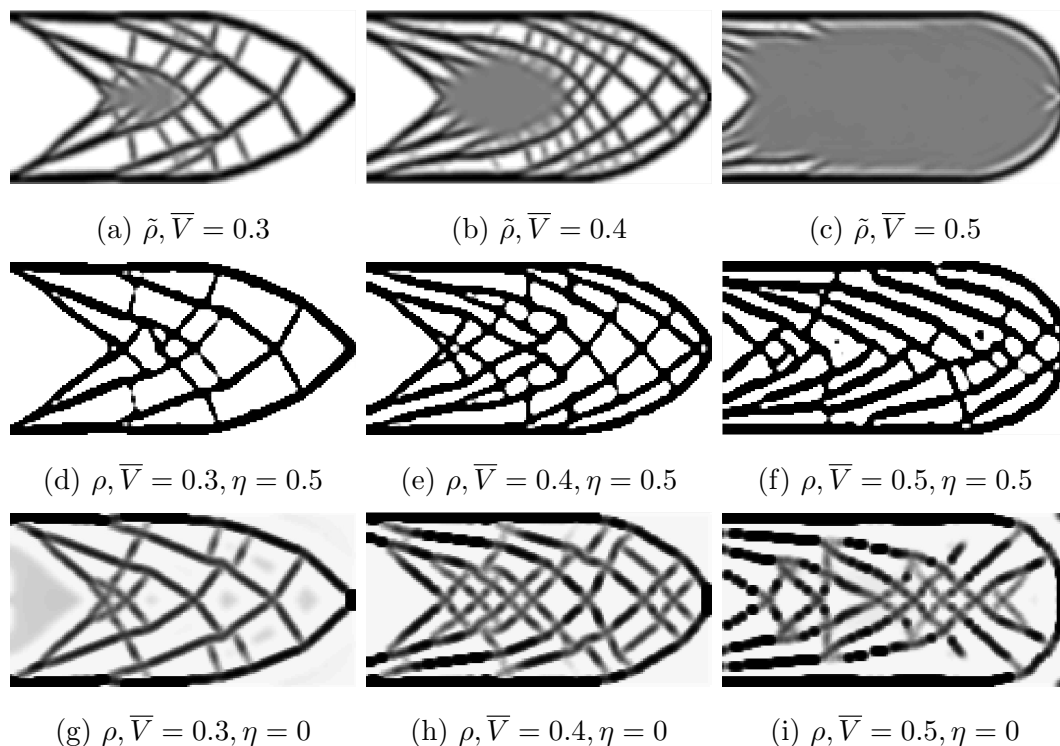
Figure 4.12. Volume and maximum radius constrained compliance minimization, $\mathbb{P}_4$, results for the Short Beam problem. Filtered density, $\eta = 0.5$ projection, $\eta = 0.0$ projection compared. $r_{min} = 3$ elements. $d_{max} = 7$ elements. $\kappa = \frac{1}{3}$.

members experience significant graying in the second optimization phase. This effect is most apparent in **Figure 4.12 (i)** where this graying leads to the detachment of key structural features.

Despite these challenges, it is apparent that the proposed three-field approach has the potential to yield practical converged structures. Importantly, it does so through an approach in which the geometry is restricted from the initial iteration of the optimization problem and does not rely on discontinuous interpretation of the structural domain. As a result, the resulting structures are drastically different from those presented by Zhang et al. In the results presented above, no clear influence of a structural skeleton is evidenced. Significantly less deviation from the principal stress lines in the domain is seen in all results. Answering the question of which approach is truly optimal remains an open question however.

Referring to the converged structural compliance given for each problem in **Table 4.3**, no discernible trend is observed for all cases. Numerically, the benefit of utilizing a three field approach is apparent for fully converged structures. These domains result in smaller compliance values for the $\overline{V}$ case because of the efficiency of fully void elements in the qp-formulation. The portion of compliance improvement which may be explained by this effect is not clear, though it is unlikely that a better compliance solution is driven by the local size restriction.

Table 4.3. Converged compliance measure for $\mathbb{P}_4$, maximum radius constrained short beam problem.

Volume	0.3	0.4	0.5
$d_{max} = \infty$	1851.3 N-mm	1285.9 N-mm	1007.4 N-mm
$\tilde{\rho}, d_{max} = 7$ mm, $\kappa = 1$	1967.1 N-mm	1590.5 N-mm	1332.8 N-mm
$\tilde{\rho}, d_{max} = 7$ mm, $\kappa = \frac{1}{3}$	2848.6 N-mm	2348.3 N-mm	2370.6 N-mm
$\rho, d_{max} = 7$ mm, $\kappa = 1, \eta = 0.5$	1561.4 N-mm	1368.9 N-mm	1161.1 N-mm
$\rho, d_{max} = 7$ mm, $\kappa = \frac{1}{3}, \eta = 0.5$	1637.6 N-mm	1430.5 N-mm	1456.3 N-mm
$\rho, d_{max} = 7$ mm, $\kappa = 1, \eta = 0$	1761.7 N-mm	1595.5 N-mm	1337.2 N-mm
$\rho, d_{max} = 7$ mm, $\kappa = \frac{1}{3}, \eta = 0$	2761.0 N-mm	2075.4 N-mm	3138.3 N-mm

4.5   Material-based size-dependent strength

4.5.1   Weibull scaling results

With the efficacy of the proposed size measure established, the optimization of structures considering size-dependent strength models may be considered. In order to explore the implications of these models, theoretical materials are assumed for each form of size-dependence. These theoretical materials share the following mechanical properties for a given reference sample configuration: $E_0 = 71,000$ MPa, $\nu = 0.33$, $\varsigma_C = 700$ MPa, and $\varsigma_{T_0} = 350$ MPa. Where these materials differ is in terms of the representative length-scale of each material for each size-dependent volume. This length-scale thus becomes the parameter to be varied to influence the optimization.

For the Weibull model of scaling, the length-scale of interest is the reference width of the tensile sample used to derive the tensile strength of the material. In addition to this length-scale, the Weibull model of size-dependence is driven by the Weibull modulus of the material. To explore the effects of Weibull size-dependent strength both the Weibull modulus and the reference width are varied.

The results for the $\mathbb{P}_5$ formulation with $\overline{V} = 0.4$ on the MBB domain are illustrated in **Figure 4.13** for materials with a Weibull modulus of 6 and varying reference specimen widths, D_0. Structural members with local size greater than D_0 are correspondingly weaker as prescribed by Eq. 3.6 while members smaller than D_0 are stronger by the same relation. It is worth reiterating at this point that this effect is only applied to the tensile fracture cutoff of the material. Thus, in practice only strengths of $\varsigma_T \leq \varsigma_{T_0}$ are realized on the domain. The generalized failure cutoff is applied using ς_{T_0} for simplicity and acts as the dominate constraining function once it is exceeded. In reality, ς_{T_0} would likely need to be distinguished from some $\varsigma_{T_{FPZ}}$ given by the scaling form of the particular material. This simplifying construction results in a discontinuous general or FPZ-dominated tensile failure limit that lacks physical justification on the continuum scale in the case of the power-law approaches.

(a) $D_0 = 1$ mm, $\kappa = 1$

(b) $D_0 = 5$ mm, $\kappa = 1$

(c) $D_0 = 10$ mm, $\kappa = 1$

(d) $D_0 = 1$ mm, $\kappa = \frac{1}{3}$

(e) $D_0 = 5$ mm, $\kappa = \frac{1}{3}$

(f) $D_0 = 10$ mm, $\kappa = \frac{1}{3}$
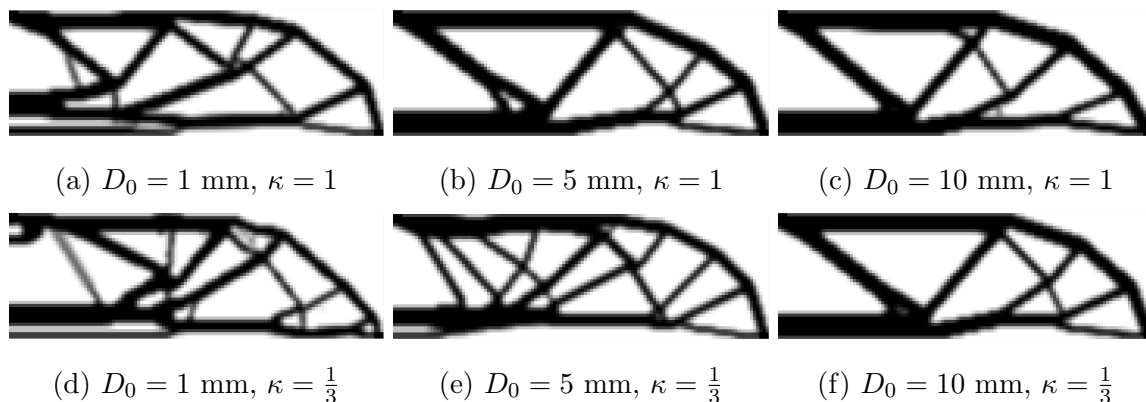
Figure 4.13. Converged structures for Weibull-based strength and volume constrained compliance minimization, $\mathbb{P}_5$, for MBB problem. Effect of Weibull reference length, D_0 and size penalization, κ considered. Filtered density formulation used. $r_{min} = 2$ elements. $\overline{V} = 0.4$. $m = 6$.

Following this relationship, **Figure 4.13 (a)** and **(b)** shift the main tensile member of the domain upwards and introduce a secondary thin tensile member to distribute the loading in this domain. Upon increasing the reference width of the specimen to 5 mm, the split tensile member disappears from **(b)** but remains in **(e)** due to the interpretation of gray regions as fully dense structures for the size measure. Finally, upon increasing the reference width to 10 mm the effect of tensile fracture strength constraints on the domain is greatly diminished. This is due to the fact that a member must grow to 1/10 the height of the domain to evidence a tensile strength marginally less than the reference value.

To illustrate the effect of the reference width on the converged structure, Eq. 3.6 is plotted for each reference width relative to the size-independent strength in **Figure 4.14**. The fully dense elements for each $\kappa = 1$ condition shown in **Figure 4.13** are overlaid on their corresponding lines. The lower gray region is a restriction on the local size based on the mesh density of the domain; the upper gray region is a restriction based on the prescribed domain of support of the size-measure. This plot illustrates that for small reference widths, the majority of the converged structure exhibits a phenomenological strength weaker than the size-independent assumption. Under this condition, the fracture constraint p-norm approximation serves to restrict

the feasible design space. For members with local strength greater than ς_{T_0}, the Christensen quadratic failure surface becomes the tighter constraint on the elemental first principal stress and restricts allowable values on the domain.
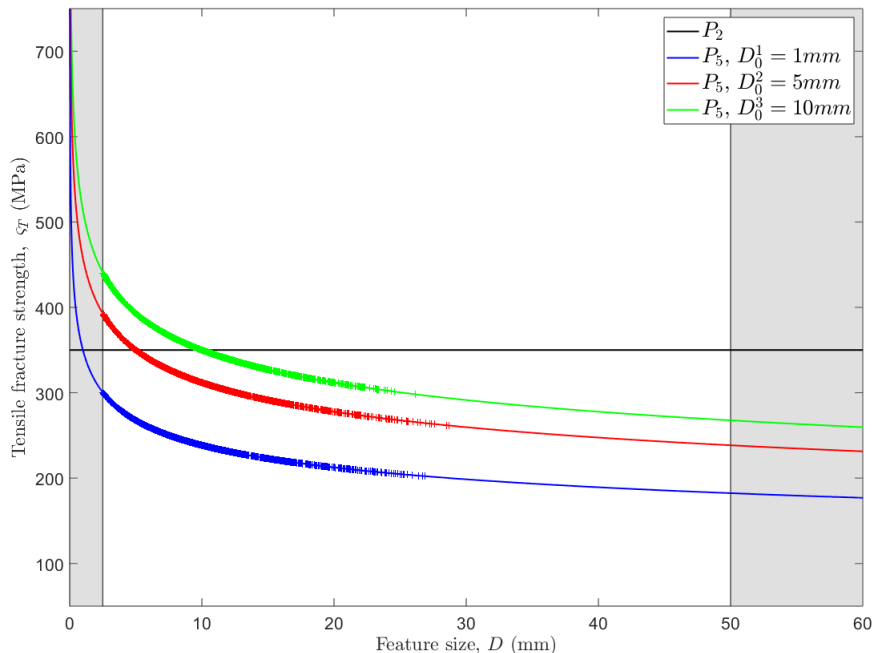
Figure 4.14. Local tensile strength versus size for $\mathbb{P}_5$ MBB problems with $m = 6$. Reference strength for the $\mathbb{P}_2$ formulation plotted against formulations with varied Weibull reference length, D_0.

Considering the $\mathbb{P}_6$ volume minimization problem, the results presented in **Figure 4.15** illustrate the stabilizing effect of the compliance objective. All volume minimization solutions illustrated exhibit significantly more intermediate density structure. It is posited that this occurs due a set of tightly grouped local minimum induced by the size-dependence of the strength measure. This effect is masked by the $\mathbb{P}_5$ formulation for which a relatively distinct global minimum exists for the given domain and regularization. However, it is noted that reasonable structural convergence is observed for all six cases. This fails to remain the case for stronger forms of material size-dependent scaling.

In addition to the results presented for the MBB test problem, converged structures are given for the $\mathbb{P}_5$ and $\mathbb{P}_6$ problem formulations on the L-bracket problem

(a) $D_0 = 1$ mm, $\kappa = 1$ (b) $D_0 = 5$ mm, $\kappa = 1$ (c) $D_0 = 10$ mm, $\kappa = 1$

(d) $D_0 = 1$ mm, $\kappa = \frac{1}{3}$ (e) $D_0 = 5$ mm, $\kappa = \frac{1}{3}$ (f) $D_0 = 10$ mm, $\kappa = \frac{1}{3}$
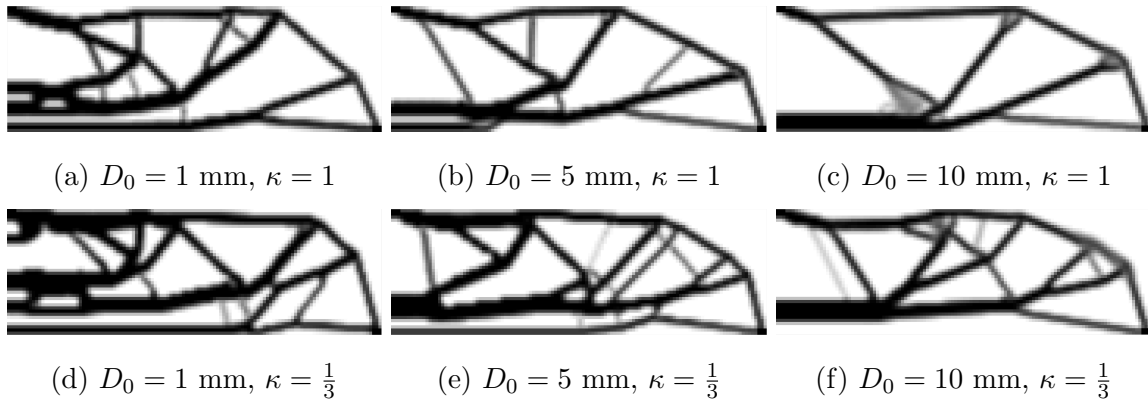
Figure 4.15. Converged structures for Weibull-based strength constrained volume minimization, $\mathbb{P}_6$, for MBB problem. Effect of Weibull reference length, D_0 and size penalization, κ considered. Filtered density formulation used. $r_{min} = 2$ elements. $m = 6$.

domain in **Figures 4.16** and **4.17**. In comparing these two formulations on this domain, it is clear that the compliance formulation again provides a strong stabilizing effect. For the $\mathbb{P}_6$ formulation at smaller reference widths, the algorithm attempts to generate additional tensile members in the vertical portion of the L-Bracket domain. Upon reaching the midpoint of the domain, these structures begin to carry compression loads as they have crossed the neutral axis the fully dense region would have in bending. The $\mathbb{P}_5$ formulation mitigates this behavior by developing stiff compression members along the outer boundary of the bracket. This in turn allows structural convergence along the tensile loading path in the domain.

Considering now the effect of the size-measure penalization on the L-bracket problem, two interesting effects arise. The first relates to the intrinsic stress-riser present in the allowable domain. For problems with a penalization of $\kappa = 1$ and a small D_0, a structural node localizes at the re-entrant corner for both the $\mathbb{P}_5$ and $\mathbb{P}_6$ conditions. The cause of this feature is not clear, but the retention of the stress-riser is a highly undesirable outcome. Implementing a gray penalization of $\kappa = \frac{1}{3}$ causes for a significant rounding of the region local to the corner. For the highly non-convergent **Figure 4.17 (d)** and **(e)** results, this rounding exceeds the filleting generally seen by stress-based TO approaches to this problem results in drastic changes to the topology.

(a) $D_0 = 1$ mm, $\kappa = 1$ (b) $D_0 = 5$ mm, $\kappa = 1$ (c) $D_0 = 10$ mm, $\kappa = 1$

(d) $D_0 = 1$ mm, $\kappa = \frac{1}{3}$ (e) $D_0 = 5$ mm, $\kappa = \frac{1}{3}$ (f) $D_0 = 10$ mm, $\kappa = \frac{1}{3}$
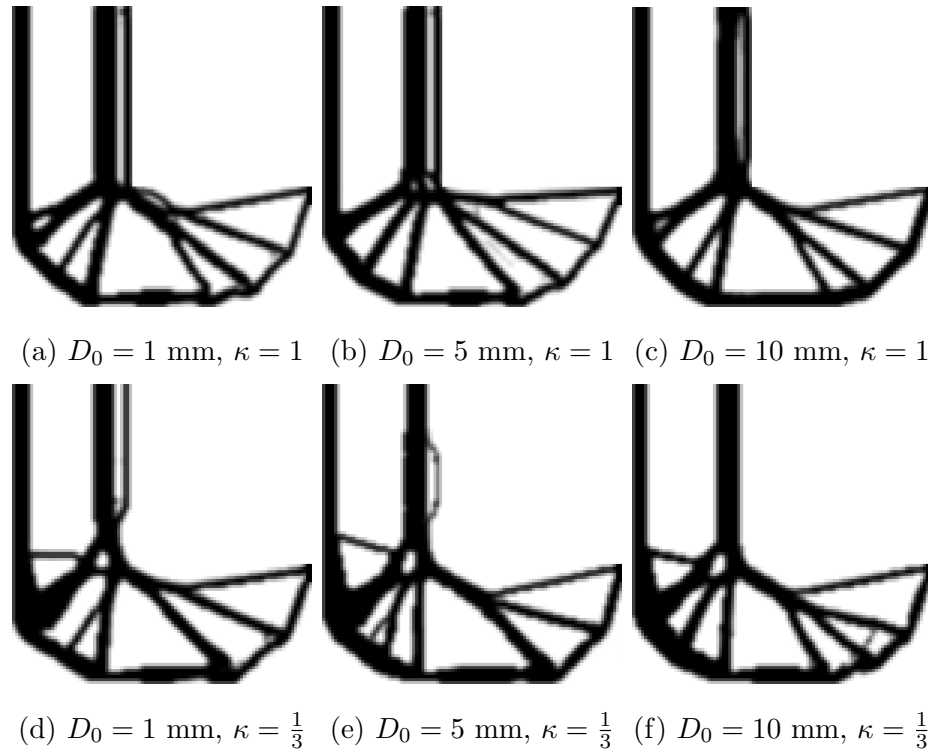
Figure 4.16. Converged structures for Weibull-based volume and strength constrained compliance minimization, $\mathbb{P}_5$, for L-Bracket problem. Effect of Weibull reference length, D_0 and size penalization, κ considered. Filtered density formulation used. $V_0 = 0.4$. $r_{min} = 2$ elements. $m = 6$.

The second effect once again deals with the treatment of shear transfer. For a fully dense L-bracket domain, the core of the structure transfers shear between the outer and inner load paths in a manner similar to a 3-point bend beam. Forcing portions of the domain to void requires the topology generated to transfer this force through largely axially dominated structural members. Under the $\kappa = \frac{1}{3}$ penalization, these axial members in the shear dominated-elbow of the L-bracket begin to evidence cellular structural regions. These regions localize near the re-entrant corner and resemble the size-independent topology further from this point. Locally, highly stressed tensile members join as spokes out to the compression loading path. The imposed penalization separates these spokes out sufficiently as to force a markedly different topology to emerge.

(a) $D_0 = 1$ mm, $\kappa = 1$ (b) $D_0 = 5$ mm, $\kappa = 1$ (c) $D_0 = 10$ mm, $\kappa = 1$

(d) $D_0 = 1$ mm, $\kappa = \frac{1}{3}$ (e) $D_0 = 5$ mm, $\kappa = \frac{1}{3}$ (f) $D_0 = 10$ mm, $\kappa = \frac{1}{3}$
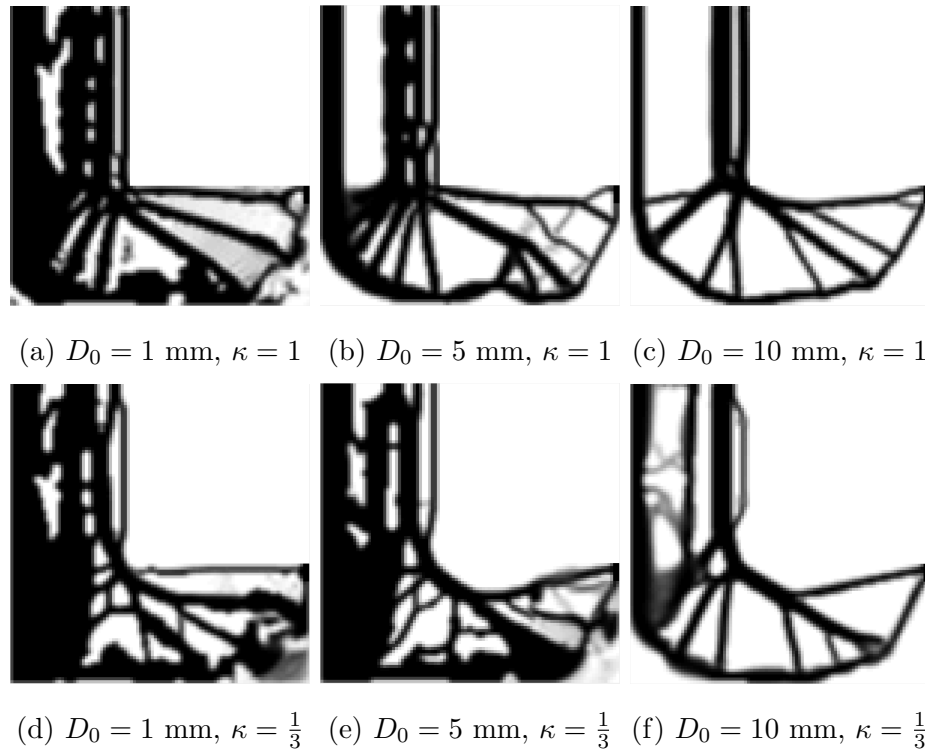
Figure 4.17. Converged structures for Weibull-based strength constrained volume minimization, $\mathbb{P}_6$, for L-Bracket problem. Effect of Weibull reference length, D_0 and size penalization, κ considered. Filtered density formulation used. $r_{min} = 2$ elements. $m = 6$.

Despite the appearance that these converged structures satisfy all strength requirements, the first principal stress normalized by the local tensile strength plotted in **Figure 4.18** shows that this is not the case. Under the prescribed conditions $\mathbb{P}_5$ results in structural convergence within the infeasible design domain. With this in mind, $\mathbb{P}_5$ formulations must be applied judiciously by designers to prevent implementation of qualitatively justifiable but physically unsafe structures.

(a) $D_0 = 1$ mm, $\kappa = 1$ (b) $D_0 = 5$ mm, $\kappa = 1$ (c) $D_0 = 10$ mm, $\kappa = 1$

(d) $D_0 = 1$ mm, $\kappa = \frac{1}{3}$ (e) $D_0 = 5$ mm, $\kappa = \frac{1}{3}$ (f) $D_0 = 10$ mm, $\kappa = \frac{1}{3}$
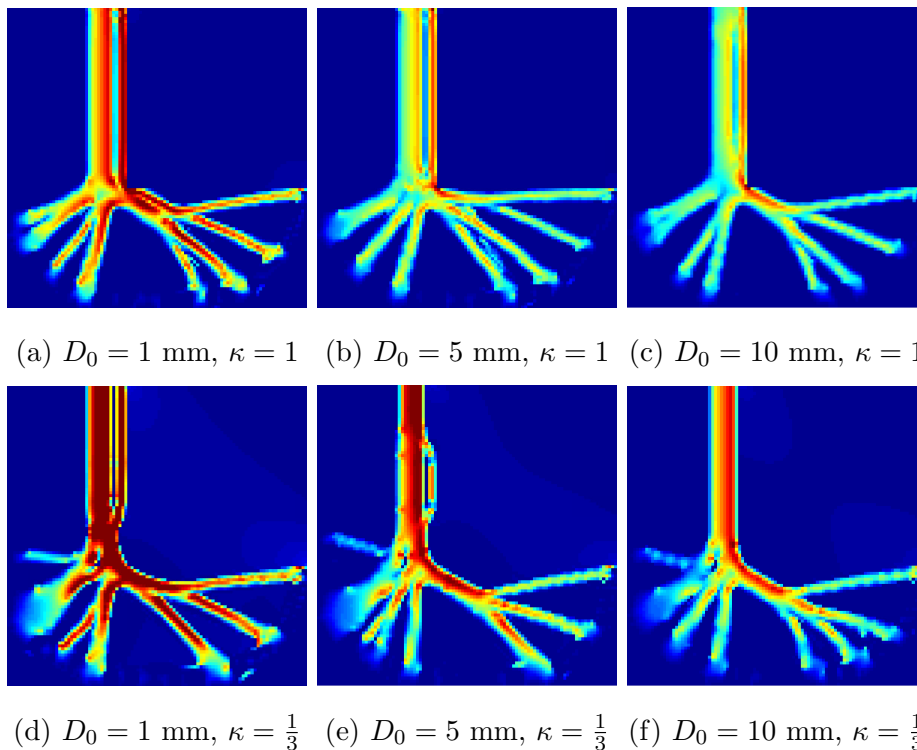
Figure 4.18. σ_I/ς_i^T plotted for L-Bracket $\mathbb{P}_5$ problem for Weibull scaling with $m = 6$. Regions in dark red indicate brittle tensile failure exceeding a safety factor of 1.0.

Repeating the analysis given above for a larger Weibull modulus material illustrates the diminishing effects of size-dependence for higher quality materials. The converged structures for the $\mathbb{P}_5$ and $\mathbb{P}_6$ for a material with $m = 15$ are shown for the MBB domain in **Figures 4.19** and **4.20**. Both formulations are illustrated for the L-bracket domain in **Figures 4.21** and **4.22**, respectively.

(a) $D_0 = 1$ mm, $\kappa = 1$ (b) $D_0 = 5$ mm, $\kappa = 1$ (c) $D_0 = 10$ mm, $\kappa = 1$

(d) $D_0 = 1$ mm, $\kappa = \frac{1}{3}$ (e) $D_0 = 5$ mm, $\kappa = \frac{1}{3}$ (f) $D_0 = 10$ mm, $\kappa = \frac{1}{3}$
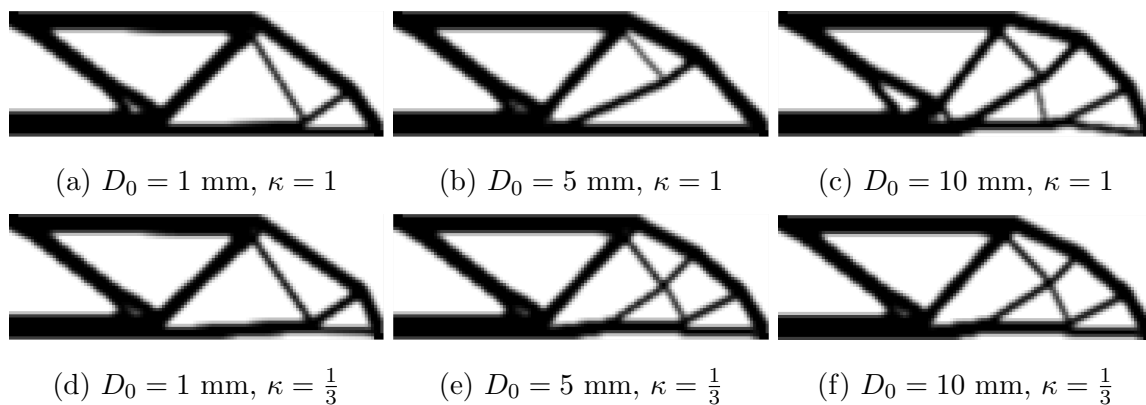
Figure 4.19. Converged structures for Weibull-based strength and volume constrained, $\mathbb{P}_5$, for MBB problem. Effect of Weibull reference length, D_0 and size penalization, κ considered. Filtered density formulation used. $r_{min} = 2$ elements. $\overline{V} = 0.4$. $m = 15$.

(a) $D_0 = 1$ mm, $\kappa = 1$ (b) $D_0 = 5$ mm, $\kappa = 1$ (c) $D_0 = 10$ mm, $\kappa = 1$

(d) $D_0 = 1$ mm, $\kappa = \frac{1}{3}$ (e) $D_0 = 5$ mm, $\kappa = \frac{1}{3}$ (f) $D_0 = 10$ mm, $\kappa = \frac{1}{3}$
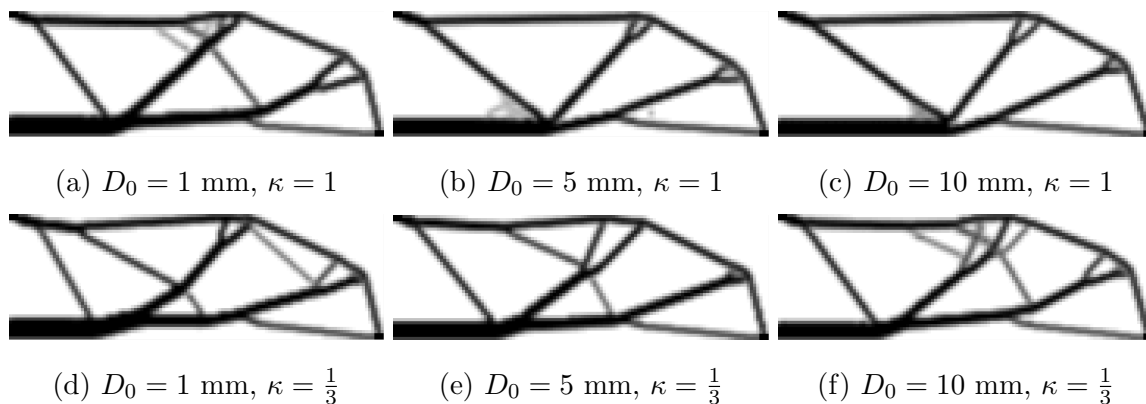
Figure 4.20. Converged structures for Weibull-based strength constrained volume minimization, $\mathbb{P}_6$, for MBB problem. Effect of Weibull reference length, D_0 and size penalization, κ considered. Filtered density formulation used. $r_{min} = 2$ elements. $m = 15$.

(a) $D_0 = 1$ mm, $\kappa = 1$ (b) $D_0 = 5$ mm, $\kappa = 1$ (c) $D_0 = 10$ mm, $\kappa = 1$

(d) $D_0 = 1$ mm, $\kappa = \frac{1}{3}$ (e) $D_0 = 5$ mm, $\kappa = \frac{1}{3}$ (f) $D_0 = 10$ mm, $\kappa = \frac{1}{3}$
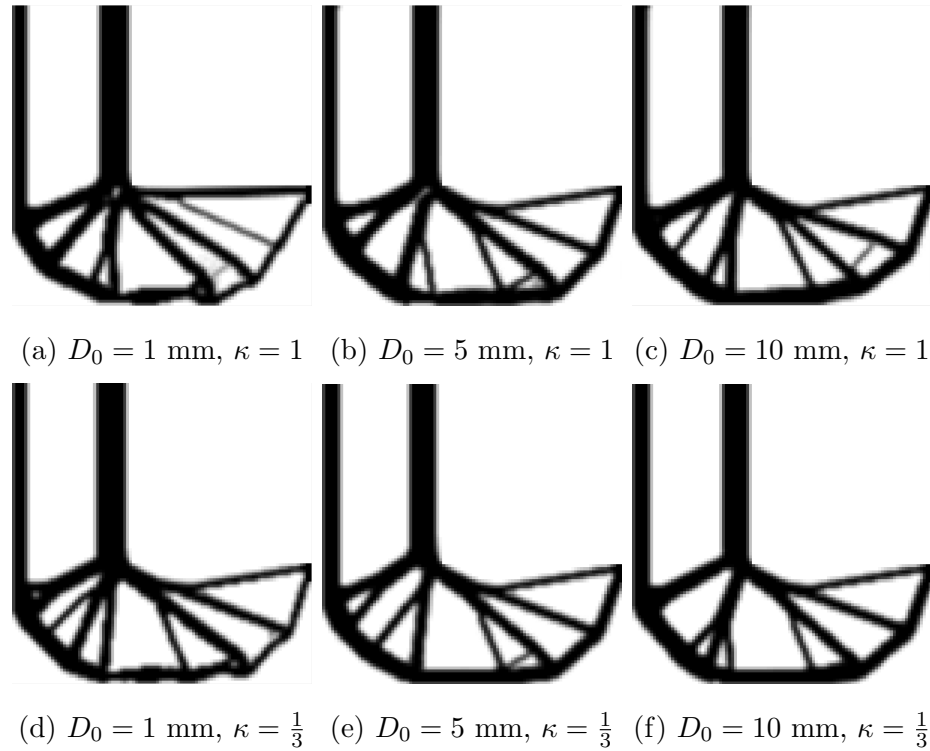
Figure 4.21. Converged structures for Weibull-based volume and strength constrained compliance minimization, $\mathbb{P}_5$, for L-Bracket test problem. Effect of Weibull reference length, D_0 and size penalization, κ considered. Filtered density formulation used. $V_0 = 0.4$. $r_{min} = 2$ elements. $m = 15$.

(a) $D_0 = 1$ mm, $\kappa = 1$ (b) $D_0 = 5$ mm, $\kappa = 1$ (c) $D_0 = 10$ mm, $\kappa = 1$

(d) $D_0 = 1$ mm, $\kappa = \frac{1}{3}$ (e) $D_0 = 5$ mm, $\kappa = \frac{1}{3}$ (f) $D_0 = 10$ mm, $\kappa = \frac{1}{3}$
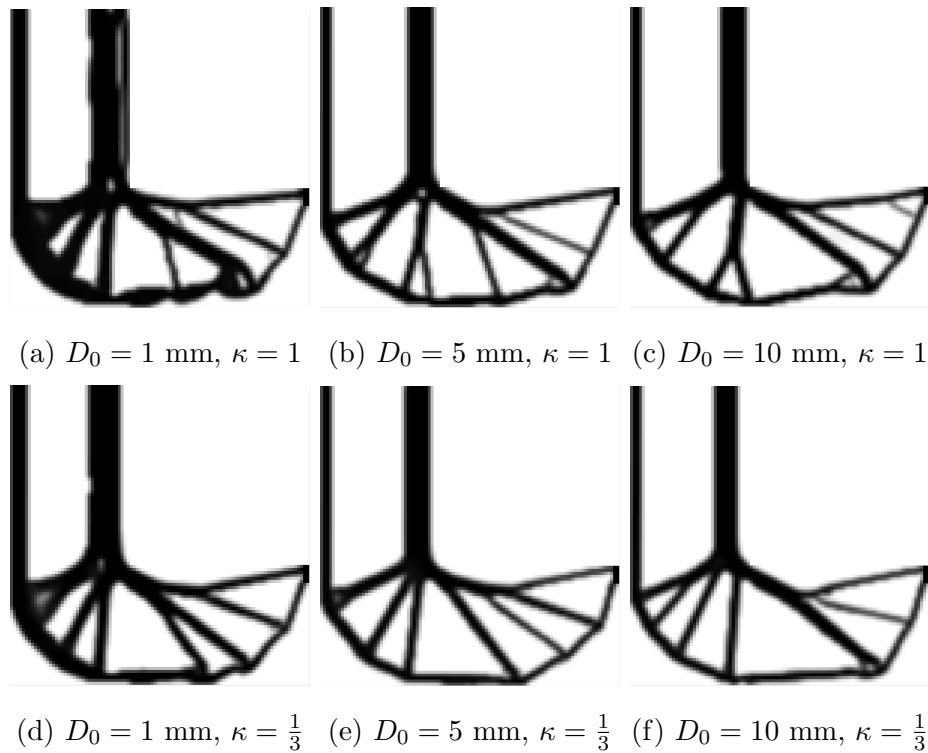
Figure 4.22.   Converged structures for Weibull-based strength constrained volume minimization, $\mathbb{P}_6$, for L-Bracket test problem. Effect of Weibull reference length, D_0 and size penalization, κ considered. Filtered density formulation used. $r_{min} = 2$ elements. $m = 15$.

Both problem domains exhibit limited size dependence in their respective converged structures, as expected from the shallowness of the scaling law plotted in **Figure 4.23**. The one notable exception occurs for small reference widths in the L-bracket problem. In this domain, the main vertical tensile member remains almost monolithic but exhibits minor thickening. This implies that for high quality materials size dependence can be accounted for by correcting sample tensile strengths from specimens orders of magnitude smaller than the structure with Eq. 3.5.
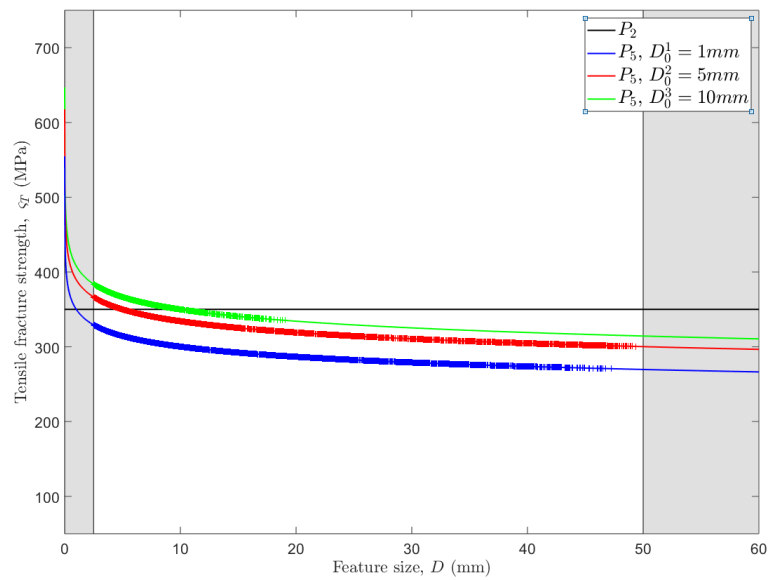
Figure 4.23. Local tensile strength versus size for $\mathbb{P}_5$ MBB problems with $m = 15$.

4.5.2 LEFM scaling results

In context of the Weibull scaling results given in the prior section, LEFM scaling amplifies the trends observed. This is intuitive as the macro-crack driven power law which underlies LEFM scaling is identical in form to the Weibull model but greater in magnitude. Converged structures for the MBB domain are shown in **Figures 4.24** and **4.25**.

Once again, the $\mathbb{P}_5$ formulation stabilizes the MMA algorithm to result in qualitatively feasible structures that fail to satisfy fracture strength constraints. Despite this fact, the results are instructive. Instead of adding a supplemental tensile member as seen in less severe scaling models, the main tensile member is split into roughly equally sized struts. Each of these struts then extends out in its entirety to the compression dominated members in the domain. For the $\kappa = 1$ cases, this results in lamellar structures. The interaction of these structures with the linear filtering scheme results in intermediate density regions that carry shear in between the layers in a non-physical fashion. By reducing κ to $\frac{1}{3}$, these gray shear regions are removed and the lamella separated. The large gray region illustrated in **Figure 4.24** occurs due to satisfaction of the Δ_c convergence criteria and could possibly be removed by tightening this parameter.

| (a) $D_0 = 1$ mm, $\kappa = 1$ | (b) $D_0 = 5$ mm, $\kappa = 1$ | (c) $D_0 = 10$ mm, $\kappa = 1$ |

| (d) $D_0 = 1$ mm, $\kappa = \frac{1}{3}$ | (e) $D_0 = 5$ mm, $\kappa = \frac{1}{3}$ | (f) $D_0 = 10$ mm, $\kappa = \frac{1}{3}$ |
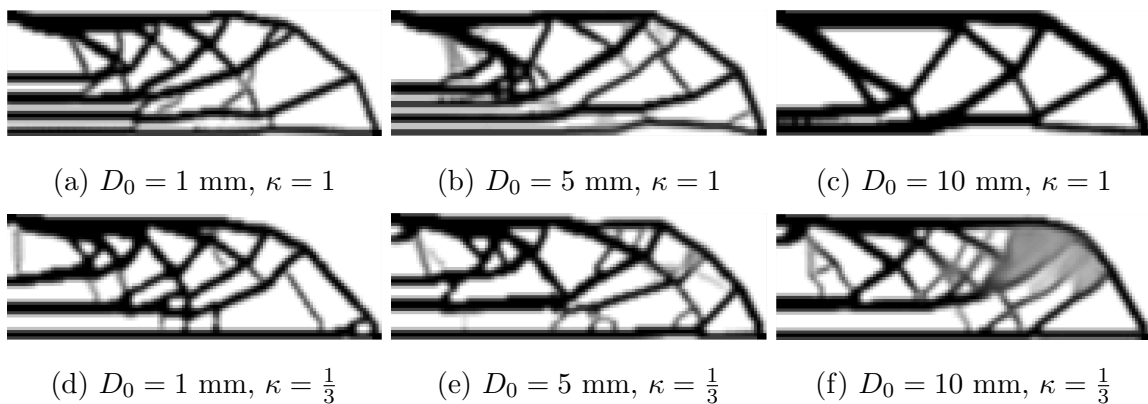
Figure 4.24. Converged structures for LEFM-based strength and volume constrained compliance minimization, $\mathbb{P}_5$, for MBB problem. Effect of LEFM reference length, D_0 and size penalization, κ considered. Filtered density formulation used. $r_{min} = 2$ elements. $\overline{V} = 0.4$.

Removing the compliance objective from the formulation results in poor structural convergence under most conditions explored. The sole numerically feasible structure observed is seen in **Figure 4.25 (c)**, though this result suffers from the same intermediate density shear transfer regions along the tensile loading path.

(a) $D_0 = 1$ mm, $\kappa = 1$ (b) $D_0 = 5$ mm, $\kappa = 1$ (c) $D_0 = 10$ mm, $\kappa = 1$

(d) $D_0 = 1$ mm, $\kappa = \frac{1}{3}$ (e) $D_0 = 5$ mm, $\kappa = \frac{1}{3}$ (f) $D_0 = 10$ mm, $\kappa = \frac{1}{3}$
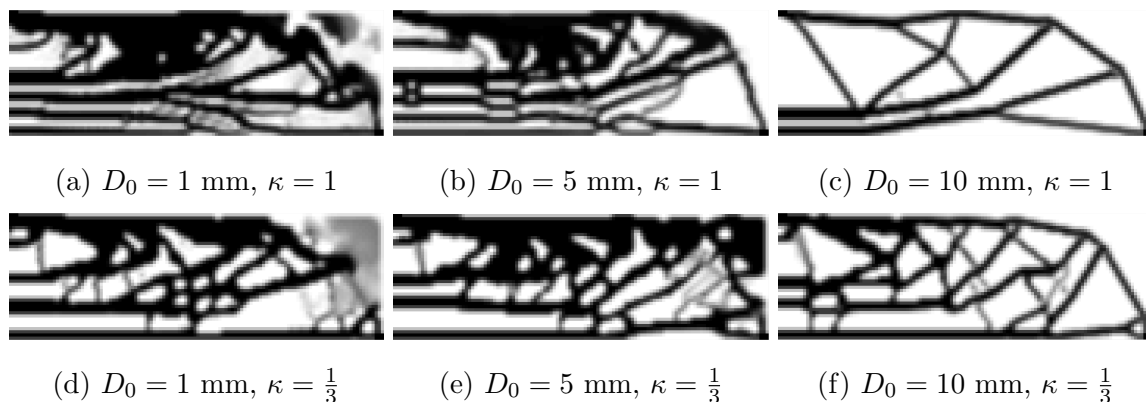
Figure 4.25.   Converged structures for LEFM-based strength constrained volume minimization, $\mathbb{P}_6$, for MBB problem. Effect of LEFM reference length, D_0 and size penalization, κ considered. Filtered density formulation used. $r_{min} = 2$ elements.

Figure 4.26 can be used to interrogate the underlying mechanism forcing poor convergence on the domain. For the $D_0 = 1$ mm material condition, the structure begins to converge with highly inefficient thick members relative to the reference length. This results in the entirety of the structural domain under tensile loading exhibiting a minimum reduction of strength of 35% compared to ς_{T_0}. The TO algorithm continues to densify these regions in an attempt to carry the requisite load while satisfying strength constraints. However, an apparent restriction on the global amount of tensile loading arises, preventing convergence.

Increasing the assumed reference length scale shifts the LEFM scaling law upwards such that features with tensile fracture strengths greater than ς_N are present in the structure. However, even under the $D_0 = 5$ mm condition a converged structure is not realized. It is not until a significant portion of the domain is no longer fracture-limited under the $D_0 = 10$ mm condition that convergence of the $\mathbb{P}_6$ is achieved. It is worth emphasizing here that using a unified ς_{T_0} for both the fracture scaling and

size-independent yield surface imposes the two asymptotic cases explored by the SEL in a discontinuous manner. Thus, members with $d_e \leq D_0$ exhibit strength-dominated failure even without the asymptotic transition described by the SEL. This effect is important when comparing the results of the two approaches.
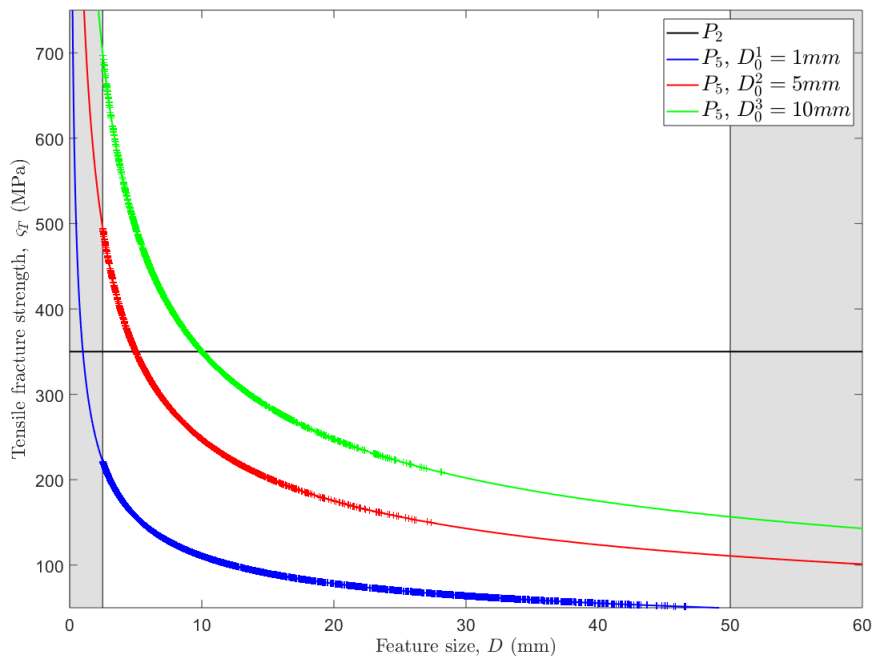
Figure 4.26. Local tensile strength versus size for $\mathbb{P}_5$ LEFM scaling MBB problems.

The converged results for the LEFM-based $\mathbb{P}_5$ and $\mathbb{P}_6$ formulations on the L-bracket domain are presented in **Figures 4.27** and **4.29**. These results reiterate the stabilizing nature of the compliance objective and the strong impact on topology of the high-power LEFM scaling. The results are particularly striking for the $D_0 = 1$ mm cases where the tensile domain develops a pronounced lamellar structure in the vertical bracket member. However, interrogating the normalized stress plots given in **Figure 4.28** reiterates the camouflaging effect of the compliance objective. Despite the qualitatively feasible structures obtained, only the $D_0 = 10$ mm, $\kappa = 1$ case satisfies stress constraints and achieves formal convergence.

(a) $D_0 = 1$ mm, $\kappa = 1$ (b) $D_0 = 5$ mm, $\kappa = 1$ (c) $D_0 = 10$ mm, $\kappa = 1$

(d) $D_0 = 1$ mm, $\kappa = \frac{1}{3}$ (e) $D_0 = 5$ mm, $\kappa = \frac{1}{3}$ (f) $D_0 = 10$ mm, $\kappa = \frac{1}{3}$
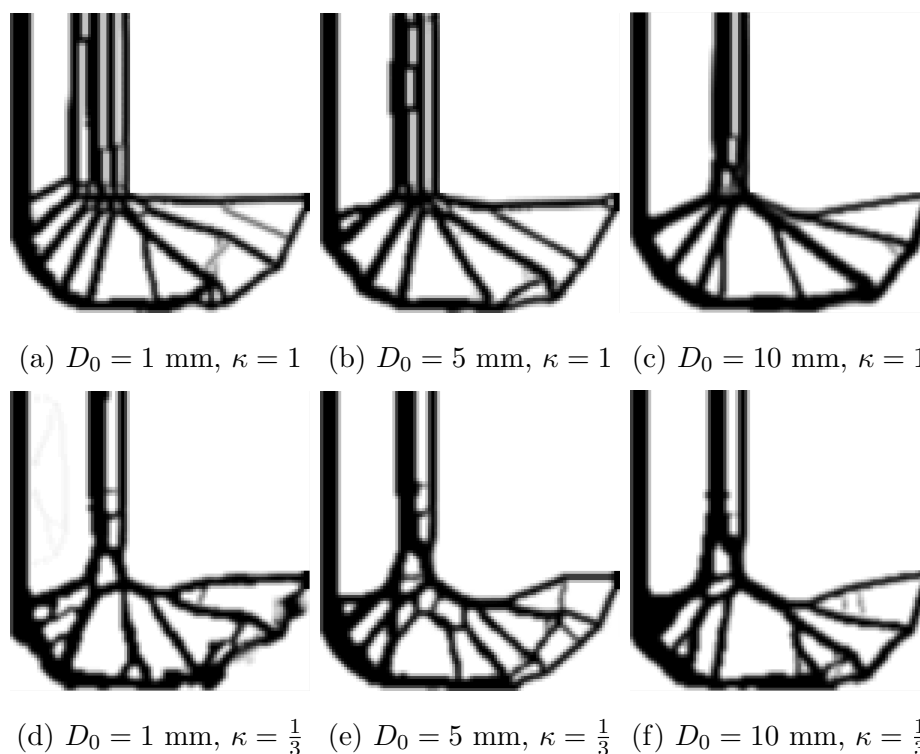
Figure 4.27.   Converged structures LEFM-based volume and strength constrained compliance minimization, $\mathbb{P}_5$, for L-Bracket problem. Effect of LEFM reference length, D_0 and size penalization, κ considered. Filtered density formulation used. $V_0 = 0.4$. $r_{min} = 2$ elements.

Notably, for both objectives on the L-bracket domain the $\kappa = \frac{1}{3}$ penalization leads to the development of significant cellular regions for all D_0 cases. This effect is particularly striking for the non-convergent $\mathbb{P}_6$ cases. It remains to be investigated if

(a) $D_0 = 1$ mm, $\kappa = 1$ (b) $D_0 = 5$ mm, $\kappa = 1$ (c) $D_0 = 10$ mm, $\kappa = 1$

(d) $D_0 = 1$ mm, $\kappa = \frac{1}{3}$ (e) $D_0 = 5$ mm, $\kappa = \frac{1}{3}$ (f) $D_0 = 10$ mm, $\kappa = \frac{1}{3}$
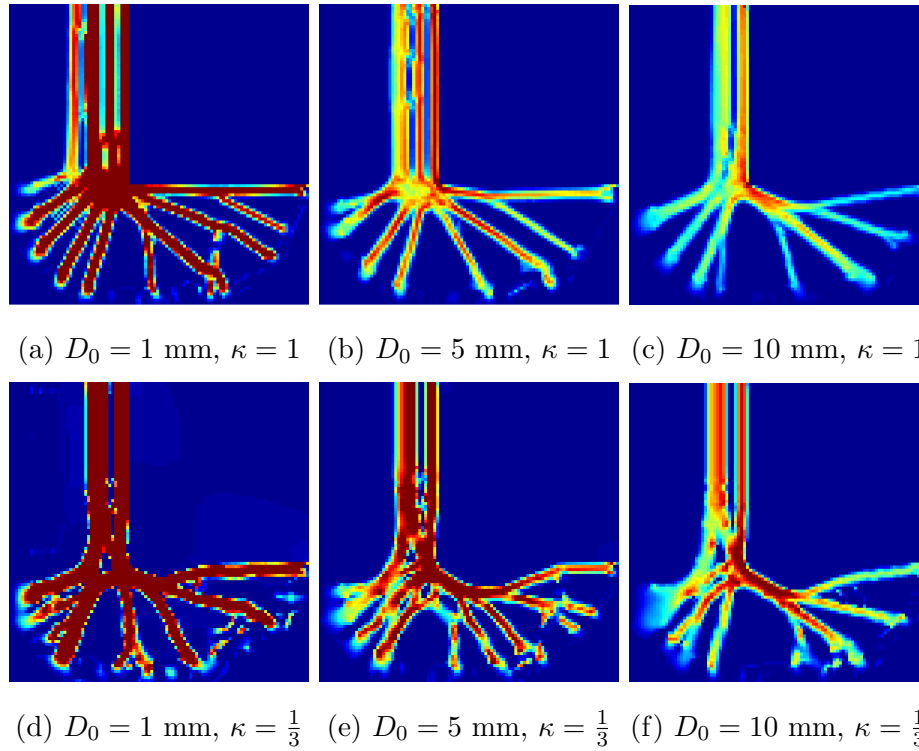
Figure 4.28. σ_I / ς_i^T plotted for L-Bracket $\mathbb{P}_5$ problem for LEFM scaling. Regions in dark red indicate brittle tensile failure exceeding a safety factor of 1.0.

these L-bracket specific structures persist for applied loads allowing convergence or if they are an artifact of severe constraint violation.

(a) $D_0 = 1$ mm, $\kappa = 1$ (b) $D_0 = 5$ mm, $\kappa = 1$ (c) $D_0 = 10$ mm, $\kappa = 1$

(d) $D_0 = 1$ mm, $\kappa = \frac{1}{3}$ (e) $D_0 = 5$ mm, $\kappa = \frac{1}{3}$ (f) $D_0 = 10$ mm, $\kappa = \frac{1}{3}$
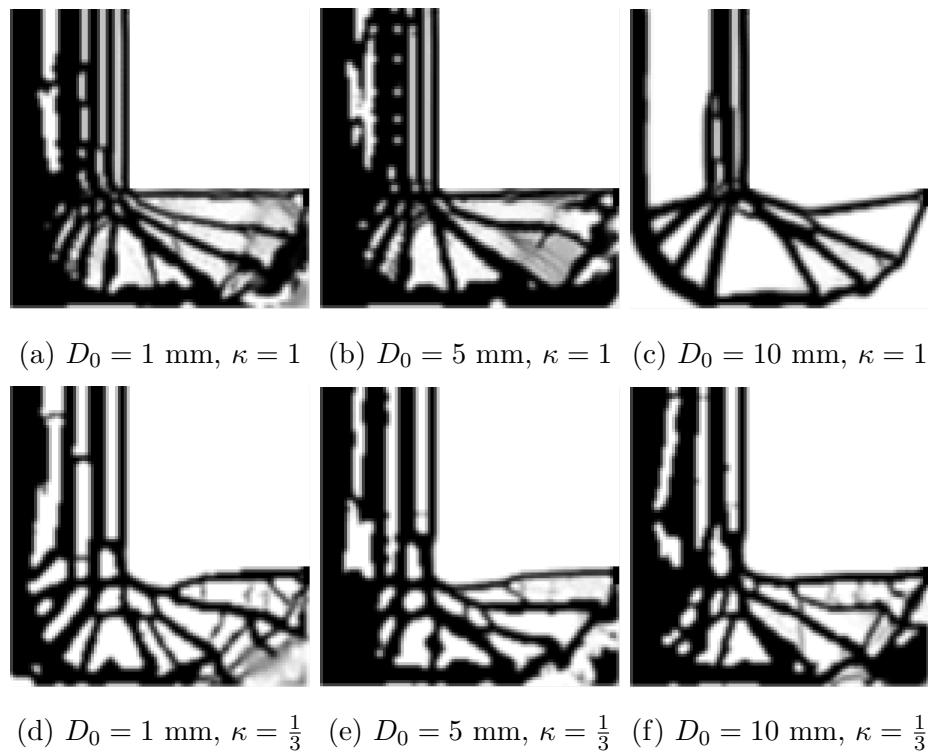
Figure 4.29.   Converged structures for LEFM-based strength constrained volume minimization, $\mathbb{P}_6$, for L-Bracket problem. Effect of LEFM reference length, D_0 and size penalization, κ considered. Filtered density formulation used. $r_{min} = 2$ elements.

4.5.3 Bažant Type II Size Effect Law scaling results

To study the effect of the Bažant SEL, initially ς_{T0} is held fixed equal to the 350 MPa used for the size-independent formulations and the material length-scale, D_0 is assumed to vary. All other mechanical and geometric parameters of the MBB and L-Bracket test problems remain unchanged. The effect of this approach is to translate the the knee of the asymptotic solution illustrated in **Figure 1.2** along the axis of scale. Larger values of D_0 shift a greater portion of the domain into the strength asymptote of the SEL while smaller values result in structures dominated by LEFM driven failure. The structures resulting from this scaling behavior are illustrated for both size dependent formulations of the MBB test problem in **Figures 4.30** and **4.31**.

(a) $D_0 = 1$ mm, $\kappa = 1$	(b) $D_0 = 5$ mm, $\kappa = 1$	(c) $D_0 = 10$ mm, $\kappa = 1$
(d) $D_0 = 1$ mm, $\kappa = \frac{1}{3}$	(e) $D_0 = 5$ mm, $\kappa = \frac{1}{3}$	(f) $D_0 = 10$ mm, $\kappa = \frac{1}{3}$
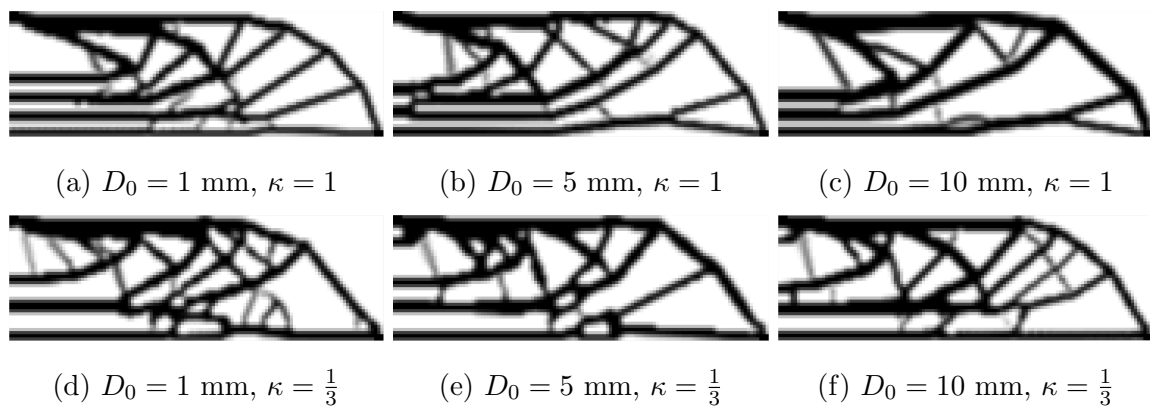
Figure 4.30. Converged structures for Bažant SEL strength and volume constrained compliance minimization, $\mathbb{P}_5$, for MBB problem. Effect of intrinsic material length, D_0 and size penalization, κ considered. Filtered density formulation used. $r_{min} = 2$ elements. $\overline{V} = 0.4$.

By holding ς_{T_0} fixed, lamellar topologies arise in the tensile regions of all problems under the both objective formulations. Again the compliance objective works to stabilize the problem, leading to qualitative convergence while violating the fracture stress constraints throughout the domain. Unlike in the power-law cases shown previously, increasing D_0 does not lead to appreciably thicker tensile members. The reason for this occurrence is illustrated by **Figure 4.32**. This plot illustrates the effect of

the SEL on a linear scale. Unlike for the power-law problems, the fracture-cutoff on strength remains as the constraining function on local stress throughout the entire scale due to the asymptotic construction of the SEL. Because of this, tensile members are driven towards the discretization-limited thickness bound in all cases.

Referring again to **Figure 4.32**, the poor convergence of the $\mathbb{P}_6$ test cases can be inferred to result from the significant strength penalization of all elements in the domain. Under the SEL assumptions, the majority of the $D_0 = 1$ mm structure possesses $\frac{1}{3}$ the strength that would be assumed under FPZ dominated conditions. Logically, it follows that convergence under these conditions would be highly unlikely. Increasing the material length-scale to $D_0 = 10$ mm allows for the smallest members in the domain to approach the strength asymptote. This results in the reasonable qualitative convergence illustrated in **Figure 4.31 (c)**, though the structure fails to satisfy the prescribed fracture constraint.

(a) $D_0 = 1$ mm, $\kappa = 1$ (b) $D_0 = 5$ mm, $\kappa = 1$ (c) $D_0 = 10$ mm, $\kappa = 1$

(d) $D_0 = 1$ mm, $\kappa = \frac{1}{3}$ (e) $D_0 = 5$ mm, $\kappa = \frac{1}{3}$ (f) $D_0 = 10$ mm, $\kappa = \frac{1}{3}$
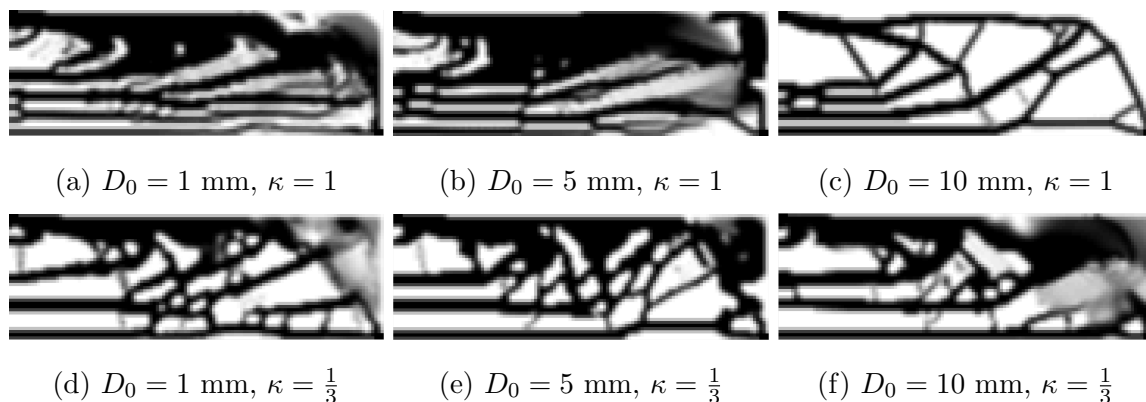
Figure 4.31.   Converged structures for Bažant SEL strength constrained volume minimization, $\mathbb{P}_6$, for MBB problem. Effect of intrinsic material length, D_0 and size penalization, κ considered. Filtered density formulation used. $r_{min} = 2$ elements.

Qualitatively, the L-bracket domain results for both SEL-dependent objectives illustrated in **Figures 4.27** and **4.34** are markedly similar to the converged LEFM-dependent results. Unlike the LEFM-scaling study, no parameters used for the L-bracket test domain exhibits formal convergence. As discussed previously, the use of ς_{T_0} in both strength constraint functions imposes both asymptotes of the SEL
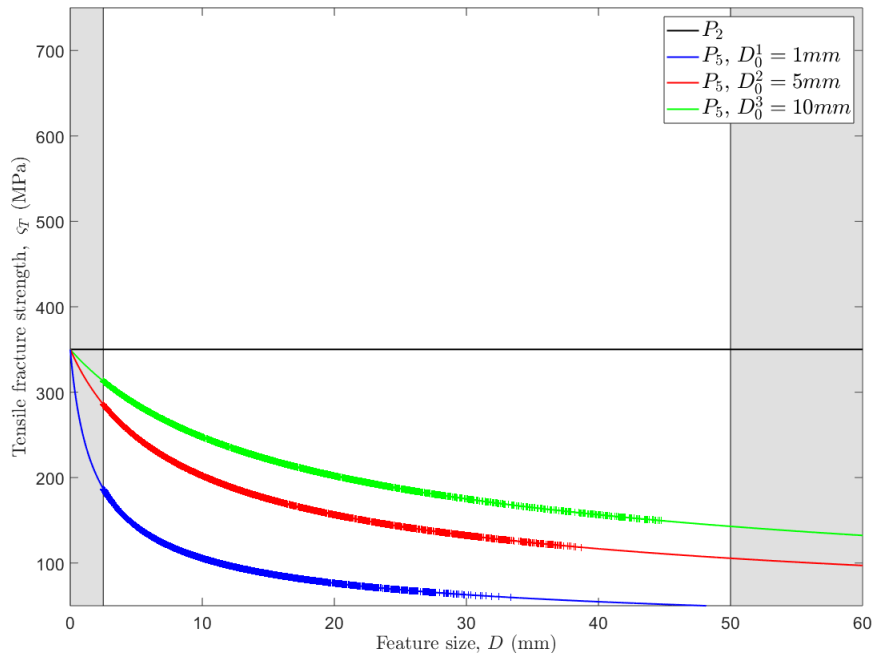
Figure 4.32.   Local tensile strength versus size for $\mathbb{P}_5$ Bažant scaling MBB problems.

on the LEFM-scaling regime. Using the SEL to bridge these asymptotes results in lower structural strengths local to D_0 as illustrated in **Figure 4.32**. Following this interpretation, the lack of structural convergence for any SEL L-bracket cases is to be expected given the tenuous convergence of even the strongest of the LEFM materials on the domain.

(a) $D_0 = 1$ mm, $\kappa = 1$ (b) $D_0 = 5$ mm, $\kappa = 1$ (c) $D_0 = 10$ mm, $\kappa = 1$

(d) $D_0 = 1$ mm, $\kappa = \frac{1}{3}$ (e) $D_0 = 5$ mm, $\kappa = \frac{1}{3}$ (f) $D_0 = 10$ mm, $\kappa = \frac{1}{3}$
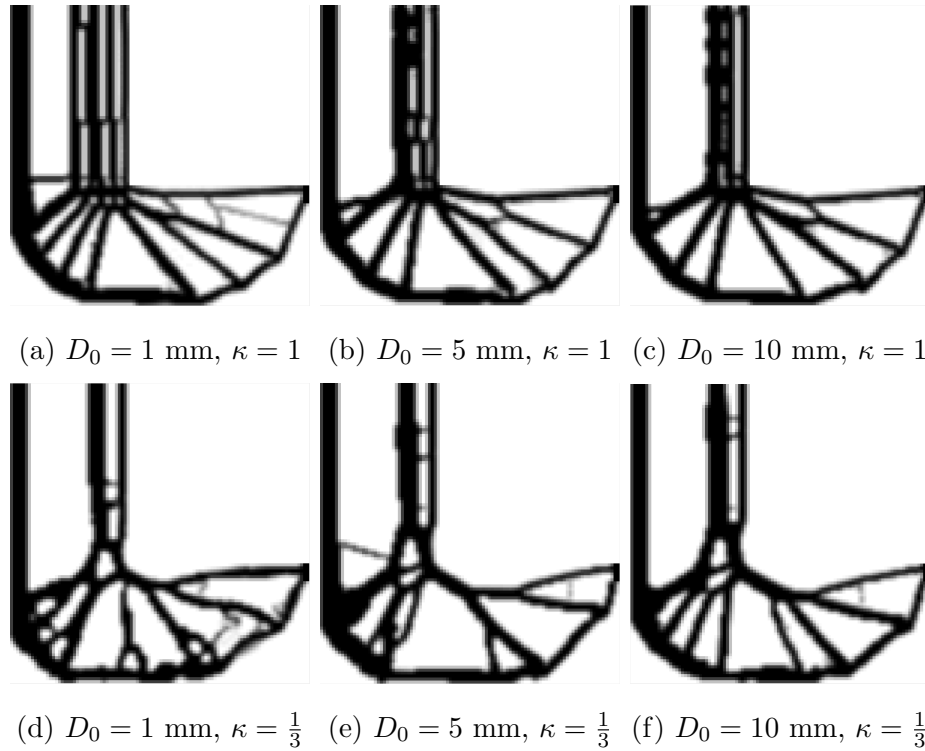
Figure 4.33. Converged structures for Bažant SEL strength and volume constrained strength constrained compliance minimization, $\mathbb{P}_5$, for L-Bracket problem. Effect of intrinsic material length, D_0 and size penalization, κ considered. Filtered density formulation used. $V_0 = 0.4$. $r_{min} = 2$ elements.

(a) $D_0 = 1$ mm, $\kappa = 1$ (b) $D_0 = 5$ mm, $\kappa = 1$ (c) $D_0 = 10$ mm, $\kappa = 1$

(d) $D_0 = 1$ mm, $\kappa = \frac{1}{3}$ (e) $D_0 = 5$ mm, $\kappa = \frac{1}{3}$ (f) $D_0 = 10$ mm, $\kappa = \frac{1}{3}$
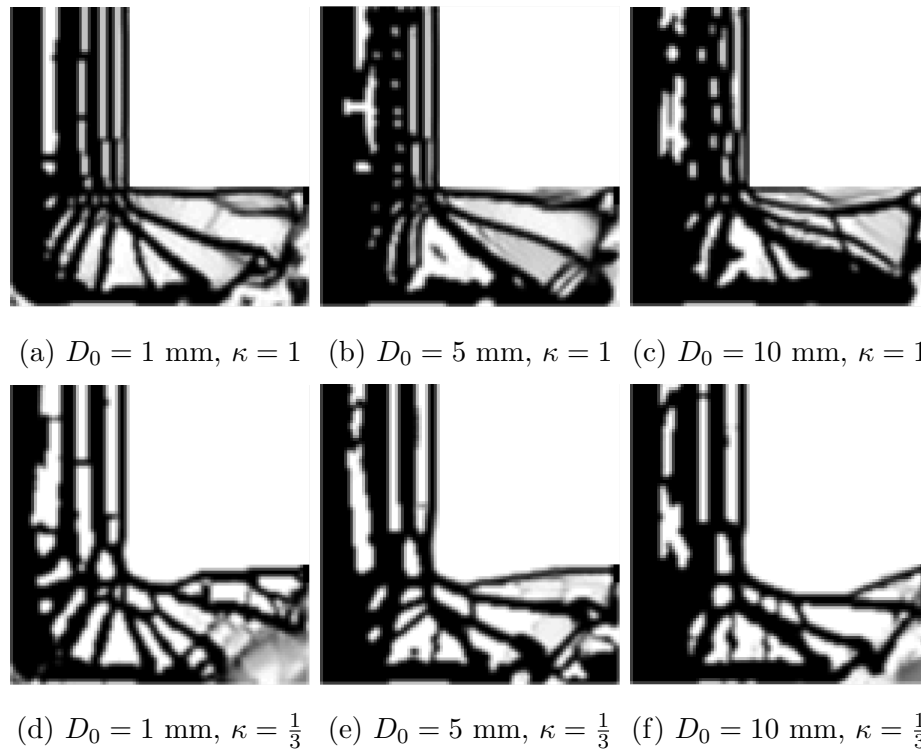
Figure 4.34.   Converged structures Bažant SEL strength constrained volume minimization, $\mathbb{P}_6$, for L-Bracket problem. Effect of intrinsic material length, D_0 and size penalization, κ considered. Filtered density formulation used. $r_{min} = 2$ elements.

The prior cases explored have assumed different materials that can be characterized by the same two failure parameters under certain conditions. The more likely engineering utility of the size-dependent TO formulation will be realized for providing feasible structures across scales for the same size-dependent material. To illustrate the effect of size-dependence for this class of problems, four geometrically similar MBB allowable domains are considered. The physical dimensions of these half-domains span from 3 meters by 1 meter down to 3 mm by 1 mm. Each domain is discretized using a fixed 120 element by 40 element mesh. Member size is implicitly restricted through an applied filter radius of $r_{min} = 2.0$ elements and a size penalization of $\kappa = 1$. This choice of mesh and radius imposes geometric scaling on all features throughout the domain, preventing the development of a more efficient micro-structure for larger physical domains. A SEL characteristic material length of $D_0 = 5$ mm is held constant as a fixed material property across all scales. The applied load considered for the 300 mm by 100 mm half-domain is reduced to 625 N to alleviate convergence issues. This load is then scaled linearly with physical domain geometry to keep the stress state in the initialized MBB domain constant.

Under these conditions, the converged structures for the $\mathbb{P}_6$ formulation are compared to their $\mathbb{P}_3$ size-independent counterparts in **Figure 4.35**. Excepting minor algorithmic effects, the $\mathbb{P}_3$ formulation results illustrate the invariance of the size independent strength constraints for geometrically similar loads and domains. Under the Bažant SEL model of strength in the domain, the converged structures vary from non-convergence to essentially size independent solutions.

In **Figure 4.36** ς_T relative to d_e is plotted for all tensile loaded members in each of the four domains. The separation between the span of local sizes for each domain is clearly apparent as is the trend of local strengths. The domains under tensile loading in the 3 m by 1 m MBB domain exhibit a broad range of ς_T, all significantly penalized relative to the assumed ς_{T_0} following the LEFM asymptote. The discretization of the structure causes the smallest allowable feature size to be an order of magnitude greater than the material length-scale. This results in a broad scatter of member sizes

and severely weakened nominal strength throughout the domain. In contrast, on the other end of the spectrum the members on the 3 mm by 1 mm domain lie on the strength asymptote of the SEL and exhibit roughly $\varsigma_T \approx \varsigma_{T_0}$ throughout the structure. Realized structural features exist two orders of magnitude below the SEL length-scale and failure is constrained through the Christensen generalized yield surface. Features on the 300 mm by 100 mm domain are comparable in scale to the material length-scale and exhibit clear size-dependence. A characteristic lamellar structure limited by the mesh regularization arises in the tension dominated region. The largest structural member sizes occur at nodal locations and remain within an order of magnitude of the material length-scale. No clear conclusions can be drawn by comparing the 30 mm by 10 mm result to the remaining cases. Some degree of size-dependence appears to manifest, but it is not clear if this is algorithmic or mechanistic in nature.

(a) $\mathbb{P}_3$, 3000 mm ×1000 mm, $P = 12500$ N

(b) $\mathbb{P}_6$, 3000 mm ×1000 mm, $P = 12500$ N

(c) $\mathbb{P}_3$, 300 mm ×100 mm, $P = 1250$ N

(d) $\mathbb{P}_6$, 300 mm ×100 mm, $P = 1250$ N

(e) $\mathbb{P}_3$, 30 mm ×10 mm, $P = 125$ N

(f) $\mathbb{P}_6$, 30 mm ×10 mm, $P = 125$ N

(g) $\mathbb{P}_3$, 3 mm ×1 mm, $P = 12.5$ N

(h) $\mathbb{P}_6$, 3 mm ×1 mm, $P = 12.5$ N
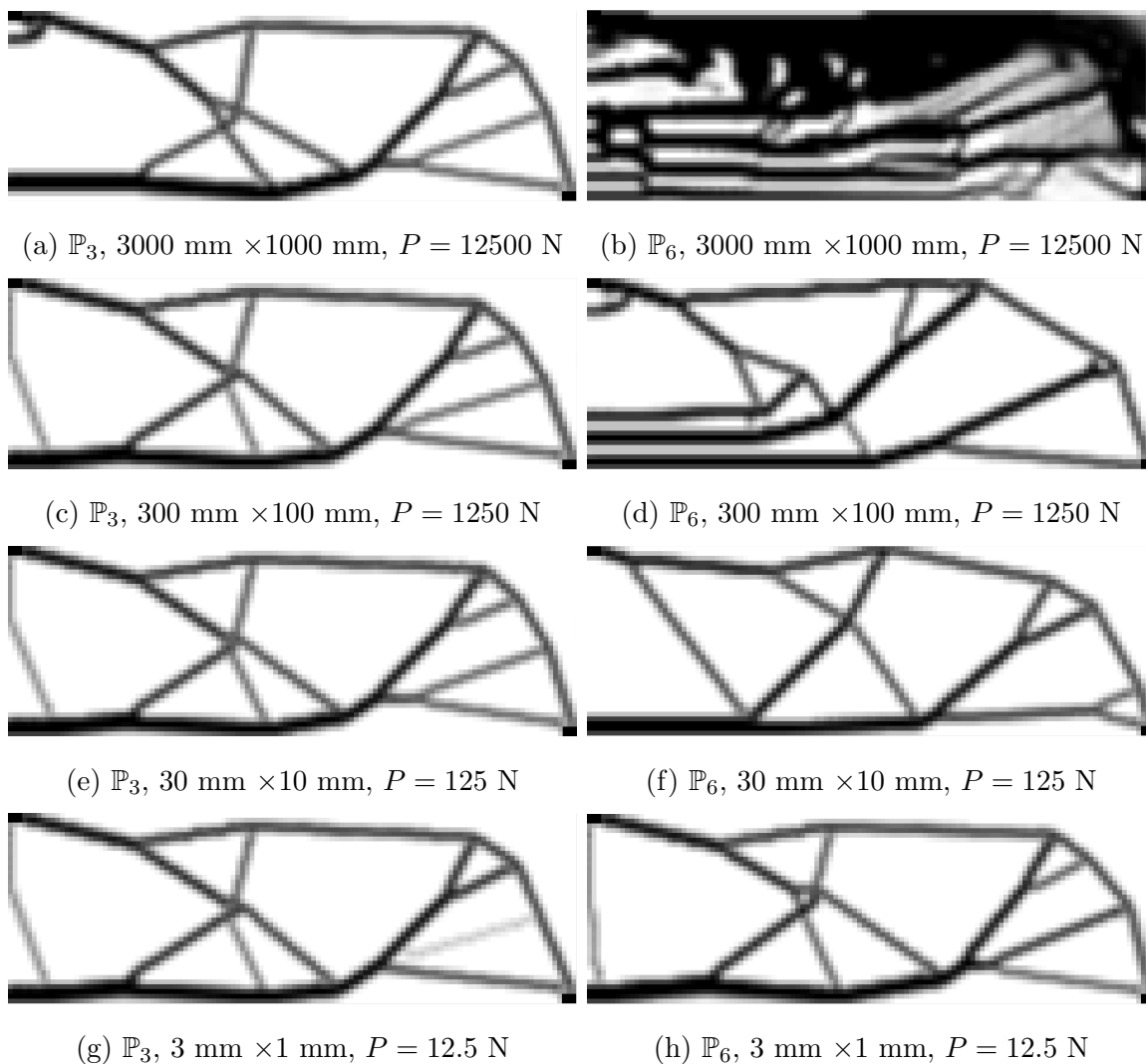
Figure 4.35. Converged structures for the Bažant SEL strength constrained volume minimization, $\mathbb{P}_6$, for the MBB problem. Filtered density formulation used. Physical domain and applied load scaled proportionally. Fixed mesh of 120 elements by 40 elements. $r_{min} = 2$ elements. $D_0 = 5$ mm.
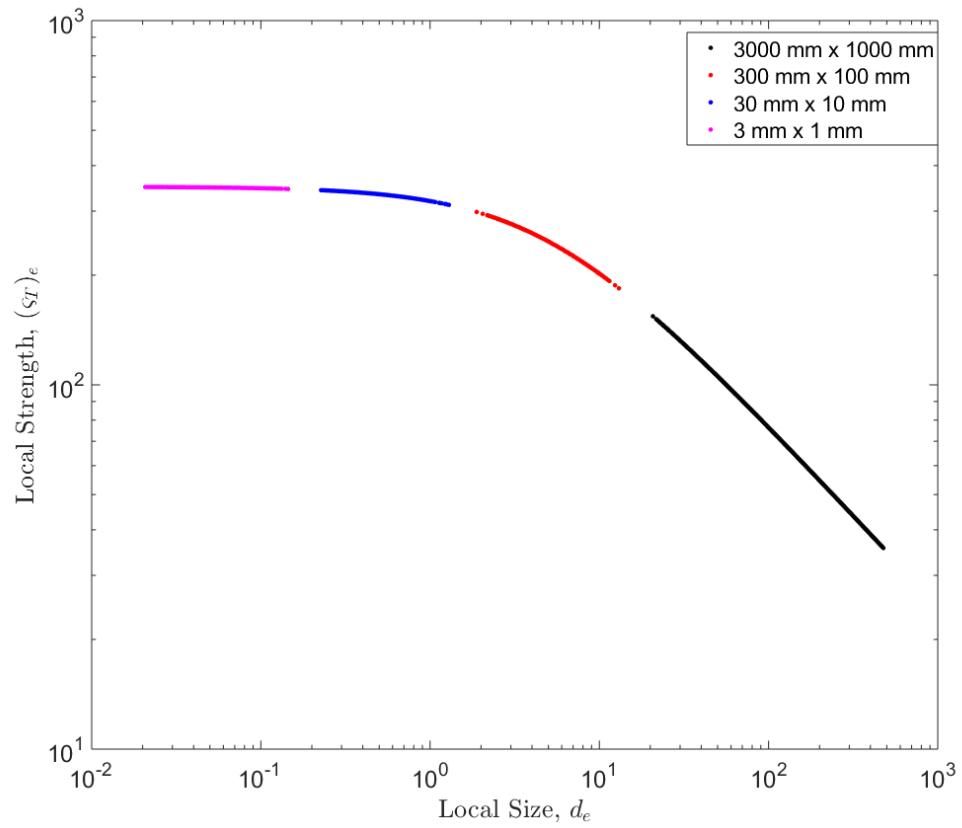
Figure 4.36. Local strength versus member size plotted across domain scaling structures illustrated in **Figure 4.35**.

4.5.4 Bažant Type II Size Effect Law mesh resolution study

The question of the effect of geometric restriction is of particular relevance to all size-dependent material failure models and is explored here for the SEL-based $\mathbb{P}_6$ problem. Typically, it is desirable to regularize the allowable domain to provide the ability to discretize the mesh for FE accuracy purposes while maintaining some form of geometric scale. For size dependent problems this regularization acts as a restriction on the convergence to efficient thin members that allow for higher ς_T values. Removing this regularization opens up the design space and allows for the evolution of new scale-dependent toplogies. This effect is illustrated in **Figure 4.37** for the MBB domain with the same 300 mm by 100 mm allowable domain. Once again, a reduced half-domain load of 625 N is applied in light of prior convergence issues. For this problem, a material length scale of $D_0 = 5$ mm is assumed for all cases. To illustrate the effects scale-dependence in the regularization, the domain is broken down into successively finer meshes with discretizations of 120 elements $\times$ 40 elements, 240 elements $\times$ 80 elements, and 360 elements $\times$ 120 elements. An attempt is made to balance the number of elements in each cluster for its respective discretization. Four, ten and ten stress clusters are used. Only ten clusters are used for the 360 elements $\times$ 120 elements case due to the extreme cost of the adjoint-sensitivity analysis for additional stress clusters.

The results shown illustrate an increasing structural complexity corresponding to finer FE meshes. For the coarsest mesh, the central tension-dominated region assumes a simple lamellar structure and quickly separates along principal stress lines. This effect is somewhat complicated for the coarse mesh with $\kappa = \frac{1}{3}$ due to the forced separation of dense structures.

Doubling the discretization extends the lamellar structure throughout the main tension load path and allows for the generation of pronounced cellular structures in the tensile region. These structures likely result from the need to carry shear between the lamella and indicate that under relaxed enough restriction the intermediate shear

(a) 4,800 elements, $\kappa = 1$ (b) 4,800 elements, $\kappa = \frac{1}{3}$

(c) 19,200 elements, $\kappa = 1$ (d) 19,200 elements, $\kappa = \frac{1}{3}$

(e) 43,200 elements, $\kappa = 1$ (f) 43,200 elements, $\kappa = \frac{1}{3}$
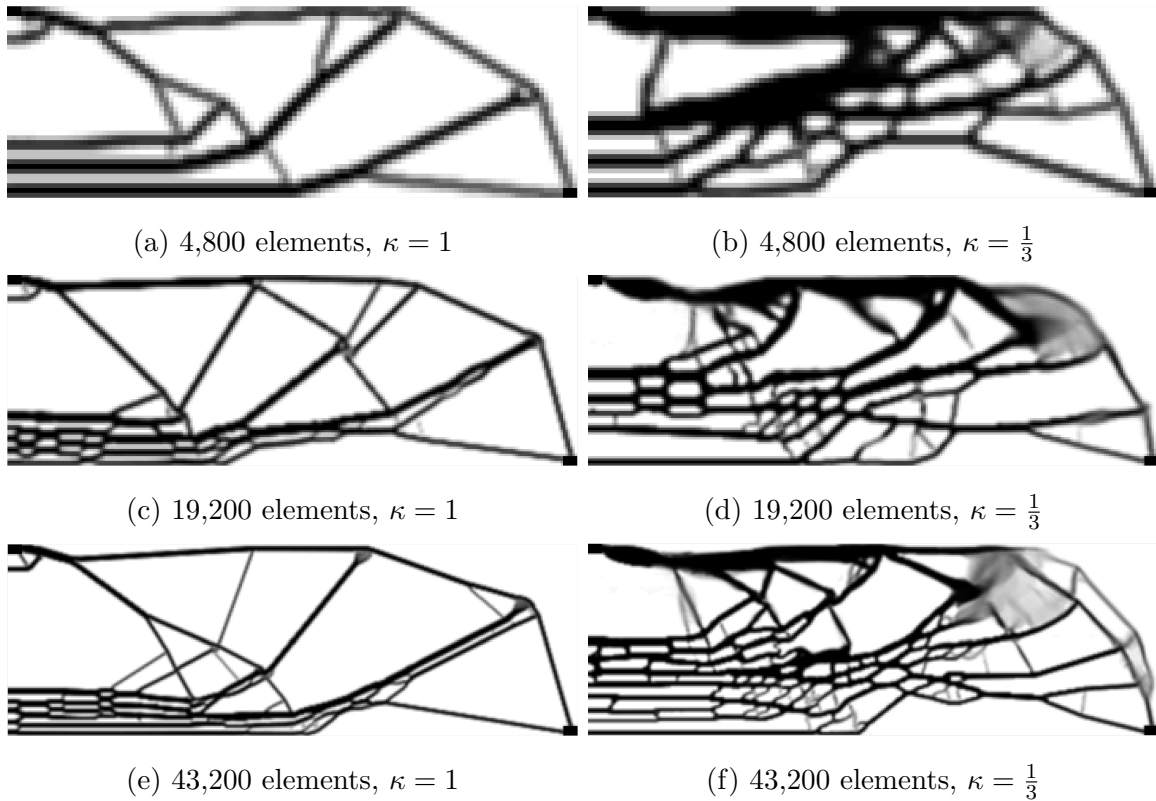
Figure 4.37. Converged structures for the Bažant SEL strength constrained volume minimization, $\mathbb{P}_6$, for the MBB problem. Filtered density formulation used. Physical domain fixed at 300 mm × 100 mm and mesh density varied. $r_{min} = 1.5$ elements, $D_0 = 5$ mm, $P = 1250$ N.

transfer regions seen previously may cease to exist. Increasing the discretization even further seems to confirm this hypothesis with more distinct lamellar and cellular structures emerging. The results for highly discretized structures with $\kappa = \frac{1}{3}$ are significantly more complex. Dense, shear transfer structures occur readily in the domain to transfer loads between the separated spaced out lamella. The separation of tensile lamella results in structures which fail to carry sufficient tensile strain energy, inhibiting qualitative structural convergence.

To further illustrate the effect of regularization driven geometric restriction, $\frac{\sigma_I}{\varsigma_T}$ versus d_e is plotted for the tension loaded members in all six cases shown in **4.37**. These plots are given in **Figure 4.38**. Coarse meshes result in a wide distribution of structural members with a mean feature size greater than the material D_0. Reducing

the element size tightens the distribution and shifts the structural members further up the the SEL strength asymptote. Comparing the form of the local size density penalization, for $\kappa = \frac{1}{3}$ the distribution is shifted towards larger features. Furthermore, a pronounced inefficient structural domain tail with lightly stressed large features arises for all cases and is especially distinct in **Figure 4.38 (f)**. This tail is likely an artifact of the poor structural convergence observed.

Key performance parameters are given for the $\kappa = 1$ penalization cases in **Table 4.4**. All three domains exhibit reasonable practical convergence as illustrated by the final KKT value. However, the highly complex feasible design space results in the two finer discretizations terminating through time-out. This table illustrates the immense computational cost associated with finer meshes, increasing 27 times the run duration for an increase of 10 times the number of elements. Of note, this run time is largely driven by the increased cost of the adjoint calculation of the stress sensitivity and need to assemble the adjoint stiffness matrix for each stress cluster, not by the calculation of the local size measure.

In addition, this table illustrates the motivation for relaxing the regularization restriction for size-dependent problems. Solely through allowing for smaller structural features to emerge, the converged volume of the structure is reduced by 8%. Prior results had indicated the necessity of the size-dependence of strength for structural robustness. The demonstrated reduction in structural mass indicates considerable design benefit can be obtained through taking advantage of the strength-limited domain for quasi-brittle materials. The finer discretizations shown begin to illustrate the advantages this framework may have in designing these material systems across material scales.

Table 4.4. Converged parameters $\mathbb{P}_6$ SEL-scaling mesh density study with $\kappa = 1$.

Domain Size	Iterations	KKT Norm	Execution Time (sec.)	Converged Volume (%)
120×40	1172	0.0024	7254.58	26.56
240×80	1500	0.0058	44435.80	21.41
360×120	1500	0.0087	195848.11	18.26
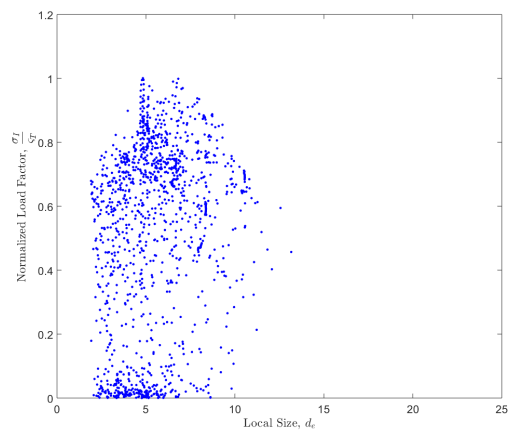
(a) $\kappa = 1$; 4,800 elements
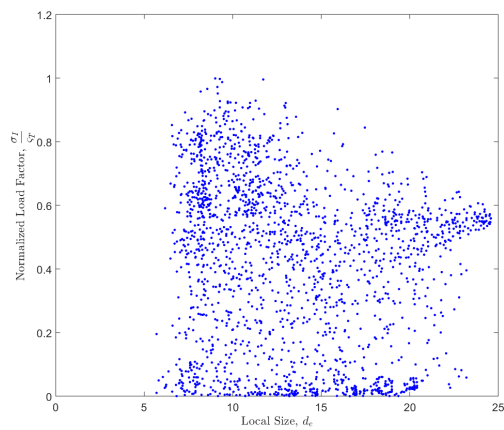
(b) $\kappa = \frac{1}{3}$; 4,800 elements
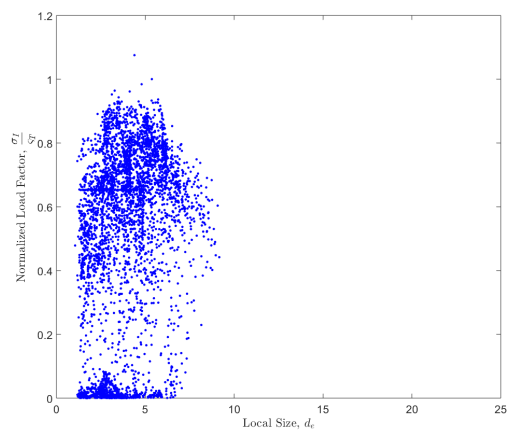
(c) $\kappa = 1$; 19,200 elements
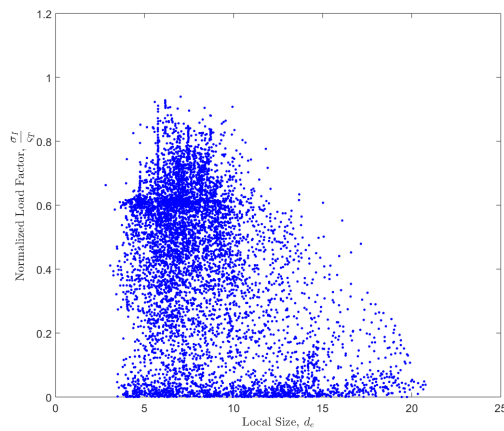
(d) $\kappa = \frac{1}{3}$; 19,200 elements
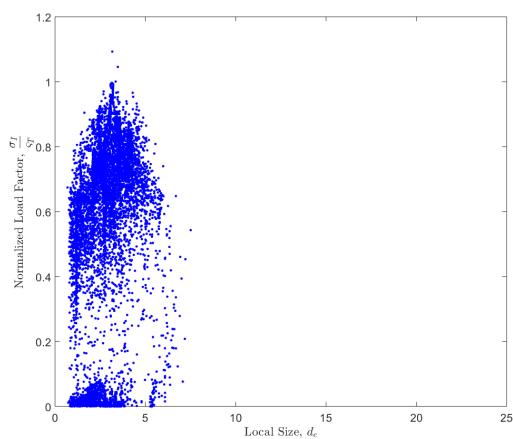
(e) $\kappa = 1$; 43,200 elements
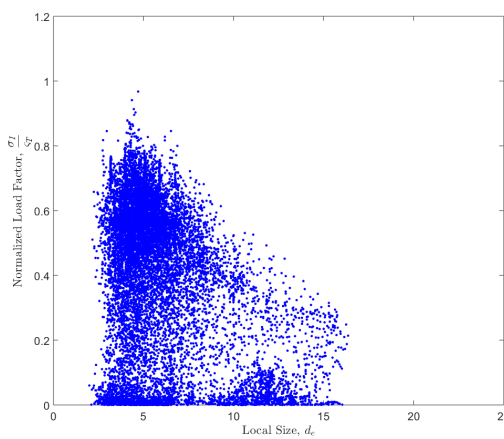
(f) $\kappa = \frac{1}{3}$; 43,200 elements

Figure 4.38. Load factor distribution versus member size for various mesh densities shown in **Figure 4.37**.

4.6 Fracture mechanics-based size-dependence

4.6.1 Fixed flaw size - Single Edge Notch Tension

Reversing the direction of the size-effect scaling, the fixed flaw models of failure exhibit greater strength with larger feature sizes. Using this framework, the $\mathbb{P}_5$ and $\mathbb{P}_6$ problems with SENT-based fixed flaw scaling are presented for the MBB test problem in **Figures 4.39** and **4.40**, respectively. Unlike traditional models of brittle size scaling, the converged structures assuming SENT-based scaling exhibit less clear trends.

First comparing the effect of the size-measure density penalization, it is clear that it is highly desirable to penalize intermediate densities for this class of problems. On the assumed domain, $a_0 \geq 2.5$ mm exceeds the local dimensions of a single element. For assumed flaws smaller than the element dimensions and $\kappa = 1$, good structural convergence is observed and the scaling law exhibits a consistent removal of thin tensile features. Exceeding this threshold results in non-convergence and significant regions of intermediate density local to tensile portions of the domain. Some portion of these gray regions occurs due to the interaction of the SENT-dependence and the elemental deactivation scheme. These results demonstrate a significant barrier to densification for formulations with large assumed cracks and a direct size-measure interpretation of the filtered density.

Increasing the local size measure penalization removes this issue from the $\mathbb{P}_5$ problem for all studied parameters and relegates it to only effecting the $a_0 = 5.0$ mm condition for the $\mathbb{P}_6$ condition. This penalization also drives the domain to the interesting result seen for the $a_0 = 5.0$ mm case of the $\mathbb{P}_6$ formulation shown in **Figure 4.39 (j)**. This structure is dominated by a large tension and compression member configured roughly like a roof truss. Limited cross-braces arise to transfer shear in the core of the beam. All tensile cross-braces including the filtered region are at least twice as thick as the assumed flaw size. This structure demonstrates a considerable shift towards a compression and bending dominated result.

This result illustrates the shortcoming of the proposed empirically based fracture model TO implementation. The specified fracture model only explicitly incorporates empirical relations for axially loaded tension members. The resulting structure contains a large, bending dominated bottom member. To account for the effects of eccentric or moment loading on this feature, relevant empirical models must be incorporated through additional fracture cutoff constraints. This approach can either be done through successive optimization problems on the existing converged results or through a mixed formulation on the original initialized domain. Either approach brings significant costs in implementation and computation.

(a) $a_0 = 0.25$ mm, $\kappa = 1$ (b) $a_0 = 0.25$ mm, $\kappa = \frac{1}{3}$

(c) $a_0 = 0.625$ mm, $\kappa = 1$ (d) $a_0 = 0.625$ mm, $\kappa = \frac{1}{3}$

(e) $a_0 = 1.25$ mm, $\kappa = 1$ (f) $a_0 = 1.25$ mm, $\kappa = \frac{1}{3}$

(g) $a_0 = 2.50$ mm, $\kappa = 1$ (h) $a_0 = 2.50$ mm, $\kappa = \frac{1}{3}$

(i) $a_0 = 5.00$ mm, $\kappa = 1$ (j) $a_0 = 5.00$ mm, $\kappa = \frac{1}{3}$
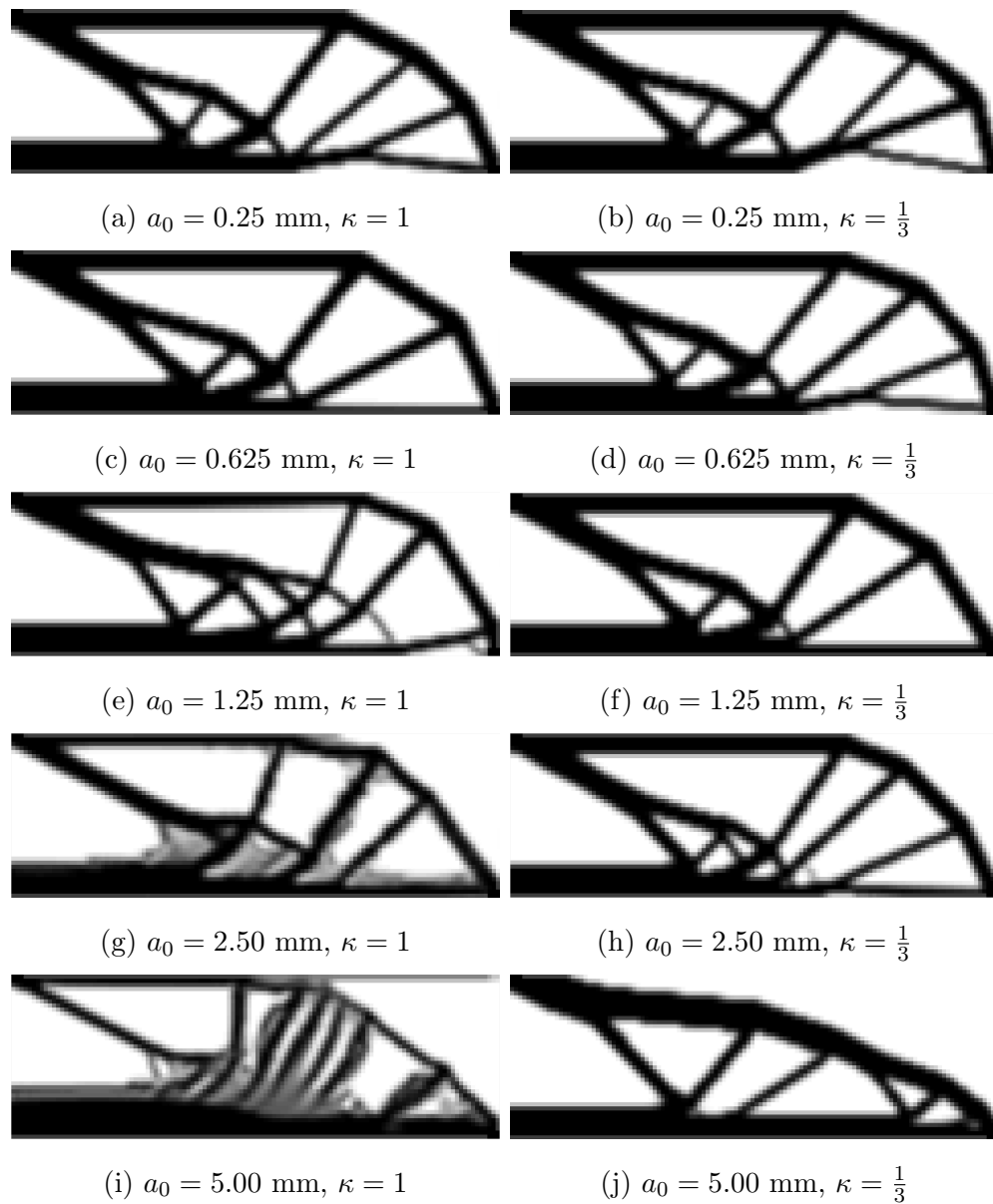
Figure 4.39. Converged structures for the SENT strength and volume constrained compliance minimization, $\mathbb{P}_5$, for the MBB problem. Effect of assumed flaw size, a_0 and size penalization, κ considered. Filtered density formulation used. $r_{min} = 2$ elements. $\overline{V} = 0.4$.

(a) $a_0 = 0.25$ mm, $\kappa = 1$

(b) $a_0 = 0.25$ mm, $\kappa = \frac{1}{3}$

(c) $a_0 = 0.625$ mm, $\kappa = 1$

(d) $a_0 = 0.625$ mm, $\kappa = \frac{1}{3}$

(e) $a_0 = 1.25$ mm, $\kappa = 1$

(f) $a_0 = 1.25$ mm, $\kappa = \frac{1}{3}$

(g) $a_0 = 2.50$ mm, $\kappa = 1$

(h) $a_0 = 2.50$ mm, $\kappa = \frac{1}{3}$

(i) $a_0 = 5.00$ mm, $\kappa = 1$

(j) $a_0 = 5.00$ mm, $\kappa = \frac{1}{3}$
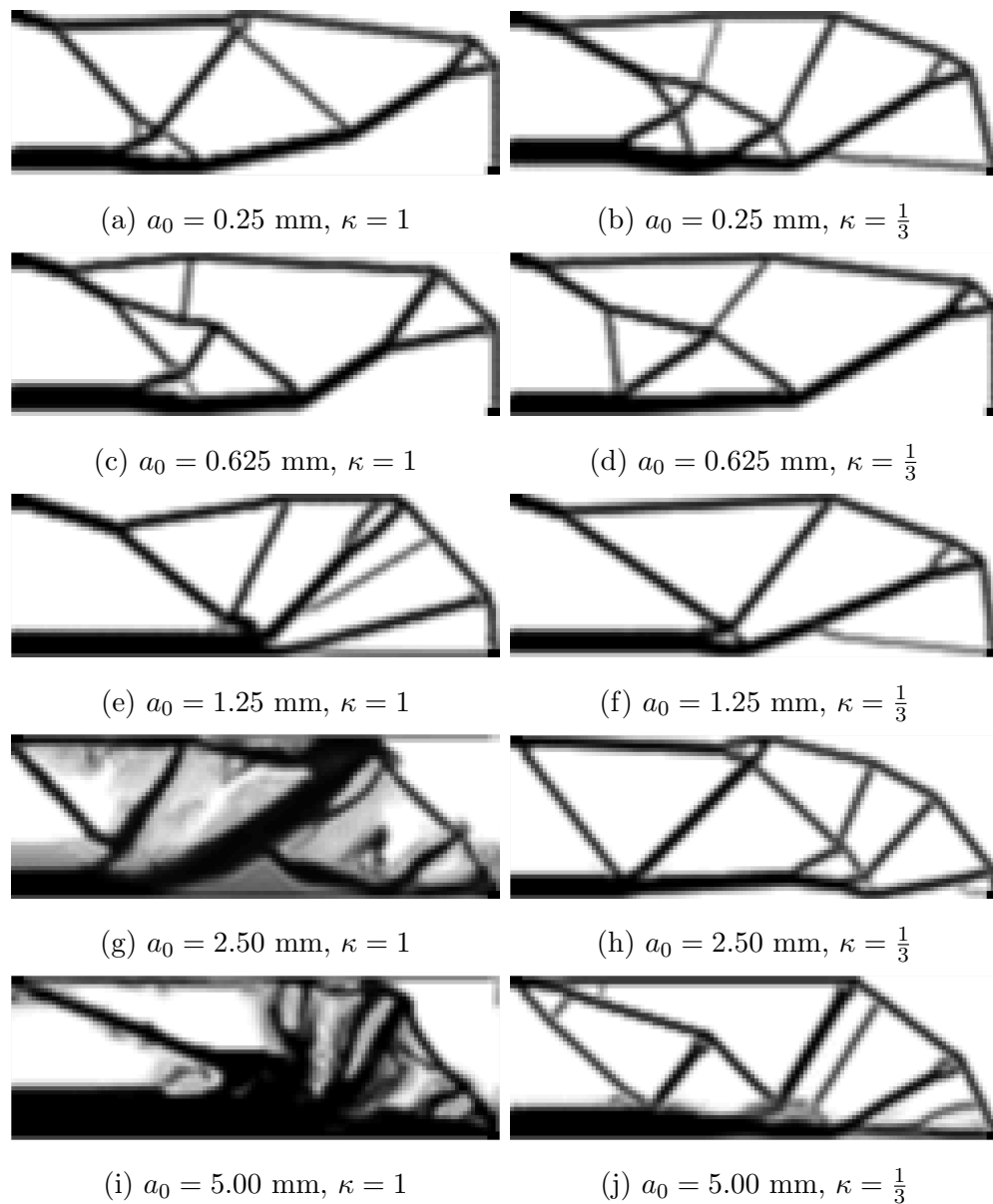
Figure 4.40. Converged structures for the SENT strength constrained compliance minimization, $\mathbb{P}_6$, for the MBB problem. Effect of assumed flaw size, a_0 and size penalization, κ considered. Filtered density formulation used. $r_{min} = 2$ elements.

Results for the SENT-based, $\mathbb{P}_5$ and $\mathbb{P}_6$ problems for the L-bracket domain in **Figures 4.41** and **4.42**. The results illustrate minimuml conclusive results under the SENT-based strength model, with the exception of the non-convergence of the $\kappa = 1$ penalized large flaw domains. Crucially, the proposed SENT-scaling does not remove the rounding of the converged structure local to the domain-imposed stress-riser.

(a) $a_0 = 0.2$ mm, $\kappa = 1$

(b) $a_0 = 0.2$ mm, $\kappa = \frac{1}{3}$

(c) $a_0 = 0.5$ mm, $\kappa = 1$

(d) $a_0 = 0.5$ mm, $\kappa = \frac{1}{3}$

(e) $a_0 = 1.0$ mm, $\kappa = 1$

(f) $a_0 = 1.0$ mm, $\kappa = \frac{1}{3}$

(g) $a_0 = 2.0$ mm, $\kappa = 1$

(h) $a_0 = 2.0$ mm, $\kappa = \frac{1}{3}$

(i) $a_0 = 4.0$ mm, $\kappa = 1$

(j) $a_0 = 4.0$ mm, $\kappa = \frac{1}{3}$
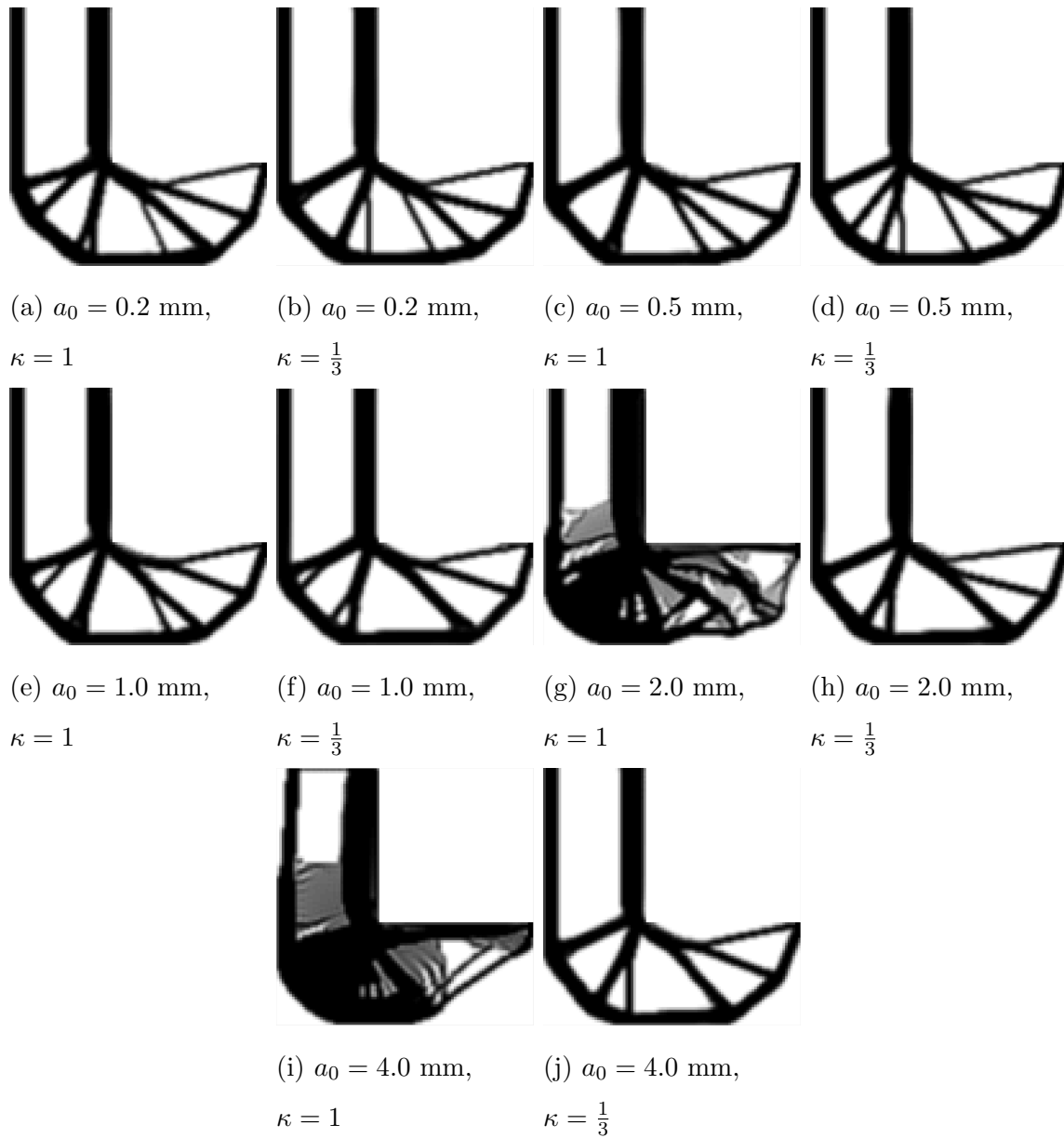
Figure 4.41. Converged structures for the SENT volume and strength constrained compliance minimization, $\mathbb{P}_5$, for the L-Bracket problem. Effect of assumed flaw size, a_0 and size penalization, κ considered. $r_{min} = 2$ elements. $\overline{V} = 0.4$

(a) $a_0 = 0.2$ mm, $\kappa = 1$

(b) $a_0 = 0.2$ mm, $\kappa = \frac{1}{3}$

(c) $a_0 = 0.5$ mm, $\kappa = 1$

(d) $a_0 = 0.5$ mm, $\kappa = \frac{1}{3}$

(e) $a_0 = 1.0$ mm, $\kappa = 1$

(f) $a_0 = 1.0$ mm, $\kappa = \frac{1}{3}$

(g) $a_0 = 2.0$ mm, $\kappa = 1$

(h) $a_0 = 2.0$ mm, $\kappa = \frac{1}{3}$

(i) $a_0 = 4.0$ mm, $\kappa = 1$

(j) $a_0 = 4.0$ mm, $\kappa = \frac{1}{3}$
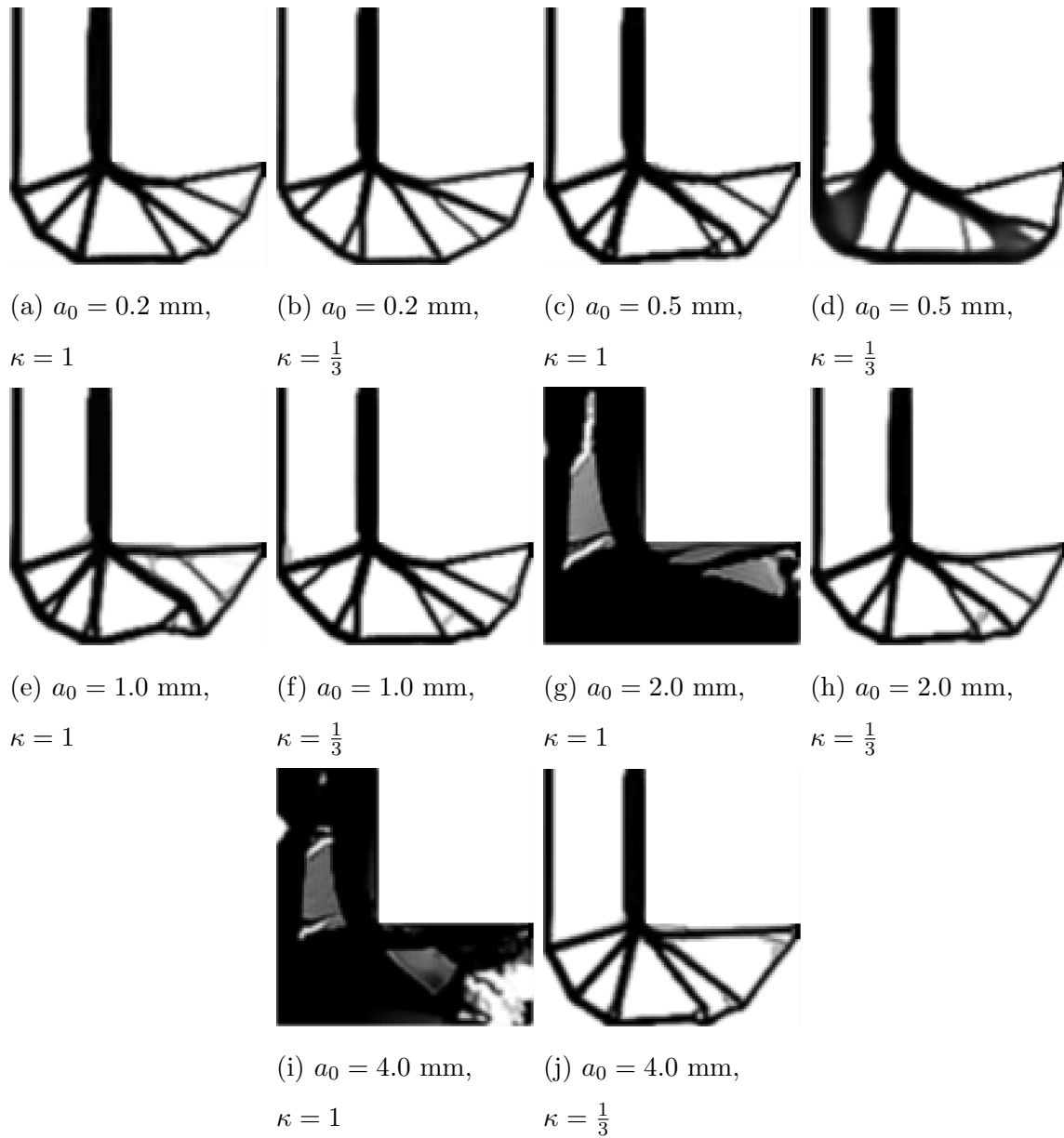
Figure 4.42. Converged structures for the SENT strength constrained volume minimization, $\mathbb{P}_6$, for the L-Bracket problem. Effect of assumed flaw size, a_0 and size penalization, κ considered. Filtered density formulation used. $r_{min} = 2$ elements.

4.6.2 Fixed flaw size - Double Edge Notch Tension

As expected, results for the DENT-based flaw model illustrate the relatively limited scaling effect illustrated in **Figure 3.6**. For flaw sizes smaller than the one half of the element size, the converged structure is independent of the DENT fracture model. However, beginning with the $a_0 = 1.25$ mm cases minor effects are observed. Tensile load carrying members with width less than two times the flaw size are removed from the structural domain. A minimum number of intermediate density tensile members that fail to meet this criteria persist such as those seen in **Figure 4.43 (g)** and **Figure 4.44 (e)** and **(f)**. Upon removing the compliance objective, DENT-constrained structures become dominated by a single, thicker tensile load path connected to a compression dominated chain of members. Tensile load transfer from the supports is cut off due to the combination of relatively low stress in members local to the support and negligible strength of thin members. Non-convergence issues with intermediate density re-emerge for the large flaw, $\kappa = 1$ cases of the $\mathbb{P}_6$ problem. This confirms that the $\kappa = 1$ penalization is largely unsuitable for the smaller-is-weaker fixed flaw size strength-scaling.

The results for DENT-scaling on the L-bracket domain are shown in **Figures 4.45** and **4.46**. On the whole, these results illustrate a similar exclusion of thin tensile members from the domain. Notably, a consistent pattern of poor structural convergence is absent, though numerous domains terminate prematurely under the previously described formal convergence criteria.

(a) $a_0 = 0.25$ mm, $\kappa = 1$

(b) $a_0 = 0.25$ mm, $\kappa = \frac{1}{3}$

(c) $a_0 = 0.625$ mm, $\kappa = 1$

(d) $a_0 = 0.625$ mm, $\kappa = \frac{1}{3}$

(e) $a_0 = 1.25$ mm, $\kappa = 1$

(f) $a_0 = 1.25$ mm, $\kappa = \frac{1}{3}$

(g) $a_0 = 2.50$ mm, $\kappa = 1$

(h) $a_0 = 2.50$ mm, $\kappa = \frac{1}{3}$

(i) $a_0 = 5.00$ mm, $\kappa = 1$

(j) $a_0 = 5.00$ mm, $\kappa = \frac{1}{3}$
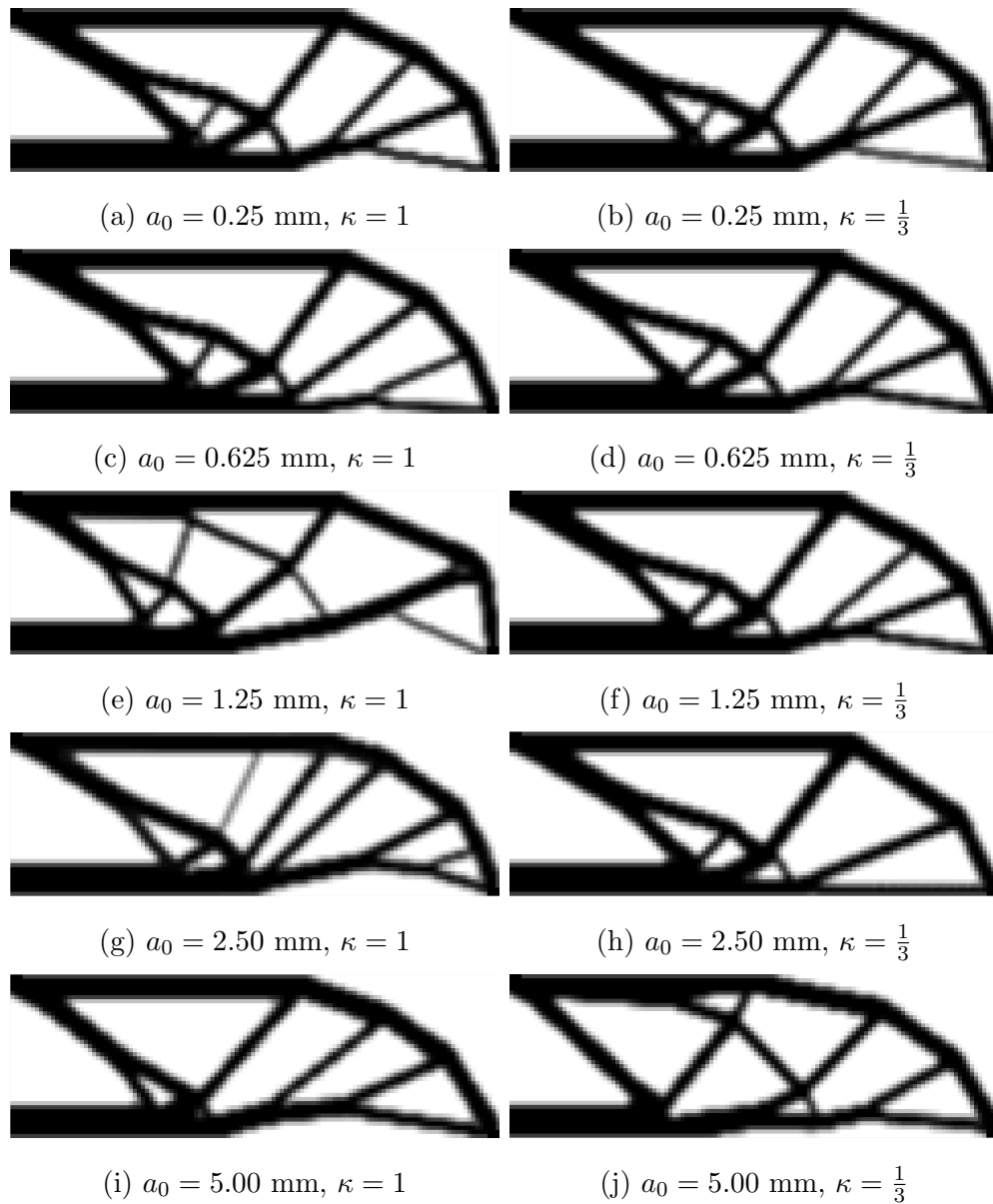
Figure 4.43. Converged structures for the DENT strength and volume constrained compliance minimization, $\mathbb{P}_5$, for the MBB problem. Effect of assumed flaw size, a_0 and size penalization, κ considered. Filtered density formulation used. $r_{min} = 2$ elements. $\overline{V} = 0.4$

(a) $a_0 = 0.25$ mm, $\kappa = 1$

(b) $a_0 = 0.25$ mm, $\kappa = \frac{1}{3}$

(c) $a_0 = 0.625$ mm, $\kappa = 1$

(d) $a_0 = 0.625$ mm, $\kappa = \frac{1}{3}$

(e) $a_0 = 1.25$ mm, $\kappa = 1$

(f) $a_0 = 1.25$ mm, $\kappa = \frac{1}{3}$

(g) $a_0 = 2.50$ mm, $\kappa = 1$

(h) $a_0 = 2.50$ mm, $\kappa = \frac{1}{3}$

(i) $a_0 = 5.00$ mm, $\kappa = 1$

(j) $a_0 = 5.00$ mm, $\kappa = \frac{1}{3}$
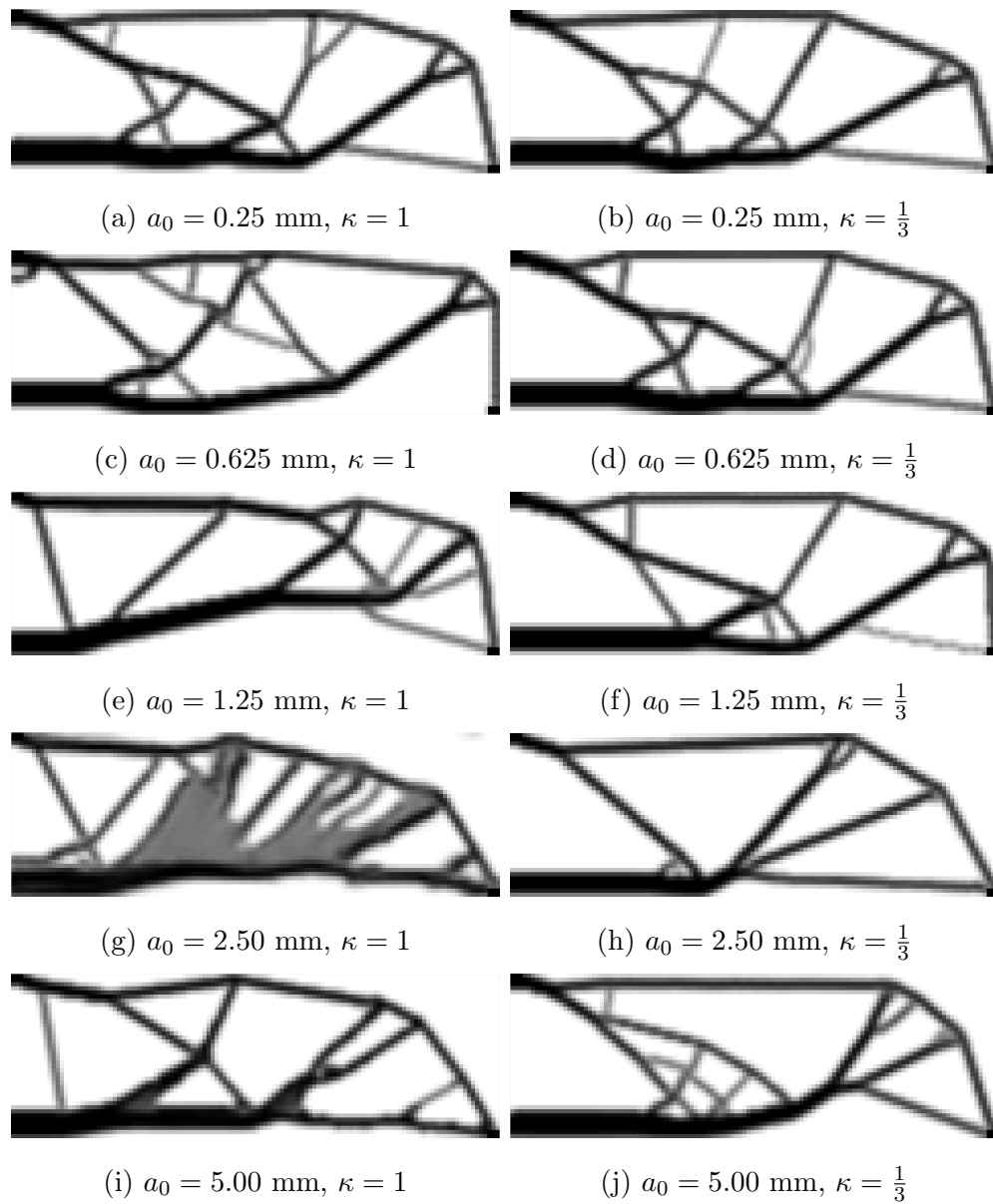
Figure 4.44. Converged structures for the DENT strength constrained volume minimization, $\mathbb{P}_6$, for the MBB problem. Effect of assumed flaw size, a_0 and size penalization, κ considered. Filtered density formulation used. $r_{min} = 2$ elements.

(a) $a_0 = 0.2$ mm, $\kappa = 1$

(b) $a_0 = 0.2$ mm, $\kappa = \frac{1}{3}$

(c) $a_0 = 0.5$ mm, $\kappa = 1$

(d) $a_0 = 0.5$ mm, $\kappa = \frac{1}{3}$

(e) $a_0 = 1.0$ mm, $\kappa = 1$

(f) $a_0 = 1.0$ mm, $\kappa = \frac{1}{3}$

(g) $a_0 = 2.0$ mm, $\kappa = 1$

(h) $a_0 = 2.0$ mm, $\kappa = \frac{1}{3}$

(i) $a_0 = 4.0$ mm, $\kappa = 1$

(j) $a_0 = 4.0$ mm, $\kappa = \frac{1}{3}$
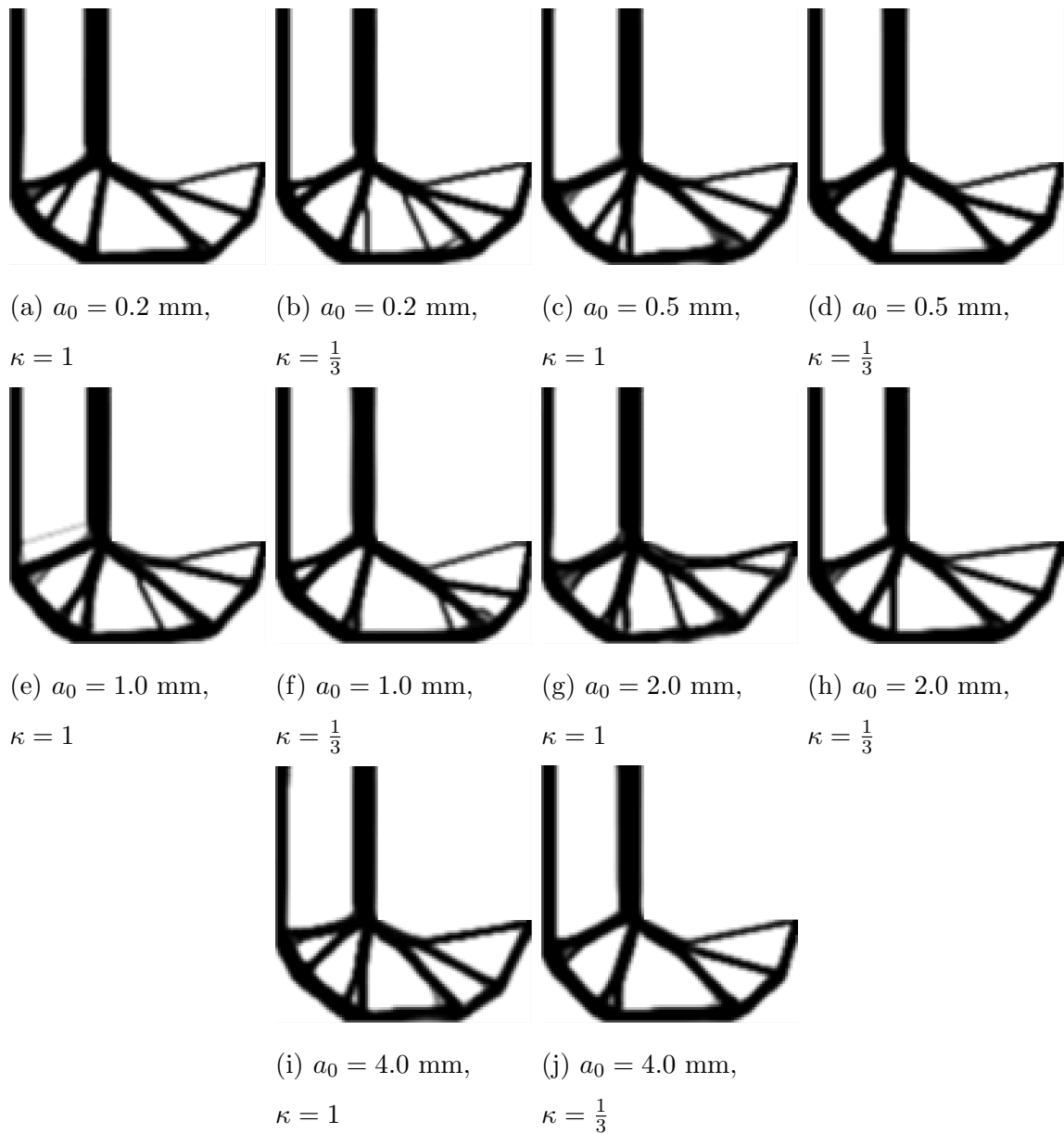
Figure 4.45. Converged structures for the DENT volume and strength constrained compliance minimization, $\mathbb{P}_5$, for the L-Bracket problem. Effect of assumed flaw size, a_0 and size penalization, κ considered. Filtered density formulation used. $r_{min} = 2$ elements. $\overline{V} = 0.4$

(a) $a_0 = 0.2$ mm, $\kappa = 1$

(b) $a_0 = 0.2$ mm, $\kappa = \frac{1}{3}$

(c) $a_0 = 0.5$ mm, $\kappa = 1$

(d) $a_0 = 0.5$ mm, $\kappa = \frac{1}{3}$

(e) $a_0 = 1.0$ mm, $\kappa = 1$

(f) $a_0 = 1.0$ mm, $\kappa = \frac{1}{3}$

(g) $a_0 = 2.0$ mm, $\kappa = 1$

(h) $a_0 = 2.0$ mm, $\kappa = \frac{1}{3}$

(i) $a_0 = 4.0$ mm, $\kappa = 1$

(j) $a_0 = 4.0$ mm, $\kappa = \frac{1}{3}$
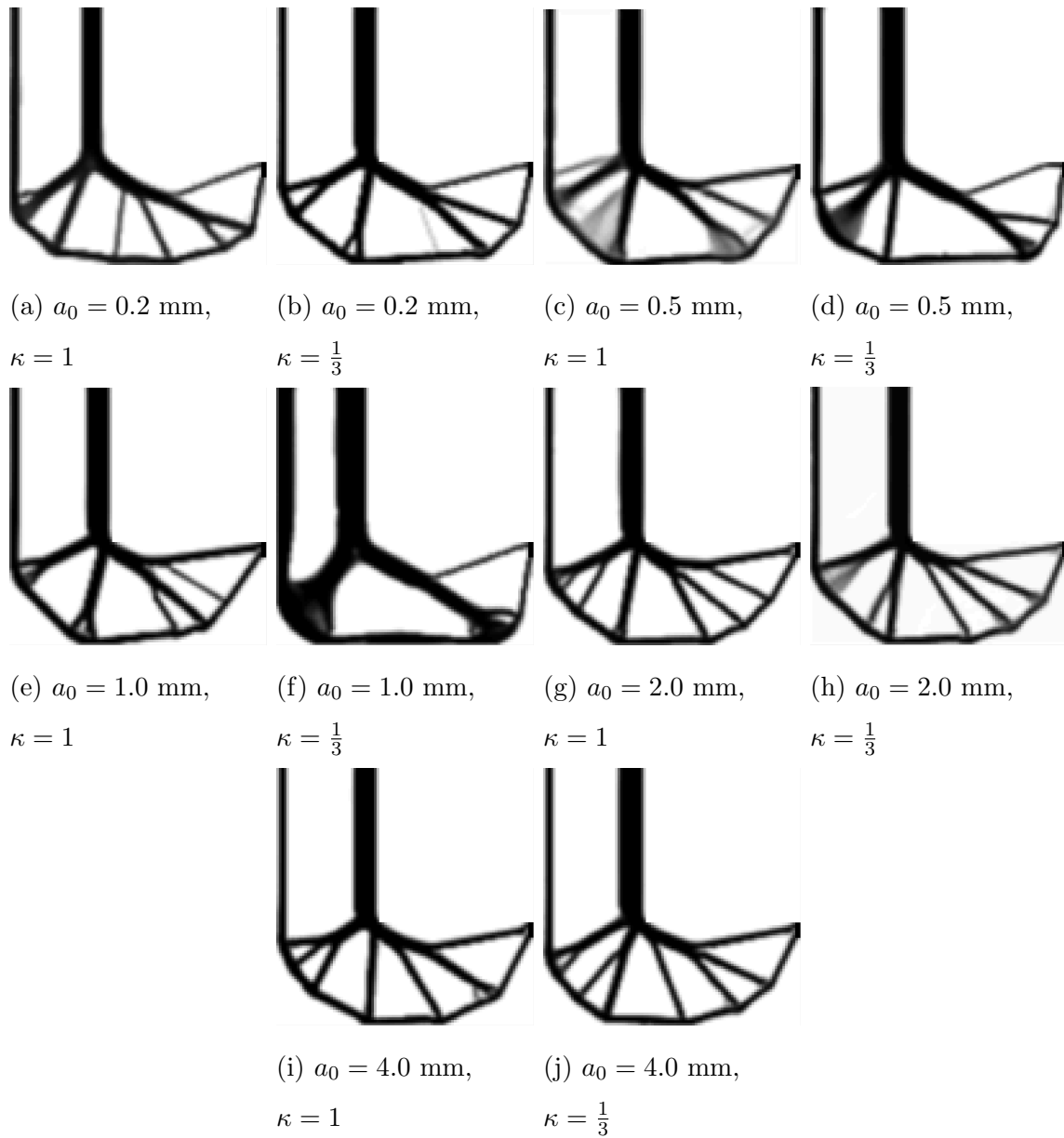
Figure 4.46. Converged structures for the DENT strength constrained volume minimization, $\mathbb{P}_6$, for the L-Bracket problem. Effect of assumed flaw size, a_0 and size penalization, κ considered. Filtered density formulation used. $r_{min} = 2$ elements.

4.7 Effect of move-limits

While the prior sections have explored the effects of the mechanics approximations on the converged structures, the performance for key parameters of the optimization algorithm must be considered as well. The most critical parameter within the MMA algorithm takes the form of the search direction move limits. Due to the dense population of local minimum and maxima in the feasible design space, TO approaches suffer from convergence issues to the true optimal solution. By introducing additional mechanical complexity, it is likely these issues will be exacerbated. To verify this assumption, the results presented in this section consider the novel formulations presented in this thesis with four levels of MMA move-limits ranging from conservative to aggressive. All problems in this section consider the MBB problem domain initially discussed in **Section 4.2.1**. The same size-independent material and structural parameters are utilized with the exception of an applied half-domain load of 625 N to allow convergence for weak material formulations. The remainder of the MMA algorithm parameters as well as the convergence criteria for the problem remain unchanged.

For the size-independent Christensen $\mathbb{P}_3$ formulation with $\alpha = 1$, results for the move-limit effects are shown in **Figure 4.47**. A marked change in topology is observed for the most conservative $move = 0.05$ search strategy, though a limited improvement in volume savings is shown. The remaining aggressive approaches result in nearly identical qualitative and quantitative performance.

Referring to **Figure 4.48** the KKT-Residual for each case in **Figure 4.47** is plotted at each iteration. This plot illustrates a relatively stable convergence within 700 iterations to the final structure for each move limit parameter. However, for the $move = 0.10$ case the algorithm fails to satisfy either the KKT or change tolerances required to stop prior to timeout of the algorithm. This result is likely spurious and not indicative of any significant trends in the algorithm as the residual continues to trend towards convergence. For all cases, the effect of the re-clustering approach

(a) $move = 0.05, V = 0.1771$ (b) $move = 0.10, V = 0.1863$

(c) $move = 0.20, V = 0.1859$ (d) $move = 0.30, V = 0.1836$
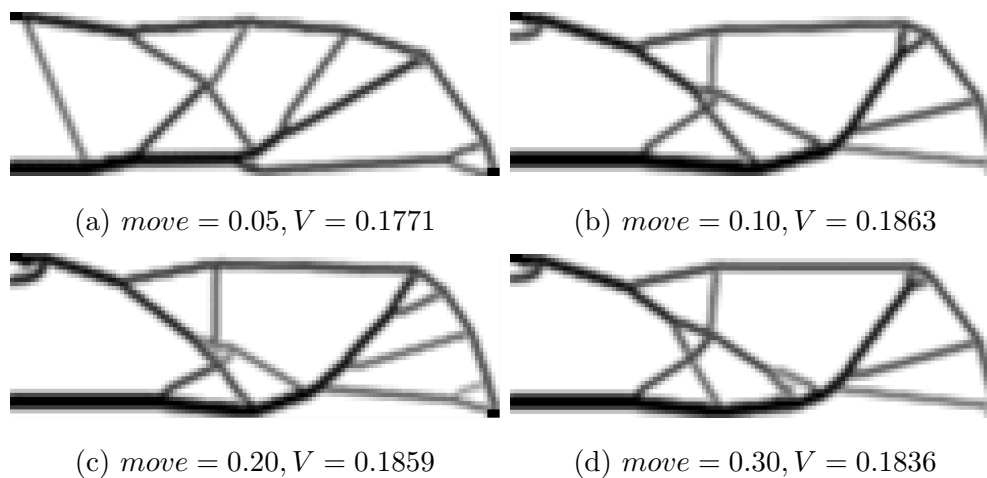
Figure 4.47. Converged structures for the size-independent strength constrained volume minimization, $\mathbb{P}_3$ for the MBB problem. Effect of MMA move-limit considered. Filtered density formulation used. $r_{min} = 2$ elements.

on two separate constraints appears not to introduce harmful discontinuity to the definition of the optimization problem.
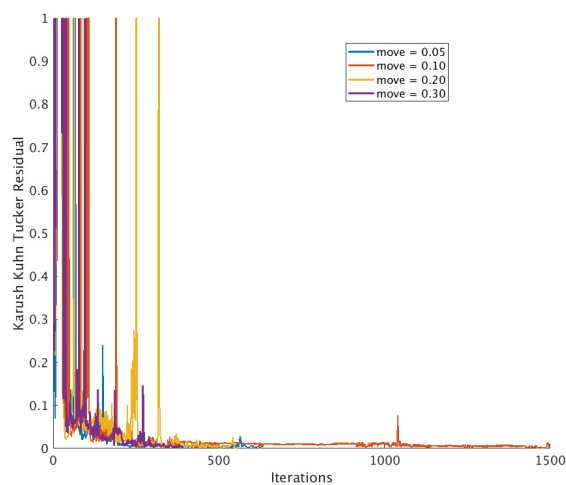
Figure 4.48. KKT Residuals for $\mathbb{P}_3$ move limit study shown in **Figure 4.47**.

The $\mathbb{P}_4$ problem with size measure penalizations of $\kappa = 1$ and $\kappa = \frac{1}{3}$ is considered next. For this problem a filter radius of $r_{min} = 2$ elements is applied and the maximum member size is restricted to $d_{max} = 6$ elements with a sampling angle of $\Theta = \frac{\pi}{8}$. A volume constraint of $\overline{V} = 0.4$ is imposed. Results for this problem are illustrated in **Figure 4.49**. Both the structures and converged compliance measures are virtually identical for all move-limit cases studied. This implies that the size-measure itself is not highly sensitive to a choice of algorithmic choices parameters. Examining the KKT residuals in **Figure 4.50** confirms this. No discontinuity of the size-measure is evidenced for any move-limit condition under the $\kappa = 1$ penalization while only minor discontinuity is seen for the $\kappa = \frac{1}{3}$ penalization.

Despite the smooth convergence behavior evidenced, all cases fail to reach the formal KKT cutoff required for termination. Instead, each algorithm terminates by reaching the condition $\Delta \leq \Delta_c$. Considering the convergence of the compliance objective given for both penalizations in **Figure 4.51**, the move limits all provide smooth descent towards the same local minimum. This implies that the passable KKT convergence observed is driven by an inability to satisfy the local size constraint completely. Whether this behavior is driven by the local size measure or the form of the diameter constraint aggregation is not clear at this point.

(a) $move = 0.05$, $\kappa = 1$,

$C = 1541$ N-mm

(b) $move = 0.05$, $\kappa = \frac{1}{3}$,

$C = 1727$ N-mm

(c) $move = 0.10$, $\kappa = 1$,

$C = 1523$ N-mm

(d) $move = 0.10$, $\kappa = \frac{1}{3}$,

$C = 1720$ N-mm

(e) $move = 0.20$, $\kappa = 1$,

$C = 1525$ N-mm

(f) $move = 0.20$, $\kappa = \frac{1}{3}$,

$C = 1720$ N-mm

(g) $move = 0.30$, $\kappa = 1$,

$C = 1531$ N-mm

(h) $move = 0.30$, $\kappa = \frac{1}{3}$,

$C = 1720$ N-mm
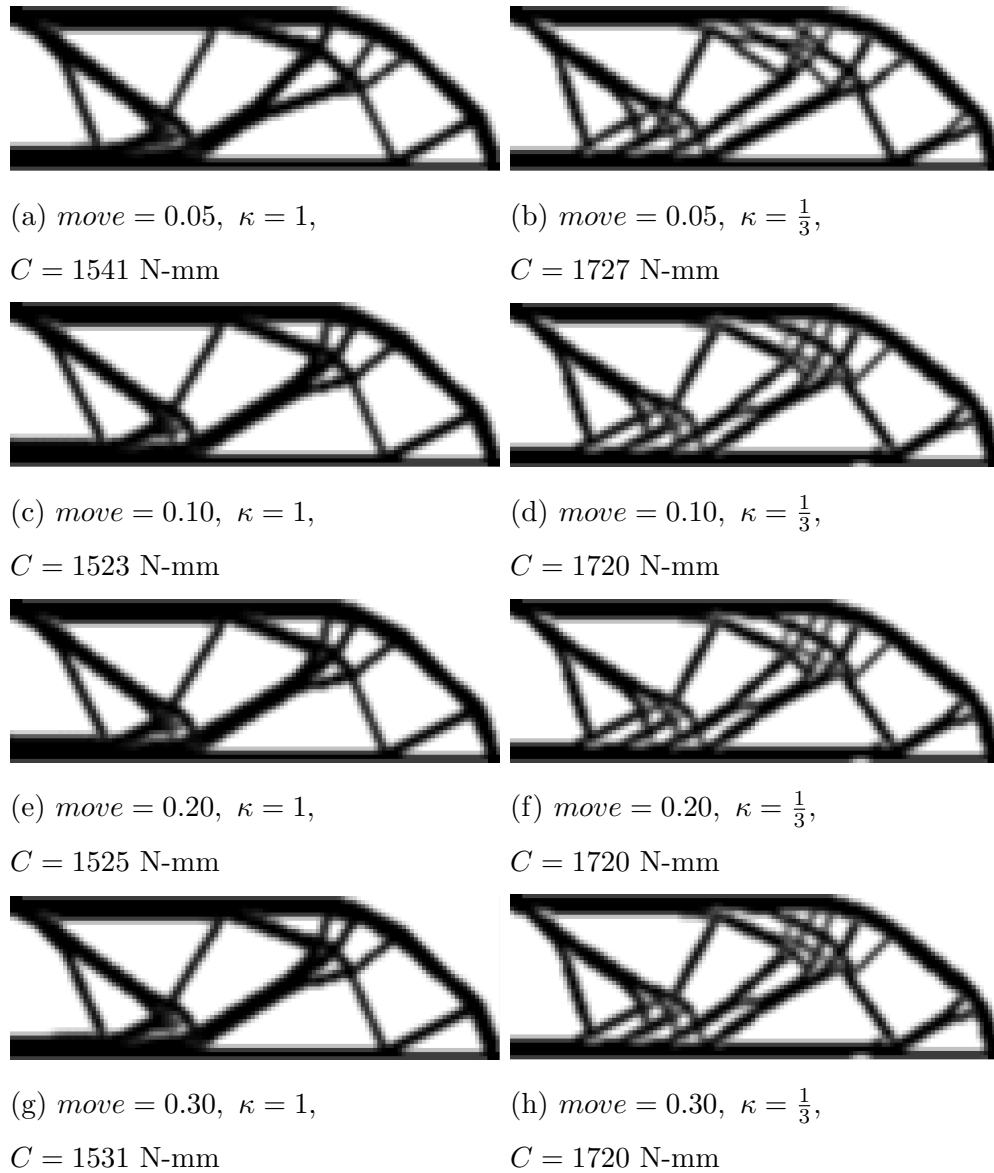
Figure 4.49. Converged structures for the volume and maximum diameter constrained compliance minimization, $\mathbb{P}_4$ for the MBB problem. Effect of MMA move-limit considered. Filtered density formulation used. $r_{min} = 2$ elements. $d_{max} = 6$ elements. $V_0 = 0.4$.

(a) $\kappa = 1$ (b) $\kappa = \frac{1}{3}$
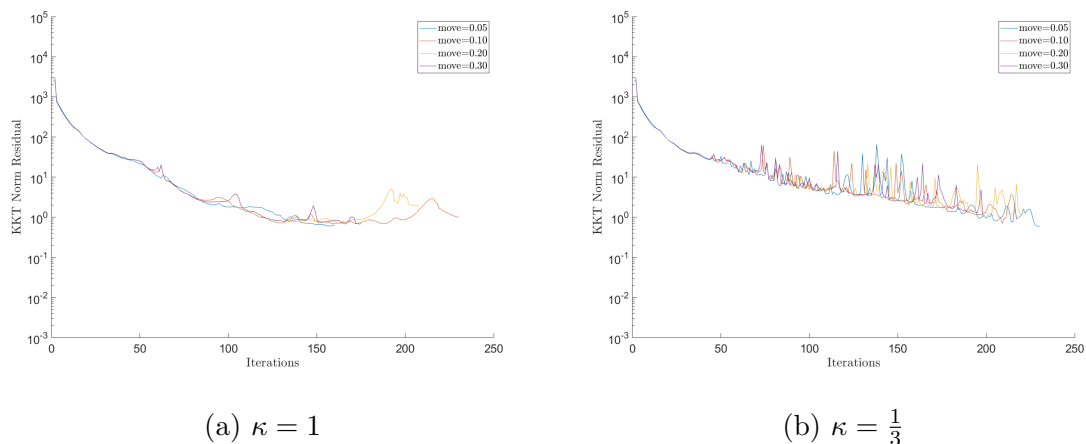
Figure 4.50. KKT Residuals for $\mathbb{P}_4$ move limit study shown in **Figure 4.49**.

(a) $\kappa = 1$ (b) $\kappa = \frac{1}{3}$
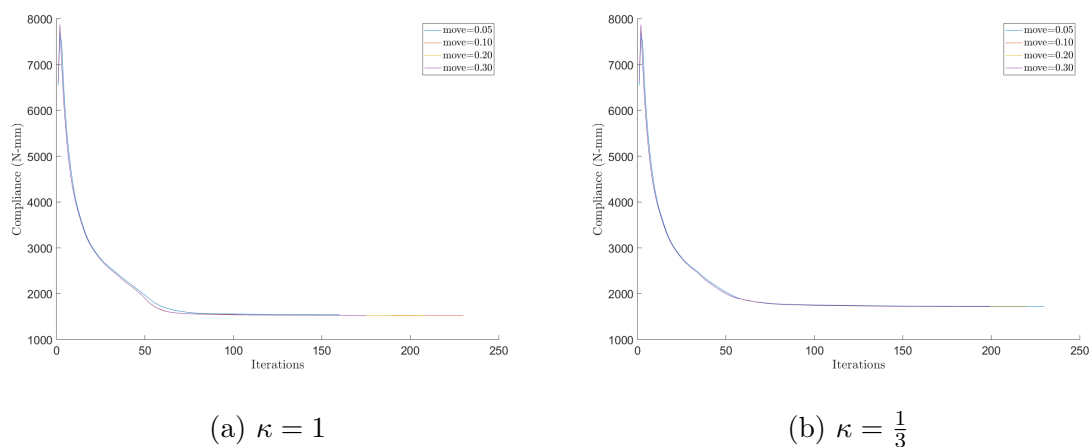
Figure 4.51. Structural compliance for the $\mathbb{P}_4$ move limit study shown in **Figure 4.49**.

To evaluate the behavior of size-dependent strength formulation, the $\mathbb{P}_6$ volume objective driven formulation is considered for all models of brittle size-effect. This choice was made due to the stabilizing effect of the compliance objective. This stabilization would likely obscure the influence of move-limits on the size-dependent strength constraints. The converse, that the $\mathbb{P}_6$ formulation is more stable under move limit variation than the $\mathbb{P}_5$, is assumed from previous results but not explicitly studied.

Considering first the LEFM-based form of the power-law scaling models in **Figure 4.52**, reasonable qualitative consistency is observed. The results shown utilize the same elastic properties as used previously. A material length scale of $D_0 = 5$ mm is applied for all cases. Structural topology under both size-measure penalizations differ only marginally for all but the most conservative move strategies. Reviewing the KKT residual plots in **Figure 4.53** illustrates highly discontinuous convergence behavior for all cases. For the $\kappa = 1$ cases, this optimization discontinuity is largely superfluous to the formal convergence as only brief violations of constraints occur. In contrast, the $\kappa = \frac{1}{3}$ cases illustrate a clear divergence of the solution paths into two separate structural topologies. This event occurs around 300 iterations into the optimization. The $move = 0.05$ case clearly evidences reasonable formal convergence despite moderate noise from temporary constraint violations. The remaining three cases diverge along a similar evolution path that leads to formal non-convergence on the domain. This lack of formal convergence doesn't appear to negatively impact the structural convergence in an obvious manner, however it does remain a concerning performance metric. For power-law scaling, is assumed that the Weibull based formulation will continue the trends observed for the LEFM-based model.

(a) $move = 0.05, \kappa = 1$

(b) $move = 0.05, \kappa = \frac{1}{3}$

(c) $move = 0.10, \kappa = 1$

(d) $move = 0.10, \kappa = \frac{1}{3}$

(e) $move = 0.20, \kappa = 1$

(f) $move = 0.20, \kappa = \frac{1}{3}$

(g) $move = 0.30, \kappa = 1$

(h) $move = 0.30, \kappa = \frac{1}{3}$
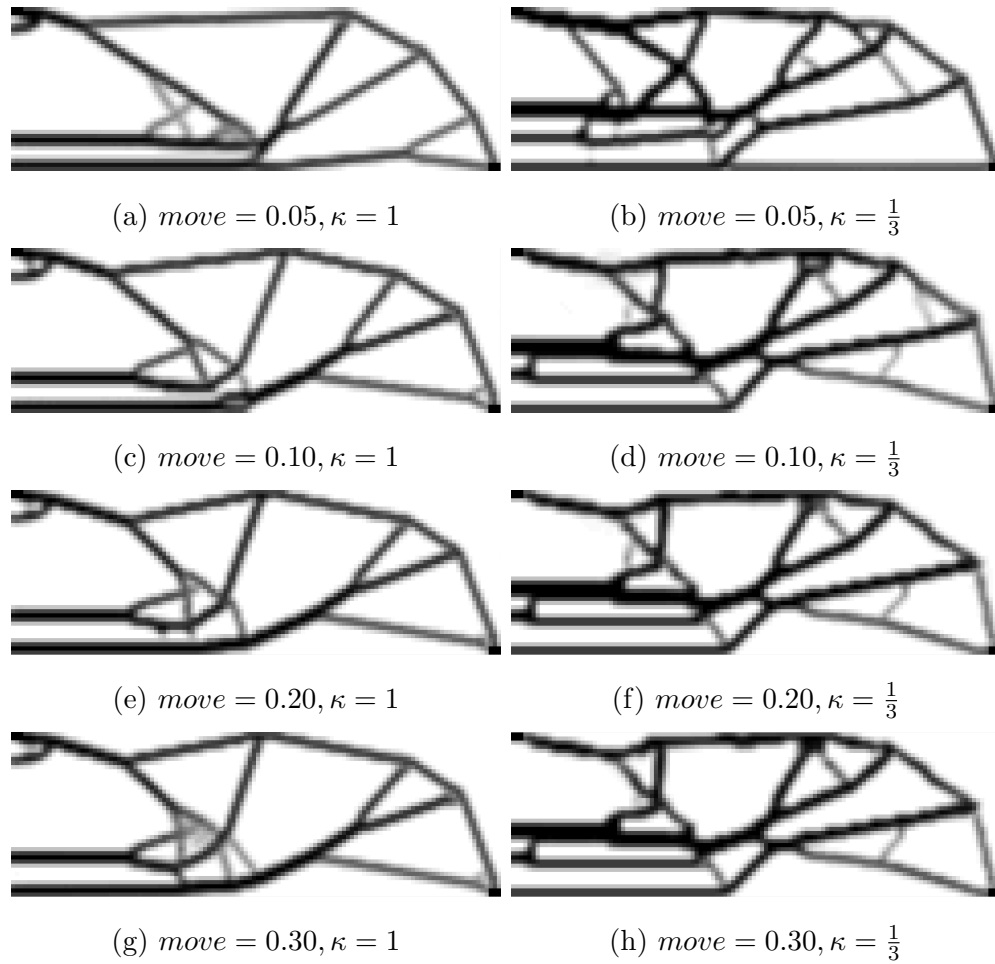
Figure 4.52. Converged structures for the LEFM-based strength constrained volume minimization, $\mathbb{P}_6$ for the MBB problem. Effect of MMA move-limit considered. Filtered density formulation used. $r_{min} = 2$ elements. $D_0 = 5$ mm.
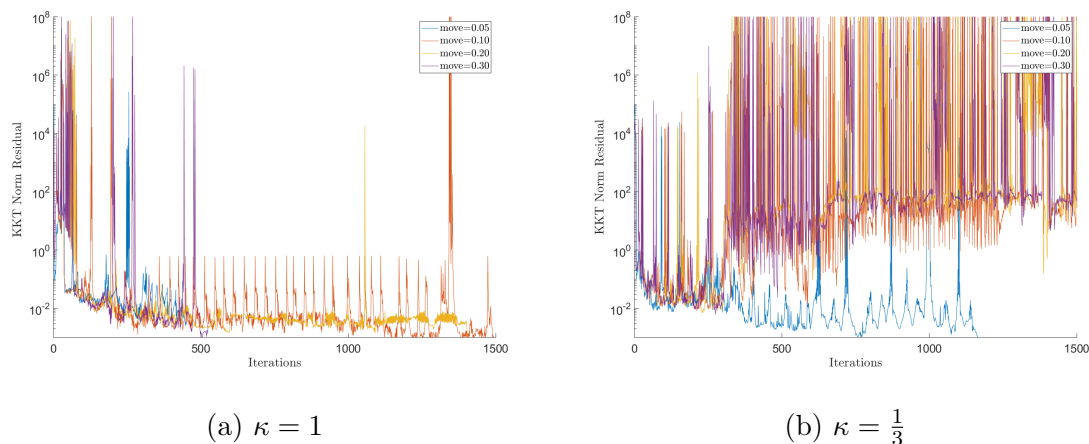
Figure 4.53. KKT Residuals for $\mathbb{P}_6$ LEFM move limit study shown in **Figure 4.52**.

Changing the form of size-dependence to the Bažant SEL, results for the move-limits considered are illustrated in **Figure 4.54**. The resulting structures with $\kappa = 1$ evidence reasonable qualitative convergence with only minor changes to topology. This convergence behavior is borne out by the KKT-residual plot illustrated in **Figure 4.55** where minimuml late iteration constraint violation is only seen for the $move = 0.30$ condition.

The results for the $\kappa = \frac{1}{3}$ are markedly different however. The conservative $move = 0.05$ and $move = 0.10$ conditions result in nearly solid-void solutions. Repeated transient constraint violations occur for both cases, however a generally convergent trend becomes clear after 1000 iterations as seen in **Figure 4.55**. Aggressive move strategies result in both significant intermediate density regions in the domain and poor formal convergence behavior. The $move = 0.20$ case becomes stuck in a infeasible local minimum while the $move = 0.30$ result oscilllates between feasible and infeasible results. It is posited that this occurs due to the limited availability of feasible domains that satisfy stress constraints. The $\kappa = \frac{1}{3}$ size-measure interprets structural members as fully thick up to the end of the filtered region, resulting in a weaker overall assumption of the fracture strength of material in the domain. This shrinks the feasible domain relative to the $\kappa = 1$ condition. Adopting an aggressive

move strategy prevents the solver from capturing these limited domains and thus
significant oscillation and poor convergence is observed.

(a) $move = 0.05, \kappa = 1$ (b) $move = 0.05, \kappa = \frac{1}{3}$

(c) $move = 0.10, \kappa = 1$ (d) $move = 0.10, \kappa = \frac{1}{3}$

(e) $move = 0.20, \kappa = 1$ (f) $move = 0.20, \kappa = \frac{1}{3}$

(g) $move = 0.30, \kappa = 1$ (h) $move = 0.30, \kappa = \frac{1}{3}$
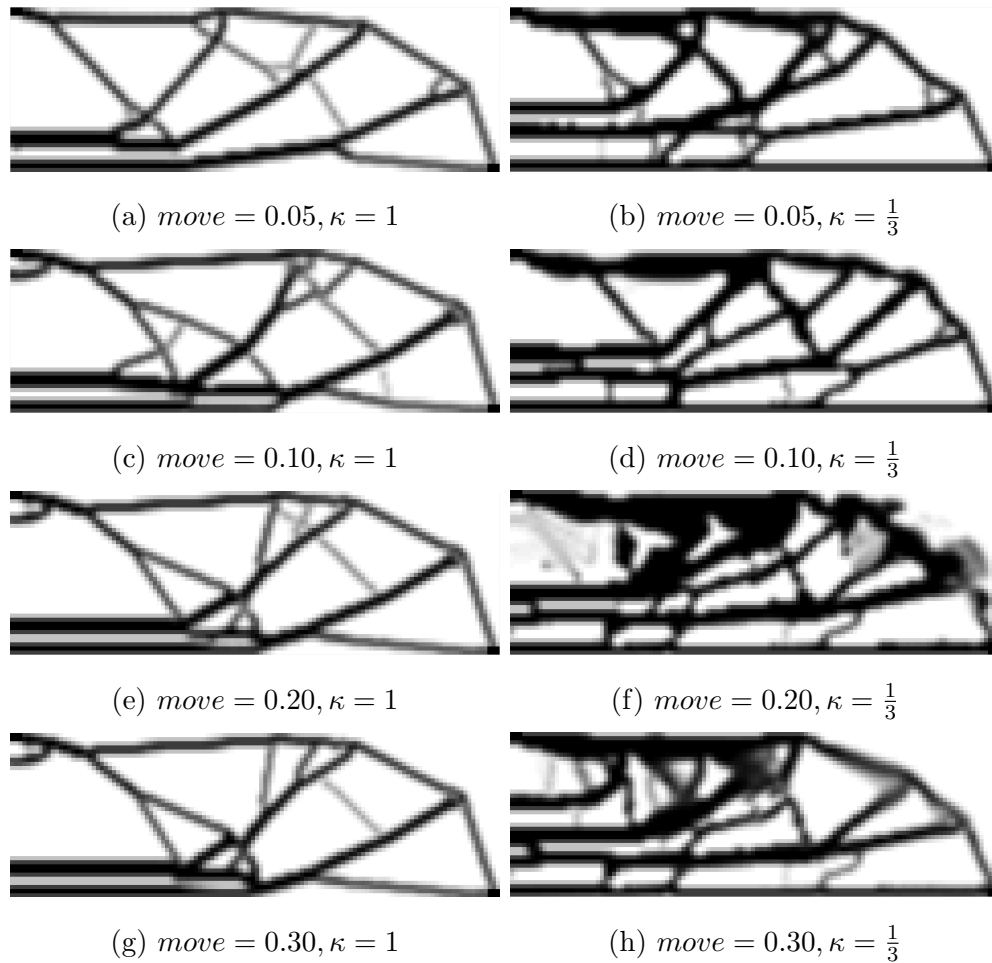
Figure 4.54. Converged structures for the Bažant SEL-based strength constrained
volume minimization, $\mathbb{P}_6$ for the MBB problem. Effect of MMA move-limit consid-
ered. Filtered density formulation used. $r_{min} = 2$ elements. $D_0 = 5$ mm.

(a) $\kappa = 1$

(b) $\kappa = \frac{1}{3}$
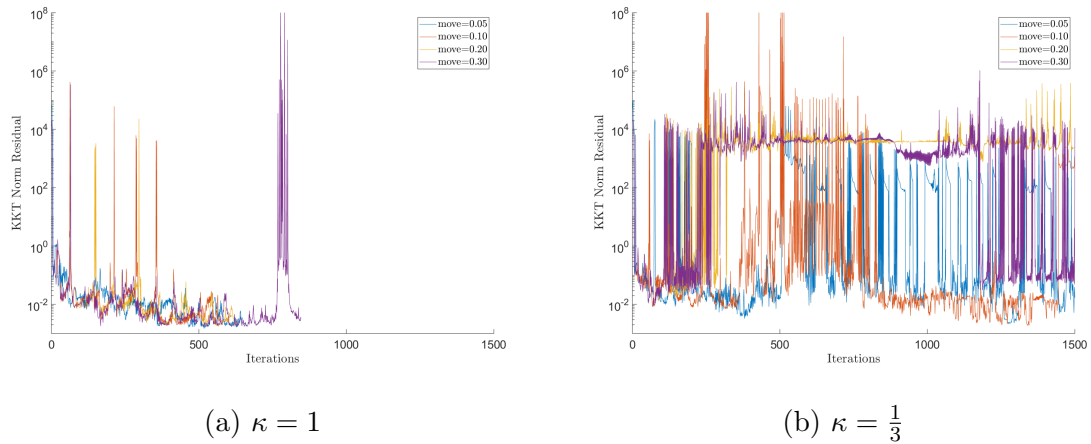
Figure 4.55. Plot of KKT Residuals for $\mathbb{P}_6$ Bažant move limit study shown in **Figure 4.54**.

Turning attention to the Irwin geometric scaling based size-dependence models, a flaw size of $a_0 = 2.5$ mm is assumed for all models presented. This flaw is equivalent in size to the cross section of a single element in the domain. The SENT based scaling form is considered first. Though significant changes in topology are observed comparing across the $\kappa = 1$ cases, it unclear if this is fundamental to the formulation or an artifact of the elemental deactivation scheme. Regarding formal convergence, significant oscillation occurs about a consistently flat trend-line. This result is indicative of a poorly constructed TO formulation that lacks the ability to effectively search the feasible design space.

Considering the $\kappa = \frac{1}{3}$ penalization, formal convergence improves for all cases. Significant constraint violations occur throughout, but a pronounced asymptotic trend emerges for early iterations. Near 800 iterations, the $move = 0.20$ case reaches formal convergence. The conclusiveness of this result is likely spurious as all other cases begin to trend upwards. Qualitatively, all optimized structures evidence reasonable convergence to solid-void conditions. However, the elemental deactivation scheme appears to maintain certain compression members throughout the optimization at the deactivation cutoff. This behavior is obviously undesirable and speaks to the

added considerations that must be made to fully develop the empirical fixed-flaw size models presented.

(a) $move = 0.05, \kappa = 1$

(b) $move = 0.05, \kappa = \frac{1}{3}$

(c) $move = 0.10, \kappa = 1$

(d) $move = 0.10, \kappa = \frac{1}{3}$

(e) $move = 0.20, \kappa = 1$

(f) $move = 0.20, \kappa = \frac{1}{3}$

(g) $move = 0.30, \kappa = 1$

(h) $move = 0.30, \kappa = \frac{1}{3}$
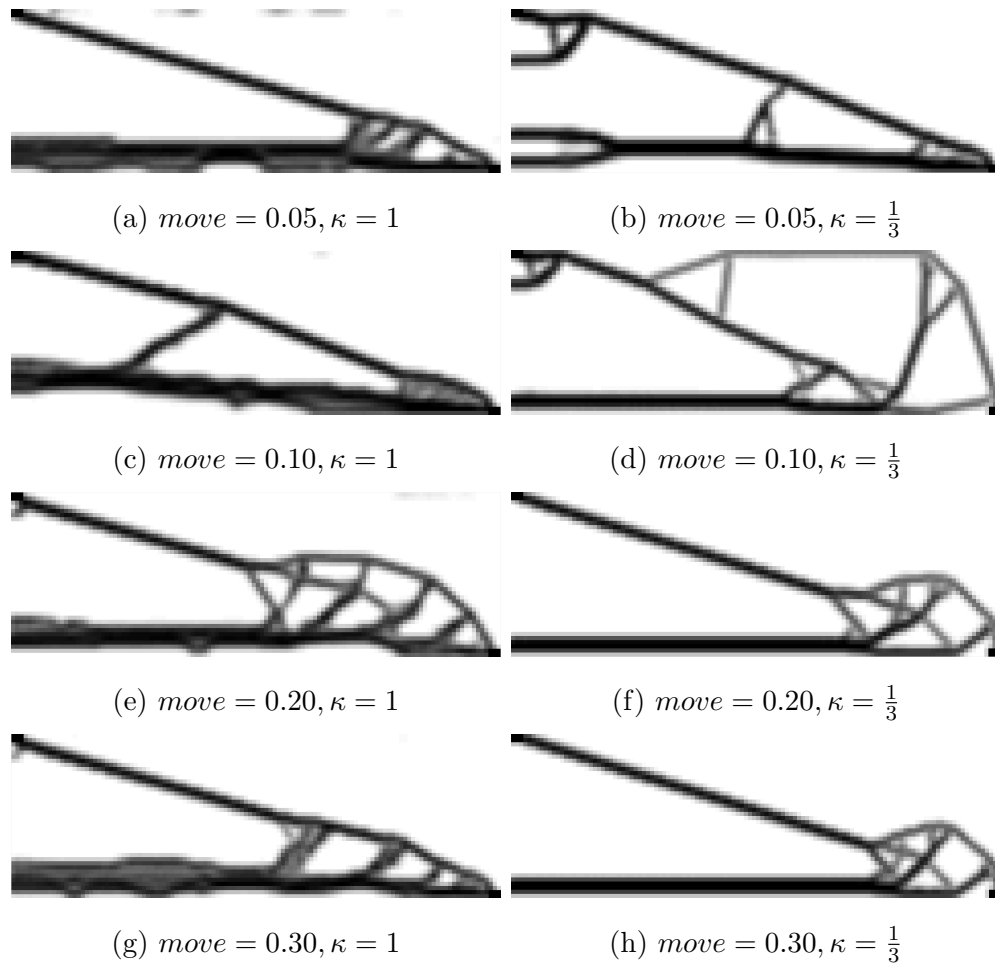
Figure 4.56. Converged structures for the SENT-based strength constrained volume minimization, $\mathbb{P}_6$ for the MBB problem. Effect of MMA move-limit considered. Filtered density formulation used. $r_{min} = 2$ elements. $a_0 = 2.5$ mm.
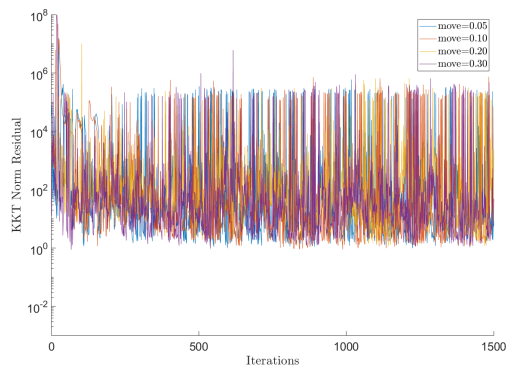
(a) $\kappa = 1$
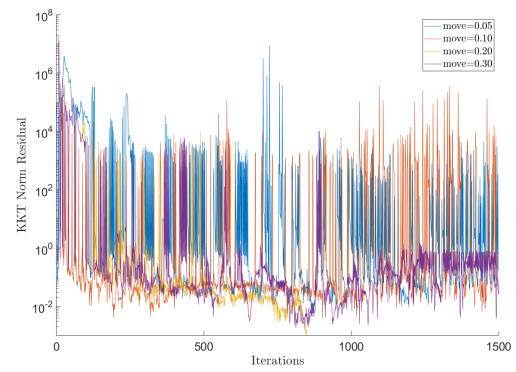
(b) $\kappa = \frac{1}{3}$

Figure 4.57. Plot of KKT Residuals for $\mathbb{P}_6$ SENT move limit study shown in **Figure 4.56**.

For the DENT scaling model, the assumed flaw size serves as a severe impediment to convergence as illustrated in **Figure 4.58**. For the $\kappa = 1$ condition, no practical convergence is demonstrated regardless of the move limit strategy employed. move limit for the DENT problem fails to alleviate these convergence challenges. Formal convergence is likewise not achieved as shown by the KKT residual plot in **Figure 4.59 (a)**. Better structural convergence is observed for the $\kappa = \frac{1}{3}$ for all move limit cases, as expected. Interestingly, increasing the move limits appears to result in more robust practical and formal convergence. This likely occurs because of the interaction between the move limits and the elemental deactivation scheme applied. It is possible that the tight $move = 0.05$ limits causes density oscillations around the deactivation threshold, activating and deactivating some elements in the domain repeatedly. Loosening these limits allows for large enough steps for reasonable convergence to a local structural minimum.

(a) $move = 0.05, \kappa = 1$

(b) $move = 0.05, \kappa = \frac{1}{3}$

(c) $move = 0.10, \kappa = 1$

(d) $move = 0.10, \kappa = \frac{1}{3}$

(e) $move = 0.20, \kappa = 1$

(f) $move = 0.20, \kappa = \frac{1}{3}$

(g) $move = 0.30, \kappa = 1$

(h) $move = 0.30, \kappa = \frac{1}{3}$
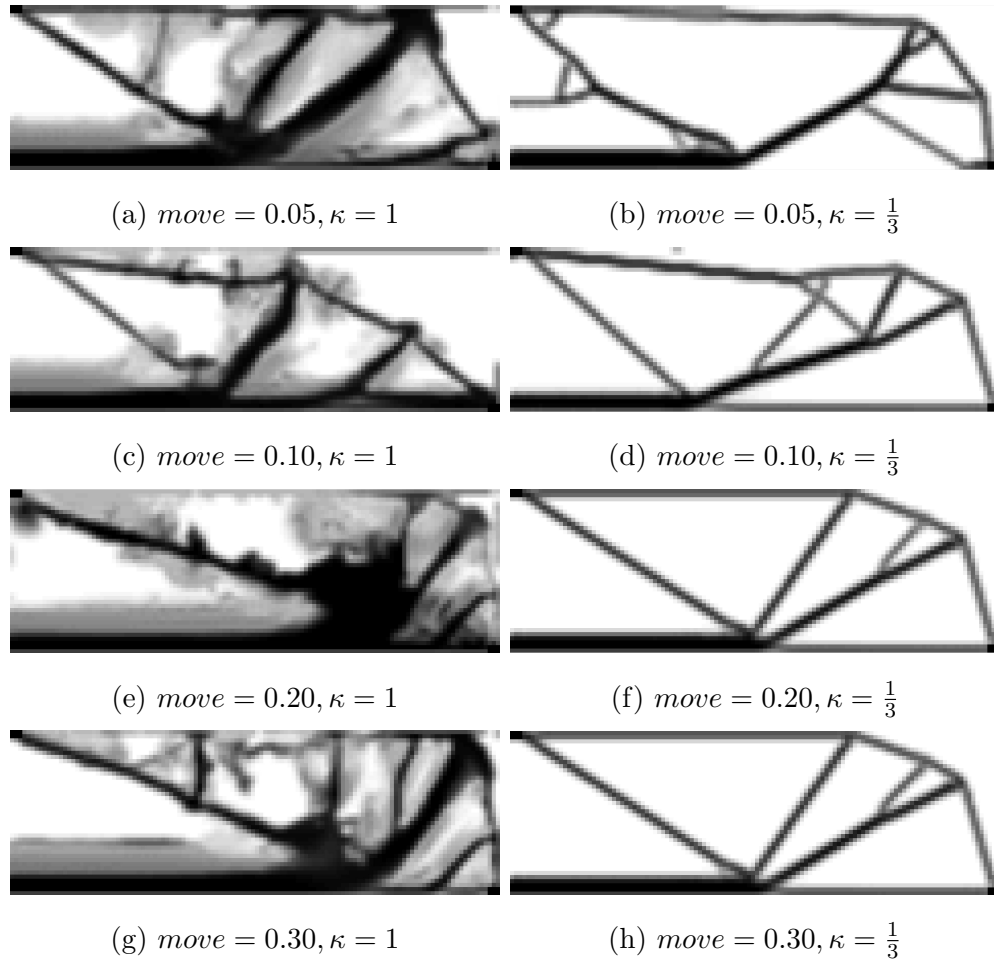
Figure 4.58. Converged structures for the DENT-based strength constrained volume minimization, $\mathbb{P}_6$ for the MBB problem. Effect of MMA move-limit considered. Filtered density formulation used. $r_{min} = 2$ elements. $a_0 = 2.5$ mm.
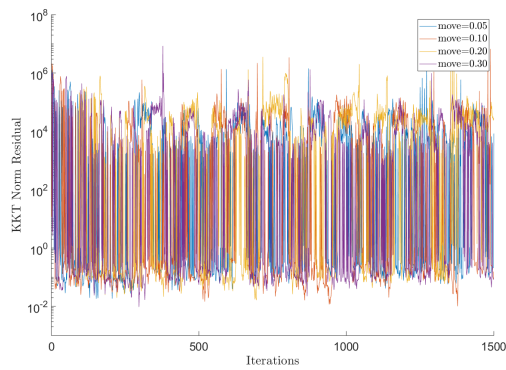
(a) $\kappa = 1$
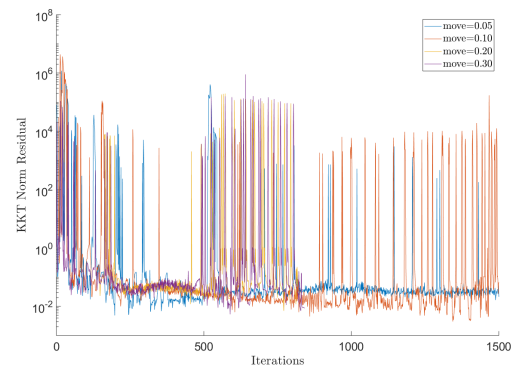
(b) $\kappa = \frac{1}{3}$

Figure 4.59. Plot of KKT Residuals for $\mathbb{P}_6$ DENT move limit study shown in **Figure 4.58**.

4.8 Effect of density projection on size-dependent strength formulations

In **Section 4.4.2** it was shown that the three-field, projected density approach appears viable for the maximum radius constrained formulation using the proposed size-measure. However, structural convergence was only observed under limited model parameters. This parameter-sensitivity and resulting poor convergence dominates the structures obtained for the variety of stress-based models. At this point, no ideal continuation strategy or projection parameters have been identified for any strength-constrained problems. With this failing in mind, the current results for limited parameters searched are presented for completeness. These results are consolidated in **Figure 4.60** for the $\tilde{\eta} = 0.5$ projection and **Figure 4.61** for the $\tilde{\eta} = 0$ projection. For all cases $\kappa = 1$ and the representative $D_0 = 10$ mm or $a_0 = 1$ mm. An applied half domain load of $P = 1000$ N is used.

Despite the variety in the underlying physical models, the challenges with the projection approach appear to stem from the nonlinearity introduced by the projection approach to the stress aggregation. The strength measure does not appear to be the overriding cause of convergence issues. It does certainly exacerbate them under certain conditions however. The resolution of these issues is necessarily left to future work due to the limitations on the timeline of this thesis.
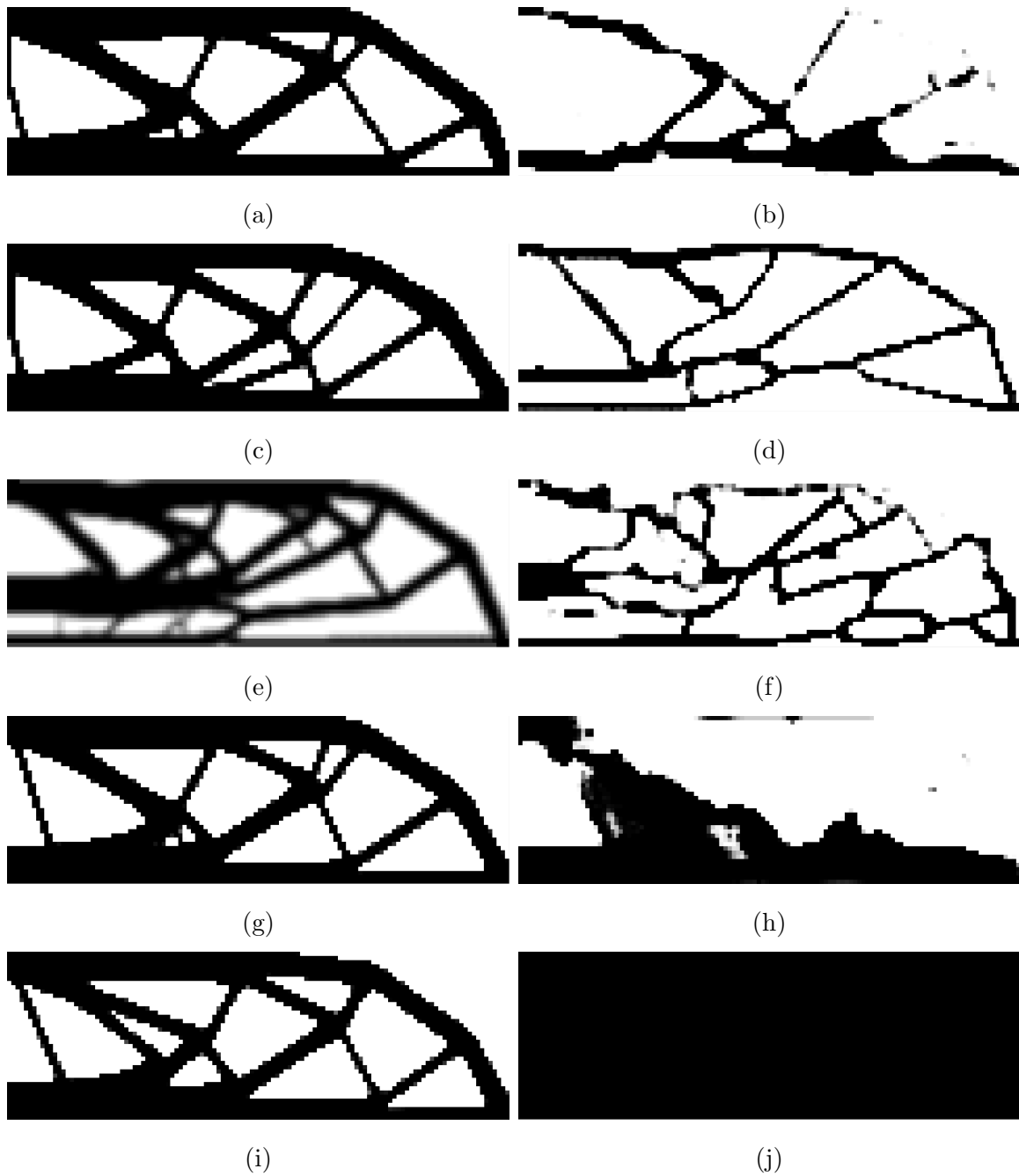
Figure 4.60. Results for strength-constrained problems with $\tilde{\eta} = 0.5$ projected density. (a) $\mathbb{P}_2$. (b) $\mathbb{P}_3$. (c) $\mathbb{P}_5$, LEFM. (d) $\mathbb{P}_6$, LEFM. (e) $\mathbb{P}_5$, Bažant SEL; no convergence for first-stage optimization problem. (f) $\mathbb{P}_6$, Bažant SEL. (g) $\mathbb{P}_5$, SENT. (h) $\mathbb{P}_6$, SENT. (i) $\mathbb{P}_5$, DENT. (j) $\mathbb{P}_6$, DENT.
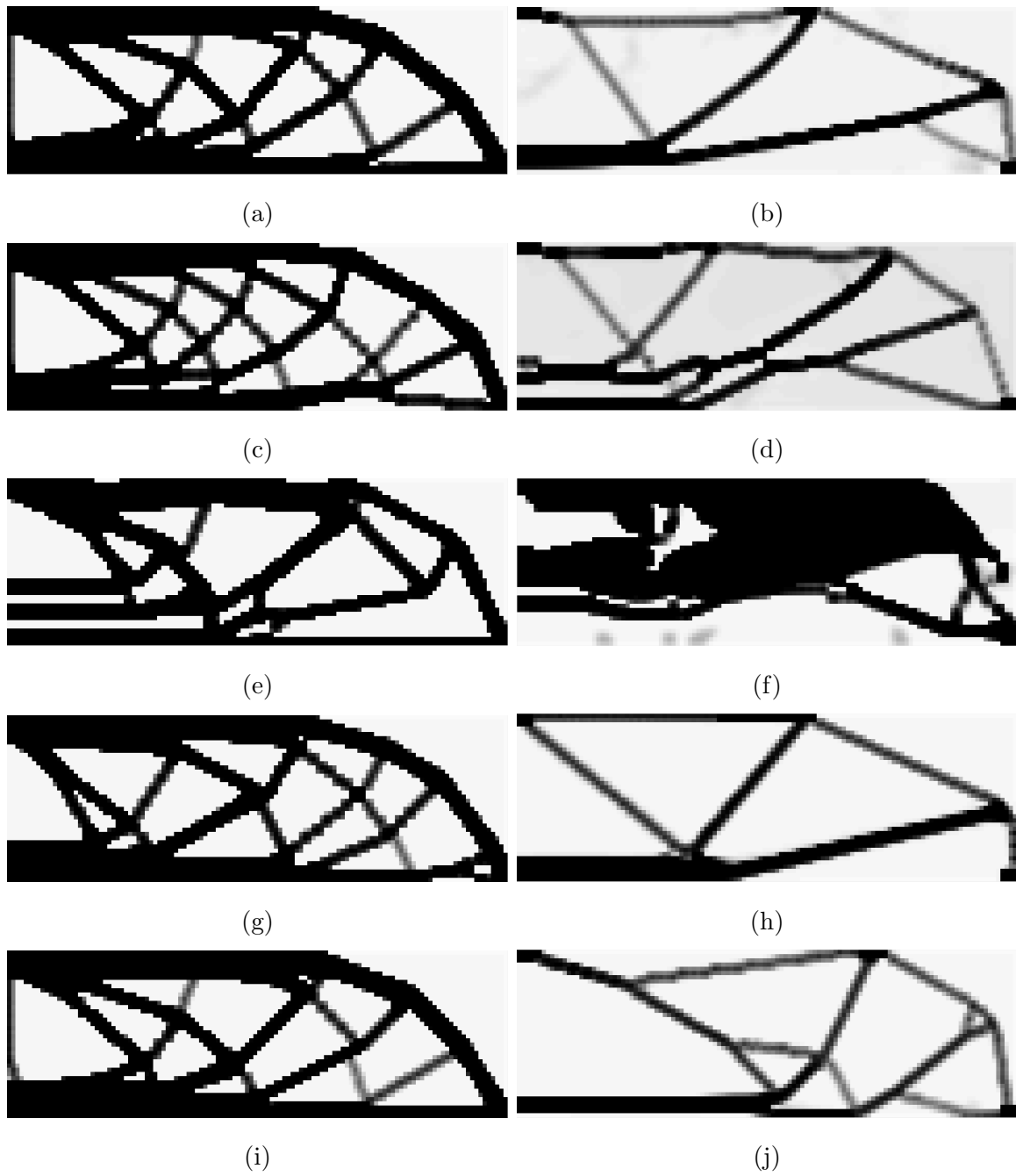
Figure 4.61. Results for strength-constrained problems with $\tilde{\eta} = 0.0$ projected density. (a) $\mathbb{P}_2$. (b) $\mathbb{P}_3$. (c) $\mathbb{P}_5$, LEFM. (d) $\mathbb{P}_6$, LEFM. (e) $\mathbb{P}_5$, Bažant SEL. (f) $\mathbb{P}_6$, Bažant SEL. (g) $\mathbb{P}_5$, SENT. (h) $\mathbb{P}_6$, SENT. (i) $\mathbb{P}_5$, DENT. (j) $\mathbb{P}_6$, DENT.

4.9 Printed specimen validation

To verify the physical significance of the resulting size-dependent TO structural outcome, a simple comparative mechanical test was completed. For this testing program, a variation of the MBB problem domain was optimized assuming both size-independent and size-dependent tensile failure characteristics of the VeroWhite Plus photopolymer. The common full-domain aspect ratio of the beam was reduced from 6:1 to 4:1 to preclude out-of-plane buckling behaviors. The $\mathbb{P}_2$ and $\mathbb{P}_5$ compliance minimization forms were applied to prevent slender compression dominated members that may lead to in-plane buckling in the optimized domain. Finally, the plane-stress elements used in the TO formulation were assigned a non-unity thickness to allow for scaling of the applied load in the TO algorithm.

An allowable structural domain with dimensions of 100 mm $\times$ 25 mm $\times$ 6 mm was prescribed. This choice was made by considering the maximum load of fully dense 3-point bending beams on the approximate dimensional scale and load capacity of the available testing equipment. This domain was also chosen to allow for features on the scale of 1 mm thick to be realized without using an extremely fine discretization of the FE domain. By doing so, optimization cost was minimized and the range of allowable applied loads leading to structural convergence could be quickly investigated.

To determine the applied load used for the optimization problem, an initial load was selected such that the midpoint stress for the fully dense domain would be equal to the assumed tensile strength of the VeroWhite photopolymer. This selection was made assuming size-independent strength. Successive optimization attempts were made for both the $\mathbb{P}_2$ and $\mathbb{P}_5$ problems until formal convergence was achieved for both formulations. The resulting applied load on the domain was 562.5 N on the full domain.

Using the parameters described above, the converged structures depicted in **Figure 4.62** were obtained. The resulting $\mathbb{P}_2$ was obtained with no active fracture constraints on the domain. The MATLAB FE implementation was used to deter-

mine that these constraints would be active at a load of 875 N. The $\mathbb{P}_5$ structure was constrained by the tensile cutoff in the lamellar region of the converged structure. Under the applied load, a mid-domain vertical displacement of 3.6 mm is predicted for the $\mathbb{P}_2$ case and 4.2 mm for the $\mathbb{P}_5$ result. If the assumed Bažant SEL scaling model is not applicable to the VeroWhite specimens, the $\mathbb{P}_2$ should be expected to support a significantly elevated load capacity. The scaling model is validated if the load capacity of the $\mathbb{P}_5$ problem is correctly predicted.

Four specimens of each structure were fabricated following the geometry generation approach detailed in **Section 3.7** and printing approach detailed in **Section 3.9**. The specimens and corresponding tensile coupons were configured in the Objet Studio in the positions shown in **Figure 4.63** and fabricated in approximately 2 hours on the aforementioned Connex 350 Polyjet print system.

(a)

(b)
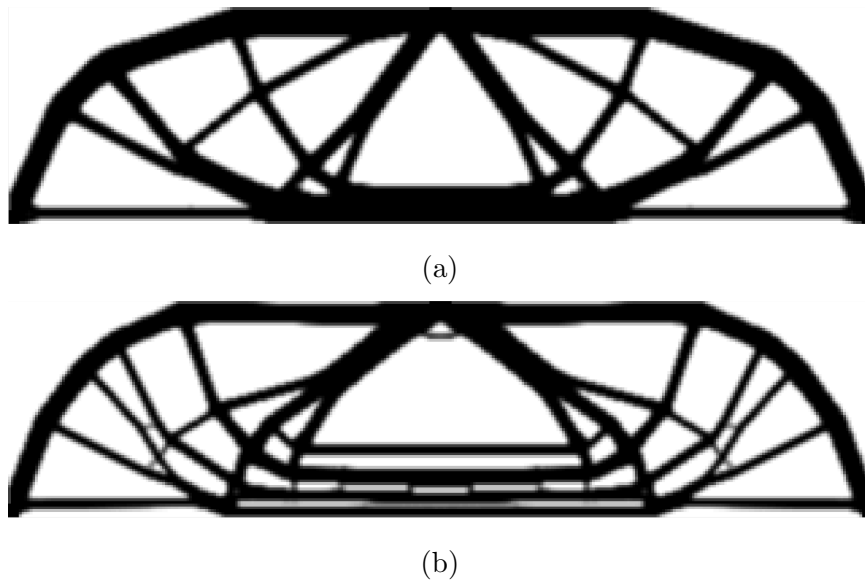
Figure 4.62. Filtered density fields of VeroWhite optimized specimens. (a) $\mathbb{P}_2$ formulation 4:1 beam domain. (b) $\mathbb{P}_5$ formulation 4:1 beam domain.

Printed specimens were carefully positioned on a 3-point bending test fixture on the previously described Instron 3345 load test frame. The testing configuration is illustrated in **Figure 4.64** for a $\mathbb{P}_2$ specimen. Load was applied using a displacement controlled approach through a prescribed displacement of 10 mm or failure, whichever

occurred first. No specimens of either the size-independent or dependent formulations survived to reach 10 mm. The cross-head rate was prescribed at 1.5 mm/min in accordance with the allowable strain rate given by ASTM D790.
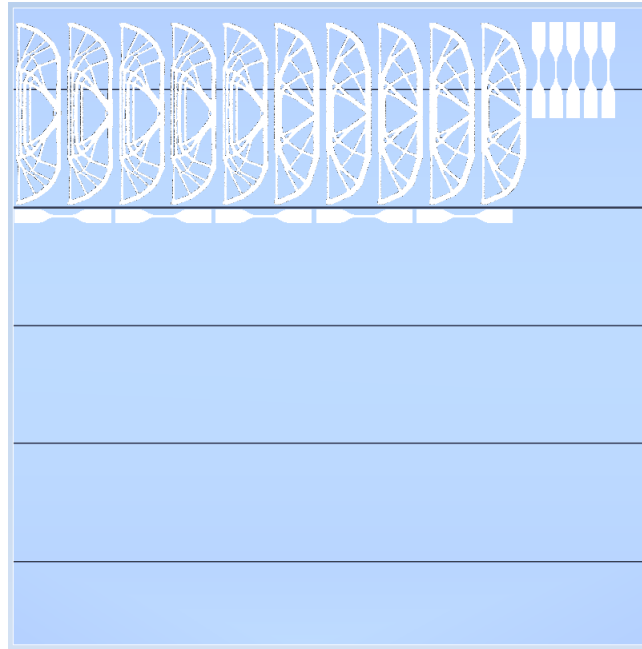
Figure 4.63.   Top view of 4:1 beam printed specimens and tensile coupons.
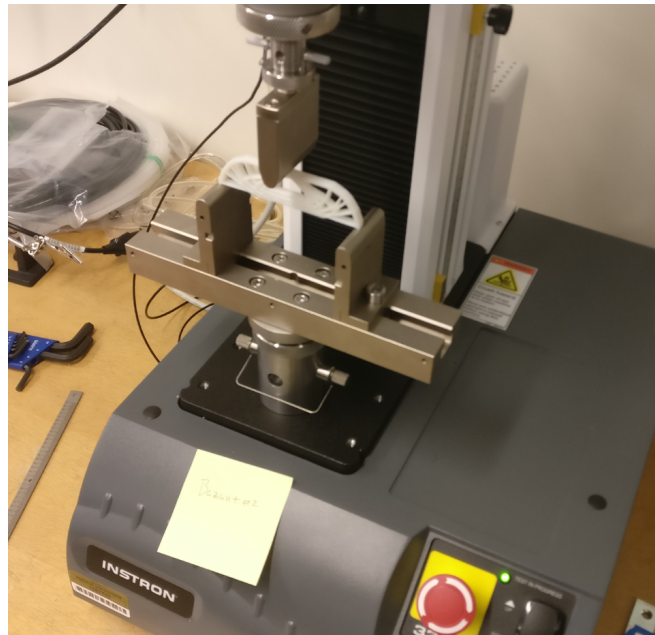
Figure 4.64.   Typical Instron 3345 3-point bend specimen testing configuration.

Under these conditions, the load displacement curves shown in **Figure 4.65** were obtained.
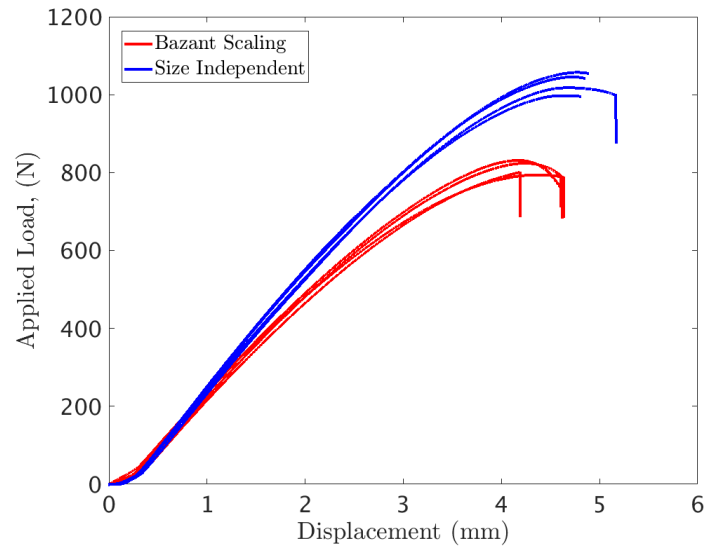
Figure 4.65. Load-displacement curves for the $\mathbb{P}_2$ and $\mathbb{P}_5$ Bažant SEL-scaling 4:1 beam specimens.

From these results, it is clear that the optimized structure exhibits a significantly different elastic response than predicted by the MATLAB FE formulation. The resulting mid-point deflection is approximately half the predicted value for both structures. Additionally, substantial structural non-linearity is observed for the $\mathbb{P}_5$ result at low displacements. The onset of non-linearity is delayed for the $\mathbb{P}_2$ case but it is still present before the peak load occurs. Beyond the issue with predicting the elastic response, it is clear that both TO formulations do not properly capture the failure loads of each structure. Both results overestimate the peak load of the structures. In observing the near-peak deformation conditions shown in **Figure 4.66**, the reasonable test response observed for all $\mathbb{P}_2$ specimens are contrasted against the shifting seen for the $\mathbb{P}_5$ samples. The shifting occurs due to the narrow fixed-support features which arise in the $\mathbb{P}_5$. These features displaced off the rounded load supports for each specimen and localized deformation in the adjacent tensile truss member. Once the specimen was off center, a secondary buckling effect took hold and increased the non-linearity of the response. In contrast, no apparent load or boundary induced non-linear effects took hold for the $\mathbb{P}_2$ specimens. Additionally, post-testing of the

fabricated tensile coupons illustrated good agreement with previous elastic and failure trends observed for the VeroWhite material and print conditions.
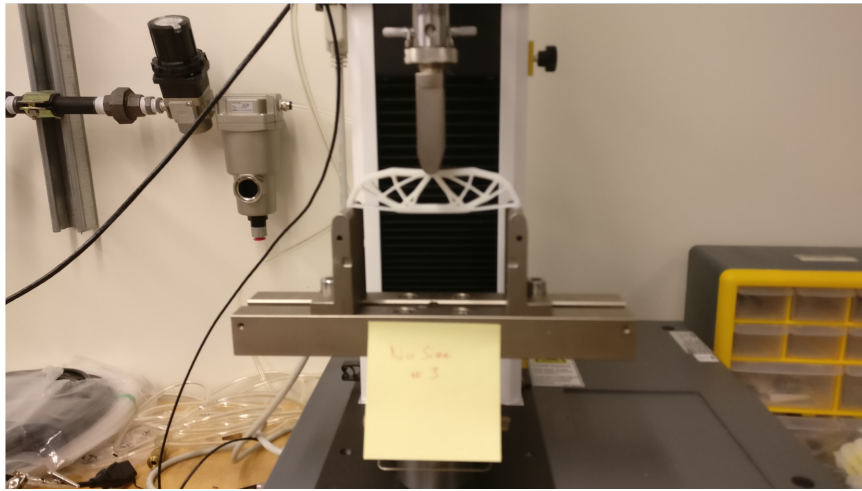
(a)

(b)

Figure 4.66.   Photographs for printed specimens at near-peak load deformation. (a) $\mathbb{P}_2$ specimen illustrating symmetric deformation. (b) $\mathbb{P}_5$ specimen illustrating shifting on end-supports and in plane buckling of the central compression-dominated truss about the load applicator.

Following testing, representative failed specimens are illustrated in **Figure 4.67** and contrasted against the normalized first principal plots for each specimen presented in **Figure 4.68**. The failure modes depicted were consistent across all spec-

imens tested in each sample. For the $\mathbb{P}_5$ specimen, failure was clearly influenced by the strain localization observed. Failure occurs in the tensile member extending to the support member. This is in contrast to the $\frac{\sigma}{s_T}$ plot which implies that a cascading fracture event through the highly loaded tensile region should dominate failure. However, for the $\mathbb{P}_2$ there is reasonable agreement between the FE and observed failure behaviors. Fracture in the specimen originates in the highly stressed region under the compression truss region of the optimized structure then progresses upwards through the main tensile member. This apparent agreement fails to provide any further insight into the discrepancy between analysis and experiment.

(a)

(b)

Figure 4.67. Representative examples of specimen failure. (a) $\mathbb{P}_2$ size-independent. (b) $\mathbb{P}_5$ Bažant SEL scaling.

Given the challenges with consistent testing and relative lack of instrumentation, little may be concluded from these results. No conclusive statement may be made about the validity of the size-dependent assumption. No comment may be made on the performance or efficacy of the TO formulation. Future attempts to experimentally validate the computational results must work to improve testing conditions and implement additional instrumentation of the specimen under load.

(a)

(b)
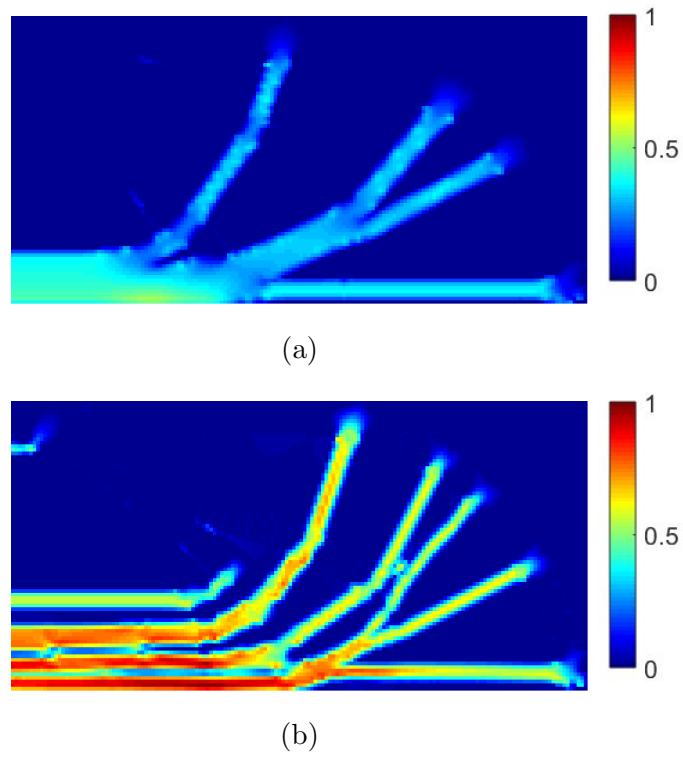
Figure 4.68. Normalized first principal, $\frac{\sigma}{\varsigma_T}$ plots for the Verowhite optimized specimens. (a) $\mathbb{P}_2$ size-independent. (b) $\mathbb{P}_5$ Bažant SEL scaling.

4.10 Bažant Size Effect Law Finite Element validation

Before proceeding to a more complicated form of analysis, the MATLAB linear-elastic FE code which solves the TO state problem is verified using the ABAQUS/-Standard commercial package. The same volumetric meshes used to generate the printed specimens are imported into ABAQUS following the process detailed in **Section 3.7**. The full domain of the 4:1 beam specimens is considered since a clear symmetry plane is difficult to define in the unstructured mesh. A pinned boundary condition is applied to the surface nodes local to the assumed TO FE support on one end of the beam. A roller condition with restricted out of plane displacement is applied to the other. These boundary conditions are applied as nodal constraints over distributed regions in an attempt to mitigate any effects of mesh perturbation. However, this in turn leads to over-constraint of the model. Given this fact, regions near the fixed boundaries are not considered in the stress analysis and the local elemental volumes are later not enriched to consider crack growth in the XFEM formulation.

Similarly, the lack of a regular mesh or parametric geometry introduces challenges in prescribing the applied displacement or load. In the case of an applied displacement, identical nodal displacements are prescribed to all nodes in a surface region $\frac{1}{20}$ the length of the domain centered on the mid-point of the beam. For applied loads, the same region is used while the load is divided evenly between the nodes. This approach minimizes the presence of numerical stress concentrations. Regardless, the local volumetric domain is again not considered in the stress analysis or later enriched.
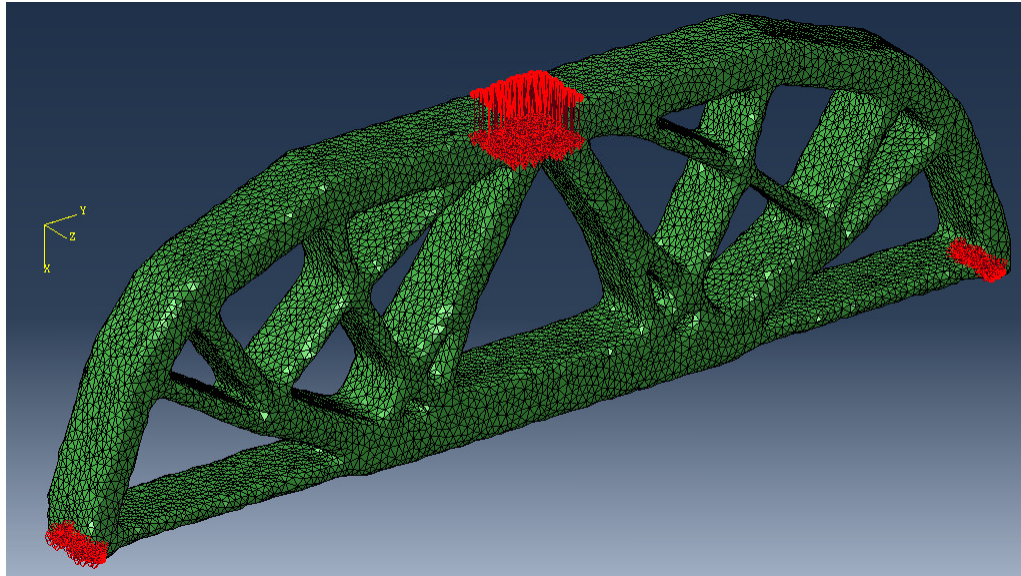
Figure 4.69. ABAQUS/Standard model for the $\mathbb{P}_2$ optimized domain. Applied load and boundary conditions used for all cases are shown.

An example free body diagram is depicted in **Figure 4.69** for the $\mathbb{P}_2$ optimized structure. Local perturbations of the mesh resulting from the unstructured mesh generation are visible throughout the domain.

An ABAQUS/Standard material is defined with the same linear-elastic properties as used for the TO formulation and applied to both the $\mathbb{P}_2$ and $\mathbb{P}_5$ optimized structures. An applied load equal to the optimized load is prescribed. The first principal stress distribution in the $\mathbb{P}_2$ domain is obtained and plotted in comparison to the MATLAB FE implementation in **Figure 4.70**. Contrasting the two plots, the stress result in both interpretations of the problem are reasonably consistent. A clear discrepancy exists local to the gray boundary regions surrounding the solidified members in the MATLAB implementation. These domains under-predict the stress-levels in these regions while their penalized stiffness leads to an elevated stress in the adjacent fully solid domains. Both models agree on the localization of strain in the main tensile member below the central compression truss geometry. A maximum first principal stress of 38.8 MPa is predicted on the bottom surface of the tensile member for the ABAQUS model. The MATLAB FE predicts a maximum first principal of

(a)

(b)
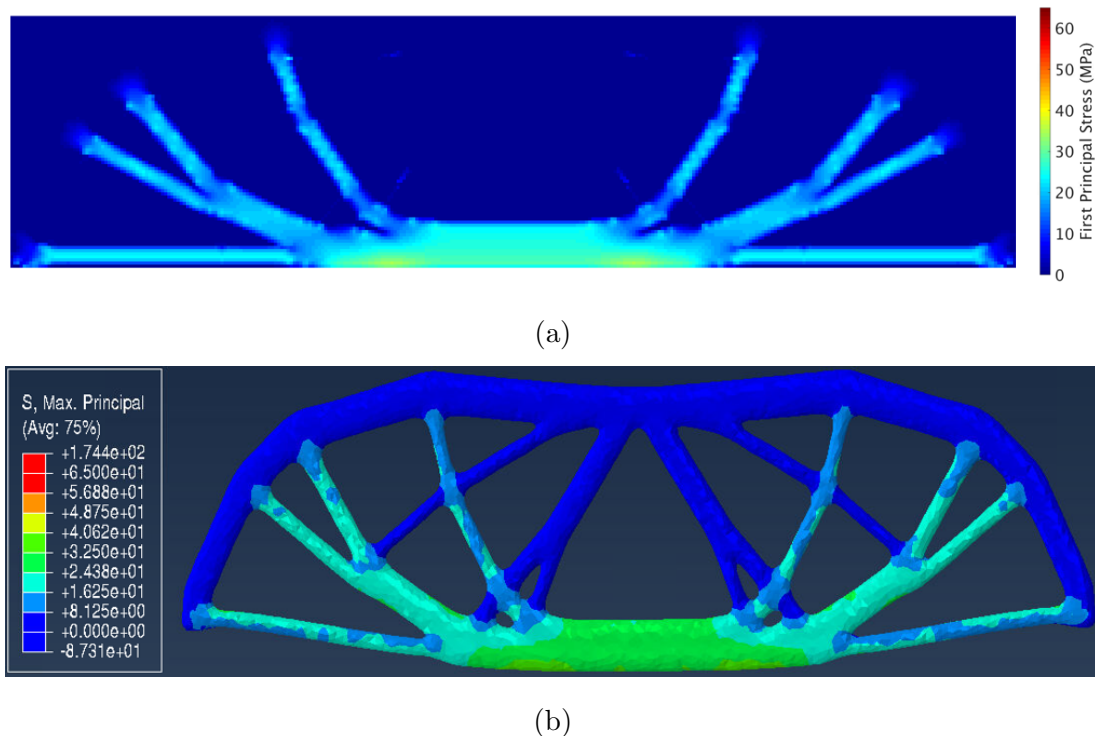
Figure 4.70. First principal stress plots for the $\mathbb{P}_2$ optimized structure. (a) MATLAB FE implementation. (b) ABAQUS/Standard, linear-elastic solution.

34.57 MPa offset from the boundary by r_{min}. The ABAQUS implementation predicts a mid-point deflection of 3.557 mm providing agreement within 2% of the MATLAB predicted displacement.

This agreement between analysis approaches indicates that the discrepancy between the MATLAB predicted load response and the experimental observations is not the result of a flawed analysis formulation. It is hypothesized that this result is driven by a difference in the tensile elastic modulus and the effective elastic modulus in the optimized structure. Significant portions of the 4:1 beam domain experience states of stress indicative of bending loading. Considering this, these domains would be best characterized by using the VeroWhite flexural modulus. Addressing this particular discrepancy between analysis and test is beyond the scope of this thesis.

Considering now the first principal stress results for the $\mathbb{P}_5$ structure, results are presented in **Figure 4.71**. Interestingly, the intermediate density shear transfer re-
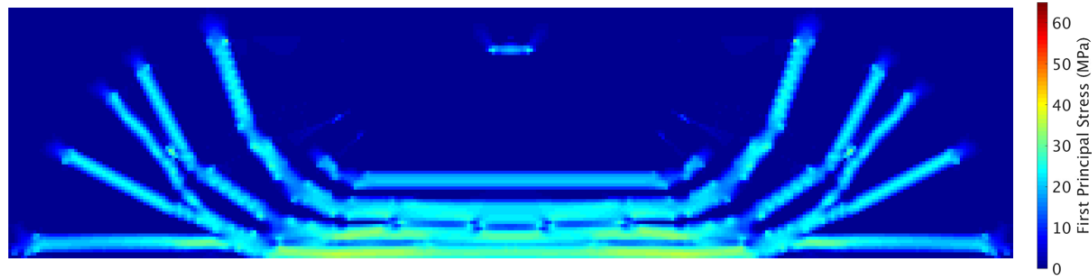
(a)
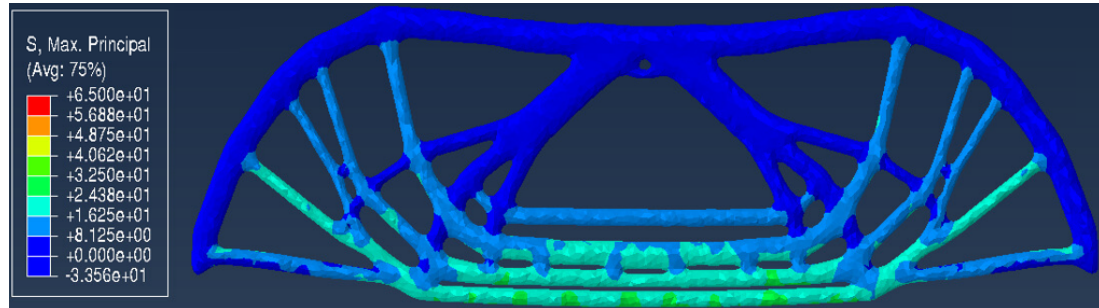
(b)

Figure 4.71. First principal stress plots for the $\mathbb{P}_5$ optimized structure. (a) MATLAB FE implementation. (b) ABAQUS/Standard, linear-elastic solution.

gions present in the TO solution and removed for the CAD geometry exhibit minimal impact on the stress solution local to the high stress regions. Instead, stress is clearly reduced in the branched tensile members transferring load to the compression arch. Stress is concentrated instead in the member that extends the bottom-most main tension strut. This comparison further illustrates the detrimental, non-physical effect of the shear transfer regions. In transferring optimized structures to physically realized constructions these features must be properly removed through size-measure penalization.

In order to extend the ABAQUS FE analysis to consider strain softening and failure, both models used above are enriched using XFEM with a linear CZ relationship. It is posited that the geometric perturbations introduced by the iso2mesh utility will induce numerical stress concentrations along surface of the optimized structures. These concentrations will in effect act as blunt notches along the structural members, activating a Bažant Type II SEL behavior over the crack nucleation driven Type I SEL. With this hypothesis in mind, the ABAQUS/Standard models of the $\mathbb{P}_2$ and $\mathbb{P}_5$ optimized structures are enriched with the parameters described in **Section 3.8**. The energy contained in the CZ traction-separation relation is assumed to equal the value of $G_f = 59.8$ MPa$\sqrt{\text{mm}}$ obtained by Bell and Siegmund. For simplicity, infinitesimal strain assumptions are made for analyzing both structures. Each simulation is displacement controlled through 20 mm applied at the mid-point. Three different discretization settings are used to generate meshes of approximately fifty thousand, one-hundred thousand, and three-hundred thousand elements for each structure. Each discretization was enriched to determine the effects of mesh size and quality on the resulting cracking behavior.

The resulting XFEM status plots are given for both the $\mathbb{P}_2$ and $\mathbb{P}_5$ problems below in **Figure 4.72**. Load-displacement results for both cases are given in **Figure 4.73**. For both converged structure formulations, severe mesh dependency is observed. Crack nucleation localizes in different regions for each level of discretization for both size-dependent and -independent structures. Even for the $\mathbb{P}_2$ cases that exhibit a stress localization under the main compression truss region, no consistent nucleation trend is observed. Comparing load-displacement results, the $\mathbb{P}_2$ structures exhibit some level of consistency for peak load for finer discretization while the coarsest mesh remains linear-elastic for an extended range of displacement. Capturing a peak load capability for the $\mathbb{P}_5$ structures is even more of a challenge, with the coarsest discretization remaining linear elastic through the entire displacement range and the finer discretizations not exhibiting a clear load reduction at any point. The one-
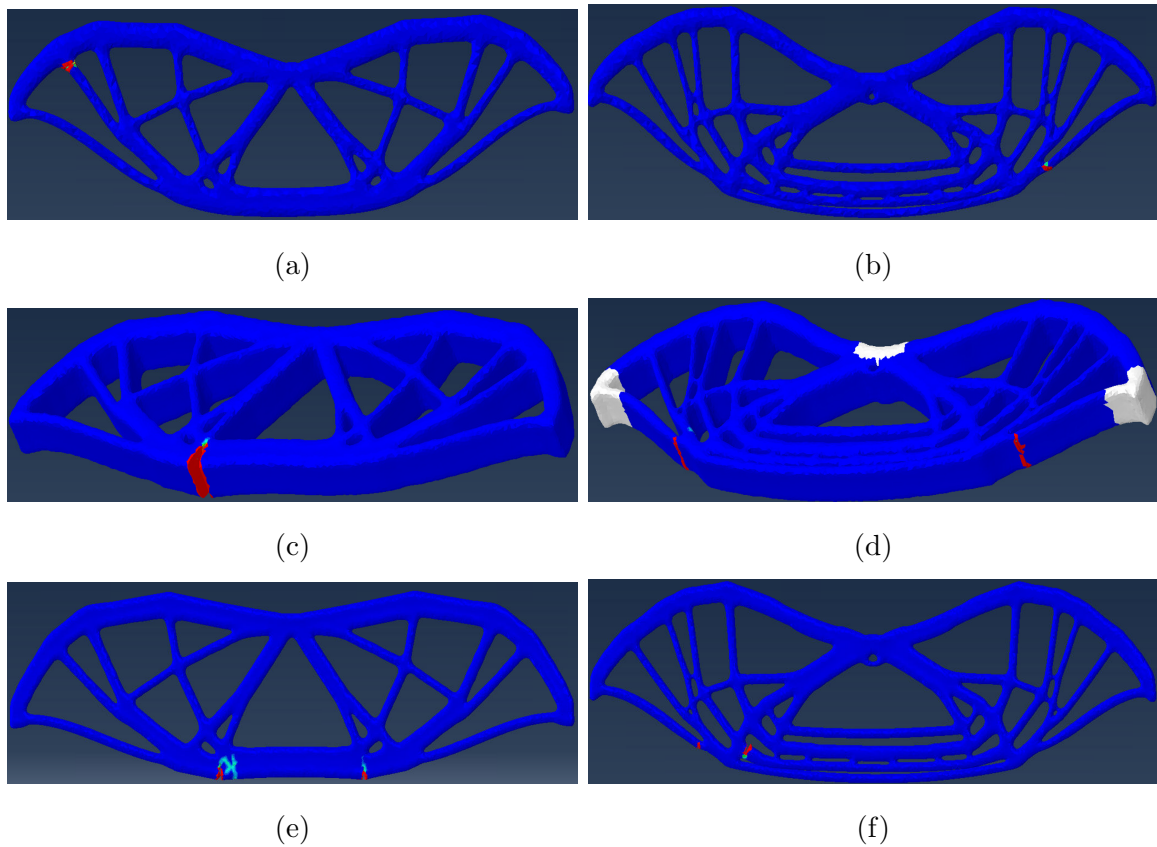
Figure 4.72. Failed element status for mesh dependence study of XFEM enriched ABAQUS/Standard models. (a) $\mathbb{P}_2$, approx. 50,000 elements; (b) $\mathbb{P}_5$, approx. 50,000 elements; (c) $\mathbb{P}_2$, approx. 100,000 elements; (d) $\mathbb{P}_5$, approx. 100,000 elements; (e) $\mathbb{P}_2$, approx. 300,000 elements; (f) $\mathbb{P}_5$, approx. 300,000 elements.

hundred thousand element discretization fails to converge for the simulation settings used.
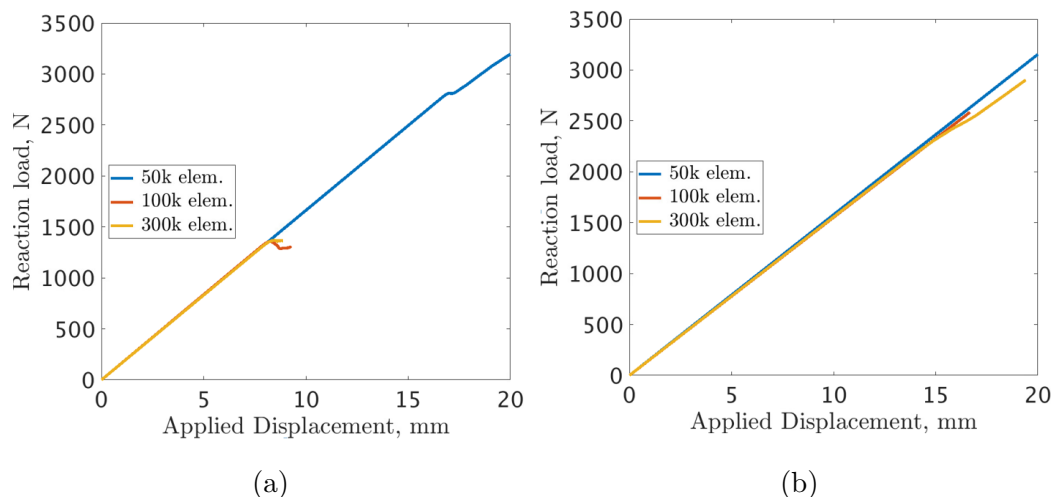
Figure 4.73. Load-displacement curves for XFEM enriched optimized structures analyzed with ABAQUS/Standard. (a) $\mathbb{P}_2$ converged structure meshes; (b) $\mathbb{P}_5$ converged structure meshes.

Having observed an extended linear-elastic region and inability of the model to resolve clear structural failure, the first principal stress results on the domain are interrogated in **Figure 4.74**. Maximum principal stress in each stress plot is capped at the traction separation strength of the CZ, 65 MPa. Regions in gray exceed this value. Both fifty-thousand element meshes are not presented due to the divergent load-displacement behavior.

From these plots, it is clear that the extended linear elastic behavior observed in the $\mathbb{P}_5$ structures occurs as a result of computational limitations. Looking at the $\mathbb{P}_2$ stress plots, both discretizations exhibit localized elevated stress regions about the propagating crack tips. Secondary high stress regions exist opposite the opening cracks for both discretizations, but their effect on load displacement likely occurs following the structure reaching peak load. In contrast, no clear principal stress localization occurs for the $\mathbb{P}_5$ structures. Instead, the majority of the tensile region deforms following linear-elasticity well past the point where strain softening should initiate. This result is indicative of the inability of the basic XFEM implementation available in ABAQUS to capture crack growth in regions of diffuse elevated stress levels. This occurs due to the limitation of the algorithm to capture strain soften-
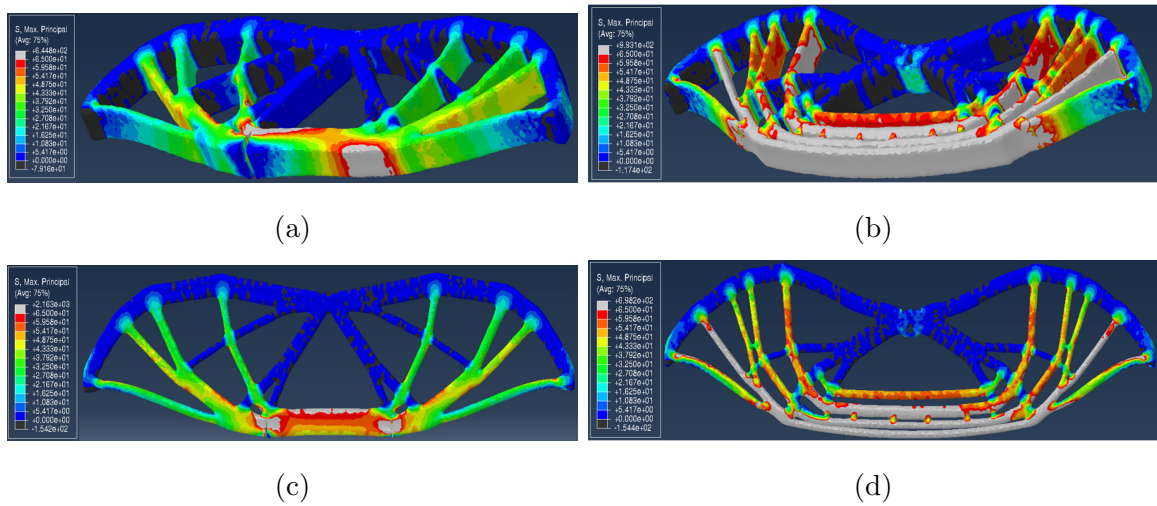
Figure 4.74. First principal stress plots for mesh dependence study of XFEM enriched ABAQUS/Standard models. (a) $\mathbb{P}_2$, approx. 50,000 elements; (b) $\mathbb{P}_5$, approx. 50,000 elements; (c) $\mathbb{P}_2$, approx. 100,000 elements; (d) $\mathbb{P}_5$, approx. 100,000 elements

ing or crack propagation in multiple elements across a single time-step. Because of this, propagation is initially computationally limited to the element which reaches the strain-softening first-principal stress criterion first. Crack growth is then largely limited to this initial nucleation location.

ABAQUS provides for an approach to limit this behavior through its multi-cracking formulation. Using this option, multiple cracks are enabled to initiate or propogation within a single computational time-step. While this feature is desirable in concept, in practice it is highly limited. Applying the multi-cracking formulation to each of the discretizations illustrated above yields computationally intractable results. Crack initiation localizes to "patches" of elements in close proximity to one another. Such crack patches are illustrated for the $\mathbb{P}_5$ structure with one-hundred thousand elements in **Figure 4.75**. Separation criteria are activated in multiple adjacent elements and ABAQUS is unable to calculate the separation surface normal in each simultaneously. This results in premature termination of the solution algorithm and lacks any meaningful physical interpretation.

Thus, despite the promise of the XFEM enriched CZM to capture the strain-softening behavior that underlies the quasi-brittle size effect, computational challenges make this form of computational validation intractable. Crack propagation may be observed under limited circumstances, however the manner in which cracks form and progress lacks consistency with the emergent stress fields and corresponding physical behavior.
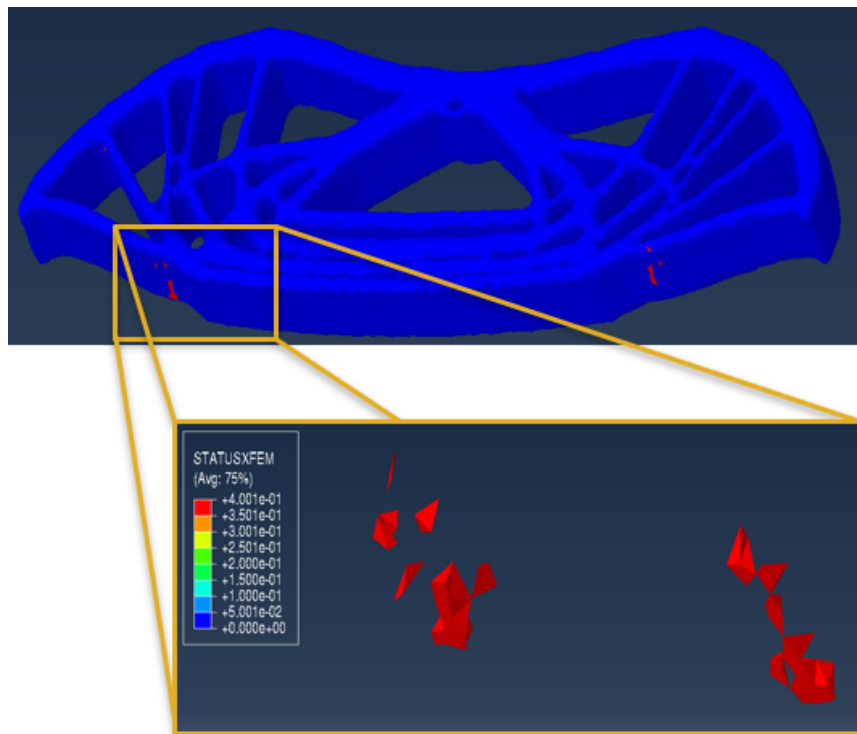
Figure 4.75. Localized activation of XFEM enriched elements in the ABAQUS multi-crack enabled framework.

5. CONCLUSIONS

Through extending traditional methods of density based topology optimization, the results of this thesis have demonstrated the necessity of size-dependent strength constraints in the Topology Optimization framework. The novel measure of local size proposed allows for reliable estimation of geometric features underlying the constraints. Together with this measure, the various empirical models of size dependence are considered within a multi-axial failure criterion framework. Care must be taken to retain consistency with the uniaxial failure characteristics of a given scaling law, however in general the chosen size-dependent failure surface was effectively enforced. With both features applied using common techniques found in academic Topology Optimization codes, formally converged structures were achieved for both volume and compliance objective formulations.

Returning to the central hypothesis, the resulting structures evidenced the significant of the various size-dependent models employed. For all scaling laws that exhibited a moderate strength-reduction across the allowable feature scale, remarkably distinct topologies arose. These ranged from the lamellar and cellular domains yielded by the traditional "smaller-is-stronger" brittle and quasibrittle frameworks to the bending dominated structures of the "smaller-is-weaker" fixed flaw models.

In investigating the effect of physical domains and implicit geometric restrictions on the Bažant SEL driven structures, further insight was gained on the effect of size dependence. Scaling the physical domain while maintaining material properties and geometric restrictions yielded converged topologies that illustrated clear correlation between feature size, the Bažant SEL, and convergence behavior. Through relaxing implicit geometric restrictions, structures were obtained that evidenced physically driven microstructures distinct from numerical artifacts such as checkerboarding.

These microstructural features are inherently tied to the mesh discretization and illustrate the mesh scale dependence when size-effects are considered.

Through all assumed scaling models, the empirical approaches used are limited by the physical assumptions required. Thus, while the proposed formulation captures complex physical failure phenomena efficiently through a simple FE framework, it loses generality. Each scaling model implies an assumed converged member configuration. To consider numerous failure models, the proposed approach requires successive treatment of the optimized structure under various failure model assumptions.

Finally, it is worth commenting on the physical validity of the proposed approach. Despite attempts to ground the assumptions of this thesis on rigorous mechanical approaches, experimental investigations validating the size-dependence of complex structures under multi-axial stress states is lacking. The physical validation efforts explored in this thesis attempted to add to this field, but were limited in scope. Thus, for real world implementation of the methods in this thesis a more rigorous experimental regime must be undertaken. This investigation must develop a clear multi-axial failure surface considering specimens across scales. Following this, optimized structures using the characterized material must realized using a fabrication approach capable of realizing complex structures across scales. Together, these efforts would validate the resulting converged structures and establish the physical implications of proposed topology optimization framework.

6. FUTURE WORK

While the arguments of this thesis have been presented in a self contained manner, numerous opportunities exist to extend and expand upon the work presented herein. Briefly, several different paths to explore are discussed below.

Strength singularity

Under the well known "smaller-is-stronger" models of size-dependence, the qp-relaxation framework for resolving the stress singularity works well. Both effects work to expand the feasible domain for vanishing material regions. However, inversiting the scaling relationship and instead considering "smaller-is-weaker" models such as the fixed-flaw framework reintroduces a singularity problem. This singularity is induced by a vanishingly small strength value for void regions that once again restricts the feasible domain. Following the qp-relaxation framework, local-strength could be relaxed to provide a consistent optimization problem. Doing so would alleviate the need for the ad-hoc elemental deactivation scheme used in this thesis.

Strain gradient size-effect: strength and elasticity

While the Bažant SEL used in this thesis provides good agreement with test results observed for physically large structures with significant FPZ and sub-critical crack growth, more general models of quasi-brittle scaling have been proposed. The more recent Universal Size Effect Law proposed by Bažant describes the scaling for quasi-brittle materials which fail at crack initiation while continuing to capture the effects of the original SEL. It is obviously desirable to incorporate this model into the proposed TO framework. However for general stress states, the Universal Size Effect Law requires calculation of stress-gradients in the domain. This would require a

significant reformulation of the underlying FE implementation and sensitivity analysis and is left to future exploration.

In implementing such a stess-gradient FE code, part of the work may be laid for also considering higher-order elasticity theories. It is well known that the Cosserat and non-local elasticity theories affect the stress state of materials across scales. These approaches have been considered separately in the field of TO. Combining size-dependent strength and elasticity models may further improve ability of TO to develop physically accurate microstructural domains.

Efficient multi-scale approaches

From the results obtained for the Bažant SEL constrained structures at finer mesh discretizations, the proposed formulation exhibits clear shortcomings for generating multi-scale features. The strength constraint clustering approach becomes prohibitively expensive at reasonable discretizations, limiting the ability of the proposed approach. Additionally, the only way to generate these microstructural features is to solve the entirety of the domain with a fine mesh, wasting significant computational resources in void dominated regions.

Future implementations of the framework of this thesis may consider more advanced clustering approaches such as those put forth by Kiyono et al. [36] or Wang and Qian [48]. Both develop a single aggregated measure of strength violation on the domain, reducing the number of constraints in the optimization problem. Further improvements may be made by implementing true multi-scale optimization techniques. These approaches explicitly consider the microstructure problem to develop efficient algorithms. Most are framed in terms of compliance objectives and significant effort may be required to consider stress-based terms.

Advanced geometry-dependent objectives and constraints

While the proposed geometry measure approach detailed in this thesis is used to generate an estimate of the local inscribed diameter, the amount of information obtained may be utilized for a diverse array of objectives and constraints. Inverting the p-norm formulation used yields the longest dense feature direction centered at the element of interest. This measure may be incorporated into a formulation that limits the length of structural members under compression as an alternate form of a buckling constraint. Different measures of local aspect ratio, undercut material, and others may also be possible.

Size-dependent materials and testing

As discussed in the conclusions section of this work, a more thorough material/process selection and characterization must be completed to validate the converged structures presented. Due to the breadth of mechanistic arguments of size-dependence considered, a similarly open scope of investigations may be undertaken. One of the more promising would consist of investigation of the size-dependence in emerging additively manufactured ceramic systems.

REFERENCES

REFERENCES

[1] M. P. Bendsøe and O. Sigmund. *Topology Optimization*. Springer Berlin Heidelberg, Berlin, Heidelberg, 2004.

[2] J. D. Deaton and R. V. Grandhi. A survey of structural and multidisciplinary continuum topology optimization: post 2000. *Structural and Multidisciplinary Optimization*, 49(1):1–38, 2014.

[3] J. Liu, A. T. Gaynor, S. Chen, Z. Kang, K. Suresh, A. Takezawa, L. Li, J. Kato, J. Tang, C. C. L. Wang, L. Cheng, X. Liang, and A. C. To. Current and future trends in topology optimization for additive manufacturing. *Structural and Multidisciplinary Optimization*, 57(6):2457–2483, 2018.

[4] M. P. Bendsøe and N. Kikuchi. Generating optimal topologies in structural design using a homogenization method. *Computer Methods in Applied Mechanics and Engineering*, 71(2):197–224, 1988.

[5] Z. P. Bažant. Size effect on structural strength: a review. *Archive of Applied Mechanics*, 69(9):703–725, 1999.

[6] A. Griffith and G. Taylor. The phenomena of rupture and flow in solids. *Philosophical Transactions of the Royal Society of London*, 221, 1921.

[7] W. Weibull. The phenomena of rupture in solids. *Proceedings of the Royal Swedish Institute*, 153:1–55, 1939.

[8] Z. P. Bažant, Y. Xi, and S. G. Reid. Statistical size effect in quasi-brittle structures: I. is weibull theory applicable? *Journal of Engineering Mechanics*, 117(11):2609–2622, 1991.

[9] H.M. Westergaard. Bearing pressures and cracks. *Journal of Applied Mechanics*, 6:49–53, 1939.

[10] G.R. Irwin. Analysis of stresses and strains near the end of a crack traversing a plate. *Journal of Applied Mechanics*, 24:361–364, 1957.

[11] J. R. Rice. A path independent integral and the approximate analysis of strain concentration by notches and cracks. *Journal of Applied Mechanics*, 35:379–386, 1968.

[12] Z. P. Bažant. Scaling laws in mechanics of failure. *Journal of Engineering Mechanics*, 119(9):1828–1844, 1993.

[13] Z. P. Bažant. Size effect in blunt fracture: concrete, rock, metal. *Journal of Engineering Mechanics*, 110(4):518–535, 1984.

[14] K. Duan, X. Hu, and F. H. Wittmann. Scaling of quasi-brittle fracture: Boundary and size effect. *Mechanics of Materials*, 38(1-2):128–141, 2006.

[15] N. A. Fleck, V. S. Deshpande, and M. F. Ashby. Micro-architectured materials: past, present and future. *Proceedings of the Royal Society A: Mathematical, Physical and Engineering Sciences*, 466(2121):2495–2516, 2010.

[16] L. C. Hwa, S. Rajoo, A. M. Noor, N. Ahmad, and M.B. Uday. Recent advances in 3d printing of porous ceramics: A review. *Current Opinion in Solid State and Materials Science*, 21(6):323–347, 2017.

[17] L. Yang and H Miyanaji. Ceramic additive manufacturing: A review of current status and challenges. In *Proceedings of the 28th Annual International Solid Freeform Fabrication Symposium - An Additive Manufacturing Conference*, pages 652–680, 2017.

[18] H. Cui, R. Hensleigh, H. Chen, and X. Zheng. Additive Manufacturing and size-dependent mechanical properties of three-dimensional microarchitected, high-temperature ceramic metamaterials. *Journal of Materials Research*, 33(03):360–371, 2018.

[19] W. X. Gu and J. R. Greer. Ultra-strong architected Cu meso-lattices. *Extreme Mechanics Letters*, 2:7–14, 2015.

[20] L. R. Meza, A. J. Zelhofer, N. Clarke, A. J. Mateos, D. M. Kochmann, and J. R. Greer. Resilient 3d hierarchical architected metamaterials. *Proceedings of the National Academy of Sciences*, 112(37):11502–11507, 2015.

[21] A. T. Lausic, A. G. Bird, C. A. Steeves, and G. B. Hibbard. Scale-dependent failure of stereolithographic polymer microtrusses in three-point bending. *Journal of Composite Materials*, 50(13):1739–1749, 2016.

[22] J. Bauer, A. Schroer, R. Schwaiger, and O. Kraft. The impact of size and loading direction on the strength of architected lattice materials. *Advanced Engineering Materials*, 18(9):1537–1543, 2016.

[23] O. Sigmund and K. Maute. Topology optimization approaches: A comparative review. *Structural and Multidisciplinary Optimization*, 48(6):1031–1055, 2013.

[24] G. I. N. Rozvany. A critical review of established methods of structural topology optimization. *Structural and Multidisciplinary Optimization*, 37(3):217–237, 2009.

[25] N. P. van Dijk, K. Maute, M. Langelaar, and F. van Keulen. Level-set methods for structural topology optimization: a review. *Structural and Multidisciplinary Optimization*, 48(3):437–472, 2013.

[26] M.P. Bendsøe. Optimal shape design as a material distribution problem. *Structural Optimization*, 1(4):193–202, 1989.

[27] M. Zhou and G.I.N. Rozvany. The COC algorithm, Part II: Topological, geometrical and generalized shape optimization. *Computer Methods in Applied Mechanics and Engineering*, 89(1-3):309–336, August 1991.

[28] T.W. Simpson, C. J. Dickman, S. N. K. Reddy, I. Ferguson, and M. Frecker. Topology optimization for additive manufacturing: a review of current capabilities and a real-world example. In *Volume 2A: 42nd Design Automation Conference*. ASME, 2016.

[29] C. Le, J. Norato, T. Bruns, C. Ha, and D. Tortorelli. Stress-based topology optimization for continua. *Structural and Multidisciplinary Optimization*, 41(4):605–620, 2010.

[30] G. Cheng and Z. Jiang. Study on toplogy optimization with stress constraints. *Engineering Optimization*, 20(2):129–148, 1992.

[31] G. D. Cheng and X. Guo. ϵ-relaxed approach in structural topology optimization. *Structural and Multidisciplinary Optimization*, 13(4):258–266, 1997.

[32] X. Guo, G. Cheng, and K. Yamazaki. A new approach for the solution of singular optima in truss topology optimization with stress and local buckling constraints. *Structural and Multidisciplinary Optimization*, 22(5):364–373, 2001.

[33] G. I. N. Rozvany and T. Birker. On singular topologies in exact layout optimization. *Structural Optimization*, 8(4):228–235, December 1994.

[34] M. Bruggi. On an alternative approach to stress constraints relaxation in topology optimization. *Structural and Multidisciplinary Optimization*, 36(2):125–141, 2008.

[35] E. Holmberg, B. Torstenfelt, and A. Klarbring. Stress constrained topology optimization. *Structural and Multidisciplinary Optimization*, 48(1):33–47, 2013.

[36] C.Y. Kiyono, S.L. Vatanabe, E.C.N. Silva, and J.N. Reddy. A new multi-p-norm formulation approach for stress-based topology optimization design. *Composite Structures*, 156:10–19, 2016.

[37] S. H. Jeong, S. H. Park, D. H. Choi, and G. H. Yoon. Topology optimization considering static failure theories for ductile and brittle materials. *Computers & Structures*, 110-111:116–132, 2012.

[38] D. Yang, H. Liu, W. Zhang, and S. Li. Stress-constrained topology optimization based on maximum stress measures. *Computers & Structures*, 198:23–39, 2018.

[39] P. Duysinx and M. P. Bendsøe. Topology optimization of continuum structures with local stress constraints. *International Journal for Numerical Methods in Engineering*, 43(8):1453–1478, 1998.

[40] O. C Zienkiewicz and R. L Taylor. *The finite element method for solid and structural mechanics*. Elsevier Butterworth-Heinemann, Amsterdam; Boston, 6th edition, 2005.

[41] G. Kreisselmeier and R. Steinhauser. Systematic control design by optimizing a vector performance index. In *IFAC Proceedings Volumes*, volume 12, pages 113–117, Zurich, Switzerland, 1979.

[42] G. Y. Qiu and X. S. Li. A note on the derivation of global stress constraints. *Structural and Multidisciplinary Optimization*, 40(1-6):625–628, 2010.

[43] Y.K. Park. *Extensions of optimal layout design using the homogenization method*. PhD thesis, University of Michigan, Ann Arbor, 1995.

[44] R. J. Yang and C. J. Chen. Stress-based topology optimization. *Structural optimization*, 12(2-3):98–105, 1996.

[45] P. Duysinx and O. Sigmund. New developments in handling stress constraints in optimal material distribution. In *7th AIAA/USAF/NASA/ISSMO Symposium on Multidisciplinary Analysis and Optimization, Multidisciplinary Analysis Optimization Conferences*. American Institute of Aeronautics and Astronautics, 1998.

[46] J. París, F. Navarrina, I. Colominas, and M. Casteleiro. Topology optimization of continuum structures with local and global stress constraints. *Structural and Multidisciplinary Optimization*, 39(4):419–437, 2009.

[47] J. París, F. Navarrina, I. Colominas, and M. Casteleiro. Block aggregation of stress constraints in topology optimization of structures. *Advances in Engineering Software*, 41(3):433–441, March 2010.

[48] C. Wang and X. Qian. Heaviside projection-based aggregation in stress-constrained topology optimization. *International Journal for Numerical Methods in Engineering*, 115(7):849–871, 2018.

[49] Y. Luo and Z. Kang. Topology optimization of continuum structures with Drucker–Prager yield stress constraints. *Computers & Structures*, 90-91:65–75, 2012.

[50] P. Duysinx, L. Van Miegroet, E. Lemaire, O. Brüls, and M. Bruyneel. Topology and generalized shape optimization: Why stress constraints are so important? *International Journal for Simulation and Multidisciplinary Design Optimization*, 2(4):253–258, 2008.

[51] J.T. Pereira, E.A. Fancello, and C.S. Barcellos. Topology optimization of continuum structures with material failure constraints. *Structural and Multidisciplinary Optimization*, 26(1-2):50–66, 2004.

[52] A. M. Mirzendehdel, B. Rankouhi, and K. Suresh. Strength-based topology optimization for anisotropic parts. *Additive Manufacturing*, 19:104–113, 2018.

[53] V. J. Challis, A. P. Roberts, and A. H. Wilkins. Fracture resistance via topology optimization. *Structural and Multidisciplinary Optimization*, 36(3):263–271, 2008.

[54] Z. Kang, P. Liu, and M. Li. Topology optimization considering fracture mechanics behaviors at specified locations. *Structural and Multidisciplinary Optimization*, 55(5):1847–1864, 2017.

[55] K. A. James and H. Waisman. Failure mitigation in optimal topology design using a coupled nonlinear continuum damage model. *Computer Methods in Applied Mechanics and Engineering*, 268:614–631, 2014.

[56] N. Aage, E. Andreassen, B. S. Lazarov, and O. Sigmund. Giga-voxel computational morphogenesis for structural design. *Nature*, 550(7674):84–86, 2017.

[57] M. Osanov and J. K. Guest. Topology Optimization for Architected Materials Design. *Annual Review of Materials Research*, 46(1):211–233, 2016.

[58] J. P. Groen and O. Sigmund. Homogenization-based topology optimization for high-resolution manufacturable microstructures. *International Journal for Numerical Methods in Engineering*, 113(8):1148–1163, 2018.

[59] H. Rodrigues, J.M. Guedes, and M.P. Bendsøe. Hierarchical optimization of material and structure. *Structural and Multidisciplinary Optimization*, 24(1):1–10, 2002.

[60] L. Xia and P. Breitkopf. Recent advances on topology optimization of multi-scale nonlinear structures. *Archives of Computational Methods in Engineering*, 24(2):227–249, 2017.

[61] J. Alexandersen and B. S. Lazarov. Topology optimisation of manufacturable microstructural details without length scale separation using a spectral coarse basis preconditioner. *Computer Methods in Applied Mechanics and Engineering*, 290:156–182, 2015.

[62] O. Pantz and K. Trabelsi. A post-treatment of the homogenization method in shape optimization. *SIAM Journal on Control and Optimization*, 47:1380–1398, 2009.

[63] S. Daynes, S. Feih, W. F. Lu, and J. Wei. Optimisation of functionally graded lattice structures using isostatic lines. *Materials & Design*, 127:215–223, 2017.

[64] O. Sigmund and K. Maute. Sensitivity filtering from a continuum mechanics perspective. *Structural and Multidisciplinary Optimization*, 46(4):471–475, 2012.

[65] B. S. Lazarov and O. Sigmund. Filters in topology optimization based on Helmholtz-type differential equations. *International Journal for Numerical Methods in Engineering*, 86(6):765–781, 2011.

[66] L. Li and K. Khandelwal. Topology optimization of structures with length-scale effects using elasticity with microstructure theory. *Computers & Structures*, 157:165–177, 2015.

[67] L. Li, G. Zhang, and K. Khandelwal. Topology optimization of structures with gradient elastic material. *Structural and Multidisciplinary Optimization*, 56(2):371–390, 2017.

[68] D. Veber and A. Taliercio. Topology optimization of three-dimensional non-centrosymmetric micropolar bodies. *Structural and Multidisciplinary Optimization*, 45(4):575–587, 2012.

[69] M. Bruggi and P. Duysinx. Topology optimization for minimum weight with compliance and stress constraints. *Structural and Multidisciplinary Optimization*, 46(3):369–384, September 2012.

[70] E. Lund. Shape optimization using Weibull statistics of brittle failure. *Structural Optimization*, 15(3-4):208–214, 1998.

[71] G. Rauchs. Shape optimization of ceramic components using a failure probability based on extended multiaxial Weibull theory. *Ceramics International*, 42(7):8360–8375, 2016.

[72] B. S. Lazarov, F. Wang, and O. Sigmund. Length scale and manufacturability in density-based topology optimization. *Archive of Applied Mechanics*, 86(1-2):189–218, 2016.

[73] A. Díaz and O. Sigmund. Checkerboard patterns in layout optimization. *Structural Optimization*, 10(1):40–45, 1995.

[74] T. E. Bruns and D. A. Tortorelli. Topology optimization of non-linear elastic structures and compliant mechanisms. *Computer Methods in Applied Mechanics and Engineering*, 190(26):3443–3459, 2001.

[75] T. E. Bruns and D. A. Tortorelli. An element removal and reintroduction strategy for the topology optimization of structures and compliant mechanisms. *International Journal for Numerical Methods in Engineering*, 57(10):1413–1430, 2003.

[76] O. Sigmund. Morphology-based black and white filters for topology optimization. *Structural and Multidisciplinary Optimization*, 33(4-5):401–424, 2007.

[77] J. K. Guest, J. H. Prévost, and T. Belytschko. Achieving minimum length scale in topology optimization using nodal design variables and projection functions. *International Journal for Numerical Methods in Engineering*, 61(2):238–254, 2004.

[78] O. Sigmund and J. Petersson. Numerical instabilities in topology optimization: A survey on procedures dealing with checkerboards, mesh-dependencies and local minima. *Structural Optimization*, 16(1):68–75, 1998.

[79] T. A. Poulsen. A new scheme for imposing a minimum length scale in topology optimization. *International Journal for Numerical Methods in Engineering*, 57(6):741–760, 2003.

[80] J. K. Guest. Imposing maximum length scale in topology optimization. *Structural and Multidisciplinary Optimization*, 37(5):463–473, February 2009.

[81] W. Zhang, W. Zhong, and X. Guo. An explicit length scale control approach in SIMP-based topology optimization. *Computer Methods in Applied Mechanics and Engineering*, 282:71–86, 2014.

[82] M. Zhou, B. S. Lazarov, F. Wang, and O. Sigmund. Minimum length scale in topology optimization by geometric constraints. *Computer Methods in Applied Mechanics and Engineering*, 293:266–282, 2015.

[83] A. T. Gaynor and J. K. Guest. Topology optimization considering overhang constraints: Eliminating sacrificial support material in additive manufacturing through design. *Structural and Multidisciplinary Optimization*, 54(5):1157–1172, 2016.

[84] M. Langelaar. An additive manufacturing filter for topology optimization of print-ready designs. *Structural and Multidisciplinary Optimization*, 55(3):871–883, 2017.

[85] M. Ohsaki. *Optimization of Finite Dimensional Structures*. CRC Press, 2010.

[86] J. Fish and T. Belytschko. *A First Course in Finite Elements*. John Wiley Sons Ltd, 2005.

[87] E. Andreassen, A. Clausen, M. Schevenels, B. S. Lazarov, and O. Sigmund. Efficient topology optimization in MATLAB using 88 lines of code. *Structural and Multidisciplinary Optimization*, 43(1):1–16, January 2011.

[88] J. D Deaton and R. V. Grandhi. Stress-based design of thermal structures via topology optimization. *Structural and Multidisciplinary Optimization*, 53(2):253–270, 2016.

[89] B. Bourdin. Filters in topology optimization. *International Journal for Numerical Methods in Engineering*, 50(9):2143–2158, 2001.

[90] M. Collet, M. Bruggi, and P. Duysinx. Topology optimization for minimum weight with compliance and simplified nominal stress constraints for fatigue resistance. *Structural and Multidisciplinary Optimization*, 55(3):839–855, 2017.

[91] F. Wang, B. S. Lazarov, and O. Sigmund. On projection methods, convergence and robust formulations in topology optimization. *Structural and Multidisciplinary Optimization*, 43(6):767–784, 2011.

[92] S. Xu, Y. Cai, and G. Cheng. Volume preserving nonlinear density filter based on heaviside functions. *Structural and Multidisciplinary Optimization*, 41(4):495–505, 2010.

[93] O. Sigmund and P.M. Clausen. Topology optimization using a mixed formulation: An alternative way to solve pressure load problems. *Computer Methods in Applied Mechanics and Engineering*, 196(13-16):1874–1889, 2007.

[94] J. H. Zhu, W. H. Zhang, and L. Xia. Topology optimization in aircraft and aerospace structures design. *Archives of Computational Methods in Engineering*, 23(4):595–622, 2016.

[95] K. Svanberg. The method of moving asymptotes - a new method for structural optimization. *International Journal for Numerical Methods in Engineering*, 24:359–373, 1987.

[96] K. Svanberg. A class of globally convergent optimization methods based on conservative convex separable approximations. *SIAM Journal on Optimization*, 12(2):555–573, 2002.

[97] Hu X. and Kai D. Size effect and quasi-brittle fracture: the role of the FPZ. *International Journal of Fracture*, 154:3–14, November 2008.

[98] Z. P. Bažant and J. Planas. *Fracture and size effect in concrete and other quasibrittle materials.* New directions in civil engineering. CRC Press, Boca Raton, 1998.

[99] Z. P. Bažant and M. T. Kazemi. Size dependence of concrete fracture energy determined by rilem work-of-fracture method. In *Current Trends in Concrete Fracture Research*, pages 121–138. Springer Netherlands, Dordrecht, 1991.

[100] A. Carpinteri, C. Marega, and A. Savadori. Size effects and ductile-brittle transition of polypropylene. *Journal of Materials Science*, 21:4173–4178, 1986.

[101] D. Bell and T. Siegmund. 3D-printed polymers exhibit a strength size effect. *Additive Manufacturing*, 21:658–665, 2018.

[102] C. G. Hoover and Z. P. Bažant. Universal Size-Shape Effect Law Based on Comprehensive Concrete Fracture Tests. *Journal of Engineering Mechanics*, 140(3):473–479, 2014.

[103] C. G. Hoover and Z. P. Bažant. Comprehensive concrete fracture tests: Size effects of types 1 and 2, crack length effect and postpeak. *Engineering Fracture Mechanics*, 110:281–289, 2013.

[104] H. Tada, P. C. Paris, and G. R. Irwin. *The stress analysis of cracks handbook*. The American Socicety of Mechanical Engineers, Three Park Avenue, New York, NY 10016, 2000.

[105] B. Gross and J. E. Srawley. Stress-instensity factors for a single-edge-notch tension specimen by boundary collocation of a stress function. *NASA TN D-3295*, 1966.

[106] R. S. Raghava and R. M. Caddell. A macroscopic yield criterion for crystalline polymers. *International Journal of Mechanical Sciences*, 15(12):967–974, 1973.

[107] D. C. Drucker and W. Prager. Soil mechanics and plastic analysis or limit design. *Quarterly of Applied Mathematics*, 10(2):157–165, 1952.

[108] R. M. Christensen. A comparative evaluation of three isotropic, two property failure theories. *Journal of Applied Mechanics*, 73(5):852–859, 2006.

[109] R. M. Christensen. Yield functions/failure criteria for isotropic materials. *Mathematical, Physical and Engineering Sciences*, 453(196):1473–1491, 1997.

[110] R. M. Christensen. A two-property yield, failure (fracture) criterion for homogenous, isotropic materials. *Journal of Engineering Materials and Technology*, 126(1):45–52, 2004.

[111] R. M. Christensen. Exploration of ductile, brittle failure characteristics through a two-parameter yield/failure criterion. *Materials Science and Engineering: A*, 394(1-2):417–424, 2005.

[112] R. M. Christensen. A comprehensive theory of yielding and failure for isotropic materials. *Journal of Engineering Materials and Technology*, 129(2):173–181, 2007.

[113] J.V. Carstensen and J. K. Guest. Projection-based two-phase minimum and maximum length scale control in topology optimization. *Structural and Multidisciplinary Optimization*, 58(5):1845–1860, 2018.

[114] J. E. Bresenham. Algorithm for computer control of a digital plotter. *IBM Systems Journal*, 4:25–30, 1965.

[115] C. Steger. An unbiased detector of curvilinear structures. *IEEE Transactions on Pattern Analysis and Machine Intelligence*, 20(2):113–125, 1998.

[116] P. Vogiatzis, S. Chen, and C. Zhou. A MATLAB code for integrated additive manufacturing and level-set based topology optimization. In *Volume 2B: 42nd Design Automation Conference*, page V02BT03A016, Charlotte, North Carolina, USA, 2016. ASME.

[117] S. Liu, Q. Li, J. Liu, W. Chen, and Y. Zhang. A realization method for transforming a topology optimization design into additive manufacturing structures. *Engineering*, 4(2):277–285, 2018.

[118] Q. Fang and D. A. Boas. Tetrahedral mesh generation from volumetric binary and grayscale images. In *2009 IEEE International Symposium on Biomedical Imaging: From Nano to Macro*, pages 1142–1145, 2009.

[119] The computational geometry algorithms library. https://www.cgal.org/. Accessed: 2019-02-18.

[120] G. Taubin. A signal processing approach to fair surface design. In *Proceedings of the 22nd Annual Conference on Computer Graphics and Interactive Techniques - SIGGRAPH '95*, pages 351–358, 1995.

[121] G.I Barenblatt. The mathematical theory of equilibrium cracks in brittle fracture. *Advances in Applied Mechanics*, 7:55–129, 1962.

[122] D. S. Dugdale. Yielding of steel sheets containing slits. *Journal of the Mechanics and Physics of Solids*, 8:101–104, 1960.

[123] N. Moës, J. Dolbow, and T. Belytschko. A finite element method for crack growth without remeshing. *International Journal for Numerical Methods in Engineering*, 46(1):131–150, 1999.

[124] C. G. Hoover and Z. P. Bažant. Cohesive crack, size effect, crack band and work-of-fracture models compared to comprehensive concrete fracture tests. *International Journal of Fracture*, 187:133–143, 2014.

[125] Connex 350 printer. Accessed: 2019-03-02.

[126] Stratasys. Vero material data sheet. Accessed: 2019-03-02.

[127] L. Bass, N. A. Meisel, and C. B. Williams. Exploring variability of orientation and aging effects in material properties of multi-material jetting parts. *Rapid Prototyping Journal*, 22(5):826–834, August 2016.

[128] Electro Force 3200 Test System. Accessed: 2019-03-02.

[129] UV Curing Apparatus (UVCA 2000). Accessed: 2019-03-02.

[130] K.P. Weiss, N Bagrets, C Lange, W Goldacker, and J Wohlgemuth. Thermal and mechanical properties of selected 3d printed thermoplastics in the cryogenic temperature regime. *IOP Conference Series: Materials Science and Engineering*, 102:012022, 2015.

[131] Instron. 3340 series universal testing systems. Accessed: 2019-03-02.

[132] Standard test methods for flexural properties of unreinforced and reinforced plastics and electrical insulating materials. Standard, ASTM International, West Conshohocken, PA, 2017.

[133] N. Olhoff, M. P. Bendsoe, and J. Rasmussen. On CAD-integrated structural topology and design optimization. *Computer Methods in Applied Mechanics and Engineering*, 89(1-3):259–279, 1991.

[134] E. Lee. *Stress-constrained structural topology optimization with design-dependent loads*. PhD thesis, University of Toronto, 2012.

[135] O. Sigmund, N. Aage, and E. Andreassen. On the (non-)optimality of Michell structures. *Structural and Multidisciplinary Optimization*, 54(2):361–373, 2016.

[136] G. I. N. Rozvany. Exact analytical solutions for some popular benchmark problems in topology optimization. *Structural Optimization*, 15(1):42–48, 1998.